GEOCHEMISTRY AND PETROGENESIS OF THE ARC-RELATED KÖSDAĞ METAVOLCANICS, SOUTHERN CENTRAL PONTIDES, NORTHERN TURKEY

A THESIS SUBMITTED TO
THE GRADUATE SCHOOL OF NATURAL AND APPLIED SCIENCES
OF
MIDDLE EAST TECHNICAL UNIVERSITY

BY

FARUK BERBER

IN PARTIAL FULFILLMENT OF THE REQUIREMENTS
FOR
THE DEGREE OF DOCTOR OF PHILOSOPHY
IN
GEOLOGICAL ENGINEERING

DECEMBER 2021

Approval of the thesis:

GEOCHEMISTRY AND PETROGENESIS OF THE ARC-RELATED KÖSDAĞ METAVOLCANICS, SOUTHERN CENTRAL PONTIDES, NORTHERN TURKEY

submitted by **FARUK BERBER** in partial fulfillment of the requirements for the degree of **Doctor of Philosophy** i**n Geological Engineering, Middle East Technical University** by,

Prof. Dr. Halil Kalıpçılar
Dean, Graduate School of **Natural and Applied Sciences** _____

Prof. Dr. Erdin Bozkurt
Head of the Department, **Geological Engineering** _____

Assoc. Prof. Dr. Kaan Sayıt
Supervisor, **Geological Engineering Dept., METU** _____

Examining Committee Members:

Assoc. Prof. Dr. Ersin Koralay
Geological Eng. Dept., Dokuz Eylül University _____

Assoc. Prof. Dr. Kaan Sayıt
Geological Eng. Dept., METU _____

Assoc. Prof. Dr. Biltan Kürkçüoğlu
Geological Eng. Dept., Hacettepe University _____

Assoc. Prof. Dr. Evren Çubukçu
Geological Eng. Dept., Hacettepe University _____

Assist. Prof. Dr. Ali İmer
Geological Eng. Dept., METU _____

Date: 27.12.2021

I hereby declare that all information in this document has been obtained and presented in accordance with academic rules and ethical conduct. I also declare that, as required by these rules and conduct, I have fully cited and referenced all material and results that are not original to this work.

Name Last name : Faruk Berber

Signature :

ABSTRACT

GEOCHEMISTRY AND PETROGENESIS OF THE ARC-RELATED KÖSDAĞ METAVOLCANICS, SOUTHERN CENTRAL PONTIDES, NORTHERN TURKEY

Berber, Faruk
Doctor of Philosophy, Geological Engineering
Supervisor : Assoc. Prof. Dr. Kaan Sayıt

December 2021, 290 pages

The Kösdağ Metavolcanics (KM) in the southern Central Pontides crops out between the Izmir-Ankara-Erzincan Suture Zone (IAESZ) in the south and the Sakarya Composite Terrane in the north. The unit is represented by a low-grade metamorphic assemblage including meta-basics, meta-intermediates, and meta-felsics, interlayered with recrystallized limestone, mudstone, and chert. While the unit is bounded to the north by the North Anatolian Fault Zone (NAFZ), the Dikmen Formation stratigraphically overlie the unit in the south.

Geochemically, the KM are sub-alkaline and divided into two main groups as Type 1 and Type 2, based on their relative Zr-Hf enrichment/depletion. The high Zr/Nb (3.3-85.8), low Zr/Y (0.6-6.9), and Nb/Y (0.02-0.19) ratios suggest that the KM have been derived from a depleted mantle source resembling that of N-MORBs. Positive ε_{Nd} values shown by the KM, ranging from + 2.9 to + 6.5, support the dominant involvement of depleted mantle source with a minor contribution from recycled and/or subduction components. Enrichment in Th and La compared to Nb (and Ta) indicates subduction-related magmatism fort he KM. The melting models imply derivation of the KM from a spinel lherzolitic source. LA-ICP-MS U-Pb

zircon ages of the KM range from 96.9 ± 1.3 Ma to 93.7 ± 1.2 Ma. Combined geological and geochemical evidence indicates an oceanic arc origin for the KM. The geodynamic model proposed in this study involves the presence of an intra-oceanic subduction zone during the early Late Cretaceous within the IAE branch of the Neotethys Ocean in the Central Pontides.

Keywords: Central Pontides, Early Late Cretaceous, Intra-oceanic Subduction, Izmir-Ankara-Erzincan Suture Zone, Kösdağ Metavolcanics

ÖZ

ORTA PONTİDLERİN GÜNEY KISMINDA YÜZEYLENEN YAY İLİŞKİLİ KÖSDAĞ METAVOLKANİKLERİNİN JEOKİMYASI VE PETROJENEZİ, KUZEY TÜRKİYE

Berber, Faruk
Doktora, Jeoloji Mühendisliği
Tez Yöneticisi: Doç. Dr. Kaan Sayıt

Aralık 2021, 290 sayfa

Orta Pontidlerde yer alan Kösdağ Metavolkanikleri güneyde İzmir-Ankara-Erzincan Kenet Zonu ile kuzeyde Sakarya Kompozit Birliği arasında yüzeylenmektedir. Birim rekristalize kireçtaşı, çamurtaşı, ve çört ile ardalanan meta-bazik, meta-ortaç ve meta-felsik kayaları içeren düşük dereceli metamorfik kayalar ile temsil edilmektedir. Birim kuzeyde Kuzey Anadolu Fay Zonu ile sınırlandırılırken, güneyde Dikmen Formasyonu birimi stratigrafik olarak üzerler.

Jeokimyasal olarak Kösdağ Metavolkanikleri subalkalendir ve Zr-Hf elementlerindeki zenginleşme/tükenmeye dayanarak Tip 1 ve Tip 2 olmak üzere iki ana gruba ayrılmaktadır. Yüksek Zr/Nb, düşük Zr/Y, ve Nb/Y oranları Kösdağ Metavolkaniklerinin N-MORB kaynağı benzeri, tüketilmiş bir manto kaynağından türediklerini göstermektedir. Birimin + 2.9'dan + 6.5'e değişen pozitif ε_{Nd} değerleri büyük ölçüde tüketilmiş bir mantodan türediğini ve daha az oranda geri dönüştürülmüş ve/veya dalma batma bileşeni katkısının da varlığını desteklemektedir. Th ve La elementlerince Nb (ve Ta)'ya kıyasla zenginleşme, dalma-batma ilişkili magmatizmayı işaret etmektedir. Ergime modelleri birimin spinel lerzolitik bir kaynaktan türediğini göstermektedir. LA-ICP-MS U-Pb zirkon

yaşları 96.9 ± 1.3 My'dan 93.7 ± 1.2 My'a değişmektedir. Jeolojik ve jeokimyasal kanıtlar Kösdağ Metavolkaniklerinin kökeni için okyanusal yayı işaret etmektedir. Bu çalışmada öne sürülen jeodinamik model Orta Pontidlerde Neotetis Okyanusunun İzmir-Ankara-Erzincan kolunun içerisinde erken Geç Kretase boyunca okyanus içi dalma-batma zonunun varlığını önermektedir.

Anahtar Kelimeler: Orta Pontidler, Erken Geç Kretase, Okyanus İçi Dalma Batma, İzmir-Ankara-Erzincan Kenet Zonu, Kösdağ Metavolkanikleri

To my beloved family

ACKNOWLEDGMENTS

First of all, I would like to thank my dissertation supervisor, Assoc. Prof. Dr. Kaan Sayıt, for his invaluable guidance, patience, endless support and encouragement throughout this thesis study. His guidance has helped me throughout the research and at every stage of this thesis study. I would like to express my appreciation to Prof. Dr. M. Cemal Göncüoğlu for his valuable recommendations and encouragements during this work. I would like to express that it is an honor for me to work with them. I am tremendously grateful for their support, both academically and personally.

I would like to thank Assoc. Prof. Dr. Biltan Kürkçüoğlu and Assist. Prof. Dr. Ali İmer, members of the thesis monitoring committee, for their contributions and recommendations improving the study. I would like to thank Daniel Stockli (The University of Texas at Austin) and Elizabeth Catlos (The University of Texas at Austin) for their collaborative approach regarding geochronological studies. I would also like to thank Assoc. Prof. Dr. Ersin Koralay for his assistance about geochronology aspect of the thesis during laboratory studies at Dokuz Eylül University.

I would like to express gratitude to my brother Samet Berber, as well as my friends Okay Çimen, Alican Aktağ, Mustafa Kaplan, Yavuz Kaya, Felat Dursun, Mustafa Yücel Kaya, Uğur Balcı, Sanem Elidemir and Çidem Argunhan for their continuous support and encouragements. I would like to thank Orhan Karaman and Zafer Kaplan for preparing thin sections. Last but not least, I would like to convey my heartfelt gratitude to my parents Nuriye Berber and Adil Berber, as well as my wife, Zeynep Başerer Berber, for their emotional support during this study. Finally, I would like to express my appreciation to the YÖK-ÖYP Programme.

TABLE OF CONTENTS

ABSTRACT……...v

ÖZ……vii

ACKNOWLEDGMENTS…….x

TABLE OF CONTENTS……..xi

LIST OF TABLES……...……..xvi

LIST OF FIGURES……..xviii

LIST OF ABBREVIATIONS……...…xxiv

CHAPTERS

1 INTRODUCTION……..1

1.1 Purpose and Scope..... 1

1.2 Previous Studies 7

1.3 Study Area 11

1.4 Methods of Study 12

1.4.1 Field Work 12

1.4.2 Laboratory Work..... 12

1.4.2.1 Analytical Methods……...……...….13

1.4.2.1.1 Petrographic Examinations……..……..13

1.4.2.1.2 Geochemical Analysis……...…...14

1.4.2.1.2.1 SEM-EDS Analysis……..…….……..……14

1.4.2.1.2.2 Whole-rock Geochemistry…….…….……....…14

1.4.2.1.2.3 Whole-rock Nd Isotope Analysis……...….15

1.4.2.1.2.4 U-Pb Geochronology Analysis……...15

2 GEOLOGY……...17

2.1 Regional Geology 17

2.1.1 Istanbul-Zonguldak Composite Terrane.....18

2.1.2 Intra-Pontide Suture Belt.....21

2.1.2.1 Çangaldağ Complex……..……22

2.1.2.2 Aylı Dağ Unit……...…….23

2.1.2.3 Arkot Dağ Unit…….……24

2.1.2.4 Emirköy Unit……..…….25

2.1.2.5 Daday Unit……25

2.1.2.6 Saka Unit……...……26

2.1.2.7 Damuz Dağ Unit……...……27

2.1.3 Sakarya Composite Terrane 28

2.1.4 Izmir – Ankara – Erzincan Suture Zone.....29

2.2 Local Geology.....31

2.2.1 Kunduz Metamorphics 31

2.2.2 Kösdağ Metavolcanics 32

2.2.3 The Dikmen Formation 44

2.2.4 The Kızılırmak Ophiolite 46

2.2.5 Cover Units 46

3 PETROGRAPHY…….49

3.1 Meta-basic Kösdağ Lithologies 51

3.1.1 Mineral Chemistry.....55

3.1.1.1 Clinopyroxene……...…55

3.1.1.2 Epidote……..…57

3.1.1.3 Chlorite……...……...59

3.1.2 Mineral Chemistry 62

3.1.2.1 Clinopyroxene……..….62

3.1.2.2 Plagioclase……...….64

3.1.2.3 Chlorite……..66

3.1.2.4 Epidote……..……68

3.2 Meta-intermediate Kösdağ Lithologies 68

3.2.1 Mineral Chemistry 71

3.2.1.1 Plagioclase……...…….….71

3.2.1.2 Epidote……..…73

3.3 Meta-felsic Kösdağ Lithologies 74

3.3.1 Mineral Chemistry 79

3.1.1.1 Chlorite……..….80

3.3.1.2 Epidote……..81

4 GEOCHEMISTRY……...83

4.1 Major and Trace Element Geochemistry..... 83

4.1.1 Effects of the Post-Magmatic Processes..... 92

4.1.2 Geochemical Classification 95

4.1.3 Major Oxide Variations 97

4.1.4 Trace Element Variations 98

4.1.5 Whole-rock Nd Isotope Geochemistry 102

4.2 Petrogenesis..... 105

4.2.1 Fractional Crystallization 105
4.2.2 Nature of the Source Region 110
4.2.3 Melting Model 118
5 GEOCHRONOLOGY……..……..127
5.1 U-Pb Geochronology 127
5.1.1 Meta-felsic Lithologies 130
5.1.2 Meta-intermediate Lithologies 135
6 DISCUSSION…….139
6.1 Field Observations 139
6.2 Petrographical Examinations 140
6.3 Geochemical Investigations 141
6.3.1 Tectonomagmatic Discrimination of the Kösdağ Metavolcanics 143
6.3.2 Magma Generation At Convergent Margins 150
6.3.2.1 Subduction derived components…….151
6.3.2.1.1 Slab derived fluids……..……152
6.3.2.1.2 Sediment addition……...….154
6.4 Mantle Wedge Modeling 158
6.5 Age of the Kösdağ Metavolcanics 162
6.6 Geodynamic Implications 163
7 CONCLUSIONS……..…...175
REFERENCES……..….177
APPENDICES
A. SEM-EDS Analysis..... 219
B. Detailed age data for the Kösdağ Metavolcanics..... 281

C. CL Images of the zircon grains from the Kösdağ Metavolcanics 287

CURRICULUM VITAE……290

LIST OF TABLES

TABLES

Table 3.1. Mineralogy, size range, abundance and distribution of the phenocrysts in the KM……..……50

Table 3.2. Mineral chemistry of the measured clinopyroxenes. Mineral formula calculations are based on 6 oxygens……...….56

Table 3.3. Mineral chemistry of the measured epidotes. Mineral formula calculations are based on 12.5 oxygens……...58

Table 3.4. Mineral chemistry of the measured chlorites. Mineral formula calculations are based on 28 oxygens…….….59

Table 3.5. Mineral chemistry of the measured clinopyroxenes. Mineral formula calculations are based on 6 oxygens……...….63

Table 3.6. Mineral chemistry of the measured plagioclases. Mineral formula calculations are based on 8 oxygens……....64

Table 3.7. Mineral chemistry of the measured chlorites. Mineral formula calculations are based on 28 oxygens…….….66

Table 3.8. Mineral chemistry of the measured epidotes. Mineral formula calculations are based on 12.5 oxygens…….…..68

Table 3.9. Mineral chemistry of the measured plagioclases. Mineral formula calculations are based on 8 oxygens……....72

Table 3.10. Mineral chemistry of the measured epidotes. Mineral formula calculations are based on 12.5 oxygens……...73

Table 3.11. Mineral chemistry of the measured chlorites. Mineral formula calculations are based on 28 oxygens……..80

Table 3.12. Mineral chemistry of the measured epidotes. Mineral formula calculations are based on 12.5 oxygens……...81

Table 4. 1. Major and trace element data of the Kösdağ Metavolcanics……..…..84

Table 4.2. Major oxide and trace element intervals of the Kösdağ Metavolcanics……101

Table 4. 3. Sm-Nd isotopic data of the Kösdağ Metavolcanics ……...……104

Table 4. 4. Element ratios used in the interpretation of the mantle source characteristics…….110

Table 4.5. Partition coefficients used in the melt modeling……...120

Table 5.1. Age data and number of zircon grains……...…..129

LIST OF FIGURES

FIGURES

Figure 1.1. Palaeogeographic reconstructions for Paleotetyhs and Neotethys oceans. 3
Figure 1.2. Subduction/accretion scenario of Okay (2000) for the Palaeotethyan ocean. 3
Figure 1.3. Northward subduction model of the Palaeotethyan ocean. 4
Figure 1.4. Tectonic map of Turkey illustrating the distribution of the Alpine terranes and suture belts. 5
Figure 1.5. Location map of the study area. 11
Figure 2.1. Geological sketch map of the Central Pontides. 20
Figure 2.2. A diagram illustrating the stratigraphy of the tectonic units within the Central Pontide Structural Complex. 22
Figure 2.3. Geological map of the study area. 33
Figure 2.4. Field view of Kösdağ meta-rhyolite on road to Karaköy village. 34
Figure 2.5. Alternation of chert, meta-rhyolite and meta-basalt on the road to the Yukarıdikmen village. 35
Figure 2.6. Development of foliation in the Kösdağ meta-andesites on the road to Dedem village. 36
Figure 2.7. The appearance of jointed Kösdağ meta-diabase on the main road connecting Tosya to Iskilip. 37
Figure 2.8. Field photograph showing cross-cutting relationship observed between meta-basalt dyke and meta-dacite members of the KM, south of the Kuşçular village. 38
Figure 2.9. Meta-basalt clasts with gas vesicles embedded in a carbonate matrix in lava breccia. 39
Figure 2.10. Boudinaged structures exhibiting effects of ductile deformation related to the faulting in the Kösdağ meta-andesites. 39

Figure 2.11. Alternation of pelagic limestone with chert nodules and meta-basalt near the Yukarıdikmen village. 40
Figure 2.12. Red chert nodules and/or bands within pelagic limestone north of the Yukarıdikmen village. 41
Figure 2.13. Field photograph of serpentinite slice within the KM, south of the Inceçay village. 42
Figure 2.14. Field view of the stratigraphic contact between the Dikmen limestone and Kösdağ meta-rhyolite in the north of the Kızılca village. 43
Figure 2.15. Field photograph of yellowish-colored, foliated recrystallized limestones of the Dikmen Formation on the Kızıltepe ridge. 44
Figure 2.16. Field photograph of the tectonic contact relationship between recrystallized limestones of Dikmen Formation and ophiolitic mélange of IAESZ. a) South of the Yukarıdikmen village, b-c) Northwestern of the village of Çukuralıç. 45
Figure 2.17. a) Field view of serpentinite within the ophiolitic mélange of the IAESZ b) Dikmen Formation is structurally underlain by the ophiolitic mélange of the IAESZ. 46
Figure 3.1. Randomly oriented plagioclase grains of varying size, indicating seriate texture in a fine-grained groundmass of non-foliated Kösdağ meta-basalt. 52
Figure 3.2. Photomicrograph of fractured clinopyroxene phenocryst in Kösdağ meta-basalt. 53
Figure 3.3. Kösdağ meta-basalt with flakes of chlorite and sericite oriented parallel to the foliation, together with abundant opaque grains 53
Figure 3.4. Photomicrograph of Kösdağ meta-basalt including chlorite and epidote 54
Figure 3.5. BSE images of the meta-basalt (AB-6-18) sample. Epidote (ep) + clinopyroxene (cpx) + titanite (ti) + chlorite (chl). 55
Figure 3.6. Pyroxene classification diagram (Morimoto et al., 1988) of the Kösdağ meta-basalt. 57

Figure 3.7. Plots of chlorite compositions in the classification scheme of Hey (1954). 60
Figure 3.8. Photomicrograph of Kösdağ meta-diabase consisting of mainly plagioclase, chlorite, and epidote 61
Figure 3.9. BSE images of the meta-diabase (KC-7-17) sample. Epidote (ep) + plagioclase (plg) + chlorite (chl) + quartz (qtz) + titanite (ti) + apatite (ap). 62
Figure 3.10. Pyroxene classification diagram (Morimoto et al., 1988) of the Kösdağ meta-diabase. 63
Figure 3.11. Classification of the plagioclases in the Kösdağ meta-diabase on ternary An-Ab-Or plot. 65
Figure 3.12. Plots of chlorite compositions in the classification scheme of Hey (1954). 67
Figure 3.13. Photomicrograph of porphyroclastic texture in the Kösdağ meta-andesite, characterized by plagioclase porphyroclasts 69
Figure 3.14. Plagioclase clusters making up glomeroporphyritic texture in the Kösdağ meta-andesite 70
Figure 3.15. Backscattered-Electron (BSE) micrographs of the Kösdağ meta-andesite (76) sample. 71
Figure 3.16. Classification of the plagioclases in the Kösdağ Metavolcanics on ternary An-Ab-Or plot. 72
Figure 3.17. Undulose extinction, which is an indicator of deformation as observed on quartz porphyroclasts in the Kösdağ meta-rhyolite 75
Figure 3.18. Quartz porphyroclast with rounded shape in meta-dacite 75
Figure 3.19. Mylonite produced by strong deformation of the meta-dacite, with quartz porphyroclasts surrounded by muscovites 76
Figure 3.20. Meta-rhyolite which comprises porphyroclasts of K-feldspar with first-order interference colors 77
Figure 3.21. The development of secondary mineral phases such as calcite and sericite on K-feldspar porphyroclast 78

Figure 3.22. Backscattered-Electron (BSE) micrographs of the Kösdağ meta-rhyolite (AD-2-18) sample. 79
Figure 3.23. Plots of chlorite compositions in the classification scheme of Hey (1954). 80
Figure 4.1. Plot of ionic radius against ionic charge for trace elements (Rollinson, (1993). 93
Figure 4.2. Diagrams depicting the variation of selected elements against Zr to check element mobility during post-magmatic events. 94
Figure 4.3. Multi-element patterns of the Kösdağ Metavolcanics 96
Figure 4.4. Classification of the KM samples on the TAS diagram 96
Figure 4.5. Chemical classification of the Kösdağ Metavolcanics 97
Figure 4.6. Classification of the KM on the basis of Th-Co diagram 100
Figure 4.7. REE patterns of the Kösdağ Metavolcanics 102
Figure 4.8. Bivariate plots of SiO_2 against selected major oxides for the Kösdağ Metavolcanics. 108
Figure 4.9. Bivariate plots of SiO_2 against trace elements for the Kösdağ Metavolcanics. 109
Figure 4.10. Plot of Zr/Y vs. Zr/Nb for the KM and modern arc environments…112
Figure 4.11. Plots of La/Yb vs. N-MORB normalized Zr value. Betts Cove boninites data from Bedard (1999). 113
Figure 4.12. Nb/Y vs. Zr/Y diagram. 114
Figure 4.13. Plot of ƐNd vs. Nb/Yb for the KM.. 115
Figure 4.14. Th/Yb vs. Nb/Yb diagram. 117
Figure 4.15. Chondrite-normalized spidergram showing modal batch melting of a spinel lherzolitic source and representative Kösdağ Metavolcanics. 119
Figure 4.16. Melting model of the Kösdağ Metavolcanics. 122
Figure 4.17. Melting model of the Kösdağ Metavolcanics. 124
Figure 4.18. Melting model of the Type 2b (boninitic) samples. 125
Figure 5.1. $^{206}Pb/^{238}U$ vs. $^{207}Pb/^{235}U$ diagram and concordia age for 197. 131
Figure 5.2. $^{206}Pb/^{238}U$ (weighted mean age) data for 197. 131

Figure 5.3. $^{206}Pb/^{238}U$ vs. $^{207}Pb/^{235}U$ diagram and concordia age for YD-1-18. 132
Figure 5.4. $^{206}Pb/^{238}U$ (weighted mean age) data for YD-1-18. 132
Figure 5.5. $^{206}Pb/^{238}U$ vs. $^{207}Pb/^{235}U$ diagram and concordia age for OR-4-18.....133
Figure 5.6. $^{206}Pb/^{238}U$ (weighted mean age) data for OR-4-18. 134
Figure 5.7. $^{206}Pb/^{238}U$ vs. $^{207}Pb/^{235}U$ diagram and lower intercept age for KR-5-18. 135
Figure 5.8. $^{206}Pb/^{238}U$ (weighted mean age) data for KR-5-18. 135
Figure 5.9. $^{206}Pb/^{238}U$ vs. $^{207}Pb/^{235}U$ diagram and concordia age for AB-6-17.....136
Figure 5.10. $^{206}Pb/^{238}U$ (weighted mean age) data for AB-6-17. 137
Figure 5.11. $^{206}Pb/^{238}U$ (weighted mean age) data for KR-13-17. 138
Figure 6.1. ƐNd value vs. major and trace elements. 143
Figure 6.2. N-MORB multi-element variation diagrams with a comparison between the Kösdağ Metavolcanics and Rio Grande Rift.. 144
Figure 6.3. Tectonomagmatic discrimination of the Kösdağ Metavolcanics 145
Figure 6.4. N-MORB multi-element variation diagrams 148
Figure 6.5. Radiogenic isotope data. 150
Figure 6.6. Ba/La vs. Th/Yb plot for the investigated Kösdağ Metavolcanics 153
Figure 6.7. Multi-element variation patterns of the sediment samples from modern arcs....155
Figure 6.8. Ba/Yb-Nb/Yb and Ba/Nb-Th/Nb plots 156
Figure 6.9. Nb/Sm vs. Th/Nb plot 158
Figure 6.10. Mantle wedge modeling based on Th and La concentrations (MW + %2 S + %3 F). 159
Figure 6.11. Mantle wedge modeling based on Th and La concentrations (MW + %1 S + %1 F). 160
Figure 6.12. Mantle wedge modeling based on Th and La concentrations (MW + %5 F). 161
Figure 6.13. Mantle wedge modeling based on Th and La concentrations (MW + %10 S). 162

Figure 6.14. N-MORB normalized multi-element and Chondrite-normalized REE spidergrams of the Kösdağ Metavolcanics, Yaylaçayı Formation and Kösdağ Formation 164
Figure 6.15. N-MORB normalized multi-element and Chondrite-normalized REE spidergrams of the Kösdağ Metavolcanics and Yerkuyu Unit. 166
Figure 6.16. N-MORB normalized multi-element and Chondrite-normalized REE spidergrams of the Kösdağ Metavolcanics and Tafano Unit 167
Figure 6.17. N-MORB normalized multi-element and Chondrite-normalized REE spidergrams of the Kösdağ Metavolcanics and Yüksekova Arc..... 169
Figure 6.18. Th/Yb vs. Nb/Yb diagram 171
Figure 6.19. Simplified cartoon depicting the geodynamic scenario of the Kösdağ Metavolcanics. 172

LIST OF ABBREVIATIONS

CPSC: Central Pontide Structural Complex

SCT: Sakarya Composite Terrane

IZCT: Istanbul-Zonguldak Composite Terrane

ATT: Anatolide-Tauride Terrane

IPS: Intra Pontide Suture

IPSB: Intra Pontide Suture Belt

IAE: Izmir-Ankara-Erzincan

IAESZ: Izmir-Ankara-Erzincan Suture Zone

MC-LA-ICP-MS: Multi Collector Laser Ablation Inductively Coupled Plasma Mass Spectrometer

ICP-MS: Inductively Coupled Plasma Mass Spectrometer

ICP-OES: Inductively Coupled Plasma Optical Emission Spectrometer

N-MORB: Normal Mid-Ocean Ridge Basalts

E-MORB: Enriched Mid-Ocean Ridge Basalts

OIB: Ocean Island Basalt

CHUR: Chondritic Uniform Reservoir

DM: Depleted Mantle

LREE: Light Rare Earth Elements

MREE: Middle Rare Earth Elements

HREE: Heavy Rare Earth Elements

LILE: Large Ion Lithophile Elements

HFSE: High Field Strength Elements

Chl: Chlorite

Ep: Epidote

Ser: Sericite

Plg: Plagioclase

Cpx: Clinopyroxene

Op: Opaque

Cal: Calcite

Qtz: Quartz

Kfs: K-feldspar

Mus: Muscovite

CHAPTER 1

INTRODUCTION

1.1 Purpose and Scope

Turkey, an E-W trending segment of the Alpine-Himalayan orogenic belt, is made up of distinct oceanic and continental microplates (Şengör and Yılmaz, 1981) or terranes (Göncüoğlu et al., 1997) originated from opening and closure of the Tethyan oceans (Göncüoğlu et al., 1997; Okay and Tüysüz, 1999; Şengör and Yılmaz, 1981). Turkey, sandwiched between the megacontinents Laurasia to the north and Gondwana to the south (Okay and Tüysüz, 1999; Stampfli, 2000; Şengör and Yılmaz, 1981), reached its current position as a result of several orogenic events (Cadomian/Pan African orogeny, Variscan orogeny, Cimmeride orogeny, and Alpine orogeny) related to the closure of the ancient oceanic domains, such as Rheic and Tethys (e.g., Göncüoğlu et al., 1997; Şengör, 1979; Şengör and Yılmaz, 1981; Şengör et al., 1988).

The Tethyan oceans were initially defined based on the time of initiation of the oceanic domain. For instance, Paleotethys is considered a Paleozoic ocean that existed from the middle/late Paleozoic until the Late Triassic (e.g., Stampfli and Borel, 2002; Şengör, 1979). On the other hand, Neotethys was initially thought to be a Mesozoic ocean (Şengör et al., 1984, 1988). Among these two, the lifetime of Paleotethys appears to be relatively well documented.

According to the geodynamic reconstructions (Bortolotti et al., 2013; Robertson, 2012; Schmid et al., 2008; Stampfli and Borel, 2002; Stampfli and Kozur, 2006) for the Eastern Mediterranean region, during the breakup of Pangea, a large east-west trending oceanic domain (i.e. the Palaeotethyan ocean) was existing between the Gondwana and Eurasian continental margins from the Early Permian to the

Triassic (Stampfli and Borel, 2002; Stampfli and Kozur, 2006). However, its geodynamic and palaeogeographic history is still controversial. The first reconstruction (Şengör and Yılmaz, 1981) claimed that the Palaeotethyan ocean was positioned north of the Sakarya microplate and was closed by southerly subductions (Figure 1.1a). Göncüoğlu et al. (1997, 2000, 2010), Sayit et al. (2010, 2011) and Sayıt and Göncüoğlu (2009, 2013) suggested the same location but recommended that Palaeotethyan Ocean was closed by two opposing dipping intra-oceanic subduction zones active at the end of the Triassic: a southward subduction beneath the Sakarya microplate, which produced the Karakaya Complex, and a northward subduction that produced a supra-subduction-type complex (i.e., Küre Complex; Kozur et al., 2000). Alternative models propose that the Paleotethys was positioned to the south of the Sakarya microplate and was closed by either a southward or northward subduction. There are two ideas that suggest different Palaeotethyan subduction polarity (Robertson et al., 1996). The occurrence of two oceanic basins separated by a magmatic arc is a common feature of both theories. However, the polarity of the subduction is a matter of debate. While several authors (Okay et al., 1996, 2002, 2006, 2015; Okay and Tüysüz, 1999; Okay, 2000; Robertson et al., 2004; Robertson and Ustaömer, 2011, 2012; Topuz et al., 2017) propose southward subduction (Figures 1.1b and 1.2), other authors (Stampfli and Borel, 2002; Ustaömer and Robertson, 1994) supported northward subduction (Figures 1.1c and 1.3). In these models, the subduction events that resulted in the closure of the Palaeotethyan Ocean led to the formation of several oceanic basins, commonly referred to as the Neotethyan oceanic domain (Bortolotti and Principi, 2005).

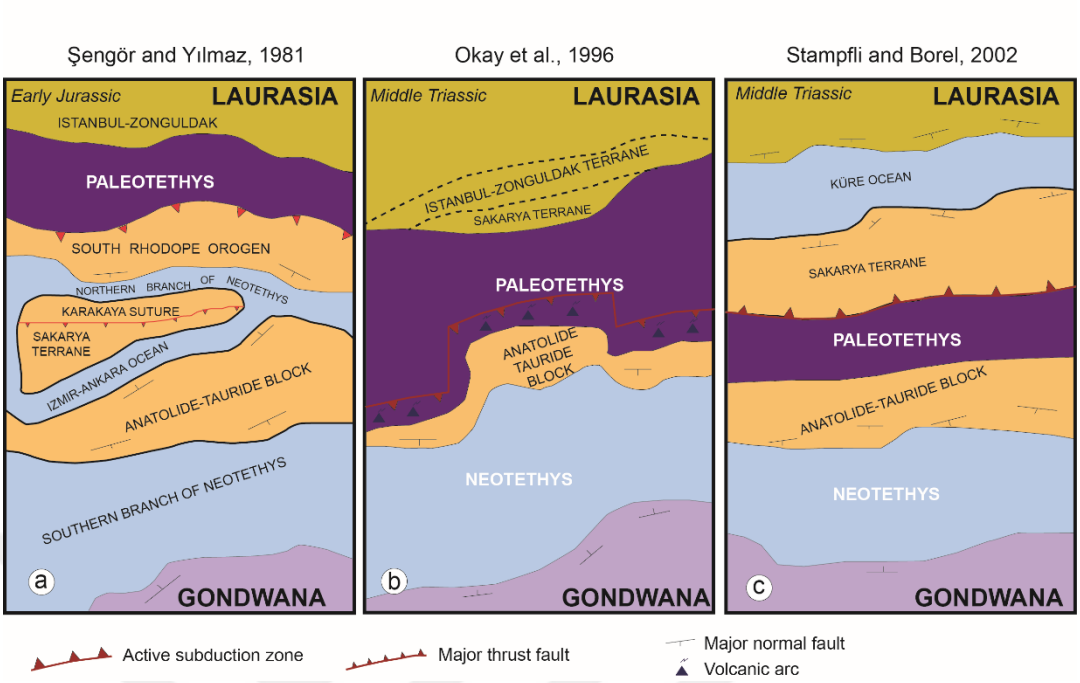


Figure 1.1. Palaeogeographic reconstructions for Paleotetyhs and Neotethys (taken from Marroni et al., 2020).

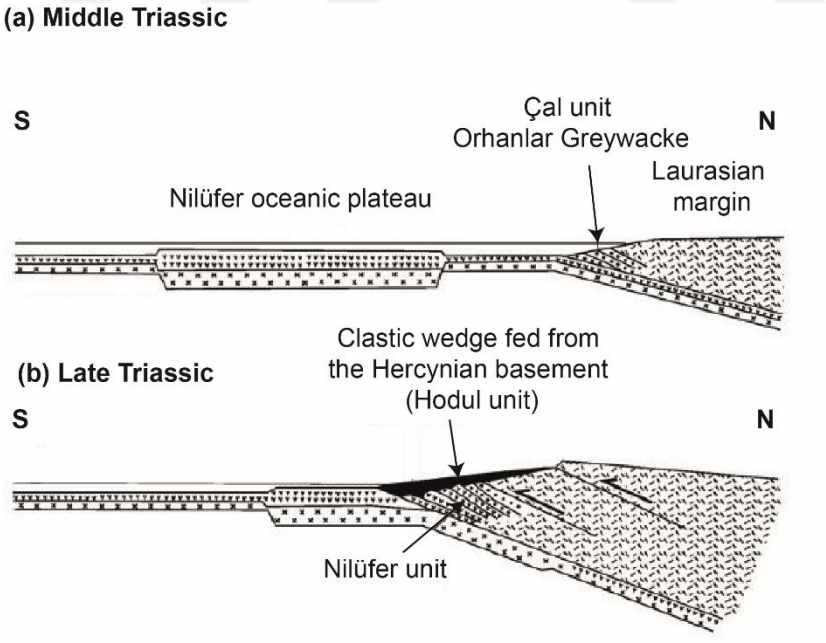


Figure 1.2. Subduction/accretion scenario of Okay (2000) for the Palaeotethyan ocean.

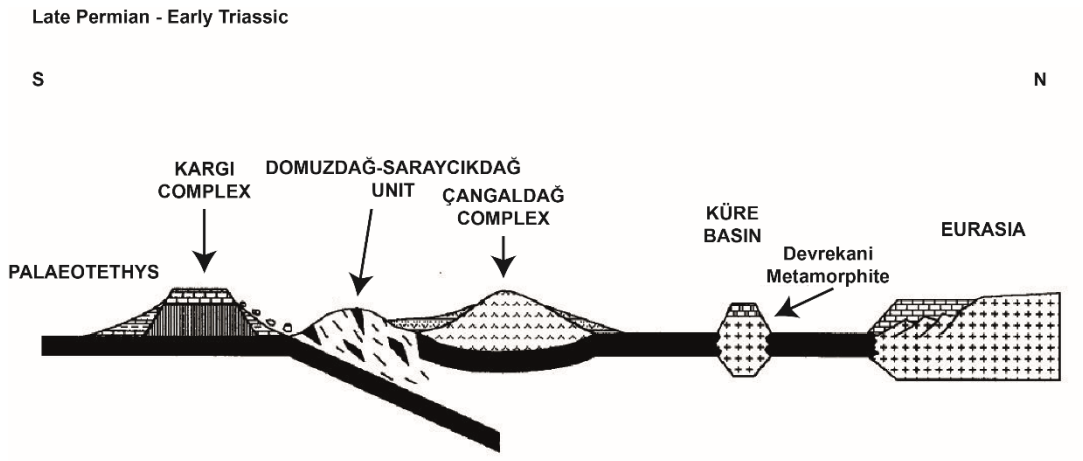


Figure 1.3. Northward subduction model of the Palaeotethyan ocean (taken from Ustaömer and Robertson, 1999).

The evolution of Neotethys, on the other hand, is hotly debated, particularly in terms of its opening history (Göncüoğlu et al., 2000; Moix et al., 2008; Sayit et al., 2017; Şengör and Yılmaz, 1981). The complexity regarding the Neotethyan history is mainly due to its multibranched character and the conjunction of some Neotethyan relics with those of Paleotethys in certain areas (e.g., Şengör and Yılmaz, 1981). Neotethys is divided into at least two branches in Turkey: northern Neotethys and southern Neotethys (Figure 1.1a).

The origin of the southern branch of Neotethys is relatively well understood; it possibly opened before the Triassic, with a rifting stage that occurred during the middle Permian (Lapierre et al., 2004; Maury et al., 2003; Şengör and Yılmaz, 1981) (Figure 1.1a). The evolution of the northern branch of Neotethys, on the other hand, is more problematic. In Turkey, the northern realm is defined by the Izmir-Ankara-Erzincan (IAE) and Intra-Pontide oceans (Şengör and Yılmaz, 1981). The opening of the IAE Ocean was previously believed to have taken place in the Liassic (Görür et al., 1983); however, recent findings suggest that the birth of this oceanic realm occurred in the pre-Liassic (Bortolotti et al., 2013; Göncüoglu et al., 2010; Sayit et al., 2017; Tekin and Göncüoglu, 2007; Tekin et al. 2002, 2016b), involving an early Permian rifting (late Asselian; Tekin et al., 2019). Based on the recent evidence, it can be inferred that the existence of Paleotethys and Neotethys oceans overlapped during the early/middle Permian-Triassic periods.

In northern Turkey, the relics of the IAE Ocean are exposed along the Izmir-Ankara-Erzincan Suture Zone (IAESZ), which consists of various components of the oceanic lithosphere as well as subduction-accretion complexes (e.g., melange complexes). The IAESZ is situated between the Sakarya Composite Terrane (SCT) to the north and the Tauride-Anatolide Terrane (TAT) to the south (Çelik et al., 2013; Göncüoğlu et al., 1997; Özkan et al., 2020; Sayit et al., 2022; Tekin et al., 2002) (Figure 1.4) and extends towards the east along the Sevan-Akera Suture (e.g., Rolland et al., 2019; Şengör and Yılmaz, 1981).

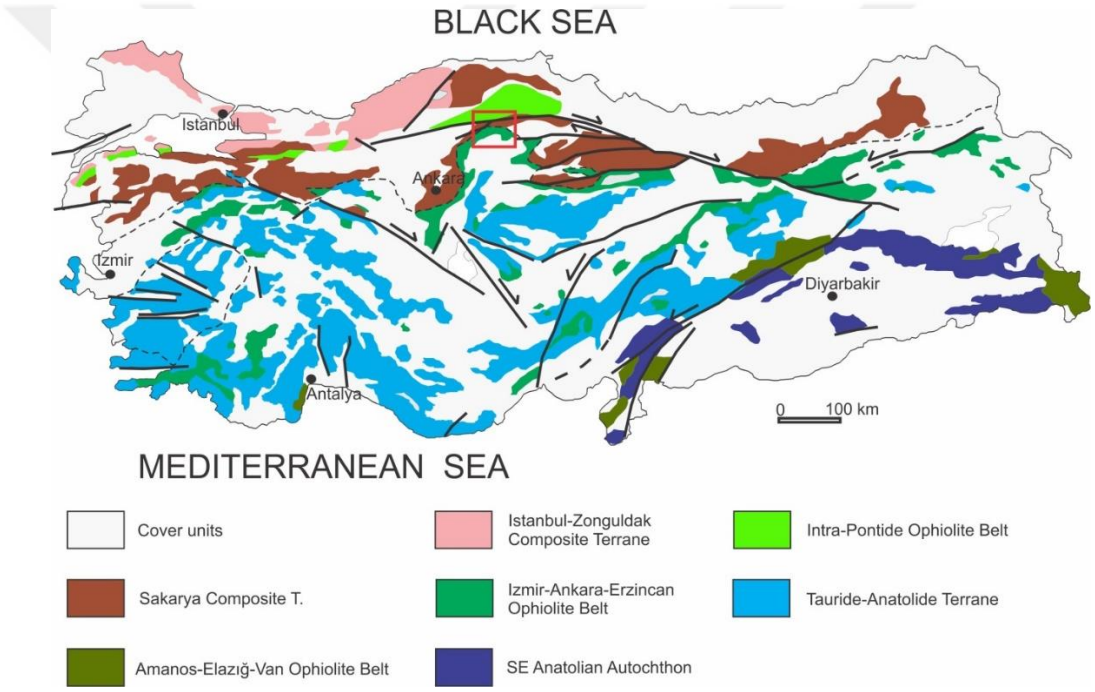


Figure 1.4. Tectonic map of Turkey illustrating the distribution of the Alpine terranes and suture belts (modified from Göncüoğlu, 2010).

The IAESZ includes several subduction-related fragments ranging in age from Middle Triassic to Late Cretaceous based on paleontological and radiometric data (Aygül et al., 2015; Balcı and Sayit, 2020; Berber et al., 2021; Bortolotti et al., 2018; Çelik et al., 2011; Çimen, 2020; Ellero et al., 2015b; Parlak et al., 2013a; Sayit et al., 2015, 2017; Tekin et al., 2019; Tüysüz, 1990; Tüysüz et al., 1995). While there are many subduction-related fragments within the ophiolitic mélange representing the IAESZ, there are few partially preserved oceanic arc sequences,

including volcaniclastics, lava flows, and associated marine sediments. These oceanic arc sequences are not a part of the suture belt but occur as distinct tectonic slices. The Kösdağ Metavolcanics (KM) is one of such oceanic arc sequences.

The KM, the main focus of this thesis, is a belt of low-grade metavolcanic rocks intercalated with pelagic limestone, chert, and mudstone. Tectonically, the unit is situated in one of the most complex regions of the country. The region was affected by the processes related to the consumption of the Neotethys ocean during the latest Mesozoic. Later tectonic events in the region occurred due to the development of the North Anatolian Fault Zone (NAFZ) (Aygül et al., 2015; Berber et al., 2014; Şengör et al., 1983, 2005). In its current position, the KM and its cover is located between the IAESZ to the south and the SCT to the north (Figure 1.4). In addition, the KM lie at the junction point of the Istanbul-Zonguldak Composite Terrane (IZCT), the SCT, and the Central Anatolian Crystalline Complex (CACC) of the TAT. However, the contact relationships of the KM with the neighboring main tectonic units are hidden by the right lateral NAFZ (e.g., Barka, 1992) that runs through the study area with its numerous splays to the north.

Most of the studies on the KM focused on the geological aspects. Although the geological maps of the unit were prepared during these studies, a detailed mapping exists only for specific sectors of the unit. For example, Tüysüz (1985) mapped a large area in his study; however, its map lacks details when the entire KM are considered. On the other hand, the geological maps by Berber (2015) and Aygül et al. (2015) include more details in this respect, yet their mapping covered only the western section of the KM. Thus, a detailed mapping focusing on the entire areal extent of the KM would be necessary to better understand the contact relationships with the surrounding units. Also, although the lithological content of the KM is known, the spatial distribution of the lithologies within the whole unit is lacking. Another essential point is that although the geology of the KM is relatively well known, the unit has been studied in terms of geochemical and tectonomagmatic aspects only in recent years. (Aygül et al., 2015; Berber, 2015; Berber et al., 2014, 2016, 2021). Among these, Berber (2015) and Berber et al. (2021) included the most detailed geochemical and petrogenetic features thus far from the KM.

However, these latter studies concentrated only on the trace element geochemistry without any isotope data and did not involve a detailed characterization of the mantle source, particularly on understanding the subduction component. In addition, the age of the unit is another issue to be clarified. The precise radiometric ages on the KM were provided recently; the study of Aygül et al. (2015) was the first to provide U-Pb zircon ages, and more ages came from Berber et al. (2021). Although both studies yielded similar ages (93.8 ± 1.9 and 94.4 ± 1.4 Ma, Aygül et al., 2015; 94.64 ± 0.77 Ma and 113.2 ± 2.3 Ma; Berber et al., 2021), their data are based on a small number of meta-rhyolitic and meta-andesitic samples collected in a limited area. Thus, the validity of this age for the entire unit has remained unclear.

This thesis study, thus, aims to fill these gaps by i) preparing a detailed geological map of the entire unit, ii) providing lithological descriptions with enhanced sampling resolution, iii) presenting trace element geochemistry on the entire unit, iv) providing the whole-rock Nd isotopic data (for the first time), and v) presenting precise U-Pb zircon age data on more samples. This will, in turn, allow putting solid constraints, particularly on the petrogenesis of the KM, and also help understanding its geodynamic evolution within the Neotethyan context.

1.2 Previous Studies

Preliminary studies carried out in Tosya and its vicinity generally focused on tectonics and economic geology, while the number of geological studies remained relatively scarce. Pilz (1937) conducted the first geological studies in Tosya and the surrounding areas for nickel exploration, whereas Blumenthal (1939, 1948, 1950) prepared 1/100.000 scaled geological maps of the region. Ayaroğlu (1980) mentioned the geology and economic significance of the northwestern part of the Tosya district. In order to clarify geological problems and contribute to the interpretation of the geological evolution of the region, Hakyemez et al. (1986) prepared a geological report on the studied area.

As stated before, the KM were studied by a limited number of researchers. These researchers named the unit differently based on the area where the unit is exposed. The first nomenclature was proposed by Yoldaş (1982) as Karabürçek Formation. Later, the unit were named the Kösdağ Metamorphics by Yılmaz and Tüysüz (1984). Hakyemez et al. (1986), on the other hand, also preferred calling the unit Karabürçek Formation. Tüysüz (1990) defined the unit as the Kösdağ Unit in his study. Towards the south, Tüysüz et al. (1995) identified a different unit, which they called the Yaylaçayı Formation. Although the Yaylaçayı Formation reflects some differences relative to the KM, it was considered in this study as the equivalent of KM in terms of age, geology, and geochemistry. Sayit et al. (2022) also recognized similar geological and geochemical features in the lithologies to the west, around the Ilgaz district, which they called the Yerkuyu Unit.

Among these studies, there is a consensus on the lithological content of the unit. Yoldaş (1982) regarded the unit as consisting of chlorite-carbonate-quartz schist, chlorite-albite-quartz-epidote schist, metavolcanic rocks, spilite, diabase, andesite, and slightly recrystallized limestone. The unit is composed dominantly of metavolcanics, and to a lesser extent volcanoclastics, pelagic sediments, and ophiolitic lithologies (Yılmaz and Tüysüz, 1984). Hakyemez et al. (1986) pointed out that the unit is characterized by schists, carbonate rocks, and metavolcanics. Tüysüz (1990) mentioned that the Kösdağ Unit consists of dominantly felsic volcanics and volcanogenic clasts. Tüysüz et al. (1995) proposed that the Yaylaçayı Formation, which is the equivalent of the KM, comprises dominantly volcanic rocks, including basalts, andesites, and dacites with a lesser amount of their pyroclastic equivalents, agglomerates, and tuffites.

While the geological features of the KM are somewhat well-constrained, the number of studies focusing on the geochemical characteristics is very limited. Berber et al. (2014) were the first to draw attention to the geochemical features of the unit. These authors stated that the KM are represented by a broad spectrum of subalkaline magmas, ranging in composition from basalt to dacites. They also indicated that the unit involved a strong slab-derived component in their genesis, thus considering the unit as reflecting arc-related magmatism. This idea was also

adopted by Aygül et al. (2015) and further supported by Berber et al. (2021). In their recent work on the Yerkuyu Unit (the equivalent of the KM), Sayit et al. (2022) also identified similar geochemical features and implied a subduction-related genesis for the unit. Tüysüz et al. (1995) also suggested arc-related features for their Yaylaçayı Formation; however, they also noted the presence of OIB-type features in the volcanics, thus differing from the previous views.

The ages ascribed to the KM vary significantly between the Early Triassic and Late Cretaceous. On the basis of regional correlation, Yoldaş (1982) suggested a Lower Triassic age for the Karabürçek Formation. In contrast, Yılmaz and Tüysüz (1984) proposed that the age of the Kösdağ Metamorphics is Liassic or pre-Liassic also based on regional correlation. From the carbonates of the Yaylacık Formation, which has been considered the equivalent of the Dikmen Formation, Hakyemez et al. (1986) revealed a microfauna representing Late Jurassic-Early Cretaceous ages. This puts an upper age limit for the KM, thus suggesting that the KM must be Late Jurassic – Early Cretaceous or older. Tüysüz et al. (1988), on the other hand, recommended a younger age, ascribing an Upper Cretaceous age to the unit, based on the microfossils from the micritic limestones intercalated with the mafic lavas. A similar age was also obtained from the pelagic limestones overlying the Yaylaçayı Volcanics, which yielded Cenomanian-Turonian ages for the unit (Tüysüz et al., 1995). On the other hand, Berber et al. (2014) highlighted the lithological and geochemical similarities between the KM and the Mudurnu Volcanics. Based on this, they claimed that the age of the Kösedağ Metavolcanics could be the Early to Middle Jurassic as the Mudurnu Volcanics. However, it was later realized that the age of the KM is not older than Cretaceous (Aygül et al., 2015; Berber et al., 2016, 2021). Aygül et al. (2015) proposed a Late Cretaceous U-Pb zircon ages (93.8 ± 1.9 Ma and 94.4 ± 1.9 Ma) for the age of magmatism, which was also supported by Berber et al. (2021). The metamorphism of the unit has occurred 69.9 ± 0.4 Ma based on ^{40}Ar-^{39}Ar dating (Aygül et al., 2015).

Apart from the works performed directly on the KM or its equivalents, there are also regional studies in which the KM were not investigated directly but included in their geological maps. For example, Ustaömer and Robertson (1999) interpreted

the Kösdağ unit as the Late Cretaceous arc rocks. Okay et al. (2006) mapped the KM as the Upper Cretaceous accretionary complex. Çelik et al. (2011), on the other hand, mapped the KM as a Jurassic-Eocene sedimentary sequence of the Sakarya Zone.

There is a general consensus that the KM developed in a subduction-related environment (Aygül et al., 2015; Berber, 2015; Berber et al., 2014, 2016, 2021; Tüysüz, 1985, 1990). Tüysüz (1985) suggested that volcanic rocks of the Kösdağ unit were formed in an island arc environment according to geochemical characteristics of the investigated rock samples. Tüysüz (1990) stated that the Kösdağ Unit characterizes a typical ensimatic island arc assemblage. The volcanic rocks of the Yaylaçayı Formation were generated in two different tectonic settings, involving island arc and hot-spot magmatisms based on geochemical features of the studied rock samples (Tüysüz et al., 1995). Recently, Berber et al. (2014) indicated that trace element systematics of the KM implies arc-like characteristics and further proposed that the KM formed above an intra-oceanic subduction zone. This idea has been supported by different studies in the following years (Aygül et al., 2015; Berber, 2015; Berber et al., 2016, 2021).

The NAFZ constituting the northern boundary of the study area has critical importance in terms of the geology of the study area and its vicinity in northern Turkey. It extends for approximately 1350 km from Gulf of Saros (Aegean Sea) in the west to Karlıova (Bingöl) in the east (Koçyiğit et al., 2001; Şengör et al., 2003; Taymaz et al., 1991). This transform fault was created by the tectonic activity between Arabian and Eurasian plates along the Bitlis Zagros Suture Zone. There are several different approaches to explain the collision process as continental subduction (Rotstein and Kafka, 1982), lithospheric thickening (Dewey et al., 1986), lithospheric delamination (Pearce et al., 1990), or another convergence accommodation between Arabian and Eurasian plates through the westward movement escape (Jackson and McKenzie, 1988; McKenzie, 1976; Şengör and Kidd, 1979) and/or the counter-clockwise rotation of the Anatolian block (Piper et al., 2010; Reilinger et al., 1997; Rotstein, 1984). Şengör et al. (1985) and Dewey et al. (1986) suggested a late Miocene (13 Ma) time was for the initiation of the

NAFZ. This age is also in agreement with the Late Miocene to Early Pliocene interval proposed by Barka (1992).

1.3 Study Area

The study area is located approximately 20 km southeast of the Tosya district, which is almost 105 km south of the city of Kastamonu (Figure 1.5). The study area is bounded by the NAFZ from the north and covers an area of around 140 km^2 in the G-32 a1, G-32 a2, G-32 b1, G-32 b2, F-32 d3, F32 c4, F-32 c3 quadrangles of 1/25.000 scale topographic maps of Turkey.

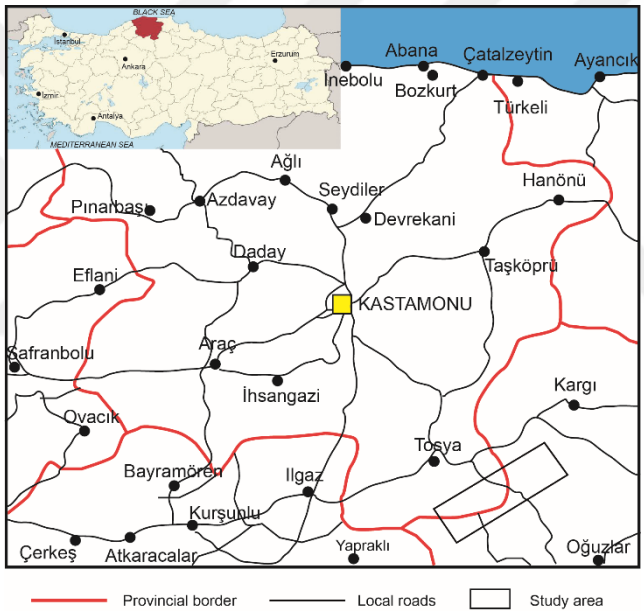


Figure 1.5. Location map of the study area.

There are asphalt roads connecting Tosya and İskilip, Tosya and Kargı, Kargı and Osmancık to reach the study area. The main villages in the western part of the study area are Aşağıdikmen, Dedem, Sofular, and Yukarıdikmen. On the other hand, the main villages located in the eastern part of the study area are Ortalıca, Karaköy, Abdullah, İnceçay, Bektaşlar, Gökomuz and Çukuralıç. Kösdağ, which gives its name to the studied metavolcanics, is the highest peak in the investigated area.

1.4 Methods of Study

There are two major components of this study; field work and laboratory work.

1.4.1 Field Work

The field work was conducted in the summers of 2016, 2017, 2018, and 2019. The field works aimed to reveal the contact relationship both within the KM and between the KM and adjacent units (Dikmen Formation and ophiolitic mélange). Also, a detailed 1/25.000 scaled geological map of the study area was prepared. This represents the first geological map covering the entire KM unit. In addition, to understand the petrological features of the KM, approximately 250 representative rock samples were collected, including dominantly metavolcanics and a lesser amount of volcaniclastic and sedimentary rocks such as recrystallized limestones, cherts, and mudstones.

1.4.2 Laboratory Work

Petrographic and geochemical examinations are the two primary stages of the laboratory work.

1.4.2.1 Analytical Methods

1.4.2.1.1 Petrographic Examinations

For the examination of the metavolcanics, a total of 110 thin sections were prepared from the relatively fresh rock samples, which have not been strongly affected by the weathering processes. The preparation of thin-sections was carried out at the laboratories of the Department of Geological Engineering at Middle East Technical University (METU, Turkey). The prepared thin-sections were examined using a polarizing microscope (Olympus CX31 PF) at the Crustal Research Laboratory of the same department. Thin-section images were taken by a digital

camera system attached to the Olympus SC30 microscope. After a careful examination of the thin sections, the samples were filtered, deciding which rock samples were to be geochemically and/or isotopically analyzed. In addition, with the help of these observations, the selection of rock samples suitable for the radiometric age dating was also realized.

1.4.2.1.2 Geochemical Analysis

Whole-rock geochemistry and isotope studies constituted the parts of geochemical analyses.

1.4.2.1.2.1 SEM-EDS Analysis

Scanning electron microscopy and energy dispersive spectrometry (SEM-EDS) analyses were performed at Hacettepe University Research and Application Center on Advanced Technologies (HUNITEK) using Tescan GAIA 3 field emission SEM and integrated Oxford XMAX 150 energy dispersive spectrometer. The working conditions were as follows: 10 kV accelerating voltage, 800 pA beam current and 35 s counting times at 9 mm working distance.

1.4.2.1.2.2 Whole-rock Geochemistry

The whole-rock geochemistry was performed on 67 relatively less weathered rock samples. Major oxides were determined by inductively coupled plasma-optical emission spectrometer (ICP-OES), whereas rare earth and other trace elements were measured by inductively coupled plasma-mass spectrometer (ICP-MS) at the Acme Analytical Laboratories Ltd. (Vancouver, Canada), following a lithium borate fusion and nitric acid digestion. In contrast, Ni and Pb were measured by ICP-MS after aqua regia digestion. The accuracy and precision of the analyses were enabled by measuring duplicate samples and standards. Based on replicate sample runs and standards, the precision for most major and trace elements was greater than 5%.

Detection limits were stated as percentage (%) for major oxides, while parts-per-million (ppm) for trace elements. The detection limits range from 0.01 ppm (Tb, Tm, and Lu) to 0.3 ppm (Nd) for REE and from 0.1 ppm (Rb, Zr, Nb, Y, Cs, Ta, Hf, and U) to 8 ppm for other trace elements in these analyses.

1.4.2.1.2.3 Whole-rock Nd Isotope Analysis

Sixteen rock samples were analyzed for neodymium (Nd) isotopic compositions in the Central Laboratory at METU utilizing multi-collector thermal ionization mass spectrometry (TIMS). Nd isotope geochemistry experiments were carried out following the instruction TLM-ARGL-02 (Nd isotope ratio analysis experiment instruction) based on the methods given in detail and conditions in Köksal (2019). All chemical preparations such as weighing, chemical dissolving, and chromotography were carried out using ultrapure water and chemical materials at class 100 cleanliness standards in clean laboratory conditions. Approximately 80 milligrams of samples were weighed and transferred to teflon PFA vials. Samples in 4 ml 52% HF were kept on the heating plate at >100 ^{0}C for four days. Accordingly, they were completely dissolved. Samples dried close to evaporation on the heating plate were resolved in 4 ml of 6 N HCI for one day on the heating plate.

Furthermore, it was dried close to evaporation on a heating plate and taken into 1 ml of 2.5 N HCI, and then prepared for chromatography. Rare earth elements were collected by using 2 ml volume Bio-Rad AG50 W-X8 (100-200 mesh) resin using 2.5 N HCI after separation of major elements in teflon pan. Nd was separated from other rare earth elements with the aid of 0.22 N HCL acid and measured in static mode using the re-filament technique. Eventually, $^{143}Nd/^{144}Nd$ ratios were normalized using a $^{146}Nd/^{144}Nd$ ratio of 0.7219. Nd La Jolla standard was measured as 0.511853 ± 5 (n=5). Thermo-Fisher Triton TIMS was used to measure isotopic ratios. No bias correction was performed for the Nd analyses. The analytical uncertainties are at 2 σ level.

1.4.2.1.2.4 U-Pb Geochronology Analysis

The heavy mineral separation procedures were carried out at the departments of Geological Engineering at METU, Hacettepe University, and Dokuz Eylül University. Firstly, all rock samples were crushed by using jaw and roll crushers. The crushed materials were broken into smaller pieces by grinding process. Then, the ground materials were sieved into different fractions between 63 μm and 500 μm by using various sieves at the sample preparation laboratories of METU and Hacettepe University. The remaining steps mentioned below were completed in the sample preparation laboratory within the Department of Geological Engineering at Dokuz Eylül University. The wilfley table was used extensively to distinguish the heavier mineral fractions such as zircon from lighter ones. On the basis of their magnetic properties, the separated heavy minerals were discriminated as magnetic and nonmagnetic ones using a Frantz Isodynamic Magnetic Separator. Further separation of heavy minerals was performed using bromoform (CHBr3) and diiodomethane, high-density liquids. Then, zircon crystals were extracted among the nonmagnetic heavy minerals under a binocular microscope.

Process Flow Chart: Grind → Sieve → Wilfley table → Magnetic separation → Heavy liquids → Mineral concentrate

The hand-picked zircon grains were then mounted in epoxy resin and polished to expose zircon interiors in the sample preparation laboratory in the Department of Geological Engineering at Dokuz Eylül University. CL imaging and the U-Pb radiometric dating of zircon grains were conducted at the Jackson School of Geosciences, the University of Texas at Austin (USA). Zircons were photographed under cathodoluminescence (CL) to enable easy and best location on the mount during ICP-MS analyses. The analyses were performed using a Laser Ablation Inductively Coupled Plasma Mass Spectrometry (LA-ICP-MS). The comprehensive process and results are presented in Chapter 5, Appendices B and C.

CHAPTER 2

GEOLOGY

2.1 Regional Geology

The Pontides are a mountain chain between the Black Sea and the IAESZ in northern Anatolia. Before the opening of the Black Sea as a back-arc basin in the Late Cretaceous (Okay et al., 1994, 2013), the Pontides belonged to the continental margin of Laurasia. The IZCT and the SCT are tectonic units constituting the Pontides. The IZCT is separated from the SCT by the IPSB (Figure 1.4) (Göncüoğlu et al., 1997; Göncüoğlu, 2010).

The geology of the Central Pontides has been studied by many researchers (Aygül et al., 2015, 2016; Aydın et al., 1986, 1995a, 1995b; Berber et al., 2014, 2016, 2021; Boztuğ, 1986, 1987, 1988, 1992a, 1992b; Boztuğ et al., 1995; Çimen et al., 2016, 2017; Ellero et al., 2015; Frassi et al., 2016, 2017, 2020; Genç and Tüysüz, 2010; Göncüoğlu et al., 2000, 2008, 2012, 2014; Gücer et al., 2016; Marroni et al., 2014, 2020; Nzegge, 2008; Nzegge et al., 2006; Okay and Göncüoğlu, 2004; Okay et al., 2004, 2006, 2013, 2014; Sayit et al., 2016; Şengün et al., 1988; Tüysüz, 1985, 1990, 1993, 1999; Uğuz and Sevin, 2007; Ustaömer and Robertson, 1993, 1999; Yılmaz, 1980, 1981, 1983, 1988; Yılmaz and Şengör, 1985; Yılmaz and Tüysüz, 1984, 1991, 1994, 1999; Yılmaz et al., 1997). This area is made up of the IZCT, the SCT, and a subduction-accretion complex known as the CPSC (Central Pontide Structural Complex), which characterizes the remnants of the Intra-Pontide Suture (Figure 1.4). The IZCT, overthrusting both the SCT and the CPSC, is situated to the west of the Central Pontides. It is distinguished by its non-metamorphic Paleozoic successions that overlie a Cadomian basement. The IZCT, the SCT and the members of the IPSB are juxtaposed in the Central Pontides by thrusts or parts of the NAFZ. The IPSB in this region is characterized by the CPSC (Tekin et al.,

2012), characterizing the relics of the IPO (Çimen et al., 2016; Frassi et al., 2016, 2017, 2020; Göncüoğlu et al., 2012, 2014; Marroni et al., 2020; Sayit et al., 2016). From north to south, the CPSC consists of the Çangaldağ Complex, Aylı Dağ Ophiolite, Arkot Dağ Mélange, Emirköy unit, Daday unit, Saka unit and Domuz Dağ unit (Figure 2.1). These tectonic units have been studied by many authors (Aydın et al., 1995; Aygül et al., 2016; Çimen et al., 2016; Frassi et al., 2016, 2017, 2020; Göncüoğlu et al., 2012, 2014; Günay et al., 2016; Marroni et al., 2014, 2020; Okay and Nikishin, 2015; Okay et al., 2013, 2014, 2015; Sayit et al., 2016; Tüysüz, 1990; Ustaömer and Robertson, 1999). To the south of the CPSC, there lie several units, including Kunduz Metamorphics, Kirazbaşı Mélange, Dikmen Formation, Late Cretaceous Mélange, Eocene volcanics, and the KM. The KM are bounded by the NAFZ and the CPSC from the north. The NAFZ is a 1200 km-long dextral strike-slip zone, has a significant impact on the geology of the studied area. The rocks influenced by the fault are strongly sheared and mylonitized, which is particularly noticable towards the northern boundary of the study area. The Late Cretaceous mélanges and fore-arc sediments, which are referred as the "Kirazbaşı Complex" of Tüysüz (1985, 1986) and Tüysüz and Tekin (2007), overthrust the KM (Aygül et al., 2015). The KM are bounded to the south stratigraphically by the Dikmen Formation. On the other hand, the contact relationship between the Dikmen Formation and ophiolitic mélange is tectonic. The mélange unit is composed by blocks of serpentinites, gabbros, pillow-basalts, pelagic limestones, and radiolarian cherts, thrust onto the recrystallized limestones of the Dikmen Formation (Tüysüz, 1990).

2.1.1 Istanbul-Zonguldak Composite Terrane

This terrane has been defined under various names by different authors; the Istanbul Nappe (Şengör, 1984); the Istanbul Zone (Okay, 1989); Istanbul–Zonguldak Zone (Yılmaz et al., 1997); Istanbul–Zonguldak Unit (IZU) (Yiğitbaş et al., 1999); or Istanbul–Zonguldak Composite Terrane (IZCT; Göncüoğlu et al., 1997). The term IZCT will be preferred in this study. The IZCT consists of a Late Neoproterozoic Cadomian crystalline basement (Göncüoğlu, 2019; Ustaömer and

Rogers, 1999) unconformably overlain by well-developed Paleozoic sequence ranging from Ordovician to the Carboniferous in age (Göncüoğlu et al., 1997, 2010; Görür et al., 1997), including fluvial conglomerates and shallow-marine clastics (Göncüoğlu, 2019). This Cadomian basement is composed of paragneisses, meta-gabbros, orthoamphibolites and amphibole-gneisses, and basic igneous rocks cut by arc-type granitoids (500 ma, Ustaömer and Rogers, 1999) are Permian granitoids intrude into the Paleozoic sequence (Okay et al., 2013; Şahin et al., 2009). Permo-Triassic red beds and Middle Jurassic lacustrine limestone unconformably cover the Paleozoic sequence (Okay et al., 2015). The depositional properties of the Istanbul and Zonguldak terranes vary significantly after the Silurian period (Göncüoğlu, 2019). For example, the Istanbul Terrane displayed a characteristic deepening from platform to slope and then flysch deposits (Özgül, 2012). In contrast, the Zonguldak Terrane underwent a thermal process between Middle Silurian and pre-Middle Devonian (Bozkaya et al., 2012b). It was a stable platform environment from the Middle Devonian to Late Lower Carboniferous and included fluvial deposits in the Middle Carboniferous (Yanev et al., 2006). It can be said that different paths were followed by both terranes during the Variscan cycle. The Permian granitoids reflect the magmatic activity of the Variscan orogeny in the Istanbul Terrane (Şahin et al., 2010). Both terranes are covered by continental clastics of the Late Permian age (Okuyucu et al., 2017).

Widespread Middle Jurassic continental arc magmatism cuts the basement units (Çimen et al., 2017, 2018; Okay et al., 2014). Çangaldağ Pluton including dacites, diorites, porphyries, and to a lesser amount of granites is one of these Jurassic units (Çimen et al., 2017). Previous studies have argued that this large intrusive body cuts the Çangaldağ Metamorphic Complex (Aydın et al., 1995; Yılmaz and Boztuğ, 1986) in the South and the Triassic Küre Complex in the east. It is overlain by Upper Jurassic Inaltı Formation. Recently, Çimen et al. (2017) provided U-Pb zircon ages of Middle Jurassic (161 ± 5 Ma and 170 ± 2 Ma). Consequently, they suggested that the Çangaldağ Pluton is part of a Middle Jurassic arc system, and developed within a continental arc during northward subduction of the Intra Pontide Ocean.

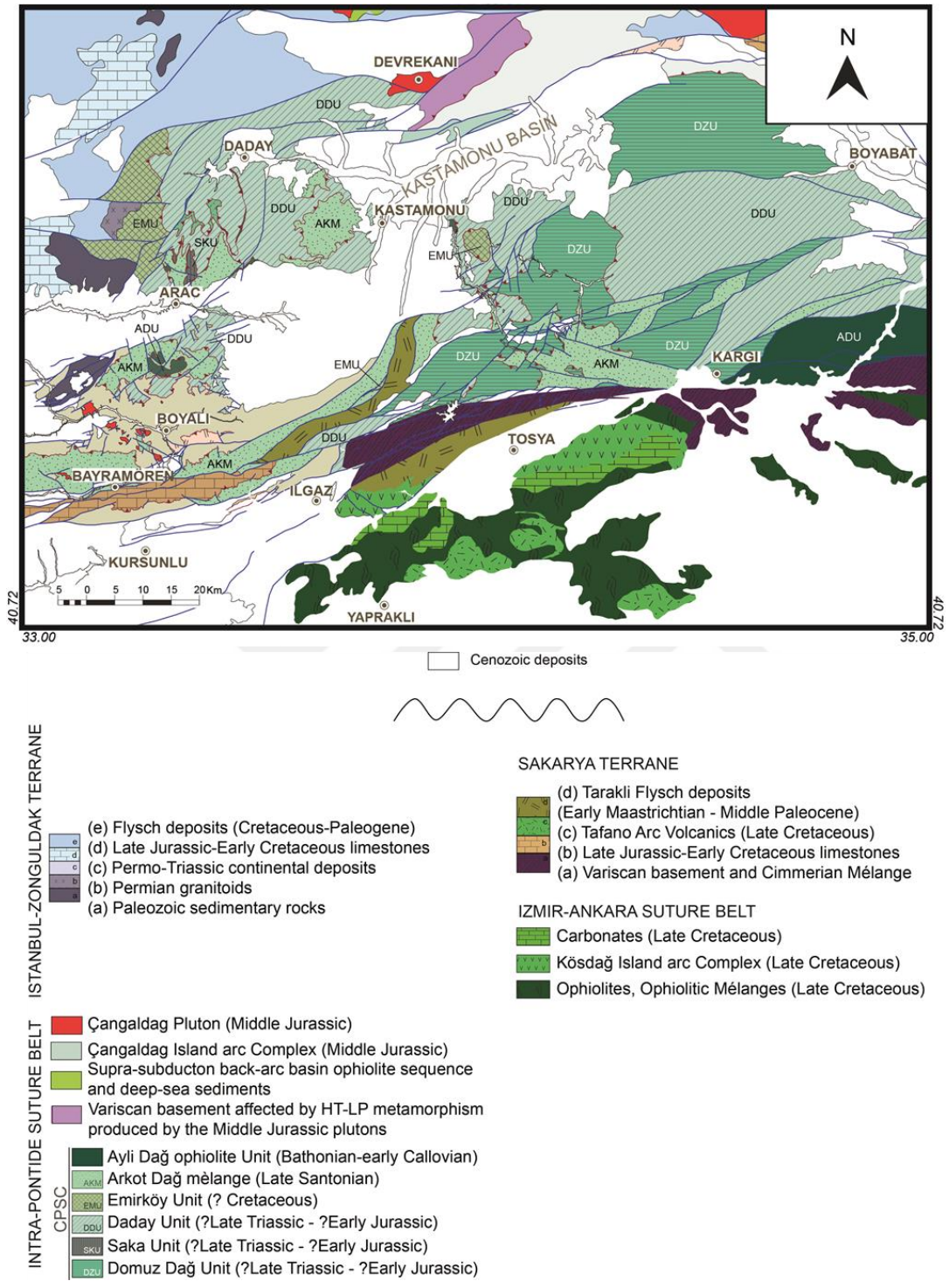


Figure 2.1. Geological sketch map of the Central Pontides (modified from Frassi et al., 2020; Marroni et al., 2020; Okay et al., 2013; Ottria et al., 2017).

2.1.2 Intra-Pontide Suture Belt

The IPSB, the northernmost ophiolite-bearing suture belt in Turkey, is situated between the IZCT to the north and the SCT to the south (Göncüoğlu et al., 1997, 2010). It extends along approximately 400 km from the Armutlu Peninsula in the west to the city of Kastamonu in Northern Anatolia in the east (Göncüoğlu, 2019; Göncüoğlu et al., 1997; Robertson and Ustaömer, 2004; Şengör et al., 1982; Yılmaz et al., 1997). In general, the IPSB has been relatively less studied compared to the other suture zones in Anatolia (Elmas and Yiğitbaş, 2001; Frassi et al., 2017, 2020; Göncüoğlu and Erendil, 1990; Göncüoğlu et al., 1997, 2008, 2012, 2014; Marroni et al., 2020; Okay and Tüysüz, 1999; Robertson and Ustaömer, 2004; Sayit et al., 2016; Şengör and Yılmaz, 1981; Yılmaz, 1990; Yılmaz et al., 1997). Most of these studies were carried out in the western part of the IPSB.

The number of studies conducted at the central part of the IPSB has increased in recent years (Frassi et al., 2017, 2020; Göncüoğlu et al., 2012, 2014; Marroni et al., 2020; Sayit et al., 2016). The IPSB comprises continental- and oceanic- derived tectonic entities with varying ages, geochemical characteristics, deformation, and metamorphic histories. Recent evidence from Central Pontides indicates that Intra-Pontide Oceanic (IPO) basin was opened in the Late Triassic (Göncüoğlu, 2019; Marroni et al., 2020; Okay et al., 2019) as a result of the northward subduction of the Paleotethys (Göncüoğlu et al., 2008, 2012; Sayit et al., 2016). On the other hand, the IPO basin was experiencing subduction in the uppermost Early Jurassic (Marroni et al., 2020). Metamorphosed bodies within the IPSB have been defined as CPSC (Tekin et al., 2012) or Central Pontide Supercomplex (CPS) (Okay et al., 2013). In this thesis, the nomenclature of the CPSC (Tekin et al., 2012) will be preferred.

The CPSC includes different tectonic units with a large areal extent in the Central Pontides (Tekin et al., 2012). In the previous studies, different nomenclatures were used for these tectonic units (e.g., Frassi et al., 2016; Göncüoğlu et al., 2012, 2014; Marroni et al., 2014; Okay et al., 2006, 2013; Sayit et al., 2016; Ustaömer and Robertson, 1999). The Domuz Dağ Unit (Frassi et al., 2016; Sayit et al., 2016;

partially equivalent of the Domuz Dağ Complex reported in Okay et al., 2006; Aygül and Oberhansli, 2017), the Saka Unit (which refers to the Saka Complex defined by Okay et al., 2013 and the Devrekani Unit identified by Marroni et al., 2014), and the Daday Unit (Frassi et al., 2016, 2018; Göncüoğlu et al., 2014; corresponding to the Martin Complex and the Kargı Complex described in Okay et al., 2006). In this thesis, the usage of the terminology of Sayit et al. (2016) and Frassi et al. (2016) will be followed. From north to south, these variably metamorphosed units are: Çangaldağ Complex, Aylı Dağ Ophiolite Unit (ADU), Arkot Dağ Mélange (AKM), Emirköy Unit (EMU), Daday Unit (DDU), Saka Unit, Domuz Dağ Unit (DZU) (Figure 2.2).

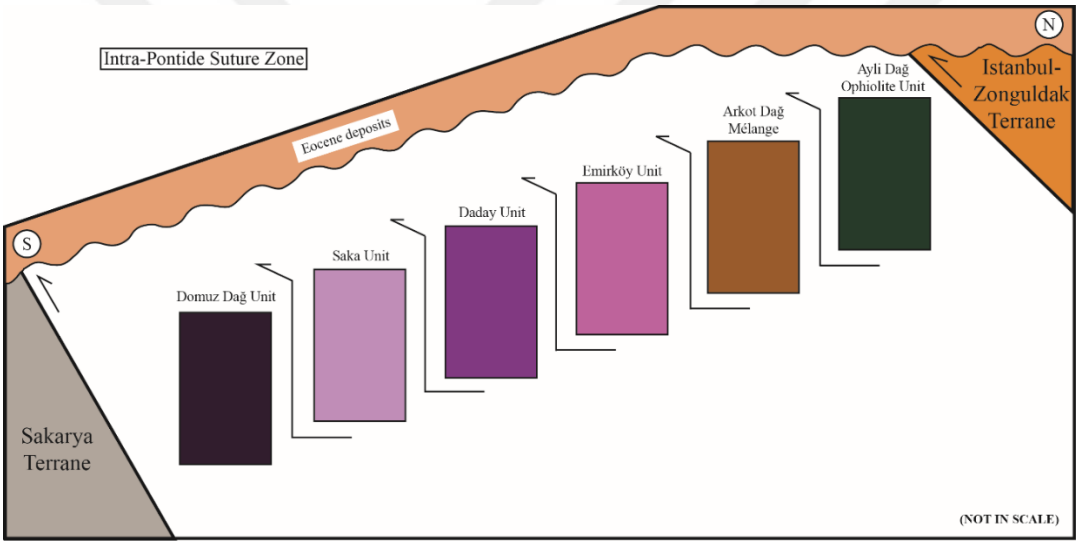


Figure 2.2. A diagram illustrating the stratigraphy of the tectonic units within the Central Pontide Structural Complex (modified from Sayit et al., 2016).

2.1.2.1 Çangaldağ Complex

The Çangaldağ Complex, the northernmost unit of the CPSC, consisting of volcanic, volcaniclastic and fine-grained clastic rocks, has undergone metamorphism under low-greenschist-facies conditions (Okay et al., 2013; Ustaömer and Robertson, 1993; Yılmaz, 1988). It crops out between Devrekani and Taşköprü towns of Kastamonu city, in the Central Pontides. It is tectonically sandwiched between the Devrekani Metamorphics to the north and the Taşköprü – Boyabat Tertiary basin to the south. Yılmaz, (1983), Boztuğ and Yılmaz, (1995)

and Tüysüz, (1990) were first to identify it as a metaophiolite body. Then, it was defined as a structurally thickened pile of essentially volcanic rocks and subordinate volcaniclastic sedimentary rock overlying basement of sheeted dykes in the north and basic extrusives in the south. Geochemically, the Çangaldağ Complex displays subalkaline affinity and is characterized by both primitive and evolved products (Çimen et al., 2016).

Ustaömer and Robertson (1993, 1994) proposed a Middle Jurassic age (168 and 169 Ma) based on zircons from dacite porphyries. A single U-Pb zircon age of 169 ± 2 Ma acquired from meta-dacite sample (Okay et al., 2014), representing protolith of the Çangaldağ Complex, suggests Middle Jurassic for the age of magmatism. Okay et al. (2013, 2014) used these age data with the geochemical results of Ustaömer and Robertson, (1999) to determine the Çangaldağ Complex as a Middle Jurassic arc. Furthermore, Çimen et al. (2018) yield Middle Jurassic U-Pb zircon ages of 176.4 ± 5.9 Ma, 156.3 ± 2.9 Ma and 161 ± 12 Ma–164 ± 13 Ma from Çangaldağ Metamorphic Complex.

Initially, Yılmaz and Bonhomme, (1991) provided K-Ar metamorphic ages as Middle Jurassic (153 Ma) for metabasic rocks and Early Cretaceous (126 and 110 Ma) for phyllites. On the basis of Ar-Ar mica dating on phyllites, Okay et al. (2013) suggested an Early Cretaceous (Valanginian-Barremian) metamorphic age (136 and 125 Ma) for the Çangaldağ Complex. The Çangaldağ Complex was generated in an arc basin system within the IPO during the Middle Jurassic, and underwent metamorphism during the closure of this ocean in the Early Cretaceous based on geochemical properties of the investigated rock samples (Çimen et al., 2017).

2.1.2.2 Aylı Dağ Unit

Göncüoğlu et al. (2012) described the unit as an ophiolite sequence cropping out around the Aylı Dağ region. The lower part of this sequence is represented by peridotites, layered gabbros alternating with spinel-bearing dunites, melatroctolites, troctolites, ol-gabbros and leucogabbros (Sayit et al., 2016). Sheeted dyke complex

which is overlain by massive basaltic lava flows (100-200 m) follows this thick gabbro sequence. 600–800 m-thick massive and pillow lavas and breccias alternating with ophiolite-bearing arenites and cherts cover this sequence. The radiolarian cherts ranging in age from the middle Bathonian to the early Callovian occur at the top of the pillow lavas (Sayit et al., 2016). Göncüoğlu et al. (2012) stated that basalts indicative of BABB and boninitic geochemical characteristics within the Aylı Dağ Unit show subalkaline nature.

2.1.2.3 Arkot Dağ Unit

This unit (named as the Kirazbaşı Mélange by Tüysüz (1990); Araç Formation by Özcan et al. (2007); Kirazbaşı Complex by Aygül et al. (2015)) consists of slide blocks embedded in a sedimentary matrix characterized by pebbly-mudstones, coarse-grained arenites, shales and pebbly-sandstones (Göncüoğlu et al., 2014; Sayit et al., 2016). The matrix material is significantly less abundant than the slide-block material, and it completely vanishes in some areas (Sayit et al., 2016). These slide blocks range in size from a few meters to several hundred square meters and comprise a broad spectrum of metamorphic and ophiolitic rocks (Sayit et al., 2016). Peridotites, gabbros and basalts are representative of the ophiolitic rocks. There are also slide blocks of Middle Triassic to Late Cretaceous cherts, neritic and pelagic limestones ranging in age from Late Jurassic to Early Cretaceous, Late Cretaceous marly-limestones, dolostones, ophiolite-bearing arenites, gneisses, and micaschists (Sayit et al., 2016). Besides, the slide blocks display deformations that occurred prior to their inclusion in the mélange. Therefore, the source region of the Arkot Dağ Unit may be considered as an imbricate stack of deformed and metamorphosed oceanic- and continental-derived slices (Göncüoğlu et al., 2014; Sayit et al., 2016).

On the basis of nannofossil assemblages identified in numerous soft marl clasts, the unit was dated as the Late Santonian (Göncüoğlu et al., 2014). In addition, cherts vary in age from the early Middle Triassic to the early Late Cretaceous (Göncüoğlu et al., 2008, 2014). The oldest cherts indicate that a deep water environment

occured in the Middle Triassic (Göncüoğlu et al., 2008, 2014). The initial stratigraphic association between early Bajocian-early Kimmeridgian cherts and basaltic breccia suggests the existence of a large oceanic basin during the Middle-Late Jurassic period. Furthermore, current $^{40}Ar/^{39}Ar$ hornblende ages between 159.4 ± 0.4 Ma and 163.5 ± 0.8 Ma (Çelik et al., 2016) are indicative of Late Jurassic metamorphic cooling ages for high-grade metabasite slide blocks (Marroni et al., 2020).

2.1.2.4 Emirköy Unit

The Emirköy unit, as defined by Sayit et al. (2016), is characterized by a metaturbiditic succession, consisting of intercalation of fine-grained metasandstones, metasiltstones, and metapelites. The thickness of the unit is about 300-400 m (Frassi et al., 2016). The unit is similar to the Martin Complex of Okay et al. (2013), composed chiefly of turbidite. However, the Emirköy unit is distinct from the Martin Complex with its lower degree of metamorphism (Sayit et al., 2016). Moreover, the Emirköy Unit may be interpreted as a deformed and partially metamorphosed equivalent of the Çağlayan Formation (Okay et al., 2013). It should be remembered, however, that the igneous rocks widely encountered in the Çağlayan Formation are not observed in the Emirköy Unit (Sayit et al., 2016).

2.1.2.5 Daday Unit

The Daday Unit (corresponding to the Kargı Complex of Okay et al. 2006; the Esenler Unit of Aygül et al. 2015) is made up of slices of fine-grained actinolite-bearing schists, mica-bearing schists, paragneisses, black quartzites, and fine-grained marbles. The unit has a thickness of roughly 400-500, and it is characterized by greenschist-facies metamorphism (Frassi et al., 2016), which was proposed to have occurred between 102 and 112 Ma (Early Cretaceous) based on Ar-Ar dating (Okay et al., 2013). Metamafic rocks of the Daday Unit have a wide range of chemical compositions exhibiting N-MORB, E-MORB, OIB, IAT, and BABB type features (Sayit et al., 2016). Furthermore, the deformation history of

the unit is similar to those of the Saka and Domuz Dağ units, indicating the existence of retrograde P-T metamorphic conditions varying from blueschist to sub-greenschist facies (Sayit et al., 2016).

2.1.2.6 Saka Unit

The Saka Unit is the least investigated unit of the CPSC. The unit was initially defined by Okay et al. (2013) as the Saka Complex consisting of dominantly micaschist, and the rest is made up of marble, calc-schist, metabasite, and small serpentinite slivers. It crops out mainly in the Daday Massif. The Saka Complex is tectonically overlain by the Martin Complex (Okay et al., 2013). The unit was renamed the Saka Unit by Sayit et al. (2016). The unit is represented by garnet-bearing amphibolites, coarse-grained banded amphibolites, garnet-bearing micaschists, and coarse-grained impure marbles (Sayit et al., 2016). The thickness of the unit can reach up to 300 m. The muscovite Ar-Ar ages range from 162 to 170 Ma, indicating Middle Jurassic cooling ages (Okay et al., 2013). Marroni et al. (2014), on the other hand, provided 163 Ma age indicating Middle Jurassic based on $^{40}Ar/^{39}Ar$ dating on white mica for the peak pressure conditions obtained during the D2 phase.

Lower to Middle Jurassic metamorphic rocks resembling those of the Saka Unit occur within IAES in the Çankırı (Çelik et al., 2011) and Erzincan regions (Topuz et al., 2013), and they were considered to represent a subduction-accretion complex in the Jurassic. The Saka Complex is most likely part of the same accretionary complex because of its tectonic environment and comparatively high pressures during metamorphism (Okay et al., 2013). In addition, the unit can be considered as a tectonic mélange in which magmatic and sedimentary rocks were combined and subsequently underwent metamorphism during the Middle-Late Jurassic boundary under epidote amphibolite facies conditions (Marroni et al., 2014).

2.1.2.7 Domuz Dağ Unit

The Domuzdağ-Saraycıkdağ Complex (Ustaömer and Robertson, 1999), the Domuzdağ Complex (Aygül et al., 2015; Okay et al., 2006, 2013) or Domuz Dağ Unit (Sayit et al., 2016) is composed of quartz-mica schists, metabasites, marble, chert, quartzites, and metaserpentinites. The thickness of the unit is roughly 800-1200 m (Frassi et al., 2016). The Domuzdağ Unit is tectonically overlain by the Çangaldağ Complex in the north, whereas slightly metamorphosed Cretaceous flysch deposits overlie the unit in the west. On the other hand, it covers the Late Cretaceous foreland basin and metamorphic rocks of the Kargı Complex in the south (Okay et al., 2006).

The Domuz Dağ Unit is metamorphosed under HP metamorphism ranging from eclogite to garnet-blueschist facies conditions (T □ 440 ± 30 ^{0}C, P □ 0.22-0.25 GPa; Aygül et al., 2016; Aygül and Oberhansli, 2017; Okay et al., 2006). Polyphase deformation histories of the Domuz Dağ Unit and Saka Unit show strong resemblance. The last three deformational stages took place under retrograde metamorphism conditions ranging from very-low grade facies to greenschist facies (Sayit et al., 2016). The metabasic rocks of the Domuz Dağ Unit exhibit dominantly subalkaline affinity, with an extensive geochemical variation involving E-MORB, OIB to BABB, and IAT-type signatures (Marroni et al., 2020; Sayit et al., 2016).

Okay et al. (2006) proposed Early Cretaceous (105 ± 5 Ma) for the metamorphism age of the unit based on ^{40}Ar/^{39}Ar dating technique. Furthermore, Aygül et al. (2016) suggested two distinct ages from phengites as 159.3 ± 1 Ma (earliest Late Jurassic) and 100.6 ± 1.3 Ma to 91.8 ± 1.8 Ma by using ^{40}Ar/^{39}Ar dating method. Marroni et al. (2020) interpreted these ages for the Domuz Dağ Unit as being related to the HP and retrograde metamorphic processes, respectively. The Domuz Dağ Unit was interpreted as a deep-seated subduction accretionary complex (Altherr et al., 2004; Aygül et al., 2016; Frassi et al., 2016; Okay et al., 2006, 2013; Sayit et al., 2016; Tüysüz, 1990; Ustaömer and Robertson, 1999).

2.1.3 Sakarya Composite Terrane

The SCT (corresponding to Sakarya Zone of Okay et al., 1996) as described by Göncüoğlu et al. (1997) is a "composite terrane", including a number of pre-Alpine terranes in its pre-Jurassic (Cimmerian and Variscan continental/oceanic assemblages) basement, each with distinct geological histories. The SCT is located between the IAESZ to the south and the IPSB to the north (Figure 1.1), and extends as a 100-200 km wide east-west trending belt along northern Turkey (Göncüoğlu, 2019; Göncüoğlu et al., 1997, 2000).

The oldest units identified within the Variscan basement of the SCT are metamorphic assemblages of poorly understood protolith age, cut by arc type granitoid ranging in age from Devonian (Aysal et al., 2012; Sunal, 2012) to Carboniferous (İlbeyli et al., 2015; Topuz et al., 2010; Ustaömer et al., 2012). These metamorphic rocks consist dominantly of ortho- and paragneiss, subordinate mafic rocks, and marbles (Göncüoğlu et al., 2000). U-Pb zircon ages of detrital zircons from sandstone suggest a northern Gondwanan origin (Ustaömer et al., 2016). The medium- to high-grade metamorphism within the basement is Late Carboniferous in age (e.g., Topuz et al., 2007; Ustaömer et al., 2016). The Lower to Middle Permian platform carbonates followed by Late Permian olistostromes are the oldest post-Variscan cover in the SCT. These platform carbonates are unconformably overlain by Triassic clastics (Turhan et al., 2004).

The Karakaya Complex, which represents the relics of the Paleotethyan (sensu Şengör et al., 1984) subduction complex, is a structural unit within the Cimmerian cycle of the SCT. The oceanic assemblages are represented by Middle Triassic (Anisian) oceanic basalts (Sayit and Göncüoğlu, 2009). The Küre Complex is one of the pre-Jurassic tectonic assemblages of the SCT (Göncüoğlu et al., 1997). It is a dismembered ophiolite alternated with a pile of thrust imbricated deep-sea sediments (Ustaömer and Robertson, 1999). The serpentinized harzburgite, sheeted dykes, massive gabbro, and basic volcanics constitute the ophiolitic rocks. The extrusives are characterized by pillow lavas, sheet flows, lava breccias, which underwent metamorphism under greenschist-facies conditions. In the western part

of the SCT, the Küre Complex is covered by Lower Jurassic basal conglomerates, then Middle Jurassic neritic carbonates passing upwards Upper Jurassic–Lower Cretaceous platform carbonates known as the Soğukçam Limestone, Late Cretaceous turbidites and ophiolite bearing units. The Upper Jurassic Bürnük clastics and Inaltı limestone represent the oldest cover of the SCT in the Central Pontides (Okay et al., 2014). The IZCT and its primary contact with the SCT are also covered by these sedimentary lithologies. The Küre Complex is cut by granitoid plutons and unconformably overlain by the Late Jurassic basal conglomerates and limestones (Ustaömer and Robertson, 1999). Ustaömer and Robertson (1999) suggest the Latest Palaeozoic-Early Jurassic for age of the Küre Complex based on fossil findings.

2.1.4 Izmir – Ankara – Erzincan Suture Zone

The IAESZ includes the relics of the Neotethyan Izmir–Ankara–Erzincan branch, and consists of various sections of the oceanic lithosphere as well as subduction-accretion mélanges. Following the closure of the IAE Ocean in the Late Cretaceous, the suture belt emerged along the subduction zones and emplaced southward onto the Tauride-Anatolide Platform (e.g., Göncüoğlu et al., 1997, 2010; Okay and Tüysüz, 1999). The IAESZ separates the Pontides in the north, from the Anatolide–Tauride Platform and the Kırşehir blocks in the south (e.g., Dilek and Moores, 1990; Okay and Tüysüz, 1999; Şengör and Yılmaz, 1981). The IAESZ spreads for hundreds of kilometers eastward from the Aegean coast to Erzincan and northern Iran (e.g., Göncüoğlu et al., 2010). In the west, it merges with the Vardar Ocean (e.g., Marroni et al., 2014). The SCT, representing the active margin of the IAE Ocean, overthrusts the IAESZ. The ophiolites comprise dismembered bodies of oceanic lithosphere produced in a variety of tectonomagmatic environments, including mid-ocean ridges, arcs, and back-arc basins, as well as intra-plate settings such as ocean islands. Serpentinized peridotites, ultramafic and mafic cumulates, layered and isotropic gabbros, plagiogranites, dyke-complexes, pillowed and massive lavas, and pelagic sediments exist as several km-thick distinct bodies or as blocks of varying sizes in the mélanges. They are frequently associated with

variable thickness of metamorphic soles composed primarily of amphibolites (Önen and Hall, 1993).

The Ar-Ar ages of these metamorphic soles range from the late Early Jurassic (Çelik et al., 2011) to early Late Cretaceous (101-89 Ma, e.g., Parlak et al., 2013a), suggesting that intra-oceanic convergence initiated at various parts of the subducting ridge at different times. Upper mantle rocks within the belt contain depleted lherzolites and chromite-bearing refractory harzburgites, exhibiting petrogenetic features of heterogeneous mantle sources (e.g., Manav et al., 2004; Parlak et al., 2013b; Üner et al., 2014). The pillow lavas can be found all over the belt as isolated thrust-sheets or blocks in the mélanges. They show a wide range of chemistries like OIB, N-MORB, E-MORB and SSZ (Aldanmaz et al., 2008; Bortolotti et al., 2013; Göncüoğlu et al., 2010; Sarıfakıoğlu et al., 2010; Topuz et al., 2013). The age of the basalts comes from the paleontological data acquired from the fossil-bearing mudstones, micritic limestones, and cherts (Göncüoğlu, 2019). The oldest ages acquired so far are Asselian-Wordian (Early/Middle Permian; Tekin et al., 2019) and Anisian (Middle Triassic, Sayit et al., 2017), whereas the youngest ages are Cenomanian, obtained primarily from the SSZ-type basalts. This implies that the generation of the Izmir-Ankara-Erzincan oceanic crust began before the Middle Triassic (possibly in the Late Permian) and continued up to the Late Cretaceous (Göncüoğlu et al., 2015; Tekin et al., 2002).

The IAESZ contains mélanges of block-block and block-in matrix varieties (Çelik et al., 2013; Göncüoğlu, 2019; Özkan et al., 2020; Sayit et al., 2017, 2020). The sizes of the blocks range from a few meters to several tens of kilometers. In addition to oceanic lithospheric lithologies, the mélanges contain blocks of HP/LT metamorphic assemblages such as blueschists and eclogites, as well as variably metamorphosed carbonate and siliciclastic sedimentary rocks. During the Late Cretaceous, allochthonous bodies originating from the closure of the IAE Ocean and its subduction-accretion prism were first emplaced onto the margin of the Tauride-Anatolide platform. Subsequently, they moved to the south for several hundreds of kilometers. The resulting imbrication eventually led to the creation of belts in the Tauride-Anatolide tectonic units, which were thought to be relics of

separate oceanic basins in the Tauride-Anatolide Platform (e.g., Intra-Tauride Ocean, Huğlu Ocean, Bornova Mélange, etc.) (Göncüoğlu, 2019).

2.2 Local Geology

This part will clarify the geological features on the units in the vicinity of the study area, including the Kunduz Metamorphics, the KM, Dikmen Formation, Late Cretaceous mélange of the IAESZ, and cover units.

2.2.1 Kunduz Metamorphics

The Kunduz Metamorphics, a part of the Karakaya Unit, is made up of alternation of sedimentary, magmatic, and pyroclastic rocks (Tüysüz and Yiğitbaş, 1994) metamorphosed under greenschist-facies conditions (Tüysüz, 1990). The Kunduz Metamorphics crop out near the vicinity of Kavakçayı village in the northeastern part of the study area. The unit thrust over the ophiolitic mélange of the IAESZ in the south of Kargı (Figure 2.3).

The geochemical characteristics of the mafic lavas of the Kunduz Metamorphics resemble those of abyssal tholeiites (Tüysüz, 1985). Yılmaz and Tüysüz (1991) and Tüysüz and Yiğitbaş (1994) suggested a Triassic age for the Kunduz Metamorphics. In contrast, Aygül et al. (2016) obtained Jurassic $^{40}Ar/^{39}Ar$ phengite ages (159.3 ± 1.0 Ma from quartz micaschist and 101.0 ± 0.6 Ma from metatuff), which was interpreted as the age of metamorphism. The Kunduz Metamorphics have been interpreted as the equivalent of Karakaya Complex (Bingöl, 1973) within the Kargı Massif (Tüysüz, 1985; Yılmaz and Tüysüz, 1984). Tüysüz (1990) proposed that the Kunduz Metamorphics formed in a tectonically active deep-sea environment. Yılmaz and Tüysüz (1991) suggested that the Kunduz Metamorphics have been generated in a marginal basin based on geological and geochemical features.

2.2.2 Kösdağ Metavolcanics

The KM is mainly composed of low-grade meta-felsic, meta-intermediate and meta-basic volcanic and volcaniclastic lithologies intercalated with sedimentary rocks such as pelagic limestone, chert, and mudstone. The KM occupy an area of around 140 km^2 and crops out in the southeastern part of the Tosya and southwestern part of the Kargı towns (Figure 2.3). Because of the short-term alternation of various metavolcanics (e.g. meta-dacite, meta-andesite, and meta-basalt), these lithologies could not be mapped separately, but they were instead collectively grouped under the term "Kösdağ Metavolcanics" (Figure 2.3). The KM is overprinted by dynamic metamorphism, which distinguishes it from the neighboring metamorphic units cropping out in the area. Within the KM, cross-cutting relationships occur in some places. However, the occurrence of intense shearing in some places makes it very difficult to determine whether the metaigneous lithology is a dyke or lava flow.

The KM are limited by the NAFZ from the north. The presence of shear zones with strongly mylonitized metavolcanic lithologies reflects the impact of faulting. Foliation is noticed widespread in these metavolcanic rocks, and it appears to have formed as a result of fault-induced deformation. In addition, the mylonitized rocks have boudinaged sections that are visible at the outcrop scale in some areas. It should also be remembered that although sheared lithologies exhibit ductile deformation, this effect weakens away from the shear zone. Like the foliated and boudinaged lithologies, the non-sheared lithologies that represent the initial appearance of the metavolcanics have also wide distribution.

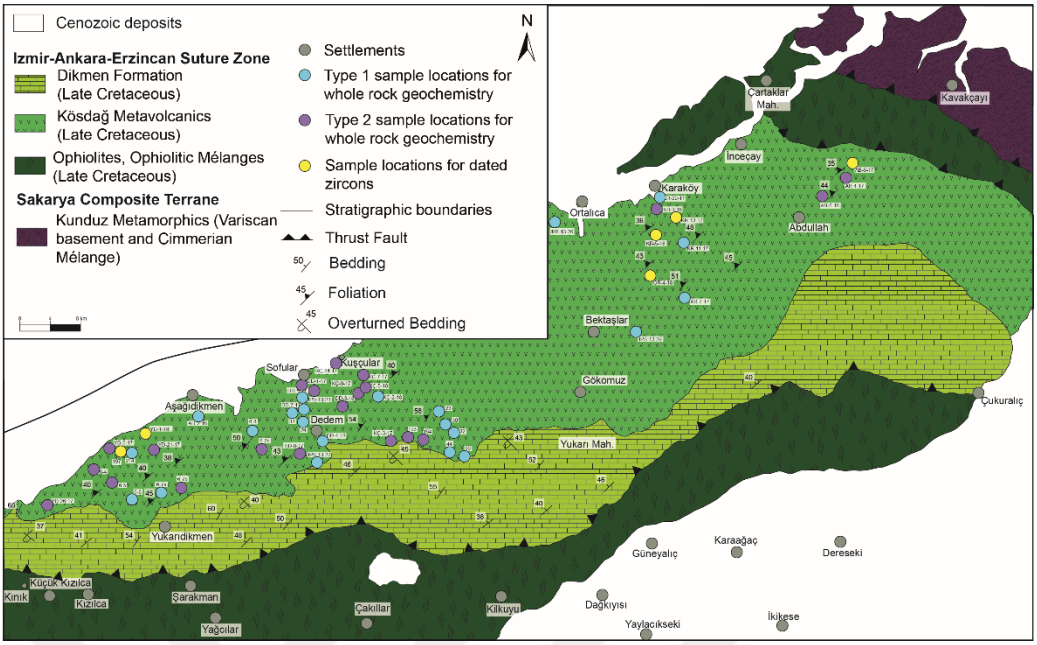


Figure 2.3. Geological map of the study area.

Meta-felsics, one of the common lithologies of the KM, appear in white, light brownish, and greenish colors in the field (Figure 2.4). The meta-felsic lithologies include meta-dacites and meta-rhyolites. Both are strongly affected by deformation, and they are typically foliated. It is difficult to distinguish between meta-dacite and meta-rhyolite on the outcrops; a petrographical examination is required for precise determination. Both meta-rhyolites and meta-dacites are porphyritic, which is observable at the outcrop scale. Meta-rhyolites largely include phenocrysts of quartz and K-feldspar, whereas meta-dacites mainly comprise plagioclase phenocrysts. The thickness of the meta-rhyolites can reach up to 45-50 meters in the field. In some places, these felsic lithologies are intercalated with mudstone and chert showing 0.5 to 1 meter thickness (Figure 2.5).



Figure 2.4. Field view of Kösdağ meta-rhyolite on road to Karaköy village.

Greenish varieties of meta-rhyolites are similar to meta-andesites and can be easily mistaken if not examined carefully. The presence of quartz phenocrysts in meta-rhyolites serves as a useful indicator in this regard. The quartz phenocrysts are noticeable in hand specimen, and they are recognized by their smoky colors and vitreous luster. The meta-dacites appear sporadically with other volcanic/volcaniclastic members of the KM in the study area. The meta-felsic lithologies are observed in many places (near Karaköy, Ortalıca, and Yukarıdikmen villages), intercalating with limestone, chert, and mudstone (Figure 2.5). In some areas, quartz and calcite veins are seen cutting through the meta-dacites.

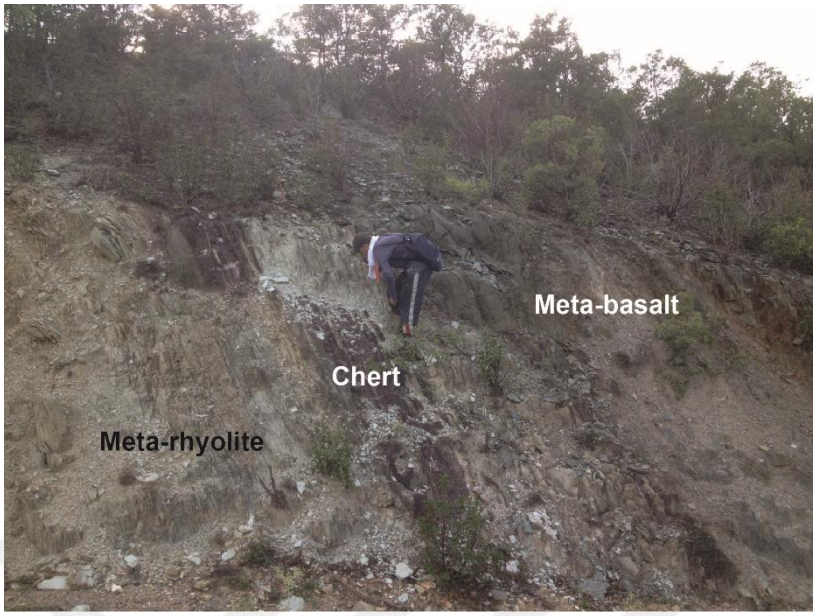


Figure 2.5. Alternation of chert, meta-rhyolite and meta-basalt on the road to the Yukarıdikmen village.

Meta-intermediate lithologies are represented by meta-andesites in the field. The majority of the meta-andesites are fine-grained and have greenish colors indicating effects of the low-grade metamorphism (Figure 2.6). Rarely, purple-colored meta-andesites also exist, and these varieties seem to be rich in epidote. Similar to meta-rhyolites and meta-dacites, these metavolcanics also experienced ductile deformation as evidenced by the presence of mylonitic texture, which can be observed at the outcrop. The mylonitic andesites consist of plagioclase surrounded by sericite grains, giving the rock an augen appearance. Micas, on the other hand, cause meta-andesites to become glossy. The thickness of meta-andesites may reach up to 15 meters in the field.

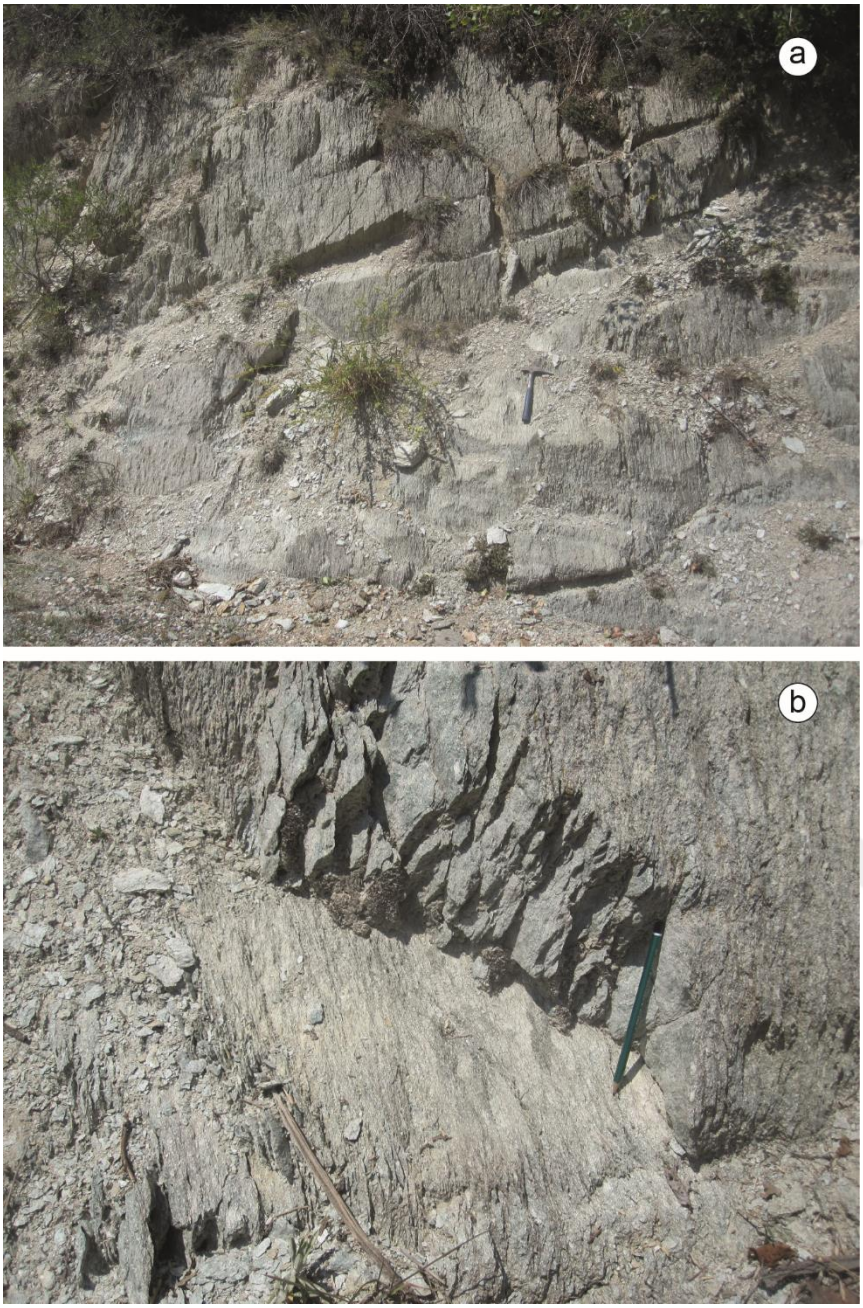


Figure 2.6. Development of foliation in the Kösdağ meta-andesites on the road to Dedem village.

Meta-basic lithologies are observed both as lava flows and dykes in the field. The lava flows are aphanitic, and characterized by meta-basalts, whereas the dykes occur as aphanitic or microphaneritic, represented by meta-basalts and meta-diabases. Meta-basalts are distinguished by their dark colors, as opposed to meta-intermediates and meta-felsics. They appear greenish to dark grey on their fresh

surfaces, whereas they display yellow-brownish colors on the weathered parts. Both foliated and nonfoliated types are encountered in the study area. Meta-basalts are generally porphyritic, which can be identified at the outcrop scale. In these lithologies, relict black-colored pyroxene phenocrysts can be seen with the naked eye. Meta-basalts form thick lava layers in some places, with thicknesses reaching up to 200 meters. They are commonly intercalated with deep-water sedimentary rocks, such as mudstone, chert, and pelagic limestone. Meta-basalts are affected by low-grade metamorphism, which is reflected by their greenish colors.

Similar to meta-basalts, meta-diabases display dark green colors. However, meta-diabases are recognized by their coarse-grained appearance in the field. While both foliated and non-foliated varieties exist in meta-basalts, meta-diabases are generally non-foliated. The thicknesses of meta-diabase dykes range from approximately 3 to 5 meters. The meta-diabases occur both as lava flows and dykes cutting the meta-dacites in the field. Their greenish colors suggest that meta-diabases underwent low-grade metamorphism (Figure 2.7).



Figure 2.7. The appearance of jointed Kösdağ meta-diabase on the main road connecting Tosya to Iskilip.

It is a definite observation that the Kösdağ meta-basics cut the meta-dacites. Mafic dykes with a thickness ranging from 50 cm to 1 m have a meta-basic character at least at this location on Tosya-Çorum main road south of the Kuşçular village

(Figure 2.8). However, it may not seem so clear the cross-cut relationship between other members of the KM.



Figure 2.8. Field photograph showing cross-cutting relationship observed between meta-basalt dyke and meta-dacite members of the KM, south of the Kuşçular village.

In addition to meta-dacites, meta-andesites, and meta-basalts that make up the majority of the KM, mafic volcaniclastic lithologies intercalated with the metavolcanics also occur. The clasts vary in size from a few millimeters to several centimeters. The nature of the fragments is particularly visible in the coarse-grained mafic volcaniclastics, such as lava breccias. These lithologies contain angular clasts of dark green, vesicular meta-basalt fragments (Figure 2.9). The clasts of the fragmental lithologies appear elongated near the shear zones, while the less affected parts preserve their initial angular shapes.



Figure 2.9. Meta-basalt clasts with gas vesicles embedded in a carbonate matrix in lava breccia.

Like other lithologies within the KM, volcaniclastic rocks are also affected by ductile deformation, evidenced by the development of boudins (Figure 2.10).



Figure 2.10. Boudinaged structures exhibiting effects of ductile deformation related to the faulting in the Kösdağ meta-andesites.

Volumetrically subordinate sedimentary lithologies such as recrystallized pelagic limestone, brick- and purple-colored chert, and mudstone are also encountered in

the study area. Pelagic limestone, which usually outcrops between Yukarıdikmen and Abdullah villages, is red-colored, hard, compact, and thin- to medium-bedded. Pinkish-colored limestones with chert nodules were also noticed in several places (Figure 2.11).

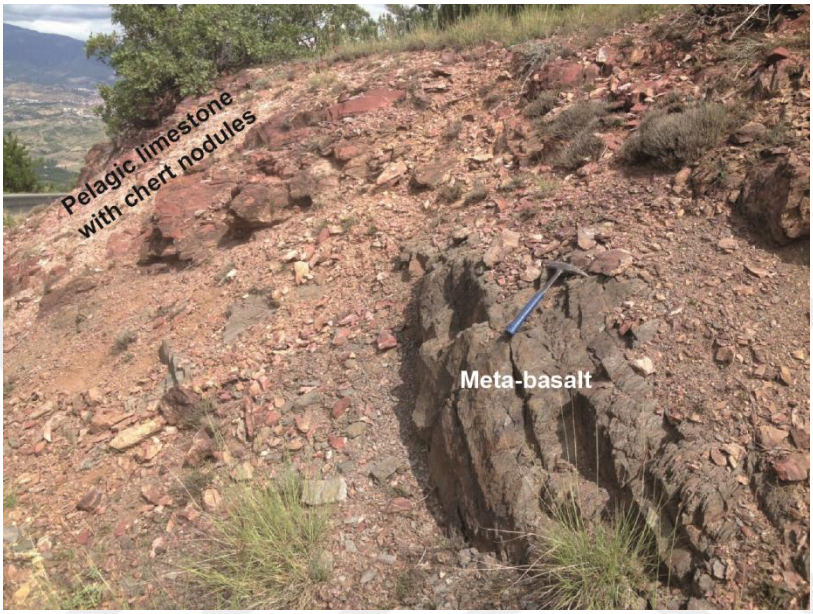


Figure 2.11. Alternation of pelagic limestone with chert nodules and meta-basalt near the Yukarıdikmen village.

While chert may occur as nodules, it is also found as thin-bedded layers intercalated with the volcanics. This case is well observed on the main road in the Yukarıdikmen village (Figure 2.12a-b). Such sedimentary contacts are important, since the paleontological age extracted from limestones and cherts also implies the crystallization age of the associated volcanics. However, no fossil could be recovered due to the intense recrystallization.



Figure 2.12. Red chert nodules and/or bands within pelagic limestone north of the Yukarıdikmen village.

The influence of tectonism on the study area is intense. It is observed that the lithologies of the KM are steeply inclined almost everywhere, which is particularly evident from the bedding planes of the sedimentary layers. Due to this, even some lava flow layers can be perceived as dyke intrusions. The effect of tectonics is also marked by the folding of the KM. This is evidenced by the repetition within the unit, which is particularly well observed on the ridge around the Kızılca village in the southwest part of the study area. In addition, in the northeastern part of the study area, tectonic slices of serpentinites extending up to 15 meters were noticed in areas dominated by meta-basic lithologies and pelagic limestones. The relationship between serpentinites and the surrounding lithologies is tectonic and characterized by steep contacts. It is probable that these serpentinite slices were

emplaced by the strike-slip movements within the KM (Figure 2.13). This case once again highlights the strong influence of tectonism (induced by the NAFZ) on the geology of the region.



Figure 2.13. Field photograph of serpentinite slice within the KM, south of the Inceçay village.

As mentioned before, the northern boundary of the KM in the study area is defined by splays of the NAFZ. Therefore, no contact relationship between the KM and the CPSC is observed in the western part of the study area. On the other hand, in the eastern part of the study area, the KM are structurally overlain by the Kunduz Metamorphics of the SCT to the north. Furthermore, Okay et al. (2006) and Aygül et al. (2015) proposed that the CPSC structurally overlies the KM further in the north. To the south, the KM is stratigraphically overlain by the recrystallized limestones of the Dikmen Formation. This is evidenced in the northwest of the Yukarıdikmen village (Figure 2.14), where the Dikmen Formation lies over the meta-rhyolites of the KM with a steep contact. The Middle Eocene clastic rocks to the east and southeast of the study area are the oldest cover unit in primary depositional contact with the KM.

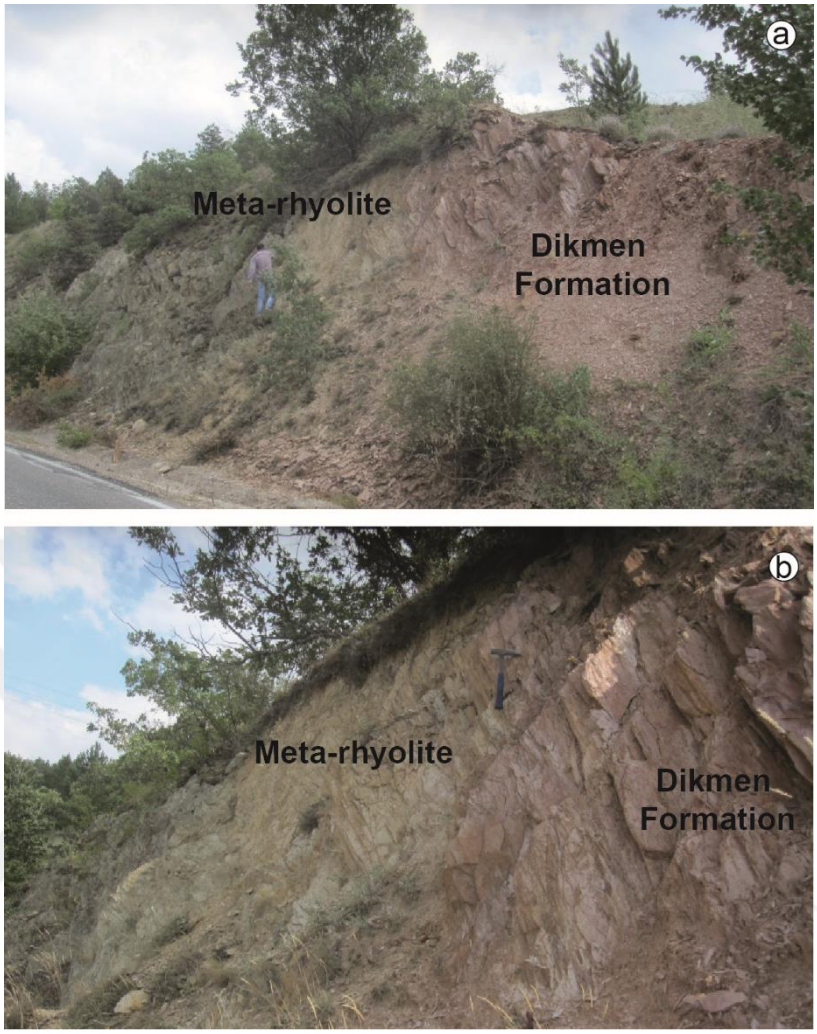


Figure 2.14. Field view of the stratigraphic contact between the Dikmen limestone and Kösdağ meta-rhyolite in the north of the Kızılca village.

Tüysüz et al. (1990) reported an Upper Cretaceous age based on the microfossil fauna from the pelagic limestone intercalated with mafic lavas. However, no fossil finding could be acquired from the pelagic limestones within the KM in this study due to the recrystallized nature of these lithologies. On the other hand, the KM comprise felsic lithologies suitable for U-Pb zircon dating. In this regard, Aygül et al. (2015) provided Late Cretaceous U-Pb ages for magmatism (93.8 ± 1.9 Ma, 94.4 ± 1.9 Ma), which is also supported by Berber et al. (2021) (94.64 ± 0.77 Ma and 113.2 ± 2.3 Ma U-Pb zircon ages). In the present study, samples were collected from both felsic and mafic lithologies. However, only the felsic lithologies yielded

zircons to perform the U-Pb age dating. This issue will be explained in the next chapters as explained in Chapter 1.

2.2.3 The Dikmen Formation

The Dikmen Formation, named by Tüysüz (1990), is represented by light grey to pinkish, yellowish colored carbonates, cropping out to the south of the KM. The Dikmen Formation is chiefly made up of micritic carbonates, which include intercalations of clayey to sandy carbonate layers and subordinate light pinkish mudstones. Cherts are present within the formation, and they are typically seen as lenses within the metacarbonates. In addition, deformation has resulted in well-developed foliation in clayey-silty places (Figure 2.15).



Figure 2.15. Field photograph of yellowish-colored, foliated recrystallized limestones of the Dikmen Formation on the Kızıltepe ridge.

The Dikmen Formation is affected by metamorphism, as demonstrated by the significant recrystallization, which led to the destruction of primary micritic textures. The Dikmen Formation stratigraphically overlies the KM in the north, while it is tectonically bounded by the ophiolitic mélange in the south. This tectonic contact is well exposed at the Kızılca ridge to the east, north of the Çukur village, and north of the Güneyalıç village (Figure 2.16-a,b,c). At these locations, it

is observed that the Dikmen Formation lies structurally above the Late Cretaceous mélange of the IAESZ. This contact relationship is also confirmed on the road connecting Yukarıdikmen and Şarakman villages, as well as along the Kızıltepe ridge.

Owing to the recrystallized nature of the Dikmen Formation, no fossils could be determined from the carbonates of the unit. An Upper Jurassic-Lower Cretaceous age proposed by Hakyemez et al. (1986) was obtained from the Akbayır Formation, which is a carbonate-bearing unit situated to the west of the study area (Akyürek et al., 1982). Tüysüz (1990, 1993) suggested a Cenomanian age for the Dikmen Formation based on the fossil evidence. On the basis of paleontological data, Uğuz et al. (2002) proposed an Early Cretaceous age for the Yaylacık Formation, which is regarded to be equivalent to the Dikmen Formation.



Figure 2.16. Field photograph of the tectonic contact relationship between recrystallized limestones of Dikmen Formation and ophiolitic mélange of IAESZ. a) South of the Yukarıdikmen village, b-c) Northwestern of the village of Çukuralıç.

2.2.4 The Kızılırmak Ophiolite

The Kızılırmak Ophiolite (Tüysüz, 1990) of the IAESZ is the main tectonic unit to the south of the KM (Figure 2.3). It also covers an area between Kargı and Vezirköprü towns, on both sides of the Kızılırmak river. In the southwest part of the study area, near the Kızılca village, the contact between the Dikmen Formation and the mélange is a thrust fault (Figure 2.17b). Cumulate pyroxenite, slided-blocks of serpentinized harzburgite, isotropic and layered gabbro, dunite, radiolarian cherts, and deformed greenschist facies meta-basaltic pillow lavas in serpentinite matrix constitute the ophiolitic mélange. This mélange unit represents the northernmost part of the Ankara Mélange and crops out as a continuous belt in the north of the Çankırı Basin (Figure 2.1).

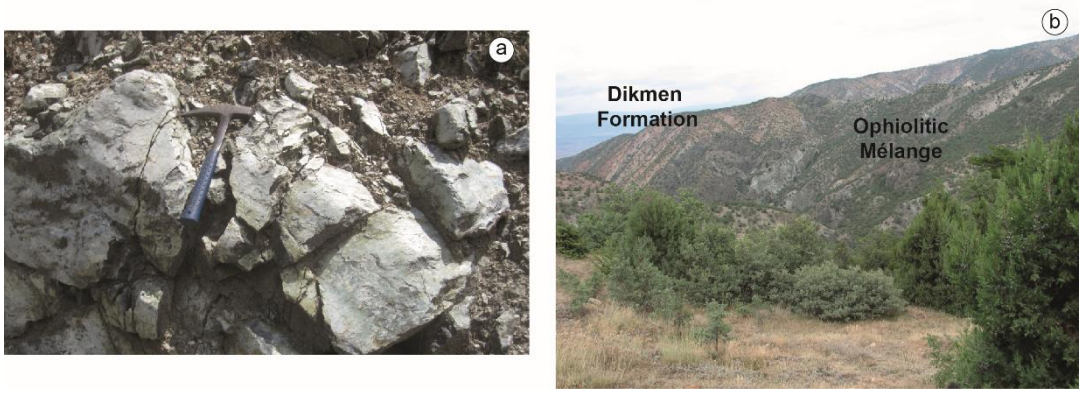


Figure 2.17. a) Field view of serpentinite within the ophiolitic mélange of the IAESZ b) Dikmen Formation is structurally underlain by the ophiolitic mélange of the IAESZ.

The existence of Campanian-Maastrichtian globotruncana (Tüysüz, 1990) within the pelagic limestones intercalated with basaltic pillow lavas indicates a Late Cretaceous age for the ophiolite.

2.2.5 Cover Units

The Meryemdere Formation and Beynamaz Volcanic Unit represent the Eocene units in the region. These units are exposed in the southeast part of the study area. The Meryemdere Formation, named by Serdar and Biçer (1981) is made up of

alternation of conglomerate, siltstone, sandstone, marl and limestone. The unit was studied by Yılmaz and Tüysüz (1984) as the Örencik Formation. It is conformably overlain by the Hamamözü Formation, which is mostly composed of lavas and volcaniclastics (Keskin et al., 2008). Sütçü et al. (1994) provided a Lutetian age for the unit based on the occurrence of Nummulites sp.. In addition, Gündoğdu (2009) obtained K-Ar radiometric ages indicating Middle-Late Eocene formation age of the volcanic rocks.

Beynamaz Volcanic Unit, defined by Yılmaz and Tüysüz (1984), consists predominantly of basaltic and andesitic lavas, tuff, and agglomerate. Basaltic and andesitic volcanic rocks of the unit intrude to the Meryemdere Formation. The unit, which crops out in the southeast of the study area, is observed at the upper levels of the Meryemdere Formation. Ketin (1962) obtained Nummulites sp., fossil suggesting an Early Lutetian age to the intercalated sedimentary rocks. Furthermore, Gündoğdu (2009) obtained K-Ar radiometric ages from volcanic rocks, as 41.4 Ma and 52.1 Ma, indicating Lutetian and Ypresian periods.

On the other hand, the Miocene volcanics were named by Türkecan et al. (1991a) as the Uludere pyroclastics, consisting of dacite, andesite, basalt, dacitic tuff, tuffite, agglomerate, and volcaniclastic conglomerate (Sevin and Uğuz, 2011). It is located to the north of the village of Çakıllar, in the southern part of the study area. While the Uludere pyroclastics unconformably overlie the older units, they are laterally in transition with the Hançili Formation and Tekke volcanics. The unit can be correlated with the Mamak Formation (Sevin and Uğuz, 2011).

CHAPTER 3

PETROGRAPHY

110 thin sections of KM were prepared for the petrographic examination. To provide a more comprehensive interpretation, 65 thin sections prepared by Berber (2015) were also studied in detail. Accordingly, a total of 175 thin sections were investigated using a polarizing microscope to understand the petrographic characteristics of the investigated rocks. Only the metavolcanic rocks, which constitute the majority of the unit, will be mentioned in this chapter. Petrographically, the KM are divided into three main groups as meta-felsic lithologies (meta-dacites, meta-rhyolites), meta-intermediate lithologies (meta-andesites), and meta-basic lithologies (meta-basalts, meta-diabases) (Table 3.1). The mineralogical assemblage and textural features of these metavolcanic rocks, as well as their alteration/metamorphism and deformation properties, are described in this chapter.

Table 3.1. Mineralogy, size range, abundance and distribution of the phenocrysts in the KM.

		Meta-diabase	Meta-basalt	Meta-andesite	Meta-dacite	Meta-rhyolite
	texture	medium to coarse grained, microphaneritic texture	fine grained, aphanitic, porphyritic, glomeroporphyritic	aphanitic, porphyritic, glomeroporphyritic	porphyritic	porphyritic
	foliation	non-foliated	include both foliated and non-foliated varieties	foliated	foliated	foliated
Phenocryst	type	plagioclase	plagioclase + clinopyroxene (more abundant relative to meta-andesites)	plagioclase is the main constituent and to a lesser extent clinopyroxene.	K-feldspar + plagioclase + quartz	quartz + K-feldspar + plagioclase +
	size (mm)	0.5 - 3	≤ 2	≤ 0.5	1 - 3	mainly 1-3 up to 5
	modal %	Plg (65%)	clinopyroxene (15%) plagioclase (10%)	Plagioclase (20%) clinopyroxene (5 %)	K-feldspar (20%), plagiocla-se (15%), quartz (10%)	quartz (30%), K-feldspar (10%), plagioclase (3%)
	secondary mineral assemblage	chlorite + epidote + sericite	chlorite + epidote + sericite ± actinolite	chlorite + epidote + sericite	chlorite + calcite + epidote + sericite	chlorite + epidote + sericite
	accessory minerals	opaque	opaque	opaque + zircon + apatite	opaque + zircon + apatite	opaque zircon + apatite
	groundmass	not determined	chlorite + epidote	chlorite + epidote	quartz + muscovite + chlorite + epidote	quartz + muscovite + chlorite + epidote

3.1 Meta-basic Kösdağ Lithologies

Meta-basic Kösdağ lithologies comprise meta-basalts and meta-diabases. The Kösdağ meta-basalts show dark green colors in hand specimen, reflecting the existence of secondary mineral assemblages such as epidote, chlorite, and actinolite. There are both foliated and nonfoliated varieties within the Kösdağ meta-basalts. It must be noted that the aphanitic and metamorphic nature of these lithologies makes it difficult to determine the exact primary mineral assemblages of the Kösdağ meta-basalts. Igneous textures, on the other hand, are mostly preserved.

The Kösdağ meta-basalts are typically porphyritic, which is recognized by the presence of large phenocrysts embedded in a fine-grained groundmass. In general, porphyritic texture indicates a multi-stage cooling history, where phenocrysts form by slow cooling in deeper parts, while groundmass results from rapid cooling, resulting in a fine-grained texture (Vernon, 2004).

Plagioclase and clinopyroxene make up the primary mineral constituents of the Kösdağ meta-basalts. Plagioclase (100-700 μm) occurs both as a phenocryst and groundmass phase. It typically exhibits subhedral to euhedral outlines. Under crossed-polarized light (XPL), it is characterized by first-order interference colors and shows albite as well as Carlsbad-albite combined twinning. Besides, oscillatory zoning is a common feature in plagioclase grains from the Kösdağ meta-basalts. Oscillatory zoning can be interpreted as a disequilibrium texture. Moreover, randomly oriented, lath-shaped plagioclase crystals of varying sizes suggest a seriate texture (Figure 3.1).

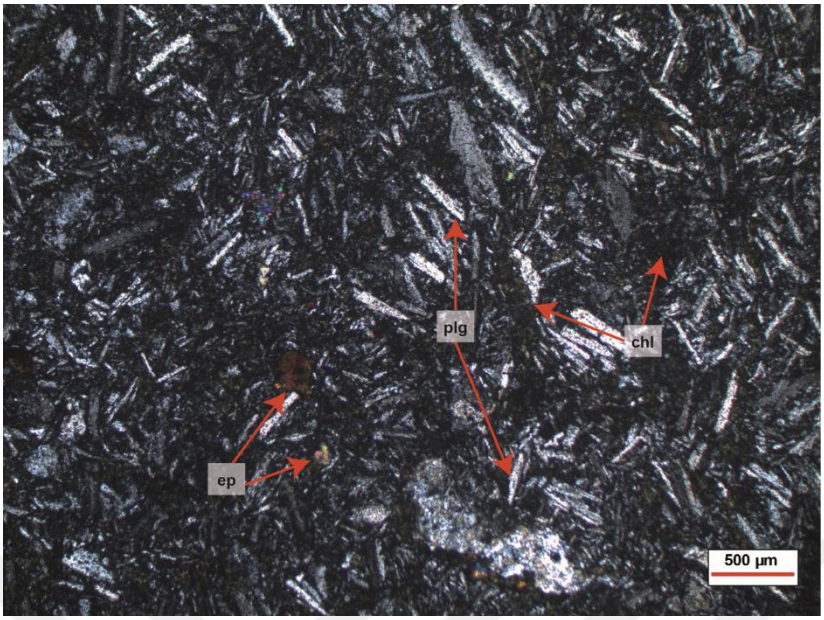


Figure 3.1. Randomly oriented plagioclase grains of varying size, indicating seriate texture in a fine-grained groundmass of non-foliated Kösdağ meta-basalt (Sample 6-7, chl: chlorite, ep: epidote, plg: plagioclase).

Clinopyroxene (>1 mm) is the dominant phenocryst and groundmass phase in the Kösdağ meta-basalts (Figure 3.2). Additionally, it forms clusters with plagioclase crystals, defining glomeroporphyritic texture. Clinopyroxene is generally considered resistant to alteration (e.g., Leterrier et al., 1982; Nisbet and Pearce, 1977; Shervais and Kimbrough, 1985). However, in the Kösdağ meta-basalts, some clinopyroxene crystals are altered to chlorite, actinolite, and calcite.

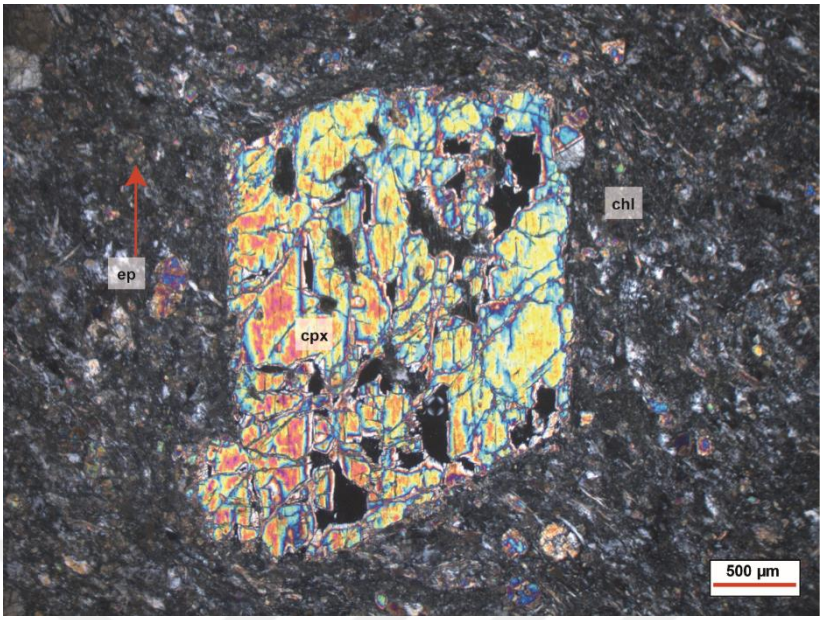


Figure 3.2. Photomicrograph of fractured clinopyroxene phenocryst in Kösdağ meta-basalt. The fine-grained groundmass consists of clinopyroxene and epidote (Sample AB-6-18, chl: chlorite, ep: epidote, cpx: clinopyroxene).

Opaque minerals are also present in the metabasalts (Figure 3.3), which can be pyrite, as indicated by their cubic outlines. However, it could not be recognized in the hand specimen.

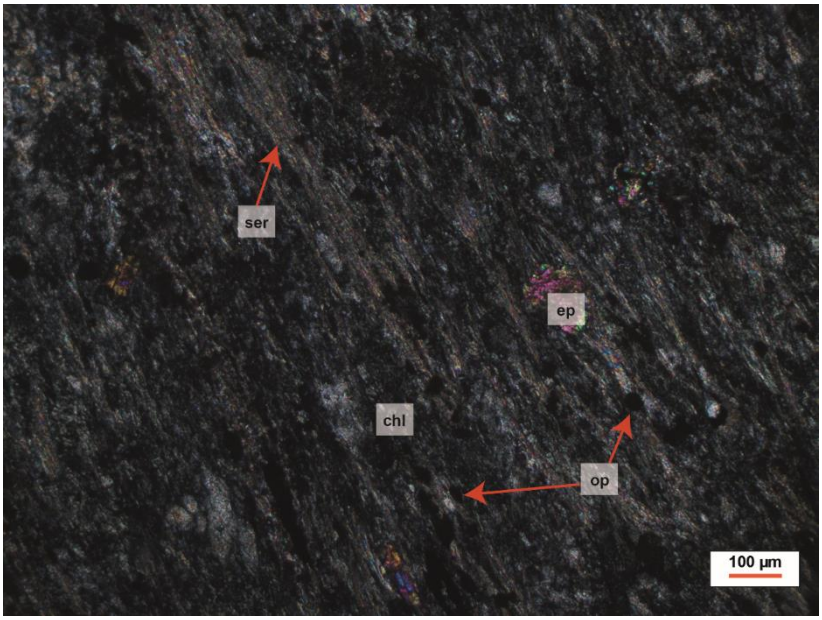


Figure 3.3. Kösdağ meta-basalt with flakes of chlorite and sericite oriented parallel to the foliation, together with abundant opaque grains (Sample YD-21-17, chl: chlorite, ep: epidote, op: opaque, ser: sericite).

While plagioclase and clinopyroxene are the main primary minerals in the metabasalts, secondary minerals are also present, including actinolite, epidote, sericite, chlorite, and calcite. Among them, chlorite and epidote replacing pyroxene and plagioclase are secondary mineral phases common to all Kösdağ meta-basalts (Figure 3.4), whereas actinolite tends to be present in only a few samples indicative for greenschist facies metamorphism. Pale green appearance of chlorite is distinctive, with a hint of pleochroism. It exhibits low-angle oblique extinction with anomalous first-order interference colors. Under PPL, epidote is distinguished by its high relief and yellowish colors (Figure 3.4). Under XPL, it exhibits typical patchy birefringence. Apart from partial replacement, individual epidote grains are also present in the Kösdağ meta-basalts. Sericite, which is recognized as small colorless flakes with second-order birefringence, typically replaces plagioclase. Actinolite is rarely present and appears as needle-like grains, replacing clinopyroxene. Based on this secondary mineral assemblage, the Kösdağ meta-basalts have undergone metamorphism mainly under subgreenschist-facies conditions, while typical greenschist facies conditions were rarely achieved. The effects of hydrothermal metamorphism, followed by dynamic metamorphism, is seen in the Kösdağ meta-basalts.

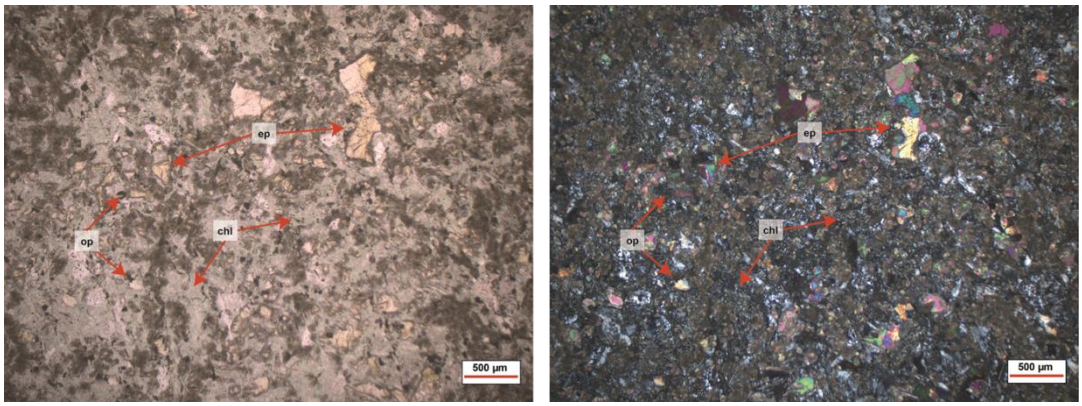


Figure 3.4. Photomicrograph of Kösdağ meta-basalt including chlorite and epidote. Epidote is characterized by patchy birefringence, chlorite is pale green under PPL (Sample KC-14-17, a: PPL, b: XPL, ep: epidote, chl: chlorite, op: opaque).

3.1.1 Mineral Chemistry

All mineral chemistry data and reports are provided in Appendices A. The minerals in the Kösdağ meta-basalt (sample AB-6-18) clinopyroxene, epidote and chlorite (Figure 3.5) were analyzed by an electron probe micro analyzer. Representative analyses are given in Table 3.2.

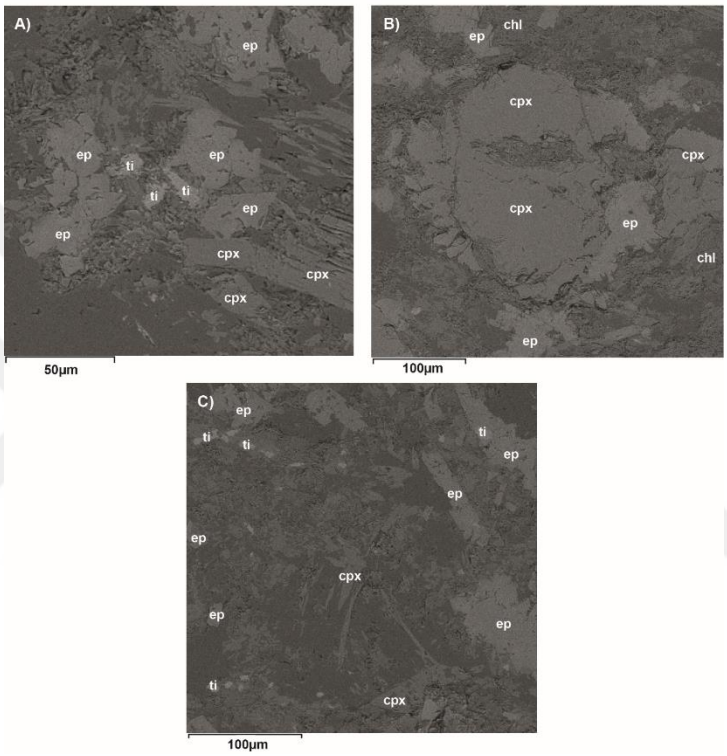


Figure 3.5. BSE images of the meta-basalt (AB-6-18) sample. Epidote (ep) + clinopyroxene (cpx) + titanite (ti) + chlorite (chl).

3.1.1.1 Clinopyroxene

Electron micro-probe analysis was conducted on certain minerals based on the chemical composition of the Kösdağ meta-basalt. Clinopyroxene is one of the most abundant mafic mineral phases noticed in the Kösdağ meta-basic lithologies (Figure 3.5). Table 3.2 includes the microprobe analyses of clinopyroxene in the KM meta-basalt. The number of cations was recalculated on the basis of 6 oxygens.

Table 3.2. Mineral chemistry of the measured clinopyroxenes. Mineral formula calculations are based on 6 oxygens.

Sample	AB-6-18	AB-6-18	AB-6-18	AB-6-18	AB-6-18	AB-6-18	AB-6-18	AB-6-18
	spectrum 92	spectrum 94	spectrum 96	spectrum 97	spectrum 98	spectrum 100	spectrum 118	spectrum 123
SiO_2	58.46	58.85	58.62	54.19	52.96	54.8	56.91	58.47
Al_2O_3	-	-	-	1.78	4	-	2.1	-
FeO	7.28	7.52	8.03	5.49	5.23	8.54	8.18	7.41
MgO	21.33	20.88	20.97	19.6	18.84	19.43	20.07	21.41
CaO	12.92	12.75	12.38	18.94	18.97	17.23	12.74	12.71
Total	99.99	100	100	100	100	100	100	100
Si	2.22	2.141	2.134	1.964	1.918	2.004	2.073	2.122
Al	-	-	-	0.076	0.171	-	0.09	-
$Fe^{(2+)}$	0.221	0.229	0.245	0.166	0.158	0.261	0.249	0.225
Mg	1.154	1.133	1.138	1.059	1.017	1.059	1.09	1.158
Ca	0.503	0.497	0.483	0.735	0.736	0,675	0.497	0.494
Total	4	4	4	4	4	4	4	4
Mg#	0.84	0.83	0.82	0.86	0.87	0.80	0.81	0.84
Wo	26.76	26.75	25.89	37.51	38.51	33.83	27.08	26.32
En	61.47	60.94	61.01	54.01	53.21	53.08	59.35	61.7
Fs	11.77	12.31	13.11	8.49	8.29	13.09	13.57	11.98

Clinopyroxenes are classified augite, with a compositional range of the $Wo_{26–38}$ $En_{53–61}$ $Fs_{8–13}$ and Mg number (Mg#) ranging from 0.80 to 0.87 (Table 3.2; Figure 3.6) by using the International Mineralogical Association classification (Morimoto et al., 1988).

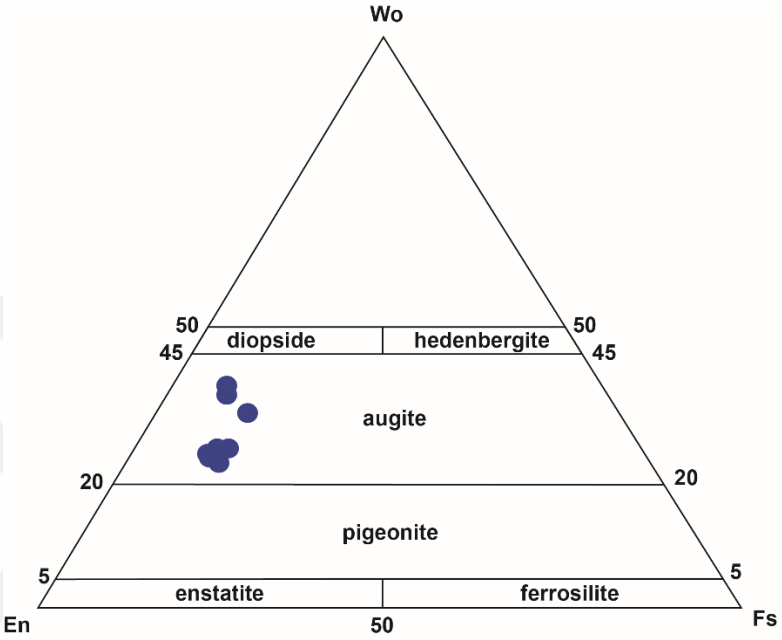


Figure 3.6. Pyroxene classification diagram (Morimoto et al., 1988) of the Kösdağ meta-basalt.

3.1.1.2 Epidote

The $Fe^{3+}/(Fe^{3+} + Al)$ ratio of epidotes ranges between 0.13 and 0.23 (Table 3.3).

Table 3.3. Mineral chemistry of the measured epidotes. Mineral formula calculations are based on 12.5 oxygens.

Sample	AB-6-18	AB-6-18	AB-6-18	AB-6-18	AB-6-18	AB-6-18	AB-6-18	AB-6-18	AB-6-18	AB-6-18	AB-6-18	AB-6-18	AB-6-18	AB-6-18
	spectrum 86	spectrum 87	spectrum 91	spectrum 93	spectrum 95	spectrum 99	spectrum 103	spectrum 105	spectrum 107	spectrum 111	spectrum 112	spectrum 114	spectrum 116	spectrum 119
SiO_2	40.86	39.72	40.93	40.74	41.08	41.12	40.9	41.18	40.53	40.47	38.99	40.65	40.87	40.73
Al_2O_3	25.87	25.12	25.71	25.7	28.4	27.64	26.5	25.74	26.54	27.76	25.94	25.7	26.81	29.6
FeO	10.73	10.86	10.7	10.59	7.62	8.38	9.75	11.06	10.04	8.95	9.59	10.56	9.35	6.49
CaO	22.54	22.41	22.67	22.96	22.9	22.85	22.86	22.02	22.9	22.81	22.4	23.09	22.97	23.18
Total	100	98.11	100.01	99.99	100	99.99	100.01	100	100.01	99.99	96.92	100	100	100
Si	3.094	3.075	3.1	3.09	3.085	3.095	3.92	3.113	3.068	3.053	3.049	3.085	3.087	3.053
Al	2.309	2.292	2.295	2.297	2.513	2.452	2.361	2.294	2.368	2.468	2.39	2.299	2.387	2.615
$Fe^{(3+)}$	0.68	0.703	0.678	0.672	0.479	0.527	0.616	0.699	0.636	0.565	0.627	0.67	0.591	0.407
Ca	1.829	1.859	1.84	1.866	1.842	1.842	1.851	1.784	1.858	1.844	1.877	1.877	1.859	1.862
Total	7.912	7.929	7.913	7.925	7.919	7.916	7.92	7.89	7.93	7.93	7.943	7.931	7.924	7.937
$Fe^{3+}/ (Fe^{3+}) + Al)$	0.23	0.23	0.23	0.23	0.16	0.18	0.21	0.23	0.21	0.9	0.21	0.23	0.20	0.13

3.1.1.3 Chlorite

EPMA results of the chlorite are listed in Table 3.4. Chlorite is a common secondary mineral in the KM. This mineral phase may result from thermal modifications and/or replacement of primary Fe-Mg pyroxene or amphibole minerals. The analyses of a total of 2 points were conducted. Chlorite contains 33.74-34.86 wt.% SiO_2, 22.67-23.32 wt.% Al_2O_3,15.61-17.87 wt.% Fe_2O_3, 24.71-26.38 wt.% MgO and 0.34–0.48 wt.% CaO with Fe/(Fe+Mg) ranging from 0.25 to 0.29 (ave. = 0.27) (Table 3.4). Chlorites are classifed as pycnochlorite (Table 3.4; Figure 3.7).

Table 3.4. Mineral chemistry of the measured chlorites. Mineral formula calculations are based on 28 oxygens.

Sample	AB-6-18	AB-6-18
	spectrum 104	spectrum 106
SiO_2	34.86	33.74
Al_2O_3	22.67	23.32
Fe_2O_3	15.61	17.87
MgO	26.38	24.71
CaO	0.48	0.34
H2O	13.94	13.78
Total	114.17	113.96
Si	5.968	5.485
Al iv	2.032	2.155
Al vi	2.566	2.63
$Fe^{(3+)}$	0.297	0.264
$Fe^{(2+)}$	1.938	2.325
Mg	6.732	6.382
Ca	0.088	0.063
OH*	16	16
Total	35.62	35.66
Fe/Fe+Mg	0.249	0.289
variety	pycnochlorite	pycnochlorite

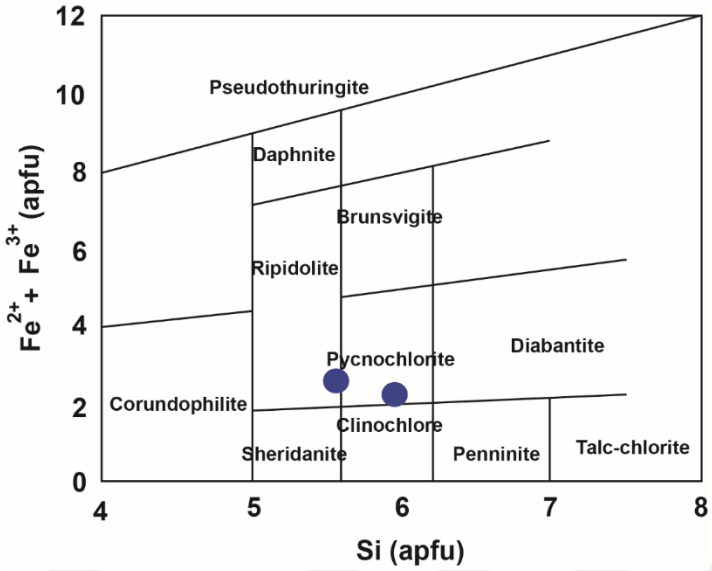


Figure 3.7. Plots of chlorite compositions in the classification scheme of Hey (1954).

Meta-diabase is a microphaneritic mafic igneous rock, also called microgabbro or dolerite. It typically occurs as a subvolcanic rock and has a similar chemical composition with gabbro and basalt. The Kösdağ meta-diabases are dark green-colored in hand specimen, attesting to the existence of secondary mineral assemblages, such as epidote and chlorite. This, in turn, suggests the influence of low-grade metamorphism. Although meta-diabases may look similar to meta-basalts in hand specimen, they are distinguished with their coarser grain size.

Meta-diabases are non-foliated in general, and they consist predominantly of plagioclase, clinopyroxene with minor amounts of epidote, chlorite, calcite, and opaque minerals (Figure 3.8). Plagioclase generally forms subhedral to euhedral tabular crystals with characteristic polysynthetic twinning. Carlsbad-albite type combined twinning rarely occurs. All of the meta-diabase samples underwent low degrees of greenschist facies metamorphism as reflected by the presence of secondary minerals as chlorite and epidote.

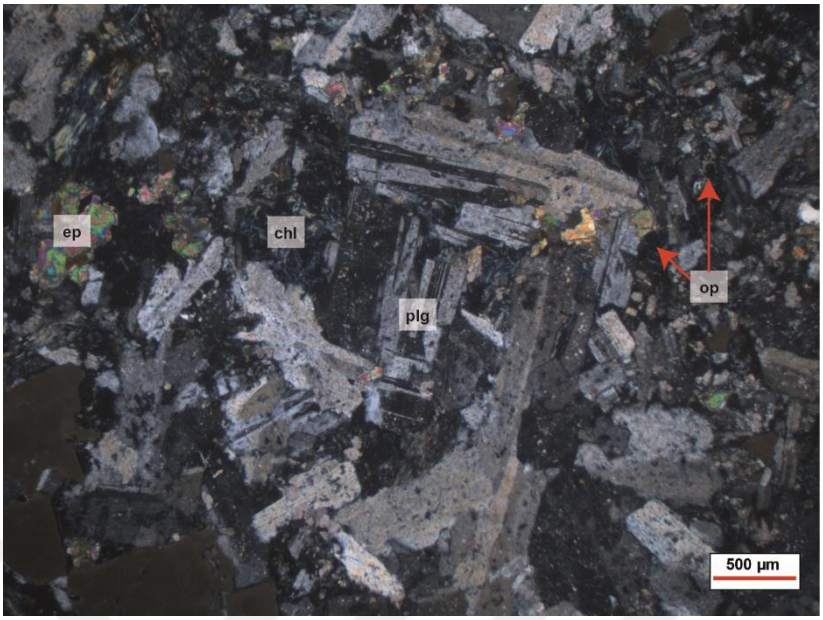


Figure 3.8. Photomicrograph of Kösdağ meta-diabase consisting of mainly plagioclase, chlorite, and epidote (Sample KC-7-17, chl: chlorite, ep: epidote, op: opaque, plg: plagioclase).

3.1.2 Mineral Chemistry

The minerals in the Kösdağ meta-diabase (sample KC-7-17) clinopyroxene, plagioclase, epidote, and chlorite (Figure 3.9) were analyzed by an electron probe micro analyzer. Representative analyses are given in Table 3.5.

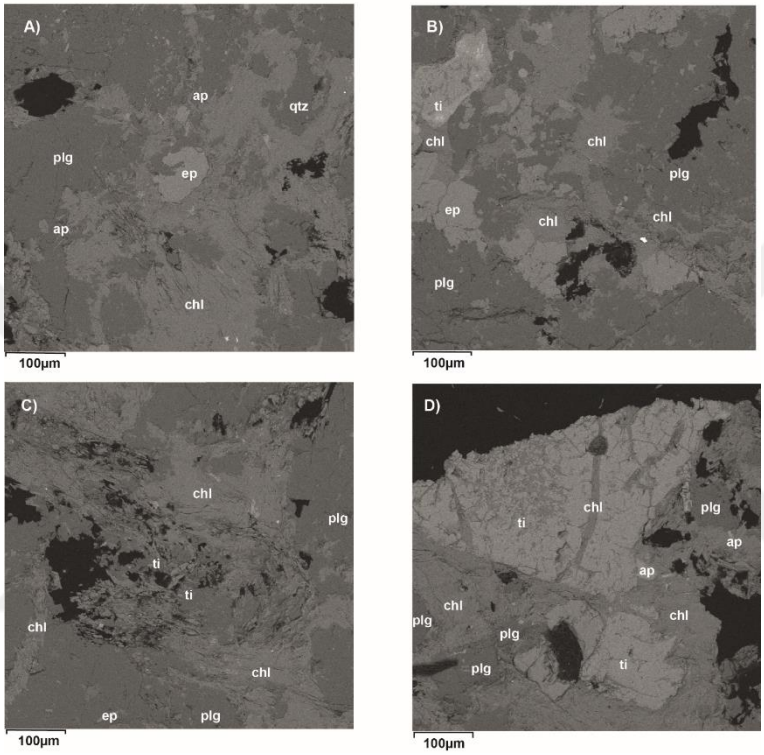


Figure 3.9. BSE images of the meta-diabase (KC-7-17) sample. Epidote (ep) + plagioclase (plg) + chlorite (chl) + quartz (qtz) + titanite (ti) + apatite (ap).

3.1.2.1 Clinopyroxene

Electron micro-probe analyses were performed on clinopyroxene based on the Kösdağ meta-diabase chemical composition. Table 3.5 includes the microprobe analyses of clinopyroxene in the KM metadiabase. The number of cations was recalculated on the basis of 6 oxygens. Clinopyroxene is augite, with a composition of the Wo_{26} En_{53} Fs_{19} and Mg number (Mg#) is 0.73 (Table 3.5; Figure 3.10).

Table 3.5. Mineral chemistry of the measured clinopyroxenes. Mineral formula calculations are based on 6 oxygens.

Sample	KC-7-17
	spectrum 63
SiO_2	57.73
Fe_2O_3	11.88
MgO	18.13
CaO	12.26
Total	100
Si	2.142
$Fe^{(2+)}$	0.369
Mg	1.003
Ca	0.487
Total	4
Mg#	0.73
Wo	26.22
En	53.95
Fs	19.83

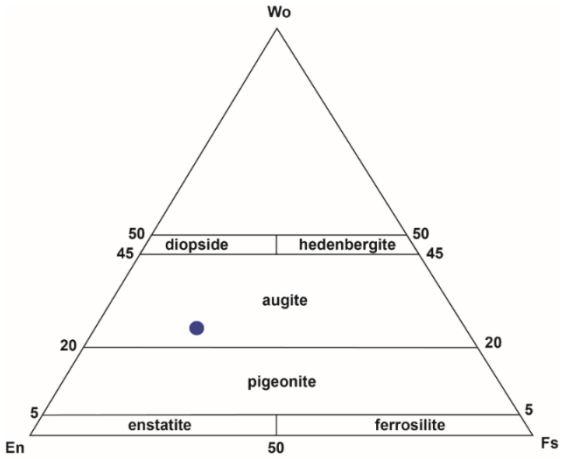


Figure 3.10. Pyroxene classification diagram (Morimoto et al., 1988) of the Kösdağ meta-diabase.

3.1.2.2 Plagioclase

Table 3.6. Mineral chemistry of the measured plagioclases. Mineral formula calculations are based on 8 oxygens.

Sample	KC-7-17	KC-7-17	KC-7-17	KC-7-17	KC-7-17	KC-7-17	KC-7-17	KC-7-17	KC-7-17	KC-7-17	KC-7-17
	spectrum 35	spectrum 36	spectrum 52	spectrum 53	spectrum 61	spectrum 69	spectrum 70	spectrum 78	spectrum 79	spectrum 81	spectrum 83
SiO2	67.53	67.14	67.44	66.91	67.81	64.72	62.14	68.11	65.55	67.42	67.1
TiO2	-	-	-	-	-	-	4.04	-	-	-	-
Al2O3	19.73	19.59	20.08	20.22	21.68	20.04	18.57	19.55	21.38	19.92	20.19
Fe2O3	-	-	-	-	-	1.6	0.4	-	0.47	-	-
MgO	-	-	-	-	-	1.51	-	-	-	-	-
CaO	0.17	0.45	0.18	0.68	0.64	0.3	4.61	-	0.39	0.37	0.56
Na2O	12.44	10.62	12.3	12.19	6.5	11.82	9.91	12.34	11.51	12.29	12.15
K2O	0.14	0.25	-	-	1.57	-	0.33	-	0.71	-	-
Total	100.01	98.05	100	100	98.2	99.99	100	100	100.01	100	100
An	0.74	2.25	0.80	2.99	4.48	1.38	20.10	0.00	1.77	1.64	2.48
Ab	98.53	96.26	99.2	97.01	82.42	98.32	78.19	98.27	94.4	98.36	97.52
Or	0.73	1.49	0	0	13.1	0	1.71	1.73	3.83	0	0

Plagioclases are observed as euhedral crystals with sizes 0.1-1 mm. The plagioclase crystals display albite twinning and/or normal zoning. The plagioclase compositions of the Kösdağ meta-diabase display a narrow compositional range from $An_{0,7}$ to An_{20} (Table 3.6) in the classification of Deer et al. (1992). The Or content of the plagioclases is between 0 and 13.1 in the Kösdağ meta-diabase sample. The plagioclase compositions range from oligoclase to albite (Figure 3.11).

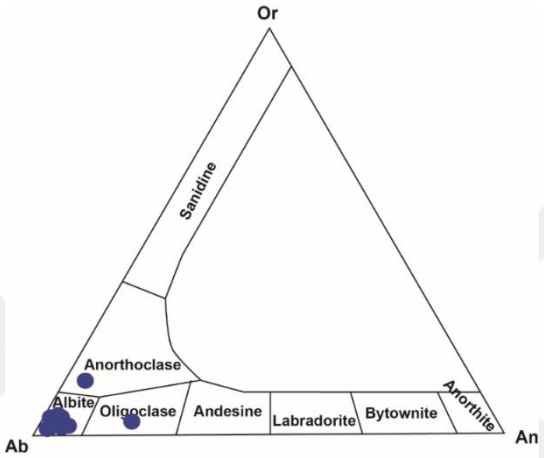


Figure 3.11. Classification of the plagioclases in the Kösdağ meta-diabase on ternary An-Ab-Or plot.

3.1.2.3 Chlorite

Table 3.7. Mineral chemistry of the measured chlorites. Mineral formula calculations are based on 28 oxygens.

Sample	KC-7-17	KC-7-17	KC-7-17	KC-7-17	KC-7-17	KC-7-17	KC-7-17	KC-7-17	KC-7-17	KC-7-17	KC-7-17	KC-7-17
	spectrum 45	spectrum 47	spectrum 51	spectrum 55	spectrum 57	spectrum 58	spectrum 65	spectrum 66	spectrum 68	spectrum 74	spectrum 76	spectrum 82
SiO2	32.37	34.17	32.67	32.71	33.45	48.71	32.72	33.22	33.31	32.39	31.94	33.05
Al2O3	22.29	22.24	22.11	22.15	22.61	20.61	22.48	22.51	23.22	23.29	22.6	22.28
Fe2O3	25.05	23.36	24.56	24.58	22.11	13.96	24.86	24.64	22.79	23.98	25.13	23.78
MgO	20.29	19.67	20.24	20.56	21.83	11.23	19.94	19.32	20.34	20.34	19.51	20.56
CaO	-	0.56	0.42	-	-	-	-	0.32	0.34	-	0.34	0.33
Na2O	-	-	-	-	-	5.49	-	-	-	-	-	-
Total	100	100	100	100	100	100	100	100.01	100	100	99.99	100
Si	5.813	6.043	5.856	5.855	5.9	7.717	5.856	5.927	5.899	5.774	5.745	5.889
Al iv	2.187	1.957	2.144	2.145	2.1	0.283	2.144	2.073	2.101	2.226	2.255	2.111
Al vi	2.549	2.715	2.546	2.548	2.626	3.775	2.621	2.689	2.778	2.691	2.557	2.591
Fe(3+)	0.202	0.422	0.223	0.224	0.293	1.212	0.265	0.342	0.376	0.258	0.238	0.267
Fe(2+)	3.561	3.033	3.458	3.456	2.969	0.638	3.456	3.334	2.999	3.317	3.542	3.277
Mg	5.432	5.186	5.408	5.486	5.74	2.652	5.32	5.138	5.369	5.406	5.231	5.461
Ca	-	0.106	0.081	-	-	-	-	0.061	-	-	0.066	0.063
Na	-	-	-	-	-	3.373	-	-	-	-	-	-
Fe/Fe+Mg	0.409	0.4	0.405	0.401	0.362	0.411	0.412	0.417	0.386	0.398	0.419	0.394
variety	pycnochlorite	pycnochlorite	pycnochlorite	pycnochlorite	pycnochlorite	Talc-chlorite	pycnochlorite	pycnochlorite	pycnochlorite	pycnochlorite	pycnochlorite	pycnochlorite

EPMA results of the chlorite are provided in Table 3.7. Chlorite contains 31.94-48.71 wt.% SiO_2, 20.61-23.29 wt.% Al_2O_3,13.96-25.13 wt.% Fe_2O_3, 11.23-20.56 wt.% MgO and 0.32-0.56 wt.% CaO with Fe/(Fe+Mg) ranging from 0.36 to 0.42 (ave. = 0.41) (Table 3.7). Chlorites are classifed as pycnochlorite except for one talc-chlorite grain (Table 3.7; Figure 3.12).

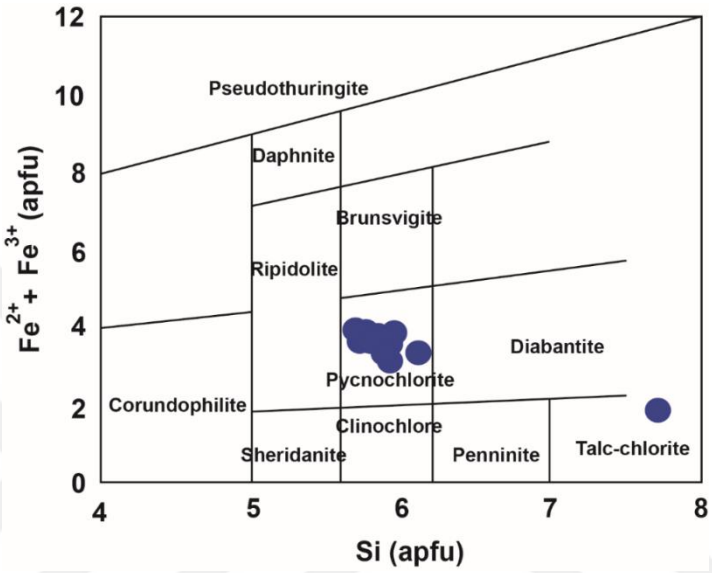


Figure 3.12. Plots of chlorite compositions in the classification scheme of Hey (1954).

3.1.2.4 Epidote

Based on the chemical composition of the KM meta-diabase, electron micro-probe analysis were also performed on epidote. Table 3.8 comprises the microprobe analyses of epidote in the KM metadiabase. The number of cations was recalculated on the basis of 12.5 oxygens.

Table 3.8. Mineral chemistry of the measured epidotes. Mineral formula calculations are based on 12.5 oxygens.

Sample	KC-7-17	KC-7-17	KC-7-17	KC-7-17
	spectrum 33	spectrum 50	spectrum 56	spectrum 71
SiO_2	40.46	40.14	40.5	41.1
Al_2O_3	24.02	22.23	23.95	28.92
Fe_2O_3	12.6	13.59	13.04	7.34
MnO	-	-	-	0.9
CaO	22.92	23.04	22.51	21.75
Total	100	99	100	100.01
Si	3.089	3.11	3.09	3.084
Al	2.161	2.03	2.154	2.557
$Fe^{(3+)}$	0.804	0.881	0.832	0.461
Mn	-	-	-	0.057
Ca	1.875	1.913	1.84	1.749
Total	7.929	7.934	7.916	7.908

3.2 Meta-intermediate Kösdağ Lithologies

The meta-intermediate Kösdağ lithologies include meta-andesites displaying greenish and dark-greyish colors in the outcrop. The Kösdağ meta-andesites are aphanitic, with a fine-grained groundmass. They are mostly foliated, though nonfoliated types also occur. If the initial textures of these rocks are considered, their crystalinity can be regarded to change between hypocrystalline and holocrystalline.

Plagioclase (>500 μm) is a major primary component of meta-andesites and can be found as subhedral to euhedral crystals (Figure 3.13). In some places, it displays concentric zoning resulting from disequilibrium.

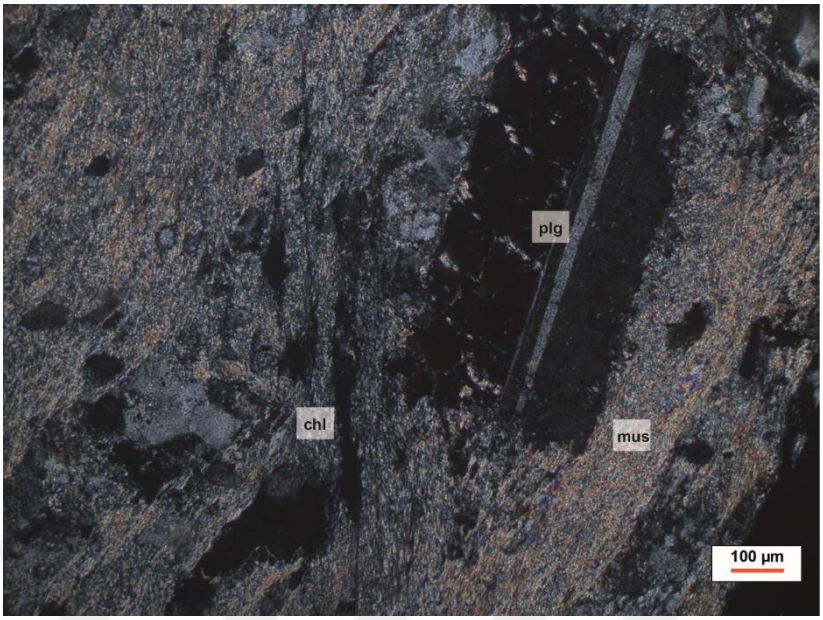


Figure 3.13. Photomicrograph of porphyroclastic texture in the Kösdağ meta-andesite, characterized by plagioclase porphyroclasts (Sample AB-6-17, a: PPL, b: XPL, mus: muscovite, op: opaque, chl: chlorite, plg: plagioclase).

Chlorite, epidote, and sericite represent the secondary mineral phases in the Kösdağ meta-andesites, as they are in the Kösdağ meta-basalts (Figure 3.14). Chlorite replaces the groundmass and plagioclase phenocrysts and is abundant in the Kösdağ meta-andesites. It is distinguished from the other minerals by its anomalous interference colors. Epidote is observed to replace clinopyroxene and plagioclase in the Kösdağ meta-andesites. Patchy birefringence, a characteristic feature of epidote, is also noticed in these lithologies. Sericite is observed to replace plagioclase and groundmass in varying degrees. Some sericite appears to have formed as a result of sericitization, a process occurring during hydrothermal alteration of igneous rocks (e.g., Meyer and Hemley, 1967). In addition, neomineralization of sericite resulting from the dynamic metamorphism was observed around large porphyroclasts. Accessory minerals in the Kösdağ meta-andesites are represented by opaques, zircon, and apatite.

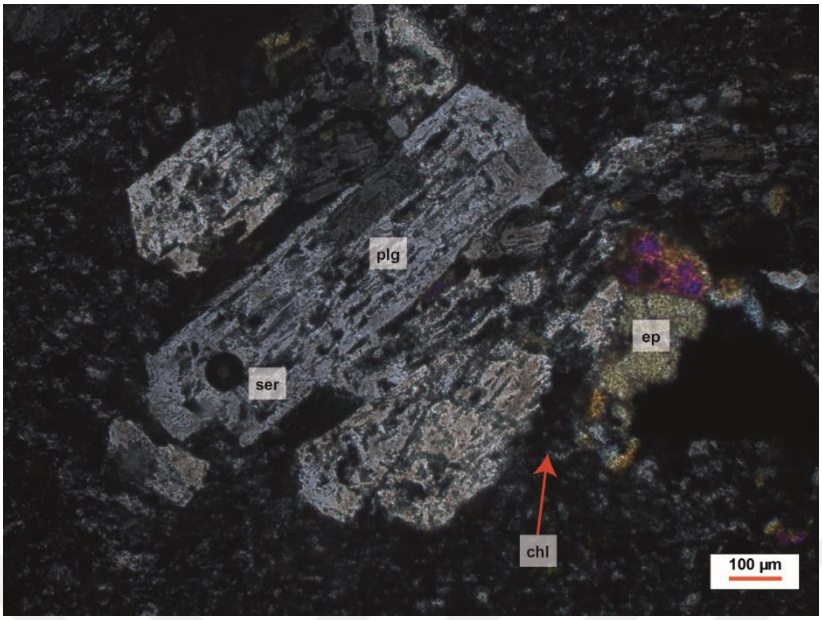


Figure 3.14. Plagioclase clusters making up glomeroporphyritic texture in the Kösdağ meta-andesite. Plagioclase is partially altered into sericite and epidote (Sample 153, a: PPL, b: XPL, chl: chlorite, ep: epidote, plg: plagioclase).

3.2.1 Mineral Chemistry

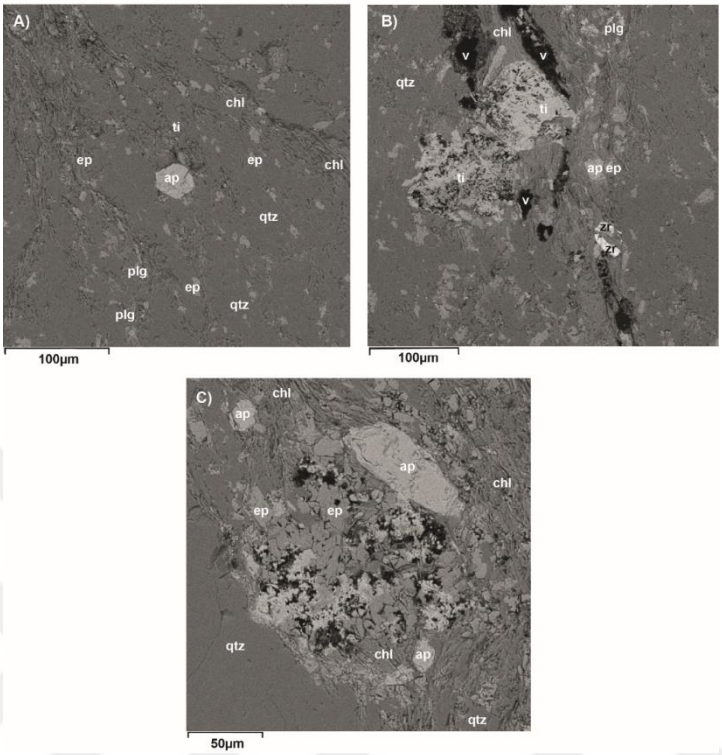


Figure 3.15. Backscattered-Electron (BSE) micrographs of the Kösdağ meta-andesite (76) sample.

3.2.1.1 Plagioclase

Plagioclases are observed as euhedral crystals exhibiting albite twinning and/or normal zoning (Figure 3.15). The plagioclase compositions of the Kösdağ meta-andesite display a compositional range from Andesine to Albite (Table 3.9; Figure 3.16) in the classification of Deer et al. (1992). The Or content of the plagioclases is between 0 and 13.1 in the Kösdağ meta-andesite sample.

Table 3.9. Mineral chemistry of the measured plagioclases. Mineral formula calculations are based on 8 oxygens.

Sample	76	76	76	76	76	76	76
	spectrum 134	spectrum 136	spectrum 139	spectrum 142	spectrum 148	spectrum 155	spectrum 165
SiO_2	66.88	84.69	55.13	59.28	58.73	66.18	69.3
Al_2O_3	19.85	10.08	24.19	18.02	22.95	19.95	18.19
Fe_2O_3	-	0.48	3.4	9.57	2.05	-	1.75
CaO	0.23	1.08	10.31	5.78	7.08	0.35	5.31
Na_2O	13.03	2.24	6.97	7.36	8.55	13.37	5.46
K_2O	-	1.43	-	-	0.64	0.16	-
Total	99.99	100	100	100.01	100	100.01	100.01
An	0.97	15.80	44.98	30.26	30.37	1.41	34.96
Ab	99.03	59.3	55.02	69.74	66.36	97.81	65.04
Or	0	24.91	0	0	3.27	0.77	0

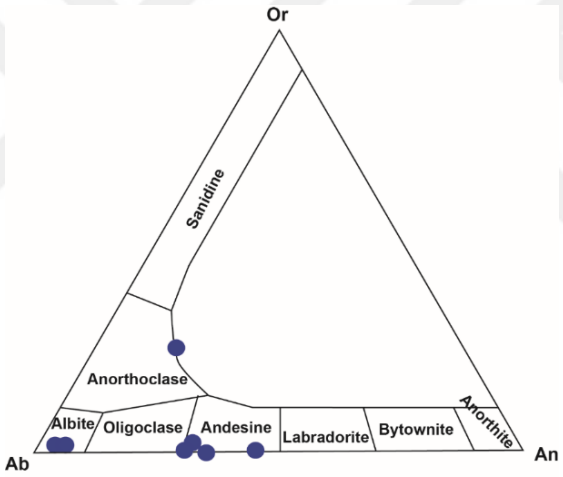


Figure 3.16. Classification of the plagioclases in the Kösdağ Metavolcanics on ternary An-Ab-Or plot.

3.2.1.2 Epidote

Table 3.10. Mineral chemistry of the measured epidotes. Mineral formula calculations are based on 12.5 oxygens.

Sample	76	76	76	76	76	76	76	76	76
	spectrum 129	spectrum 133	spectrum 135	spectrum 138	spectrum 147	spectrum 154	spectrum 159	spectrum 160	spectrum 170
SiO_2	44.72	42.98	44.29	42.16	42.37	42.09	42.39	41.77	47.99
Al_2O_3	26.53	28.17	28.62	27.51	29.03	28.51	29.67	28.68	25.53
Fe_2O_3	8.32	7.88	7.22	8.73	7.17	7.69	6.52	5.11	6.66
MnO	-	-	-	-	-	-	-	0.84	-
MgO	-	-	-	-	-	-	-	1.46	-
CaO	20.42	20.98	18.84	21.6	21.43	21.7	21.42	22.14	18.46
K_2O	-	-	1.04	-	-	-	-	-	-
Total	99.99	100.01	100.01	100	100	99.99	100	100	98.64
Si	3.314	3.196	3.274	3.155	3.152	3.141	3.147	3.122	3.544
Al	2.317	2.468	2.494	2.426	2.545	2.508	2.596	2.526	2.222
$Fe^{(3+)}$	0.516	0.49	0.446	0.546	0.446	0.48	0.405	0.319	0.411
Mn	-	-	-	-	-	-	-	0.053	-
Mg	-	-	-	-	-	-	-	0.163	-
Ca	1.622	1.671	1.492	1.732	1.708	1.735	1.704	1.773	1.461
Total	7.769	7.825	7.706	7.859	7.851	7.864	7.852	7.956	7.638

3.3 Meta-felsic Kösdağ Lithologies

The meta-felsic Kösdağ lithologies comprise meta-dacites and meta-rhyolites. However, it is not easy to distinguish meta-dacite from meta-rhyolite in hand specimen, though their identification is possible through thin-section observations. The Kösdağ meta-felsics are usually white in hand specimen. Some Kösdağ meta-felsics, on the other hand, resemble the Kösdağ meta-andesites with their greenish colors. Despite this resemblance, the existence of quartz grains, which are seen with the naked eye, helps differentiate these rocks from the Kösdağ meta-andesites. The Kösdağ meta-felsics are aphanitic and porphyritic, including visible phenocrysts of quartz, plagioclase, and K-feldspar. They typically exhibit foliation similar to most Kösdağ meta-andesites and some Kösdağ meta-basalts.

Quartz, plagioclase, and to a lesser extent K-feldspar are the primary constituents of the Kösdağ meta-felsics. Opaque minerals are present but occur in smaller amounts. The widespread primary mineral phase is quartz. It can be identified by the naked eye with shades of grey. In general, quartz has rounded, anhedral shapes and remains very fresh due to its high resistance to post-magmatic processes (Figure 3.17). Some quartz grains in the Kösdağ meta-felsics are embayed with internal voids, suggesting resorption. Stable minerals can become unstable with decreasing temperature during magmatic evolution, causing them to interact with the melt. This phenomenon is known as magmatic corrosion, and it can be seen in the Kösdağ meta-felsics by the existence of corroded quartz grains (Figure 3.18). Also, quartz is found as porphyroclast in the Kösdağ meta-felsics. Quartz porphyroclasts exhibit undulatory (wavy) extinction under XPL, and surrounded by aligned muscovite and sericite grains.

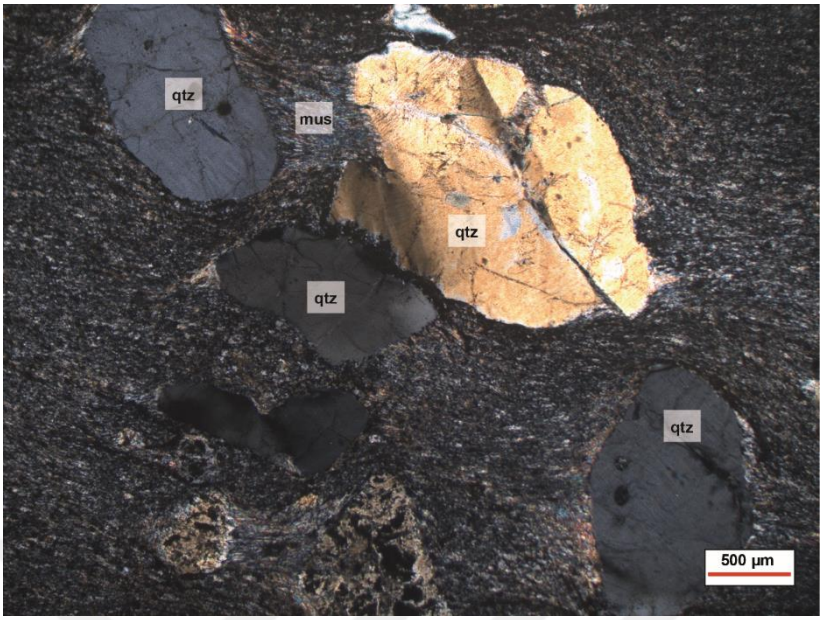


Figure 3.17. Undulose extinction, which is an indicator of deformation as observed on quartz porphyroclasts in the Kösdağ meta-rhyolite (Sample AD-2-18, a: PPL, b: XPL, qtz: quartz, mus: muscovite).

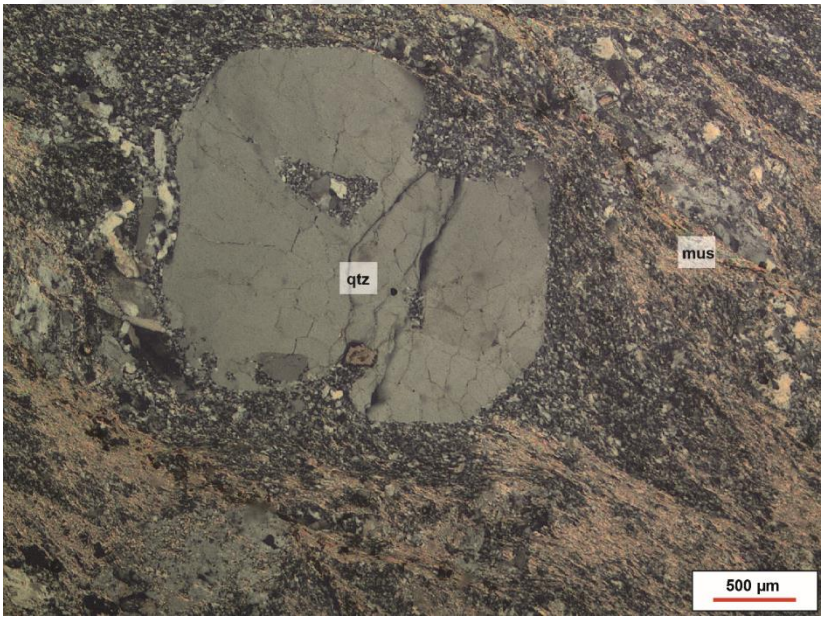


Figure 3.18. Quartz porphyroclast with rounded shape in meta-dacite. Rounding is caused by dynamic metamorphism, whereas corrosion is caused by dissolution during interaction with magma (Sample DD-7-17, qtz: quartz, mus: muscovite).

Plagioclase, which is mainly present as subhedral to anhedral crystals, is the second most common constituent in the Kösdağ meta-felsics. It is found as a porphyroclast and also occurs in the groundmass similar to quartz. Polysynthetic twinning is

common and seen in the less altered plagioclase grains. Sector twinning occurs in rare cases.

K-feldspar (>1 mm) also occurs as subhedral slightly larger phenocryst relative to plagioclase and is distinguished by Carlsbad twinning. It is cloudy on the surface, with partial alteration into clay minerals, and shows first-order interference colors. Secondary mica minerals enveloping K-feldspar quartz and minerals in the Kösdağ meta-felsics, suggest a mylonitic texture indicating extreme ductile deformation (e.g., Passchier and Trouw, 2005) (Figure 3.19).

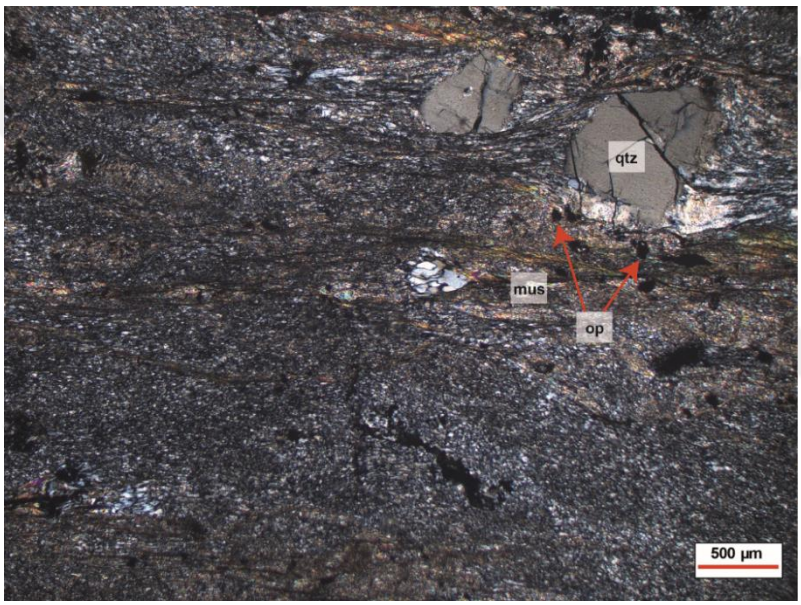


Figure 3.19. Mylonite produced by strong deformation of the meta-dacite, with quartz porphyroclasts surrounded by muscovites (Sample IPS-13-29, mus: muscovite, op: opaque, qtz: quartz).

Since primary mafic phases have been completely replaced by chlorite and epidote group minerals, Kösdağ meta-dacites have no primary mafic phase such as biotite, hornblende, pyroxene, and olivine.

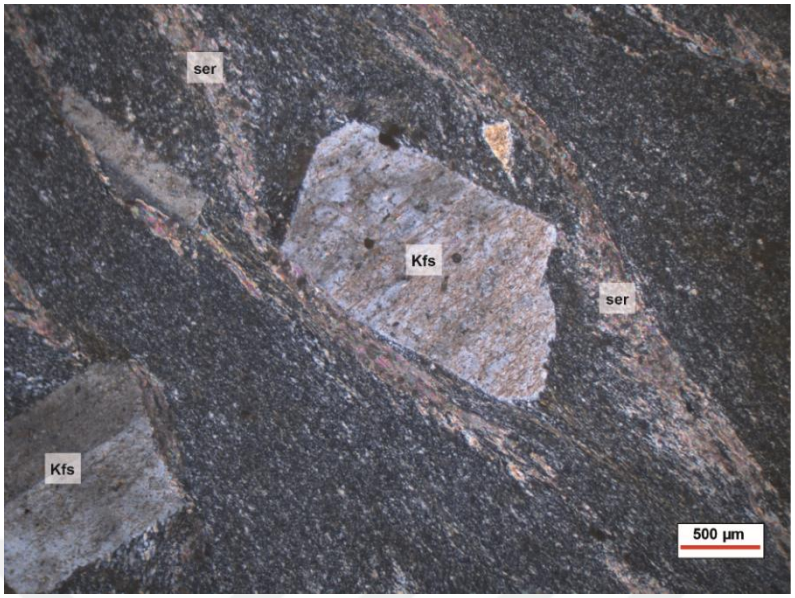


Figure 3.20. Meta-rhyolite which comprises porphyroclasts of K-feldspar with first-order interference colors. Note the strong sericitization on K-feldspar, which is represented by small patches with high-order interference colors. (YD-1-18, Kfs: K-feldspar, ser: sericite).

Pressure shadows, which form around rigid minerals (Bard, 1986), are typical in metamorphic rocks formed by dynamic and/or dynamothermal metamorphism (Williams, 1972). These pressure shadows exist in Kösdağ meta-felsics and seem to have evolved around quartz and K-feldspar porphyroclasts (Figures 3.18, 3.20, 3.21).



Figure 3.21. The development of secondary mineral phases such as calcite and sericite on K-feldspar porphyroclast (Sample IPS-13-23, cal: calcite, Kfs: K-feldspar, ser: sericite).

The secondary mineral assemblage in Kösdağ meta-dacites is similar to Kösdağ meta-andesites, consisting of chlorite, epidote, sericite, and calcite. Chlorite is a common secondary mineral phase in Kösdağ meta-dacites. The anomalous purple interference color may mean that chlorite is Fe-rich. Epidotization is also widespread, and it appears that plagioclase and clinopyroxene have been affected from it. Calcite is a secondary mineral which replaces plagioclase and mafic phases. It is colorless under PPL but has very high-order interference colors under XPL. Calcite also has rhombohedral twinning. The secondary mineral assemblage in Kösdağ meta-dacites suggests that they have been subjected to low-grade metamorphism. Zircon, apatite, and opaque minerals constitute the accessory minerals in the Kösdağ meta-dacites.

3.3.1 Mineral Chemistry

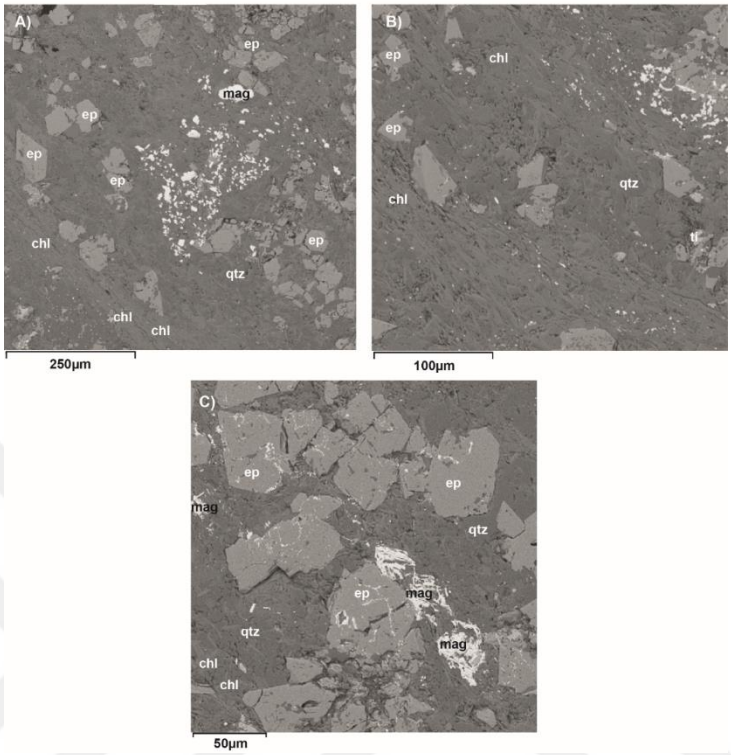


Figure 3.22. Backscattered-Electron (BSE) micrographs of the Kösdağ meta-rhyolite (AD-2-18) sample.

3.3.1.1 Chlorite

Table 3.11. Mineral chemistry of the measured chlorites. Mineral formula calculations are based on 28 oxygens.

Sample	AD-2-18	AD-2-18	AD-2-18
	spectrum 6	spectrum 15	spectrum 20
SiO2	45.5	33.28	47.96
Al2O3	26.14	24.02	27.71
Fe2O3	9.07	13.49	6.81
MgO	13.62	29.2	9.08
K2O	5.67	-	8.44
Total	100	99.99	100
Si	7.535	5.677	7.555
Al iv	0.465	2.323	0.445
Al vi	4.767	2.515	4.949
$Fe^{(3+)}$	1.259	0.107	0.897
$Fe^{(2+)}$	-	1.818	-
Mg	3.37	7.425	2.132
OH*	16	16.00	16.00
Total	33.396	35.865	35.370
Fe/Fe+Mg	0.272	0.206	0.296
variety	diabantite	pycnochlorite	diabantite

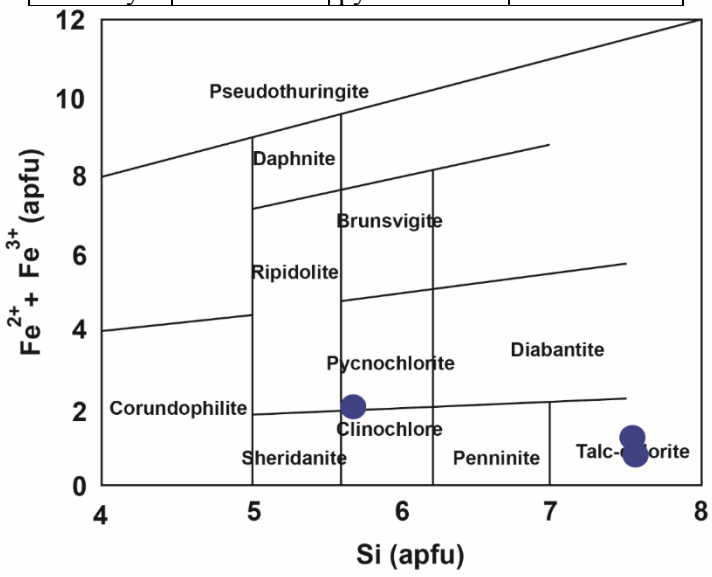


Figure 3.23. Plots of chlorite compositions in the classification scheme of Hey (1954).

3.3.1.2 Epidote

Table 3.12. Mineral chemistry of the measured epidotes. Mineral formula calculations are based on 12.5 oxygens.

Sample	AD-2-18	AD-2-18	AD-2-18	AD-2-18	AD-2-18	AD-2-18	AD-2-18	AD-2-18	AD-2-18
	spectrum 1	spectrum 2	spectrum 3	spectrum 4	spectrum 13	spectrum 14	spectrum 23	spectrum 24	spectrum 25
SiO_2	39.95	40.04	39.92	39.91	40.12	39.82	39.89	40.09	39.76
Al_2O_3	24.13	24.13	24.21	24.08	24.35	23.81	24.12	23.85	24.56
Fe_2O_3	12.72	12.75	12.59	12.76	12.35	13.28	12.69	12.94	12.8
CaO	23.21	23.07	23.28	23.25	23.18	23.09	23.3	23.13	22.87
Total	100.01	99.99	100	100	100	100	100	100.01	99.99
Si	3.056	3.062	3.054	3.055	3.065	3.051	3.053	3.068	3.04
Al	2.176	2.175	2.183	2.172	2.192	2.15	2.176	2.151	2.213
$Fe^{(3+)}$	0.814	0.815	0.806	0.817	0.789	0.851	0.812	0.828	0.818
Ca	1.903	1.89	1.908	1.907	1.897	1.896	1.911	1.896	1.873
Total	7.949	7.942	7.951	7.951	7.943	7.948	7.952	7.943	7.944

CHAPTER 4

GEOCHEMISTRY

4.1 Major and Trace Element Geochemistry

In an attempt to assess the geochemical features of the KM, whole-rock geochemical data were obtained on 52 rock samples. 15 samples analyzed in Berber (2015) were also added to allow a more comprehensive petrogenetic interpretation (Table 4.1). As a result, 67 metavolcanic rocks were examined utilizing distinct geochemical diagrams of Harker, multi-element, binary, and tectonomagmatic discrimination. The KM display a wide range of compositions, including both primitive and evolved members. In the following parts, all major oxides were given on a volatile-free basis.

Table 4. 1. Major and trace element data of the Kösdağ Metavolcanics.

Sample	Type	SiO_2	MgO	Al_2O_3	Fe_2O_3	CaO	Na_2O	K_2O	TiO_2	P_2O_5	MnO	Cr_2O_3	LOI	Sum
6-6	Type1a	63.62	3.25	16.49	8.19	3.54	2.31	1.86	0.44	0.13	0.11	bdl	5	99.83
6-7a	Type1a	58.59	2.93	17.77	7.54	6.81	2.22	3.08	0.54	0.10	0.21	0.00	5.5	99.77
6-8	Type1a	73.50	1.77	14.25	2.54	0.86	4.17	2.30	0.36	0.07	0.05	bdl	2.8	99.85
44	Type1a	76.88	1.17	12.00	3.15	2.54	1.43	2.22	0.39	0.10	0.05	0.01	2,4	99.89
32	Type1a	56.09	5.21	23.93	7.19	1.24	0.74	4.73	0.72	0.06	0.06	0.01	4,8	99.8
214	Type1a	78.35	0.57	12.37	1.56	1.80	4.27	0.2	0.28	0.05	0.01	0.00	1.4	99.93
168	Type1a	58.17	4.85	17.31	11.09	0.55	6.31	0.35	1.03	0.17	0.13	0.01	3.2	99.89
IPS-13-23	Type1a	63.38	6.23	16.30	7.41	1.21	4.31	0.29	0.57	0.05	0.10	0.00	3.9	99.86
23	Type1a	74.88	2.80	13.86	2.73	0.23	2.22	2.67	0.38	0.05	0.02	0.01	2.7	99.93
IPS-13-29	Type1a	84.66	0.84	9.60	1.01	0.32	0.78	2.07	0.22	0.04	0.01	bdl	2.4	99.99
54a-PW	Type1a	71.34	1.03	14.04	3.79	2.84	4.12	1.99	0.53	0.10	0.06	0.01	2	99.93
190	Type1a	46.36	7.40	18.79	15.76	6.92	2.89	0.08	1.13	0.09	0.27	0.00	4.9	99.76
132	Type1a	70.94	1.06	13.88	5.77	3.18	4.20	0.28	0.43	0.11	0.11	0.01	1.7	99.93
30	Type1a	61.86	6.54	18.06	7.00	0.74	2.34	2.39	0.76	0.06	0.04	bdl	4.5	99.84
1	Type1a	75.51	1.84	13.73	3.02	1.59	2.01	1.75	0.35	0.05	0.05	0.01	2.4	99.92
AD-2-18	Type1a	77.76	0.45	12.92	1.59	1.59	3.12	2.00	0.27	0.06	0.06	0.00	1.6	99.88
197	Type1a	79.94	0.33	11.39	1.46	1.49	4.26	0.64	0.26	0.05	0.02	0.01	0.9	99.97
KR-5-18	Type1a	77.75	0.44	12.54	1.55	2.20	2.72	1.33	0.17	0.06	0.02	bdl	1.1	99.88
DD-7-17	Type1a	75.81	2.85	12.67	2.69	0.59	2.63	2.25	0.34	0.06	0.03	bdl	2.5	99.92
YD-18-17	Type1a	58.82	5.76	17.83	9.33	3.60	2.82	0.65	0.93	0.04	0.04	bdl	4.1	99.83
AB-6-17	Type1a	70.02	2.13	16.27	3.76	0.42	1.06	5.41	0.58	0.10	0.05	bdl	3	99.92
KR-20-17	Type1a	75.81	1.08	13.09	2.68	2.73	2.01	1.95	0.39	0.05	0.06	bdl	1.7	99.93
KR-11-17	Type1a	79.89	2.11	9.55	3.01	0.24	4.35	0.03	0.37	0.06	0.28	bdl	1.4	99.94
24	Type1a	77.65	2.86	11.05	2.63	1.14	0.76	1.10	0.27	0.08	0.03	0.00	2.3	99.93
DD-4-18	Type1a	75.91	0.51	13.28	1.88	0.64	5.19	2.12	0.18	0.04	0.02	0,00	1	99.89
KC-2-18	Type1a	75.52	2.29	12.63	3.47	0.30	0.87	4.12	0.39	0.08	0.02	bdl	3.4	99.9
YD-1-18	Type1a	79.22	0.33	11.73	1.50	1.57	4.63	0.53	0.25	0.06	0.01	0.00	1.3	99.88
33	Type1a	74.04	3.06	13.79	3.56	0.39	2.91	1.66	0.40	0.07	0.05	0.01	2.6	99.93
39	Type1a	66.08	2.94	15.02	6.13	3.08	5.44	0.18	0.69	0.21	0.15	0.01	3.7	99.9
83	Type1a	80.55	3.14	9.60	2.84	0.18	1.51	1.79	0.22	0.05	0.03	0.01	2.4	99.94
184	Type1a	76.77	2.37	12.75	1.98	0.22	2.16	3.31	0.24	0.05	0.05	0.01	2.2	99.95
IPS-13-26	Type1b	63.27	6.80	14.19	10.05	1.51	3.16	0.03	0.65	0.03	0.08	bdl	4.5	99.82
76	Type1b	55.47	6.96	18.30	9.56	3.98	2.74	1.85	0.78	0.02	0.09	0.01	4.4	99.8
136	Type1b	50.44	9.60	16.01	10.98	10.38	1.43	0.06	0.55	0.02	0.18	0.06	5.4	99.76
AB-10-17	Type1b	63.27	3.60	14.71	9.94	2.15	5.43	0.07	0.55	0.04	0.12	bdl	2.9	99.88
IPS-13-22	Type1b	53.47	4.96	13.58	9.62	13.46	2.20	1.07	0.74	0.03	0.60	0.00	10.4	99.85

bdl = below detection limit

Table 4.1. Cont.ed.

Sample	Type	Ba	Rb	Sr	Ni	Co	Sc	V	Zr	Hf	Y	Nb	Ta	La
6-6	Type1a	498	27.2	162.2	3.9	7	14	17	164.2	4.5	28.8	4.4	0.3	11.8
6-7a	Type1a	535	35.3	524.7	11.7	7.3	12	124	185.4	5.7	26.9	5	0.4	23.5
6-8	Type1a	520	37.2	60.6	1.9	2.7	9	31	126	3.4	22.4	4.3	0.2	18.1
44	Type1a	533	31	74.7	1.1	3.6	11	42	110.2	3.1	28.8	4.4	0.2	12.4
32	Type1a	444	58	258	7.4	9.6	25	55	121.9	3.9	23.2	3.2	bdl	7
214	Type1a	333	10	150.9	1	1.1	8	60	136	3.7	41.1	3.1	0.2	12.1
168	Type1a	53	4.7	66.8	3.8	23	29	244	84.6	2.6	20.8	1.6	bdl	6.7
IPS-13-23	Type1a	55	4.1	97.6	9	16.8	27	162	58.4	1.9	19.8	1.1	0.1	5.3
23	Type1a	386	35.8	29.5	1.7	3.3	13	41	105	3.4	14.8	2.1	0.1	2.9
IPS-13-29	Type1a	3613	21.9	53.5	2.4	1.7	6	23	92.2	2.6	10.7	1.9	0.1	5.7
54a-PW	Type1a	415	16.6	205.3	2.9	3.3	11	26	135.7	3.9	32.4	3.4	0.2	14.2
190	Type1a	20	1.4	89.1	17.4	48.8	64	357	48.3	1.7	25.2	0.8	bdl	3.2
132	Type1a	101	3.9	221.7	2.1	5.4	20	bdl	82.6	2.7	33.3	1.7	bdl	6.4
30	Type1a	496	29.2	60.6	5	10.4	23	150	92.7	3.2	24.6	1.7	bdl	4.9
1	Type1a	517	22.2	144.8	1.5	3.6	11	24	146	4.3	38.6	3.1	0.2	11.4
AD-2-18	Type1a	448	17.3	64.7	bdl	0.7	7	77	144.3	3.6	23.8	3.7	0.2	9.8
197	Type1a	649	7.5	75.4	1.4	1.7	8	14	118	3.7	29.6	2.5	0.1	9.5
KR-5-18	Type1a	471	23	426.3	3	1.1	2	8	90.1	2.2	12.4	4.1	0.30	21.1
DD-7-17	Type1a	226	28.1	37	0.7	3.6	11	34	100.8	3.2	22.9	2.4	0.1	7.7
YD-18-17	Type1a	375	12.7	105.1	1	15.7	33	155	92.3	2.7	29.1	2.3	0.1	8.9
AB-6-17	Type1a	1114	70.4	44.3	1	1.5	16	11	172.2	5.2	36.4	4.6	0.3	9.9
KR-20-17	Type1a	386	19.3	178.5	0.5	1.4	12	bdl	139.6	4.4	51.7	2.9	0.2	11.3
KR-11-17	Type1a	26	<0.1	36.1	1.1	1.5	8	bdl	97.5	3.1	26.7	2.1	0.1	4.5
24	Type1a	114	15.6	44.4	5.6	4.1	8	20	55.8	1.7	18.2	1.8	bdl	7.7
AB-10-17	Type1a	17	0.2	45.5	0.8	26.3	34	269	35.6	1.2	15.9	0.5	bdl	1.6
DD-4-18	Type1a	788	14	66.2	1.9	1.8	5	19	125.8	3.8	23.9	11.7	0.2	13.2
KC-2-18	Type1a	1593	53.4	10	2.3	5.1	14	62	102.9	3.5	20.6	4	0.1	5.7
YD-1-18	Type1a	221	6.9	135.2	1.4	1.4	12	24	134.3	3.8	39.4	4.6	0.3	12.1
33	Type1a	169	18.5	49.1	1.7	3.7	14	34	62.6	2.2	16.3	1.4	0.1	4.4
39	Type1a	39	2.7	69.3	0.6	8	15	59	92.8	2.9	27.1	3.6	0.2	3.8
83	Type1a	176	20.2	16.8	2.2	3.3	7	27	71.9	2	12.5	3.1	0.1	4.9
184	Type1a	550	33.5	24	1.5	2.3	3	18	112.5	2.7	11.8	2.8	0.2	10.2
IPS-13-26	Type1b	17	0.8	123.5	6.6	23.3	30	228	31	1	10.8	0.4	bdl	1.8
76	Type1b	324	31.8	250.4	15.5	28.8	37	253	38.5	1.3	8.8	0.7	bdl	2.6
136	Type1b	27	0.7	135.9	51.3	35.9	51	309	8.2	0.3	7.4	bdl	bdl	0.5
AB-10-17	Type1b	17	0.2	45.5	0.8	26.3	34	269	35.6	1.2	15.9	0.5	bdl	1.6
IPS-13-22	Type1b	254	16.1	48.2	16	25.3	34	234	24.3	0.8	20.5	0.4	bdl	3.2

Table 4.1. Cont.ed.

Sample	Type	Ce	Pr	Nd	Sm	Eu	Gd	Tb	Dy	Ho	Er	Tm	Yb	Lu
6-6	Type1a	27.4	3.59	16.6	4.02	1.08	4.49	0.83	5.07	0.99	3.37	0.51	3.74	0.54
6-7a	Type1a	40.7	5.4	20.4	4.43	1.23	4.61	0.82	4.92	1.06	3.67	0.57	4.06	0.69
6-8	Type1a	41.2	4.04	17.7	3.42	0.92	3.81	0.65	3.53	0.8	2.74	0.43	3.23	0.51
44	Type1a	23.5	3.17	13.2	3.35	0.81	4.27	0.8	4.95	1.07	3.36	0.47	2.95	0.48
32	Type1a	17.3	2.39	11.6	3.48	0.95	4.05	0.78	4.74	1.14	3.37	0.58	3.9	0.65
214	Type1a	25.9	3.68	17.4	4.4	1.14	5.89	1.06	6.65	1.43	4.55	0.63	4.43	0.75
168	Type1a	19.6	2.1	10.5	3.2	0.8	3.42	0.65	3.86	0.7	2.66	0.35	2.65	0.39
IPS-13-23	Type1a	9.8	1.43	6.6	1.94	0.56	2.55	0.48	3.27	0.74	2.33	0.36	2.32	0.37
23	Type1a	11.5	0.94	4.3	1.24	0.31	1.8	0.34	2.51	0.59	2.13	0.36	2.65	0.48
IPS-13-29	Type1a	13.7	1.94	9.2	2.01	0.97	1.87	0.29	1.88	0.41	1.27	0.21	1.53	0.24
54a-PW	Type1a	26.6	3.77	16	3.96	1.1	4.94	0.78	5.44	1.09	3.72	0.54	3.69	0.58
190	Type1a	7.9	1.3	6.7	2.26	0.85	3.82	0.63	4.51	0.95	2.89	0.43	2.9	0.48
132	Type1a	16.6	2.51	12.8	3.89	1.41	5.74	0.93	6.4	1.35	4.23	0.62	4.27	0.72
30	Type1a	11.2	1.77	8.2	2.57	0.78	3.62	0.64	4.4	0.95	3.14	0.49	3.33	0.54
1	Type1a	24.6	3.64	16	4.22	1.17	5.52	0.91	6.32	1.28	4.15	0.63	4.21	0.67
AD-2-18	Type1a	18.9	2.67	11.5	2.64	0.68	3.33	0.58	3.61	0.87	2.86	0.43	2.98	0.52
197	Type1a	21.6	2.96	13.4	3.36	1	4.51	0.77	5.29	1.11	3.45	0.55	3.79	0.61
KR-5-18	Type1a	32.4	3.33	10.6	1.79	0.45	1.67	0.3	1.84	0.42	1.34	0.22	1.44	0.24
DD-7-17	Type1a	17.9	2.18	9.8	2.54	0.58	3.21	0.58	3.86	0.92	2.97	0.46	3.24	0.58
YD-18-17	Type1a	18.1	2.47	11.3	2.82	1.05	3.72	0.64	4.1	0.94	3.13	0.43	3.02	0.49
AB-6-17	Type1a	22.5	3.33	15.9	4.79	1.05	6.1	1.06	6.84	1.53	4.8	0.76	5.15	0.85
KR-20-17	Type1a	24.7	3.69	17.7	5.29	1.47	6.93	1.27	8.52	2	6.08	0.92	6.33	0.96
KR-11-17	Type1a	11.8	2	10.4	2.96	0.75	3.76	0.69	4.59	1.1	3.44	0.54	3.84	0.61
24	Type1a	14.9	1.88	7.9	1.93	0.48	2.65	0.44	2.81	0.62	1.99	0.3	2.08	0.34
DD-4-18	Type1a	22.1	2.93	11.6	2.63	0.5	3.03	0.55	3.62	0.86	2.7	0.46	3.07	0.53
KC-2-18	Type1a	16.7	1.76	8.9	2.36	0.47	3.07	0.53	3.55	0.78	2.6	0.4	2.93	0.53
YD-1-18	Type1a	25.3	3.46	15.3	4.11	1.1	5.26	0.99	6.77	1.45	4.62	0.73	4.83	0.76
33	Type1a	11	1.4	6.3	1.83	0.44	2.42	0.42	2.88	0.67	2.18	0.37	2.63	0.43
39	Type1a	8.5	1.37	6.3	2.24	0.62	3	0.63	4.14	1.02	2.96	0.47	2.86	0.53
83	Type1a	9.6	1.11	3.9	1.09	0.27	1.44	0.32	1.76	0.46	1.45	0.23	1.81	0.29
184	Type1a	19	2.21	8.1	1.62	0.51	1.78	0.27	1.78	0.4	1.34	0.21	1.53	0.27
IPS-13-26	Type1b	3.9	0.62	3.6	1.22	0.42	1.7	0.32	2.15	0.45	1.43	0.2	1.29	0.2
76	Type1b	4.4	0.72	3.2	0.97	0.51	1.61	0.26	1.76	0.34	1.16	0.17	1.2	0.18
136	Type1b	1.2	0.2	1.2	0.38	0.31	0.96	0.16	1.27	0.23	0.79	0.12	0.71	0.13
AB-10-17	Type1b	3.9	0.61	3.5	1.29	0.41	2.09	0.4	2.86	0.65	2	0.3	1.97	0.33
IPS-13-22	Type1b	5.4	0.88	5	1.62	0.62	2.55	0.47	3.4	0.78	2.33	0.35	2.44	0.38

Table 4.1. Cont.ed.

Sample	Type	**Th**	**U**	**Pb**	Sample	Type	**Th**	**U**	**Pb**
6-6	Type1a	3	0.7	1.4	**DD-7-17**	Type1a	3	0.7	0.8
6-7a	Type1a	7.2	0.8	3.2	**YD-18-17**	Type1a	1.9	0.6	0.5
6-8	Type1a	5.8	1	3.4	**AB-6-17**	Type1a	2.9	0.8	1.6
44	Type1a	2.9	1.1	6.7	**KR-20-17**	Type1a	2.4	0.8	1.2
32	Type1a	3.6	bdl	0.6	**KR-11-17**	Type1a	1.5	0.3	1.1
214	Type1a	2.1	0.4	2.1	**24**	Type1a	1.6	0.4	1.5
168	Type1a	1.1	0.4	1.4	**DD-4-18**	Type1a	4.2	0.7	4.9
IPS-13-23	Type1a	1.7	0.3	2.1	**KC-2-18**	Type1a	2	0.6	0.6
23	Type1a	3.1	0.6	13.8	**YD-1-18**	Type1a	2.3	0.5	1.2
IPS-13-29	Type1a	1.5	1.3	17.5	**33**	Type1a	2	0.5	17.3
54a-PW	Type1a	3.6	0.9	43.5	**39**	Type1a	1.2	0.3	1.4
190	Type1a	0.6	0.2	14.8	**83**	Type1a	1.9	0.8	0.7
132	Type1a	0.7	0.2	29.7	**184**	Type1a	4	1	26.1
30	Type1a	2.5	0.6	11.9	**IPS-13-26**	Type1b	0.4	0.2	2.6
1	Type1a	2.7	0.7	22.8	**76**	Type1b	1	0.3	15.6
AD-2-18	Type1a	1.7	0.5	8.1	**136**	Type1b	bdl	bdl	17.8
197	Type1a	2	0.6	16.8	**AB-10-17**	Type1b	0.3	0.2	1
KR-5-18	Type1a	6.3	1.1	2.9	**IPS-13-22**	Type1b	0.3	bdl	0.7

Table 4.1. Cont.ed.

Sample	Type	SiO_2	MgO	Al_2O_3	Fe_2O_3	CaO	Na_2O	K_2O	TiO_2	P_2O_5	MnO	Cr_2O_3	LOI	Sum
6-4	Type2a	56.79	5.35	17.29	11.31	1.74	5.63	0.04	1.24	0.29	0.31	0.00	4.4	99.88
6-5	Type2a	69.26	1.95	15.08	5.70	1.77	4.91	0.49	0.58	0.17	0.08	bdl	2.2	99.9
6-7c	Type2a	48.07	10.29	19.64	12.79	4.05	3.95	0.13	0.71	0.13	0.27	0.00	5.4	99.86
49	Type2a	68.73	2.87	15.00	5.49	1.56	4.83	0.80	0.45	0.11	0.12	0.01	2	99.92
50	Type2a	54.82	4.93	15.38	13.15	7.08	3.15	0.03	1.10	0.14	0.19	0.00	3.7	99.8
169	Type2a	54.19	5.52	18.63	10.35	4.15	5.53	0.26	0.95	0.16	0.20	0.01	4	99.81
182	Type2a	60.96	4.35	15.93	8.78	3.64	4.43	0.37	1.07	0.25	0.18	bdl	3.3	99.85
IPS-13-18	Type2a	69.17	1.15	14.92	5.60	1.82	5.17	0.70	0.76	0.20	0.41	bdl	1.7	99.94
IPS-13-20	Type2a	48.43	5.78	18.06	11.56	10.22	4.08	0.08	1.09	0.12	0.34	bdl	7.2	99.8
153	Type2a	70.49	1.40	13.97	4.98	3.03	5.22	0.02	0.55	0.17	0.04	0.01	1.6	99.93
154	Type2a	71.23	1.40	13.71	5.08	1.66	5.81	0.23	0.52	0.14	0.10	0.01	1.8	99.95
6-7b	Type2a	73.57	1.76	12.28	4.83	0.69	5.84	0.15	0.61	0.16	0.08	0.01	1.4	99.94
YD-5-17	Type2a	51.42	5.57	19.10	11.55	8.94	1.68	0.24	1.05	0.06	0.12	bdl	4.5	99.79
DD-1-17	Type2a	52.83	6.53	16.44	14.28	5.42	2.73	bdl	1.17	0.13	0.19	bdl	4.8	99.77
KC-14-17	Type2a	45.50	8.17	19.32	13.10	10.42	1.91	0.04	0.79	0.18	0.20	bdl	4.9	99.67
KC-7-17	Type2a	54.88	5.41	18.55	9.90	3.74	5.88	0.26	0.80	0.17	0.19	bdl	4.2	99.8
KR-13-17	Type2a	73.27	3.76	14.02	2.52	3.09	1.18	1.32	0.48	0.08	0.10	bdl	3	99.88
YD-26-17	Type2a	48.08	4.19	17.37	14.67	14.09	0.03	bdl	0.98	0.11	0.24	bdl	3.9	99.81
KC-3-17	Type2a	68.53	3.30	13.57	6.64	1.19	5.12	0.23	0.98	0.23	0.16	bdl	2.3	99.91
DD-8-17(b)	Type2a	52.13	4.14	17.33	15.30	4.86	4.39	0.02	1.21	0.13	0.20	bdl	3.2	99.74
KC-9-17	Type2a	52.44	5.95	19.94	11.67	1.91	6.10	0.38	1.13	0.17	0.19	bdl	4.8	99.85
AB-4-17	Type2a	53.39	5.38	18.68	10.34	6.21	4.16	0.01	1.30	0.21	0.10	bdl	3.9	99.81
SD-8-17	Type2a	58.93	3.38	16.40	9.15	7.10	3.67	0.02	0.95	0.09	0.18	bdl	2.9	99.87
DD-3-18	Type2a	58.24	3.86	15.61	9.84	8.79	2.40	0.07	0.83	0.09	0.09	0.00	3.8	99.83
OR-4-18	Type2a	79.12	0.79	14.07	0.40	0.09	0.75	3.57	0.31	0.09	bdl	bdl	2.9	99.87
DD-5-17	Type2a	53.79	5.00	18.09	11.19	6.78	3.63	bdl	1.03	0.15	0.17	bdl	3.8	99.83
KC-5-18	Type2a	44.95	11.08	19.65	12.82	6.72	3.46	0.06	0.72	0.13	0.24	0.00	7	99.83
KR-7-17	Type2b	51.62	10.59	15.00	9.12	10.80	1.49	0.42	0.48	0.03	0.14	0.07	3.9	99.77
AB-6-18	Type2b	52.18	9.94	16.47	8.76	9.91	1.99	0.02	0.37	0.03	0.13	0.06	4.4	99.86
KR-3-18	Type2b	51.59	8.40	16.58	9.76	11.26	1.07	0.24	0.63	0.05	0.21	0.04	5.8	99.84
YD-21-17	Type2b	59.22	11.81	15.51	10.27	0.55	0.20	0.98	0.71	0.04	0.44	bdl	6.7	99.76

Table 4.1. Cont.ed.

Sample	Type	**Ba**	**Rb**	**Sr**	**Ni**	**Co**	**Sc**	**V**	**Zr**	**Hf**	**Y**	**Nb**	**Ta**	**La**
6-4	Type2a	15	0.6	84.3	7.4	22.1	38	226	57.5	2	36.3	1.8	bdl	5.5
6-5	Type2a	103	6.7	119.5	1.2	5.3	21	35	79.3	2.4	29.9	2.4	0.1	7
6-7c	Type2a	38	1.4	270	19.6	30.8	35	236	32.7	1.3	15.4	1.5	bdl	8.9
49	Type2a	156	15.2	135.4	3.6	8.6	17	60	54.9	1.6	17.1	2.3	bdl	7.9
50	Type2a	36	0.4	147.9	9.5	35	41	398	49.4	1.6	24.5	1.2	bdl	5.1
169	Type2a	122	2.9	183.4	8.5	22.2	34	341	44.5	1.2	20.8	1.2	bdl	5.6
182	Type2a	123	5.2	163.2	0.9	14.1	27	110	88.4	2.5	36.3	2.3	bdl	9.5
IPS-13-18	Type2a	511	8.4	82.3	3	12.2	24	67	75.4	2.4	27.4	2.6	0.2	11.8
IPS-13-20	Type2a	45	1.3	119.3	6.9	31.3	37	380	34.3	1.2	20.3	0.4	bdl	3.3
153	Type2a	16	0.3	169.6	2.6	4.8	20	18	71.6	2.1	35.6	1.4	bdl	6.3
154	Type2a	54	3.2	73.7	2.8	5.1	17	28	61.4	2.1	27.9	1.5	0.1	5.7
6-7b	Type2a	36	1.5	32.3	2.6	5.3	16	41	73.8	2.3	25.5	2.1	0.1	8.3
YD-5-17	Type2a	51	3.7	187.9	7.6	27.6	40	416	43.9	1.3	21.1	1.2	bdl	5.2
DD-1-17	Type2a	26	bdl	161	10.3	41.1	44	371	53.2	1.7	27.7	1.5	bdl	5.5
KC-14-17	Type2a	24	0.2	753.7	23.1	42.6	35	398	37.9	1	20.7	2	bdl	15.3
KC-7-17	Type2a	101	2.2	155.2	8.3	23.2	34	283	50.8	1.6	24.5	1.2	bdl	7.9
KR-13-17	Type2a	657	14.2	129.2	2.6	1.4	17	8	137.8	4.3	69.1	3.1	0.2	15.6
YD-26-17	Type2a	8	bdl	62.9	26.8	47.2	52	413	45.2	1.5	29	0.8	bdl	4.2
KC-3-17	Type2a	68	2.3	68.8	0.6	10.1	24	96	74.7	2.2	30.9	2.3	0.2	7.5
DD-8-17(b)	Type2a	24	bdl	574.3	11.1	42.9	45	479	52.9	1.8	33.1	1.1	bdl	9.9
KC-9-17	Type2a	81	4.6	117.8	8.9	27.9	37	295	56.6	1.6	24.2	2.7	bdl	5.7
AB-4-17	Type2a	91	bdl	211.2	10.3	36	41	293	39.1	1.1	22.4	0.8	bdl	2.8
SD-8-17	Type2a	9	bdl	96.5	10.6	30.5	41	240	34.1	1.1	20.8	0.6	bdl	3.2
DD-3-18	Type2a	0.6	45	230	10.6	37.1	40	319	37.4	1.3	20.8	2.7	bdl	5.3
OR-4-18	Type2a	6096	39	84.1	0.5	0.5	9	17	147.6	4.3	32.3	5	0.3	14
DD-5-17	Type2a	33	bdl	157.1	10.3	27.2	37	348	50.9	1.5	24.6	4.1	bdl	5
KC-5-18	Type2a	25	bdl	322.1	20	45.4	40	286	33.2	0.8	14.9	2.8	bdl	11
KR-7-17	Type2b	62	4	124	74.9	38.1	41	245	8.4	0.4	9.8	bdl	bdl	0.6
AB-6-18	Type2b	16	bdl	218.2	79.7	36.4	46	228	5.2	0.2	8.6	1.6	bdl	0.4
KR-3-18	Type2b	100	2.8	318.5	61.1	17.2	38	261	10.5	0.4	14.8	1.2	bdl	1.4
YD-21-17	Type2b	134	12.7	17.2	10.7	30.2	26	229	13.1	0.5	7.1	bdl	bdl	1.4

Table 4.1. Cont.ed.

Sample	Type	**Ce**	**Pr**	**Nd**	**Sm**	**Eu**	**Gd**	**Tb**	**Dy**	**Ho**	**Er**	**Tm**	**Yb**	**Lu**
6-4	Type2a	10.6	2.19	11.6	3.42	1.38	5.13	0.91	5.69	1.26	3.75	0.59	3.81	0.61
6-5	Type2a	15.9	2.55	13.1	3.64	1.28	5.36	0.88	5.86	1.08	3.41	0.48	3.23	0.46
6-7c	Type2a	17.3	2.15	9	2.13	0.79	2.51	0.46	2.91	0.62	1.93	0.29	2	0.28
49	Type2a	14	1.84	9	2.39	1.01	2.72	0.54	3.15	0.67	1.87	0.32	2.21	0.33
50	Type2a	10.4	1.76	9.3	2.71	1.04	3.69	0.68	4.45	0.89	2.69	0.4	2.7	0.39
169	Type2a	12.3	1.89	9.4	2.24	0.96	3.43	0.61	4.06	0.77	2.39	0.36	2.22	0.34
182	Type2a	20.6	3.15	15.4	4.35	1.48	5.6	1	6.01	1.3	4.19	0.62	3.89	0.59
IPS-13-18	Type2a	26.2	3.56	16.3	4.02	1.23	4.88	0.79	5.04	1.1	3.2	0.47	2.9	0.47
IPS-13-20	Type2a	8.7	1.4	7.6	2.47	0.97	3.05	0.55	3.31	0.73	2.14	0.32	1.98	0.31
153	Type2a	13.6	2.52	13.3	3.93	1.3	5.9	0.95	6.69	1.36	4.08	0.57	3.66	0.58
154	Type2a	11.9	2.3	12.7	3.91	1.37	5.41	0.85	5.45	1.04	3.05	0.42	2.42	0.39
6-7b	Type2a	18.7	2.68	11.9	3.16	0.87	4.29	0.69	4.58	0.93	3.02	0.43	3.04	0.47
YD-5-17	Type2a	11.1	1.53	8.1	2.22	0.93	3.25	0.6	3.81	0.87	2.57	0.4	2.48	0.39
DD-1-17	Type2a	12.6	1.91	10.2	2.98	1.1	3.99	0.73	4.85	1.08	3.23	0.45	3.01	0.46
KC-14-17	Type2a	28.2	3.56	16.1	3.61	1.26	3.96	0.62	3.69	0.78	2.36	0.33	2.2	0.35
KC-7-17	Type2a	17.4	2.34	11.1	3.04	1.08	3.98	0.65	4.17	0.99	2.82	0.43	2.7	0.44
KR-13-17	Type2a	36	5.13	24.9	7.16	1.9	9.15	1.66	10.65	2.53	7.73	1.13	7.41	1.16
YD-26-17	Type2a	7.9	1.36	7.2	2.47	0.94	4.04	0.74	4.9	1.08	3.17	0.48	3.05	0.5
KC-3-17	Type2a	16.7	2.54	12.3	3.69	1.3	4.96	0.85	5.47	1.26	3.6	0.53	3.2	0.51
DD-8-17(b)	Type2a	20.8	3.31	15.5	4.39	1.47	5.44	0.99	6.38	1.42	4.3	0.64	4.09	0.6
KC-9-17	Type2a	13.8	2.2	10.6	3.24	0.94	3.95	0.7	4.57	0.97	3.06	0.4	2.79	0.41
AB-4-17	Type2a	7.6	1.28	7.3	2.68	1.04	3.69	0.66	4.39	0.98	2.71	0.38	2.56	0.4
SD-8-17	Type2a	7.1	1.07	6.2	1.97	0.75	2.99	0.54	3.59	0.79	2.41	0.34	2.31	0.35
DD-3-18	Type2a	7.9	1.14	5.8	2.06	0.77	2.89	0.52	3.43	0.77	2.35	0.37	2.23	0.38
OR-4-18	Type2a	31.2	4.63	25.2	6.85	3.47	6.48	0.98	5.96	1.34	3.68	0.57	3.98	0.58
DD-5-17	Type2a	12.4	2	10	2.83	0.99	3.79	0.67	4.29	0.91	2.85	0.41	2.67	0.38
KC-5-18	Type2a	19.3	2.48	10.2	2.61	0.83	2.64	0.44	2.78	0.59	1.5	0.21	1.34	0.26
KR-7-17	Type2b	1.5	0.28	1.8	0.74	0.35	1.29	0.25	1.67	0.39	1.19	0.19	1.16	0.19
AB-6-18	Type2b	1.2	0.19	1.1	0.62	0.28	0.87	0.2	1.42	0.34	1.05	0.16	1.11	0.16
KR-3-18	Type2b	2.8	0.48	2.9	1.18	0.7	1.87	0.32	2.2	0.49	1.74	0.22	1.41	0.22
YD-21-17	Type2b	2.2	0.42	2.6	0.95	0.25	1.25	0.22	1.4	0.32	0.95	0.13	0.89	0.14

Table 4.1. Cont.ed.

Sample	Type	**Th**	**U**	**Pb**	Sample	Type	**Th**	**U**	**Pb**
6-5	Type2a	0.7	0.2	0.7	**YD-26-17**	Type2a	0.6	0.2	0.8
6-7c	Type2a	2.9	0.7	0.8	**KC-3-17**	Type2a	0.7	0.2	1.6
49	Type2a	1.5	0.1	0.8	**DD-8-17(b)**	Type2a	0.4	0.2	2.5
50	Type2a	0.2	bdl	0.5	**KC-9-17**	Type2a	0.4	0.1	1.3
169	Type2a	0.4	bdl	0.5	**AB-4-17**	Type2a	bdl	0.5	0.9
182	Type2a	0.8	0.2	1.1	**SD-8-17**	Type2a	0.4	0.3	0.4
IPS-13-18	Type2a	1.8	0.4	1.5	**DD-3-18**	Type2a	0.6	0.3	1.5
IPS-13-20	Type2a	bdl	bdl	1.3	**OR-4-18**	Type2a	3.5	2.1	24.9
153	Type2a	0.6	0.1	44.4	**DD-5-17**	Type2a	0.4	0.2	1.2
154	Type2a	0.5	bdl	54	**KC-5-18**	Type2a	2.7	0.6	1.1
6-7b	Type2a	2.2	0.6	47.9	**KR-7-17**	Type2b	bdl	bdl	0.1
YD-5-17	Type2a	0.8	0.4	1.3	**AB-6-18**	Type2b	bdl	bdl	bdl
DD-1-17	Type2a	0.5	0.2	0.7	**KR-3-18**	Type2b	bdl	bdl	bdl
KC-14-17	Type2a	2.1	0.4	1.4	**YD-21-17**	Type2b	bdl	0.2	0.5
KC-7-17	Type2a	0.5	bdl	0.4					

4.1.1 Effects of the Post-Magmatic Processes

The investigated rock samples have varying loss on ignition (LOI) values between 0.9 and 10.4 wt.%, implying the possible effects of post-magmatic events, such as low-grade alteration/metamorphism. That the KM comprise secondary minerals, such as chlorite, epidote, and calcite is in harmony with the observed LOI values, thus reflecting the influence of low-grade alteration/metamorphism on the samples.

Element mobility is likely to occur in rocks subjected to low-grade alteration/metamorphism. Therefore, it is essential to show which elements have remained relatively unaffected by secondary processes, which will allow making reliable petrogenetic interpretation. The phenomenon of mobility is determined by the mineralogical changes that occur during post-magmatic processes, which is aided by the presence of an aqueous fluid phase (Rollinson, 1993). In general, elements with low (<3) and high (>12) ionic potentials are regarded as mobile, whereas those with intermediate values are considered as immobile (e.g., Loughnan, 1969) (Figure 4.1). Small, highly charged cations include lanthanides (REE), Sc, Y, Th, U, Pb^{+4}, Zr, Hf, Ti, Nb, and Ta, and these are described as high-field strength elements (HFSE). When hydrous fluids react with the rock, these elements tend to be immobile. Large cations of small charge including K, Rb, Cs, Ba, Pb^{+2}, Sr, Eu^{+2}, on the other hand, are known as low-field strength cations or LILE, and they tend to be mobile in hydrous fluids (Rollinson, 1993).

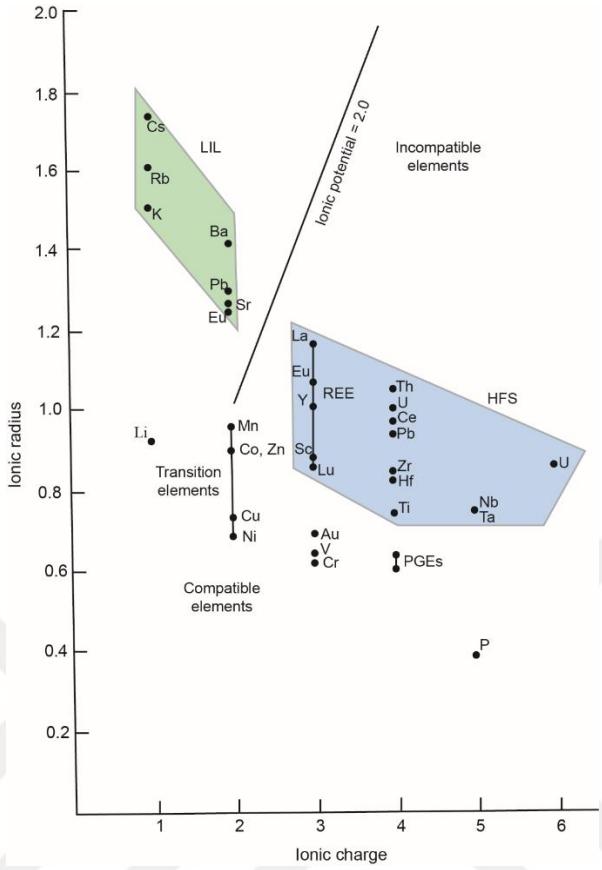


Figure 4.1. Plot of ionic radius against ionic charge for trace elements (Rollinson, (1993).

Zr is known to be one of the least mobile elements during secondary processes (Pearce and Cann, 1973; Pearce and Peate, 1995); thus, it can be used to assess the effects of alteration/metamorphism on the other elements. In this regard, several elements were plotted against Zr to reveal whether they have been mobilized by secondary processes or not (Figure 4.2). Two chemical types of the KM, which are referred to as Type 1 and Type 2, are included in these plots to provide a better insight into the distribution of these elements under such conditions. The chemical subdivision of the KM will be explained in detail in the following sections. In the plots, it is seen that Sr displays a weak trend in general, which may imply the relatively mobile behavior of this element. Rb and Ba, also show still weak but somewhat a higher degree of correlation, thus suggesting their partial conservation during post-magmatic processes. Th, Nb, and La exhibit well-defined linear trends

against Zr, indicating their relatively immobile behavior during the evolution of the investigated rocks.

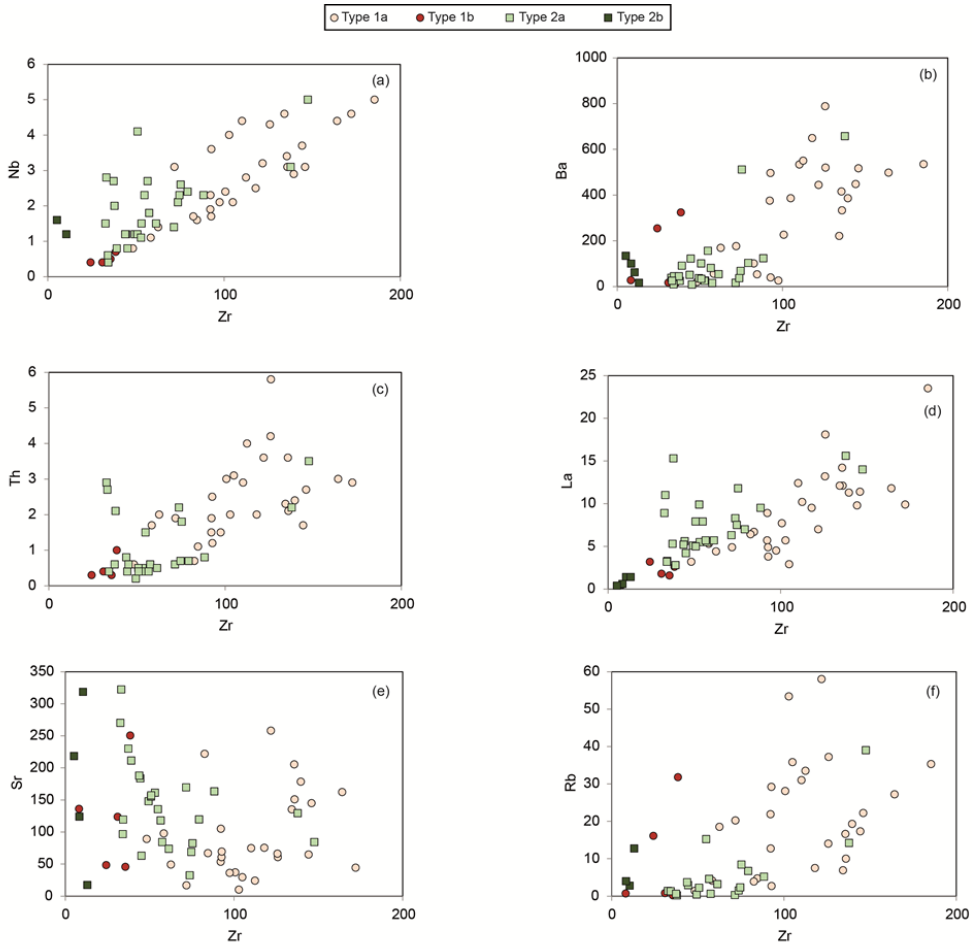


Figure 4.2. Diagrams depicting the variation of selected elements against Zr to check element mobility during post-magmatic events.

It appears, therefore, that LILE behaved mobile (e.g., Humphris and Thompson, 1978; Thompson, 1991; Wood et al., 1976), whereas HFSE and REE have remained immobile during post-magmatic events. Thus, the focus will be on HFSE and REE while making petrogenetic interpretations. Ba and Rb, on the other hand, are partially mobilized, therefore they will be used with caution.

4.1.2 Geochemical Classification

To better interpret geochemical and petrogenetic features, it is critical to identify possible geochemical types in the KM. Multi-element variation diagrams were used for this purpose since they enable the comparison of many elements simultaneously. In these diagrams, the partially preserved elements (e.g. Ba, Rb, Sr) are also included; however, the discrimination was made solely based on the immobile elements.

Multi-element variation diagrams exhibit notable peak and troughs in specific elements as Th, Nb, La, Zr, Hf, and Ti (Figure 4.3). When this broad spectrum in peak and troughs is examined carefully, the samples can be divided into two main groups as Type 1 and Type 2. Type 1 samples display slight or no depletion in Zr, whereas Type 2 samples are represented by depletion in Zr (ave. $(Nd/Zr)_N$ = 1.10 for Type 1; ave. $(Nd/Zr)_N$ = 2.12 for Type 2; where "N" denotes N-MORB normalized). A further subdivision can be made such that the Type 1 samples can be separated into two subgroups as Type 1a and Type 1b based on their absolute Ce (ppm) abundances, Ce/Ti ratio, and absence or presence of negative Ti anomaly. Type 1a samples have higher Ce (ppm) abundance (1.05-5.49), Ce/Ti ratio higher than 1.25 except for one sample (sample 190), and display strong depletion in Ti. Type 1b samples, on the other hand, are represented by lower Ce (ppm) abundance (0.16-0.72), absence of depletion in Ti, and lower Ce/Ti ranging from 0.37 to 1.25. Similarly, Type 2 samples can also be subdivided into Type 2a and Type 2b based on the Sm/Ti ratio. Type 2a samples have greater Sm/Ti ratio than 1, whereas Type 2b samples have Sm/Ti ratio less than 1 (ave. Sm/Ti = 2.33 for Type 2a; ave. Sm/Ti = 0.79 for Type 2b) (Figure 4.3).

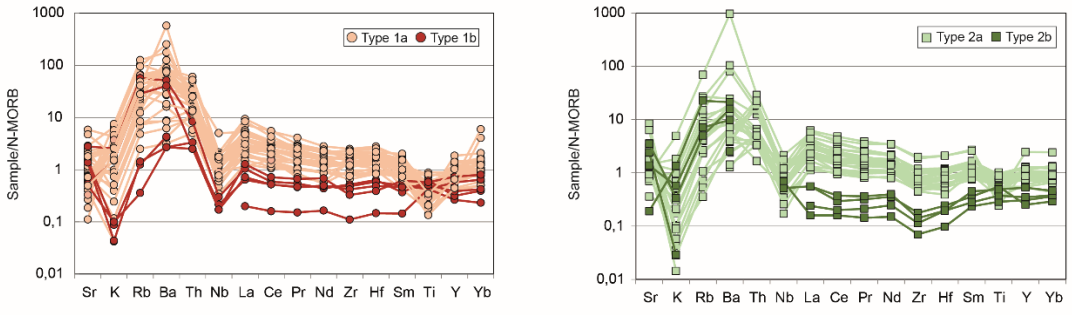


Figure 4.3. Multi-element patterns of the Kösdağ Metavolcanics (normalization values for N-MORB from Sun and McDonough, 1989).

On the total alkali versus silica (TAS) diagram, the KM samples display a wide range of compositions from basalt to rhyolite without any apparent compositional gaps (Figure 4.4). While most of the samples fall into the subalkaline field, only two Type 2 samples plot on the alkaline field. Thus, the KM samples can be regarded to have subalkaline characteristics. Both Type 1 and Type 2 groups have primitive and evolved products. However, Type 1 samples are more akin to felsic compositions in general.

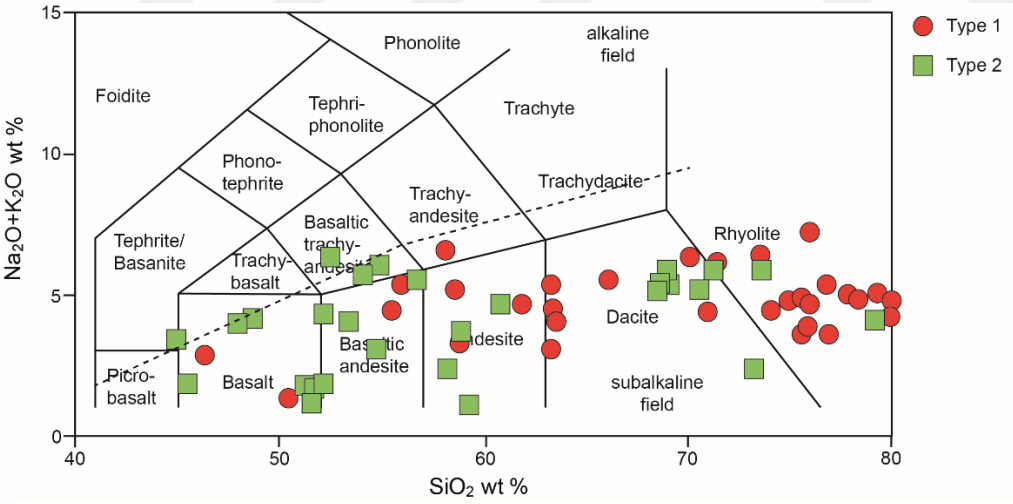


Figure 4.4. Classification of the KM samples on the TAS diagram of Le Bas et al. (1986).

Considering the potential mobility of alkalies during alteration/metamorphism, the KM samples were also plotted on the $Zr/TiO_2*0.0001$ vs. Nb/Y plot (Winchester and Floyd, 1977), which is based on immobile elements. The KM have relatively low Nb/Y ratios, implying their sub-alkaline nature (Nb/Y for the KM = 0.02-0.49)

(Figure 4.5). In the diagram, the samples are distributed over a wide area, plotting onto basalt, basalt/andesite, andesite, rhyodacite/dacite fields. This supports the idea obtained from the TAS diagram and suggests that SiO_2 and alkalies appear to be somewhat conserved during the post-magmatic processes.

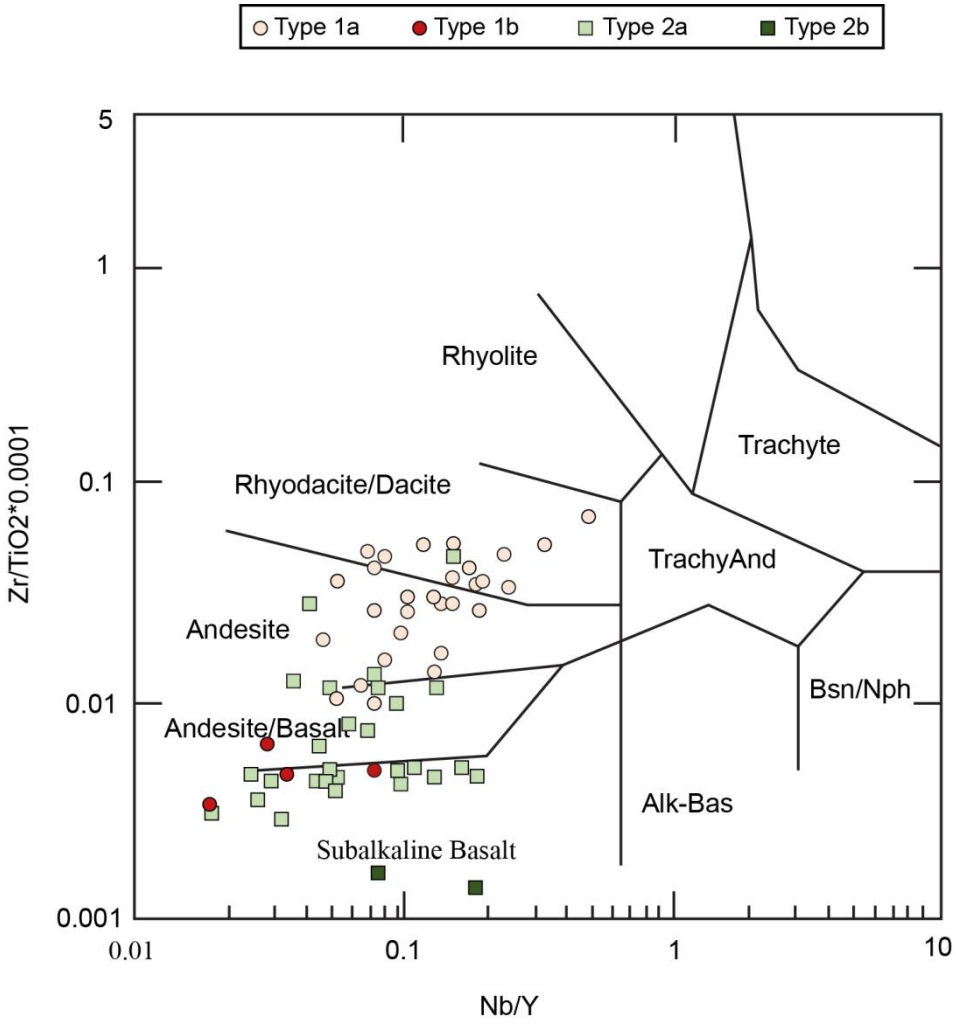


Figure 4.5. Chemical classification of the Kösdağ Metavolcanics (after Winchester and Floyd, 1977).

4.1.3 Major Oxide Variations

As noted previously, the investigated rocks are classified into two types as Type 1 and Type 2, with subgroups Type 1a-Type 1b and Type 2a-Type 2b. The silica concentrations of Type 1 (46.36 to 84.66 wt.%) and Type 2 (44.95 to 79.12 wt.%)

are similar. Total alkali values ($Na_2O + K_2O$) range from 1.49 to 7.31 wt.% for Type 1, whereas it varies between 1.18 and 6.48 wt.% for Type 2. Both Type 1 and Type 2 exhibit a wide range of MgO contents (0.33 to 9.60 wt.% and 0.79-11.81 wt.%, respectively), but the Type 2 samples show higher values at the upper end, and they appear to be more Mg-rich in average (ave. MgO for Type 1 = 3.11 wt.%, ave. MgO for Type 2 = 5.29 wt.%). In terms of Al_2O_3 concentrations, Type 1 samples vary between 9.55 and 23.93 wt.%, covering the interval represented by Type 2 (12.28 - 19.94 wt.%). Fe_2O_3 concentrations of the two types are similar, ranging between 1.01 and 15.76 wt.% for Type 1 and 0.40 and 15.3 wt.% for Type 2. Type 1 samples have TiO_2 concentrations ranging from 0.17 to 1.13 wt.%, whereas the TiO_2 concentrations of Type 2 change between 0.31-1.30 wt.%, with a slightly broader range. P_2O_5 concentrations of the two types are similar, changing between 0.02 and 0.21 wt.% for Type 1 and 0.03 wt.% and 0.29 wt.% for Type 2.

4.1.4 Trace Element Variations

During magmatic processes, trace elements tend to partition into the liquid (melt) phase or the solid (mineral) phase. Trace elements with a preference for the mineral phase are called compatible, whereas elements with a preference for the melt phase are called incompatible elements (Wilson, 1989). Incompatible elements are also known as hygromagmatophile, a term first proposed by Treuil and Varet (1973).

Elements with small ionic radii and a relatively low valence appear compatible, including Ni, Cr, Cu, W, Ru, Rh, Pd, Os, Ir, Pt, and Au (Winter, 2001). Compatible elements such as Ni, Cr, and Co have partition coefficients greater than unity ($Kd>1$). In the initial stage of fractional crystallization, they enter the crystallizing solid phase or remain in the residual solid during partial melting. Incompatible elements display a strong affinity for the melt phase (Rollinson, 1993). The partition coefficients (Kd) of incompatible elements such as Zr, Nb, and Y are much less than unity ($Kd<<1$). The chemistry of the source region and crystal/melt fractionation that occurs during melting and magmatic modification processes control the elemental budget of the rocks. Apart from the partitioning of

elements in the crystal-melt systems, concentrations of some elements, such as LILE, can also be controlled by the presence of a fluid phase.

While Ni values range between 0.6 and 51.3 ppm for Type 1, a much wider variation is displayed by Type 2, between 0.5 and 79.7 ppm (Table 4.2). Both types show a similar range of Co contents, with 0.7-48.8 for Type 1 and 0.5-47.2 for Type 2. On the other hand, Sc (ppm) and V (ppm) values are 2-64 and 11-357 for Type 1, 9-52 and 8-479 for Type 2, respectively. Type 1 and Type 2 samples display variable enrichment in Th relative to N-MORB (ave. Th abundance of Type 1 = 2.43; ave. Th abundance of Type 2 = 1.12; Th abundance of N-MORB = 0.12). However, this feature could not be evaluated on the highly depleted Type 2b samples since their Th concentrations are below the analytical detection limits (0.2 ppm). Type 1 and Type 2 samples are also enriched in La (Figure 4.3). Exceptions are Type 2b samples and some Type 1b samples, which are very depleted and exhibit La values lower than N-NORB. In addition, both types are variably enriched in Th and La over Nb, creating "saw teeth" patterns (Figure 4.3) typically displayed by arc-related magmas (e.g., Elliott et al., 1997; Pearce and Peate, 1995). However, Type 2 samples have a wider range of Th/Nb ratios with respect to those of Type 1 (Th/Nb = 0.33-1.55 for Type 1; Th/Nb = 0.10-1.93 for Type 2; ave. N-MORB Th/Nb = 0.05; Sun and McDonough, 1989) (Figure 4.3). Considering the depletion/enrichment of the samples, Type 2 samples are relatively depleted compared to that of Type 1 according to certain absolute abundances and elemental ratios (ave. La/Sm ratio of Type 1 = 3.26; average La/Sm ratio of Type 2 = 2.24; ave. absolute abundance of Nb for Type 1 = 1.23; ave. absolute abundance of Nb for Type 2 = 0.82) (Figure 4.3).

Because the KM samples exhibit Nb depletion (arc signature), they can also be evaluated using the Co-Th diagram (Hastie et al., 2007). In this plot, the KM samples are classified as basalt, basaltic andesite, andesite, dacite and rhyolite (Figure 4.6). While Type 1 samples plot in the 'dacite and rhyolite' field in general, Type 2 samples plotted on the fields of 'basaltic andesite and andesite' and 'basalt'. The Co-Th diagram appears to match better compared to the $Zr/TiO_2*0.0001$ vs. Nb/Y if the high silica concentrations of the Type 1 samples are taken into account.

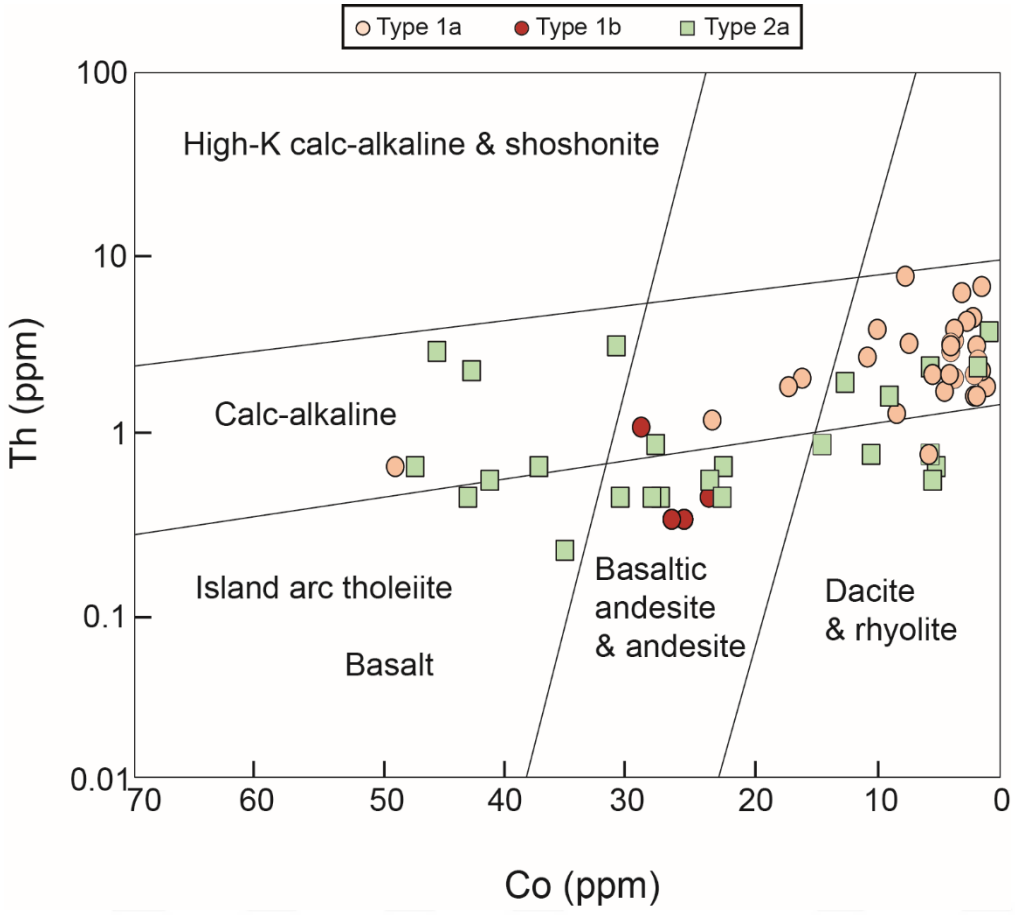


Figure 4.6. Classification of the KM on the basis of Th-Co diagram (after Hastie et al., 2007).

Table 4.2. Major oxide and trace element intervals of the Kösdağ Metavolcanics.

Type	Major oxide or trace element	Range	n	Average	Standard deviation
Type 1	SiO_2(%)	46.36-84.66	36	69.5	9.9
	MgO	0.33-9.6	36	3.1	2.4
	Al_2O_3	9.55-23.93	36	14.3	2.9
	Fe_2O_3	1.01-15.76	36	5.2	3.7
	TiO_2	0.17-1.13	36	0.5	0.2
	P_2O_5	0.02-0.21	36	0.07	0.03
	Ni(ppm)	0.6-51.3	36	3.9	9.10
	Co	0.7-48.8	36	9.5	11.5
	Sc	2-64	36	17.9	13.8
	V	8-357	33	97.3	101.2
	Y	7.4-51.7	36	23.8	10
	Zr	8.2-185.4	36	98.3	42.9
Type 2	SiO_2(%)	44.95-79.12	31	58.3	9.5
	MgO	0.79-11.81	31	5.3	3.1
	Al_2O_3	12.28-19.94	31	16.5	2.1
	Fe_2O_3	0.4-15.3	31	9.4	3.7
	TiO_2	0.31-1.3	31	0.8	0.2
	P_2O_5	0.03-0.29	31	0.14	0.06
	Ni(ppm)	0.5-79.7	31	15.00	20.4
	Co	0.5-47.2	31	24.5	14.4
	Sc	9-52	31	32.7	10.8
	V	8-479	31	231.1	143.8
	Y	7.1-69.1	31	24.9	11.3
	Zr	5.2-147.6	31	53.4	31.6

REE abundances vary between 1 and 100 times the chondrite values (Figure 4.7). Even though the REE characteristics of the two groups seem to be similar at the first glance, the existence of negative Eu anomalies makes differ Type 1 samples from Type 2 samples (Figure 4.7). In addition, Type 1 samples are quite enriched in LREE ($[Ce/Sm]_N$ = 0.76-4.53; $[La/Sm]_N$ = 0.80-7.61; "N" denotes chondrite-normalized) and display slightly fractionated HREE patterns ($[Ce/Yb]_N$ = 0.47-6.25), while Type 2 samples display moderate enrichment in LREE ($[Ce/Sm]_N$ =

0.48-2.03; $[La/Sm]_N$ = 0.42-2.74; "N" denotes chondrite-normalized) coupled with a slight depletion in HREE ($[Ce/Yb]_N$ = 0.30-4.00) (Figure 4.7).

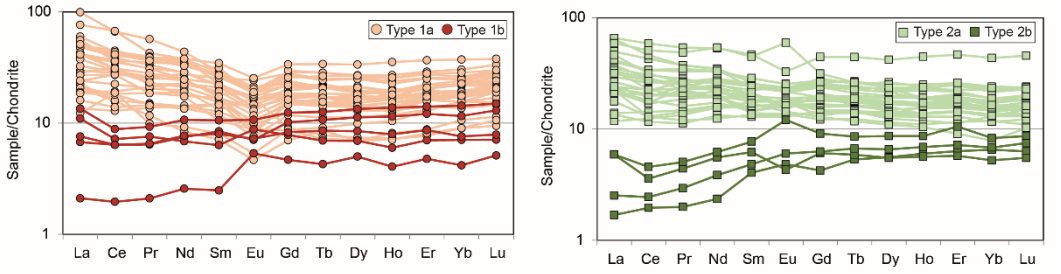


Figure 4.7. REE patterns of the Kösdağ Metavolcanics (normalization values for chondrite from Sun and McDonough, 1989).

4.1.5 Whole-rock Nd Isotope Geochemistry

Various radiogenic isotope systems have been used to unravel the characteristics of the mantle source regions in petrogenetic studies. This is mainly because the melt imparts the same isotopic ratios with the mantle source during partial melting. Among the several radiogenic isotopic systems, the ^{147}Sm-^{144}Nd is frequently utilized for the studies of altered/metamorphosed rocks because both Sm and Nd are relatively immobile. Since the KM are Late Cretaceous in age, an age correction procedure is necessary due to the modification of the ratios via isotopic decay. In this regard, the initial values were calculated using 95 Ma. DePaolo and Wasserburg, (1976) introduced the ε_{Nd} notation to compare differences between $^{143}Nd/^{144}Nd$ ratios of igneous rocks and CHUR. A chondritic mantle source is suggested if $\varepsilon_{Nd}(T) = 0$. $\varepsilon_{Nd(i)}$ values were calculated relative to CHUR with present-day values of $^{143}Nd/^{144}Nd$ = 0.512638 and $^{147}Sm/^{144}Nd$ = 0.1967 (Jacobsen and Wasserburg, 1980). Whole-rock Sm and Nd isotope data are listed in Table 4.3.

The following equation was used to determine the $^{147}Sm/^{144}Nd$ values of the samples;

$$\frac{147Sm}{144Nd} = \left(\frac{Sm}{Nd}\right) * [0{,}53151 + 0{,}14252\,\frac{143Nd}{144Nd}]$$

$^{147}Sm/^{144}Nd(i)$ values of the samples were calculated by the following equation;

$$\left(\frac{143Nd}{147Nd}\right) p = \left(\frac{143Nd}{147Nd}\right) i + \left(\frac{147Sm}{144Nd}\right) p * e^{\lambda t}-1$$

where:

t is the age of the sample (95 Ma)

λ is the decay constant of ^{147}Sm ($6.54*10^{-12}$)

($e^{\lambda t}$-1) denotes the slope of the isochron that determines the age of the system

The $\varepsilon_{Nd(i)}$ values were calculated using the following equation;

$$\varepsilon_{Nd(i)} = \left[\frac{\left(\frac{143Nd}{144Nd}\right) i - \left(\frac{143Nd}{144Nd}\right) CHUR(i)}{\left(\frac{143Nd}{144Nd}\right) CHUR(i)}\right]*10000$$

The initial isotopic compositions of Nd are based on the age of 95 Ma determined from the U-Pb zircon dating. The MgO contents of the samples selected for the isotopic analyses vary between 3.38 and 9.94 wt.%. The $^{143}Nd/^{144}Nd(i)$ ratios are constrained within an interval of 0.51267–0.51285, corresponding to $\varepsilon_{Nd(i)}$ values between +2.9 and +6.5 (Table 4.3).

Table 4. 3. Sm-Nd isotopic data of the Kösdağ Metavolcanics

Sample	*Type*	*Lithology*	*Sm (ppm)*	*Nd (ppm)*	*143Nd/144Nd*	*147Sm/144Nd*	*143Nd/144Nd(i)*	$\varepsilon_{Nd(i)}$
AD-2-18	Type 1	Meta-rhyolite	2.64	11.5	0.512846	0.138795	0.51276	4.8
KR-5-18	Type 1	Meta-rhyolite	6	25	0.512783	0.145102	0.51269	3.5
24	Type 1	Meta-rhyolite	1.6	8	0.512866	0.120920	0.51279	5.4
197	Type 1	Meta-rhyolite	3.36	13.4	0.512905	0.151603	0.51281	5.8
184	Type 1	Meta-dacite	1.62	8.1	0.512866	0.120920	0.51279	5.4
YD-18-17	Type 1	Meta-basalt	2.82	11.3	0.512884	0.150884	0.51279	5.4
76	Type 1	Meta-basalt	0.97	3.2	0.512779	0.183266	0.51267	2.9
OR-4-18	Type 2	Meta-rhyolite	6.85	25.2	0.512907	0.164348	0.51280	5.6
KR-13-17	Type 2	Meta-andesite	7.16	24.9	0.512939	0.173856	0.51283	6.1
KR-3-18	Type 2	Meta-basalt	1.18	2.9	0.512993	0.246018	0.51284	6.3
AB-6-18	Type 2	Meta-basalt	0.62	1.1	0.513037	0.340790	0.51283	6.0
KÇ-14-17	Type 2	Meta-basalt	3.61	16,1	0.512849	0.135565	0.51276	4.9
YD-5-17	Type 2	Meta-basalt	2.22	8.1	0.51292	0.165708	0.51282	5.9
SD-8-17	Type 2	Meta-basalt	1.97	6.2	0.51297	0.192112	0.51285	6.5
KR-7-17	Type 2	Meta-basalt	0.74	1.8	0.512994	0.248566	0.51284	6.3
DD-5-17	Type 2	Meta-basalt	2.83	10	0.512832	0.171101	0.51273	4.1

4.2 Petrogenesis

4.2.1 Fractional Crystallization

The KM display a wide range of chemical compositions ranging from basalt to dacite (Figures 4.4, 4.5 and 4.6), which may suggest the role of fractional crystallization. In this respect, the relatively low MgO and Ni contents of the samples indicate that they are not primary magmas, but they likely represent compositions evolved from more Mg-rich melts via fractional crystallization. To understand the influence of this process on the KM, the samples were plotted on the Harker-type binary variation diagrams.

The Harker diagrams (Harker, 1909) typically involve SiO_2 as a differentiation index, and it is also preferred in the present study due to its wide range (Figures 4.8, 4.9). As seen in Figures 4.8 and 4.9, SiO_2 is correlated with major oxides MgO, Fe_2O_3, Al_2O_3, TiO_2, MgO, CaO, P_2O_5, MnO, and trace elements Ni, Co, Sc. Such trends can be attributed to the fractional crystallization of specific mineral phases during magma evolution. It is also important to note that a wide range of SiO_2 and MgO exists for both Type 1 and Type 2 samples, implying that these two groups were not derived from fractional crystallization of a single magma source, but they instead followed separate magmatic histories.

SiO_2 displays a well-defined negative trend against MgO (Figure 4.8a). This can be interpreted as the fractionation of ferromagnesian minerals such as olivine and pyroxene. Since Ni is highly compatible with olivine (Kd of Ni is 5.9-29 for olivine; Rollinson, 1993), it is expected that fractionation of olivine should cause a decrease in Ni with increasing SiO_2. Indeed, the KM display decreasing concentrations of Ni from the mafic members to the felsic ones, thus supporting fractionation of olivine (Figure 4.9a). It must be noted that Type 2b samples have higher Ni abundances (10.7-79.7 ppm) at a given SiO_2, which may suggest olivine accumulation. Alternatively, such high Ni abundances can be a genetic feature and may have been inherited from the mantle source. If the multielement systematics

are considered, it can be deduced that Type 2b samples are most likely the products of different genesis, with highly depleted characteristics similar to boninites.

Co is also negatively correlated with SiO_2 (Figure 4.9b). Co tends to enter into Fe^{2+} lattice sites because of their similar electronegativity and ionic radii (McDougall and Lovering, 2007). This makes Co highly compatible with olivine (Kd of Co is 6.60 for olivine; Rollinson, 1993). Thus, the negative trend of Co can be attributed to olivine fractionation. In addition, Co is also compatible with clinopyroxene (Kd of Co is 2-4 for clinopyroxene; Rollinson, 1993); hence this mineral may have also joined fractionation assemblage for the KM. This idea can be tested using Sc, which strongly partitions into clinopyroxene (Kd of Sc is 1.7-3.2 for clinopyroxene; Rollinson, 1993). For both groups, Sc contents decrease with increasing SiO_2, thus supporting clinopyroxene removal during the magmatic evolution of the KM (Figure 4.9c). Well-defined trends are also observed in the plot of Fe_2O_3 against SiO_2, which further supports the fractionation of ferromagnesian minerals such as olivine and pyroxene (Figure 4.8b).

In both groups, SiO_2 shows a significant negative correlation with Al_2O_3 (Figure 4.8c). Because Al_2O_3 is mainly controlled by feldspar crystallization, this trend can be explained by plagioclase removal. The decreasing concentrations of CaO with increasing SiO_2 support this view, suggesting plagioclase fractionation (Figure 4.8e). Because Eu is compatible with feldspars, removal of feldspar from the melt would result in a negative Eu anomaly in the residual melt. The existence of negative and positive Eu anomalies, which are encountered in some samples from both groups, signifies fractionation and accumulation of plagioclase, respectively (Eu/Eu* = 0.53-1.57 for Type 1 and 0.7-1.59 for Type 2; Eu/Eu* ratio was calculated using the equation $Eu/Eu^* = Eu_N/\sqrt{[(Sm_N)*(Gd_N)]}$. It is observed in Figure 4.9g that as SiO_2 increases, Eu/Eu* values decrease below 1. This negative trend suggests plagioclase fractionation, which is in agreement with the results obtained from Al_2O_3 and CaO.

Within Type 1, the onset of decreasing in TiO_2 is about 58 wt.% SiO_2 (Figure 4.8d). On the other hand, TiO_2 increases until 53 wt.% SiO_2 then decreases dramatically

at higher SiO_2 contents within Type 2 (Figure 4.8d). This marked decline can be explained by Fe-Ti oxides (e.g. magnetite, ilmenite) fractionation. However, the higher TiO_2 concentrations of some samples at a given SiO_2 may indicate the accumulation of Fe-Ti oxides (Figure 4.8d). Amphibole fractionation may also be responsible for the decrease in TiO_2 with increasing SiO_2. Y is mostly compatible with garnet and amphibole minerals (Rollinson, 1993). Furthermore, an increasing trend of Y exhibits the fractionation of those minerals (Figure 4.9e). However, the absence of relative depletion in the middle REE (MREE) with respect to LREE and HREE (concave-upward shapes) on the REE patterns reflects that fractionation of amphibole was insignificant in the petrogenesis of KM. The fractionation of Fe-Ti oxides is also consistent with decreasing concentrations of V with increasing SiO_2 since V is known to be strongly partitioned into Fe-Ti oxides (Wilson, 1989). For both chemical types, P_2O_5 starts to decrease below ~ 60% SiO_2 wt.% (Figure 4.8f). This decrease indicates that apatite fractionation played a critical role for both Type 1 and Type 2 samples. The increase in Zr with increasing SiO_2 can be explained by fractionation of zircon or baddeleyite (Figure 4.9f).

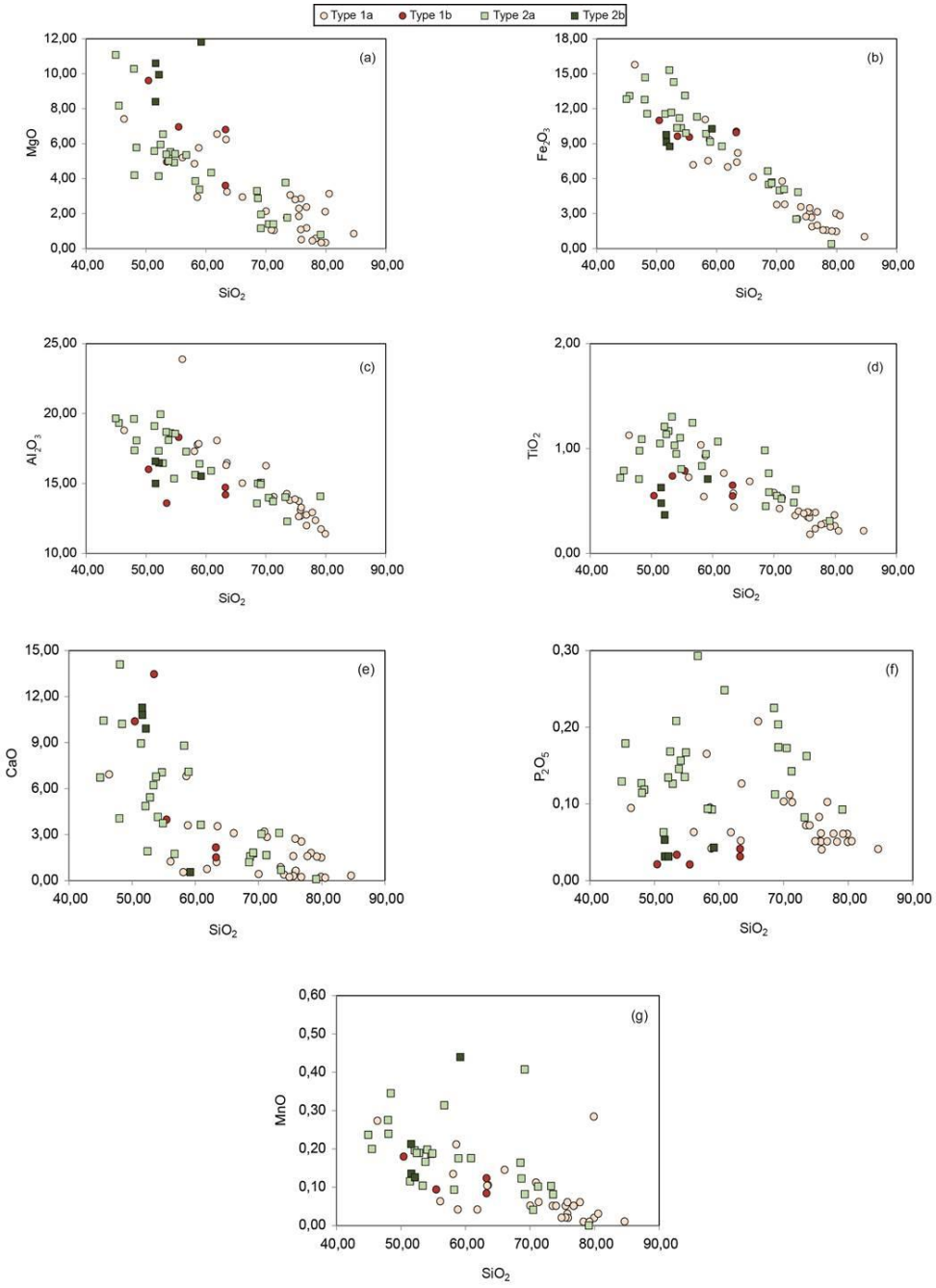


Figure 4.8. Bivariate plots of SiO_2 against selected major oxides for the Kösdağ Metavolcanics.

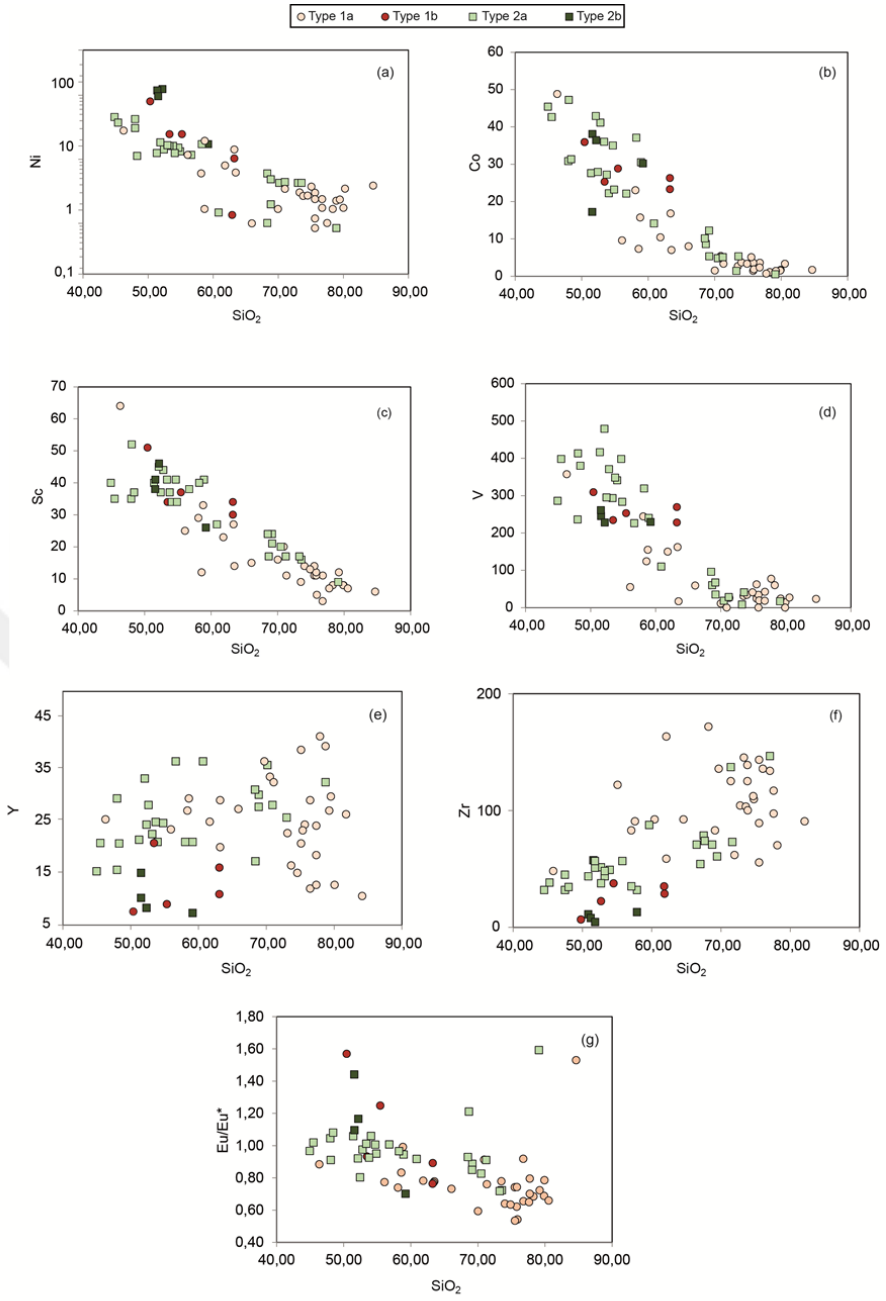


Figure 4.9. Bivariate plots of SiO_2 against trace elements for the Kösdağ Metavolcanics.

To summarize, the variations in major oxides and trace elements suggest that the fractionation of olivine, pyroxene, plagioclase, and Fe-Ti oxides may have played an essential role in the magmatic history of the KM. In addition, Type 1 and Type 2 groups have approximately the same range in SiO_2, with significant overlap, implying that the two groups are not cogenetic.

4.2.2 Nature of the Source Region

As previously mentioned, the KM demonstrate a broad range of SiO_2 content, including lithologies from basalts to dacites. However, to interpret source characteristics, only the samples with $SiO_2 \leq 65.00$ wt.% were taken into account to minimize the effects of fractional crystallization.

Table 4.4. Element ratios used in the interpretation of the mantle source characteristics.

Type	Elemental ratio	Range	n	Average	Standard deviation
Type 1	Zr/Nb	37.1-77.5	11	53.2	13.9
	Zr/Y	1.11-6.89	12	3.5	1.7
	Nb/Y	0.02-0.19	11	0.08	0.05
	Nb/Yb	0.16-1.23	11	0.59	0.36
	Th/Yb	0.12-1.77	11	0.66	0.47
	Lu/Hf	0.12-0.48	12	0.23	0.12
	Ba/La	6.25-124.62	12	47.2	38.9
	Ba/Yb	6.9-270	12	93.04	78.5
	Ba/Nb	25-635	11	224.8	228.7
	Th/Nb	0.6-1.55	11	1.05	0.35
	Nb/Sm	0.25-1.13	11	0.66	0.31
	La/Nb	2.19-8	11	4.05	1.56
Type 2	Zr/Nb	3.3-85.8	20	33.5	6
	Zr/Y	0.79-11.81	22	1.76	0.5
	Nb/Y	12.28-19.94	20	0.08	0.05
	Nb/Yb	0.2-2.09	20	0.73	0.5
	Th/Yb	0.07-2.01	16	0.42	0.56
	Lu/Hf	0.22-0.8	22	0.33	0.13
	Ba/La	1.9-103.33	22	21.5	30.04
	Ba/Yb	2.62-150.56	22	29.1	32.6
	Ba/Nb	8.05-113.75	20	40.2	37.3
	Th/Nb	0.1-1.93	18	0.57	0.46
	Nb/Sm	0.16-2.58	20	0.72	0.56
	La/Nb	0.25-9	20	4.31	2.38

The Zr/Nb ratio is one of the trace element ratios used to unravel mantle source features (Erlank and Kable, 1976; Le Roex et al., 1983; Pearce and Norry, 1979). Also, since both Zr and Nb are fluid-immobile, it is particularly useful to understand the depletion/enrichment features of the altered/metamorphic rocks (Arculus et al., 1999; John et al., 2004; Ludden et al., 1982; Pearce, 1975; Wood et al., 1979). Because these elements possess distinct incompatibilities during partial melting of lherzolite, it is reasonable to assume that they will be fractionated as the relative compatibilities of trace elements are taken into consideration. Nb is considered more incompatible relative to Zr (Sun and McDonough, 1989). Thus, during mantle-crust differentiation, melt extraction events produced relatively Nb-poor reservoirs, forming the depleted mantle (Hofmann, 1997). As a result, the depleted mantle, which is the common source of N-MORBs, has a high Zr/Nb ratio (31.7, Sun and McDonough, 1989). Thus, elevated Zr/Nb ratios may imply contribution from depleted sources associated with moderate/high degrees of partial melting, as seen in N-MORBs. Lower Zr/Nb ratios, on the other hand, may reflect the contribution from Nb-rich, enriched mantle sources (e.g., primitive mantle, Zr/Nb = 15.7; Sun and McDonough, 1989), as is the case for OIBs (5.83; Sun and McDonough, 1989). Concerning the KM, the Zr/Nb ratios of Type 1 vary from 37.1 to 77.5 (ave. = 53.2), while this ratio varies from 3.3 to 85.8 (ave. = 33.5) for Type 2 samples (Table 4.4). Based on the high Zr/Nb values observed in both groups, it is apparent that depleted mantle sources have been involved in their petrogenesis (Figure 4.10). The samples with very high Zr/Nb may suggest derivation from mantle sources even more depleted than the typical N-MORB source, thus requiring a previous melt extraction. On the other hand, the somewhat lower ratios (compared to N-MORB) may indicate involvement from enriched sources.

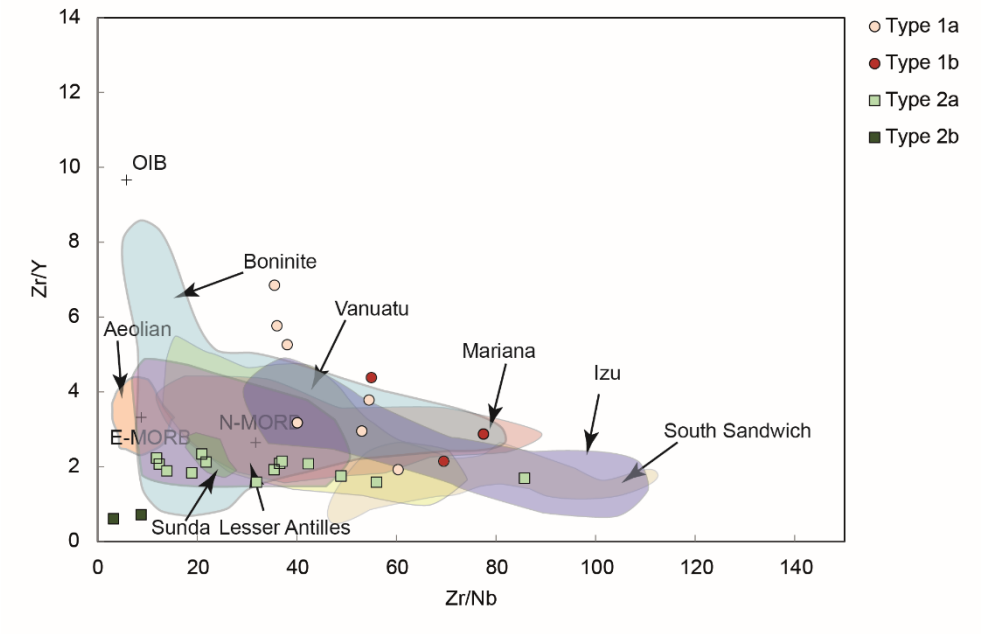


Figure 4.10. Plot of Zr/Y vs. Zr/Nb for the KM and modern arc environments. Sunda from Stolz et al. (1990); South Sandwich from Pearce et al. (1995); Lesser Antilles from Turner et al. (1996); Vanuatu from Peate et al. (1997); Izu from Taylor and Nesbitt, (1998); Boninite from Bedard, (1999); Aeolian from Calanchi et al. (2002); Mariana from Pearce et al. (2005).

Although the Type 2 samples reflect depleted characteristics in general, it is observed that the Zr/Nb values of Type 2b samples are quite lower than those of Type 2a samples (ave. Zr/Nb for Type 2a is 36.6, ave. Zr/Nb for Type 2b is 6). At first glance, these low Zr/Nb ratios may suggest an enriched contribution to the mantle source for this group. However, the multi-element patterns of these samples contrast this result, implying highly depleted characteristics (Figure 4.4), similar to boninitic melts. Indeed, when the geochemical features of well-known boninites are considered, it appears that the Zr/Nb ratios of the boninites can attain low values, below 7 (Cameron et al., 1983). Therefore, Type 2b samples appear similar to boninitic melts, considering their trace element systematics. In addition, these samples display resemblance to boninitic rocks in terms of high SiO_2 (51.59-59.22 wt.%) and MgO (8.40-11.81 wt.%) concentrations. Another support on the boninitic nature of Type 2b comes from the Zr(M) vs. La/Yb diagram (Figure 4.11). Here, Type 2b samples plot within the field of Betts Cove Boninite, indicating their similarity. Therefore, the low Zr/Nb signatures of Type 2b samples

do not imply derivation from enriched sources but rather related to their boninitic characteristics, which are contrastingly inherited from ultra-depleted harzburgitic sources (Crawford et al., 1989).

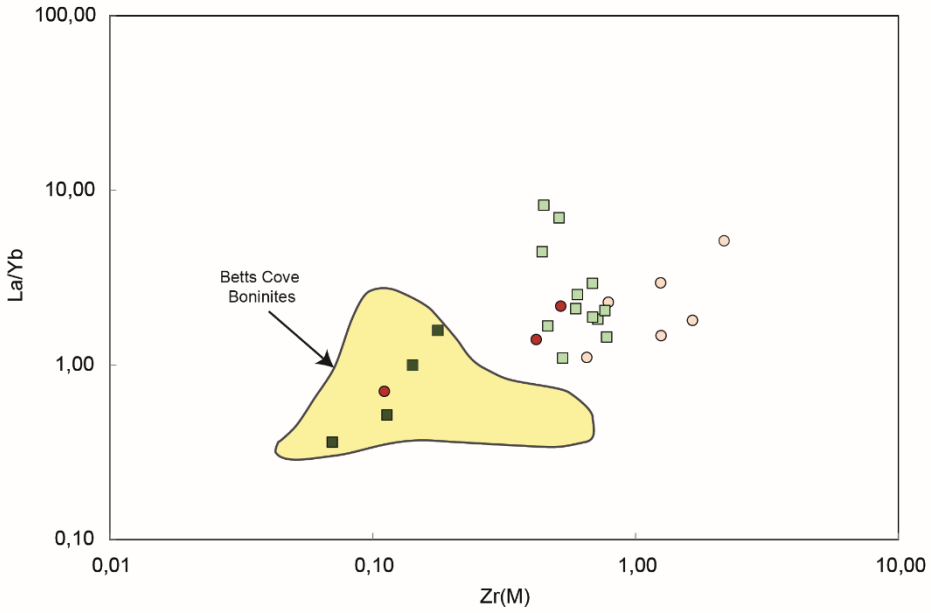


Figure 4.11. Plots of La/Yb vs. N-MORB normalized Zr value. Betts Cove boninites data from Bedard (1999).

Another parameter to evaluate the nature of the source is the Zr/Y ratio. As in the Zr/Nb ratio, the elements are of different incompatibilities. Zr is relatively more incompatible than Y during partial melting of upper mantle peridotite (e.g., Salters and Longhi, 1999). Therefore, while Y prefers to remain in the source region, Zr tends to go to the melt phase and migrates away from the source region. As a result, the depleted mantle source domains will be relatively depleted in Zr, and characterized by low Zr/Y ratios. Upon moderate/high degrees of melting, the melt products of such sources (e.g., N-MORB) will also reflect low Zr/Y signatures (N-MORB Zr/Y = 2.64; Sun and McDonough, 1989). On the other hand, a major contribution from enriched sources is marked by high Zr/Y values (OIB Zr/Y = 9.66; Sun and McDonough, 1989) (Figure 4.12). Type 1 samples have a Zr/Y ratio varying between 1.11 and 6.89, while Zr/Y ratios of Type 2 samples range from 0.6 to 2.44. It can be therefore proposed that both Type 1 and Type 2 samples have dominantly involved the contribution of the depleted mantle sources, whereas the

relatively lower ratios may imply that enriched components were also present. Similar to Zr/Y, Nb/Y ratios can be used in such a way that low Nb/Y ratios are associated with the depleted mantle sources, while high Nb/Y ratios can indicate the contribution of the enriched sources (N-MORB Nb/Y = 0.08, OIB Nb/Y = 1.65; Sun and McDonough, 1989). The range of Nb/Y for both Type 1 and Type 2 samples changes between 0.02 and 0.19 (Figure 4.12). This agrees with the idea that the KM have acquired a dominant contribution of the depleted sources.

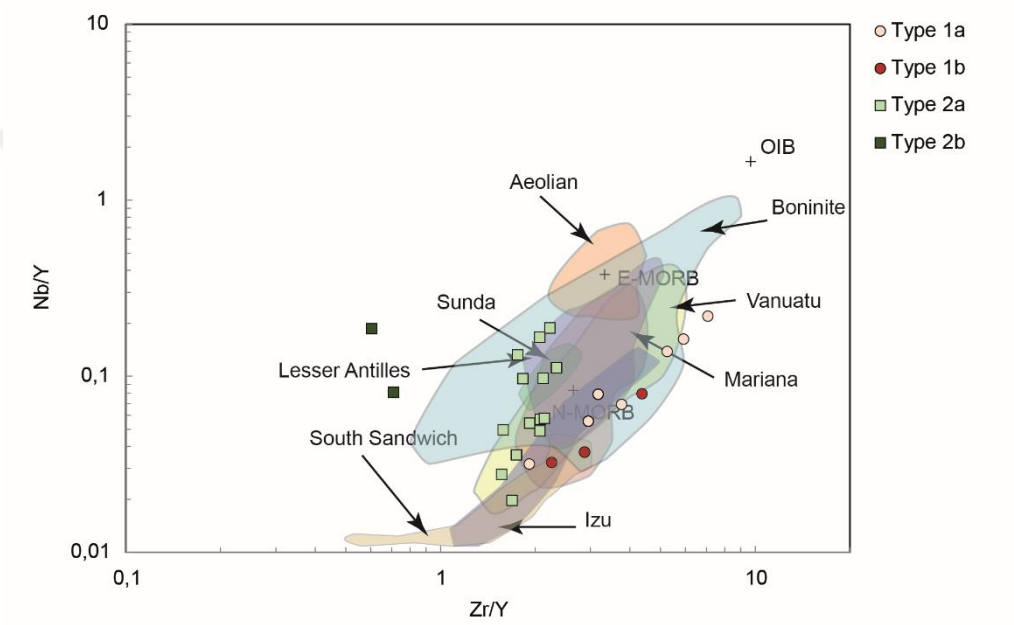


Figure 4.12. Nb/Y vs. Zr/Y diagram (ave. N-MORB, E-MORB, OIB values from Sun and Mc Donough, 1989). Sunda from Stolz et al. (1990); South Sandwich from Pearce et al. (1995); Lesser Antilles from Turner et al. (1996); Vanuatu from Peate et al. (1997); Izu from Taylor and Nesbitt, (1998); Boninite from Bedard, (1999); Aeolian from Calanchi et al. (2002); Mariana from Pearce et al. (2005).

Both samarium (Sm) and neodymium (Nd) are incompatible, but Nd is more incompatible than Sm. Therefore Nd prefers to remain in the liquid phase compared to Sm. Accordingly, during crust-mantle differentiation, Nd was removed from the mantle and transferred to the crust, whereas Sm concentrated in the depleted mantle. As a consequence, the depleted mantle (i.e. the MORB source) has high Sm/Nd and $^{143}Nd/^{144}Nd$ ratios as well as positive ε_{Nd} values. The melt products of the depleted mantle (e.g. N-MORBs) would also be characterized by high ε_{Nd} values (ε_{Nd} = 7.15-13.54 for the South Atlantic MORB; Hoernle et al.,

2011). The initial ε_{Nd} values of the KM samples are all positive between +2.9 and +6.5, implying contribution from the depleted mantle sources. However, although ε_{Nd} values of KM samples are positive, they are lower than those of MORBs (Table 4.3; Figure 4.13). This may suggest the involvement of an enriched component (e.g., recycled components) and/or subduction-related input in the mantle source. These results, obtained from the Nd whole-rock isotopes, are consistent with those based on the Zr/Nb ratios, signifying the importance of depleted mantle sources in the petrogenesis of KM. Yet, there is still a need for contribution from enriched mantle sources.

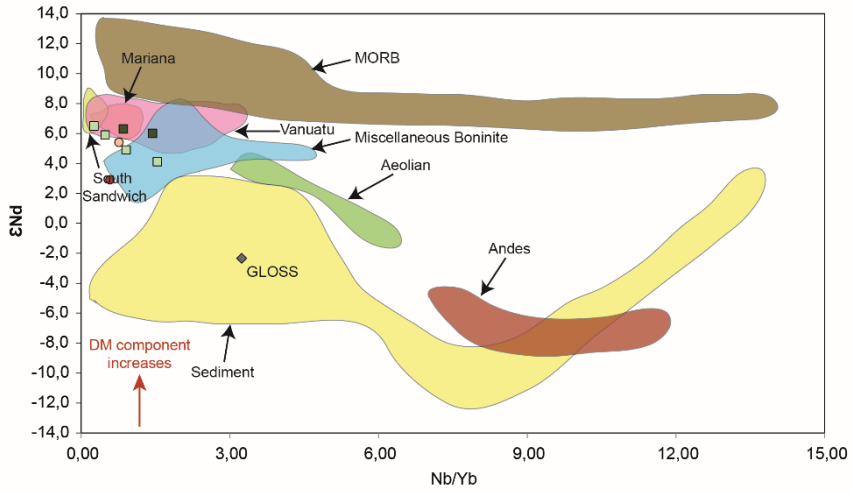


Figure 4.13. Plot of ƐNd vs. Nb/Yb for the KM. South Sandwich from Pearce et al. (1995); Vanuatu from Peate et al. (1997); ave. GLOSS from Plank and Langmuir, (1998); Sediment from Plank and Langmuir, (1998); Miscellaneous Boninite from Bedard, (1999); Andes from Winter, (2001); Aeolian from Calanchi et al. (2002); Mariana from Pearce et al. (2005); MORB from Hoernle et al. (2011).

KM samples display depletion in Nb (and Ta) compared to Th and La, similar to subduction zone magmas (e.g., Pearce and Peate, 1995). This decoupling results from fluid/melt transport in the shallow parts of subduction zones (Baier et al., 2008). Kelemen et al. (2004) favor the hypothesis of fractionation of Nb and Ta from other highly incompatible elements through partial melting of subducting eclogite-facies basalt or sediment with residual rutile (Elliott et al., 1997; Kelemen et al., 1993; Ryerson and Watson, 1987; Turner et al., 1997). During dehydration and melting of the slab, Th and La are mobilized by the slab-derived melt, whereas

Nb is confined in the slab. Consequently, Th and La are effectively eliminated from the slab and then incorporated into the mantle wedge. As a result, the mantle wedge is enriched in Th and La compared to Nb, resulting in high Th/Nb and La/Nb ratios for magmas formed at subduction zones (ave. Mariana Arc Th/Nb = 0.25, La/Nb = ~2.50, Pearce et al., 2005). The KM display similar features, with La/Nb varying between 2.19 and 8.00 for Type 1, 0.25 and 9.00 for Type 2. Therefore, such high ratios may imply that the KM have been derived from a subduction-modified mantle source (Figure 4.3) (Pearce and Peate, 1995; Pearce et al., 1992).

Th/Yb vs. Nb/Yb plot of Pearce and Peate (1995) provides useful information regarding the source features and the events associated with subduction process (Pearce, 1983; Pearce and Peate, 1995) (Figure 4.14). It is known that Nb and Th show similar geochemical behavior during partial melting of MORB and OIB (Pearce et al., 2005; Wood et al., 1979). However, these elements become decoupled during subduction, resulting in enrichment in Th over Nb. On the other hand, Yb is a subduction-immobile element, like Nb, and can be used as a normalizing factor to minimize fractional crystallization and crystal accumulation effects (Pearce and Peate, 1995; Pearce et al., 2005). In this respect, on the plot of Th/Yb vs. Nb/Yb, slab-derived additions would cause deviations from the compositional array of non-subduction magmas, such as MORB and OIB.

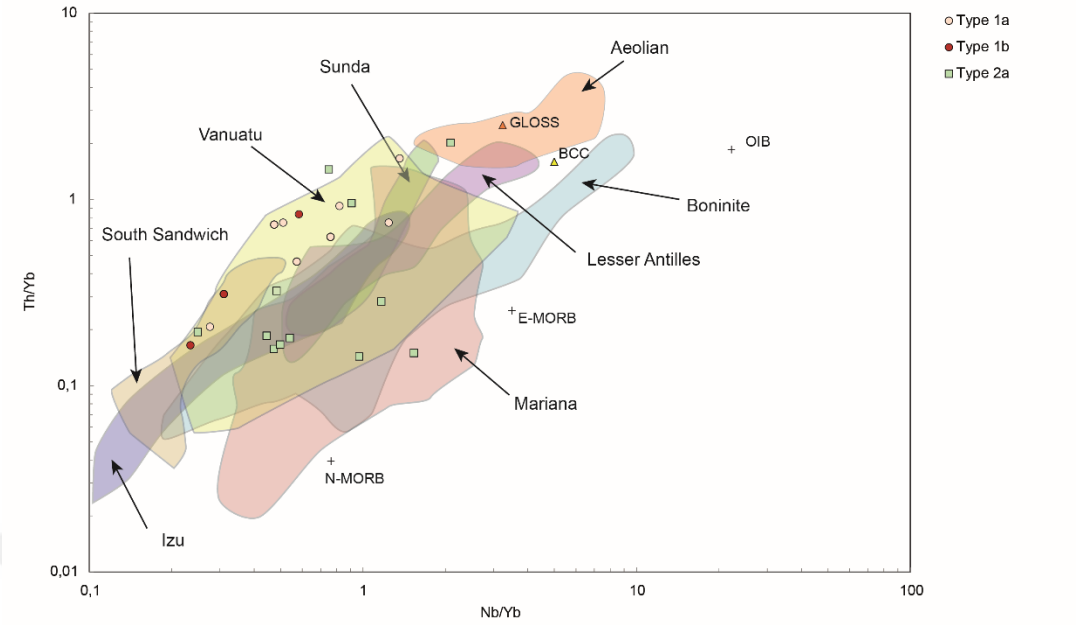


Figure 4.14. Th/Yb vs. Nb/Yb diagram (after Pearce and Peate, 1995). Average N-MORB, E-MORB and OIB values from Sun and McDonough (1989). BCC from Taylor and McLenan, (1985). GLOSS from Plank and Langmuir, (1998). Sunda from Stolz et al. (1990); South Sandwich from Pearce et al. (1995); Lesser Antilles from Turner et al. (1996); Vanuatu from Peate et al. (1997); Izu from Taylor and Nesbitt, (1998); Boninite from Bedard, (1999); Aeolian from Calanchi et al. (2002); Mariana from Pearce et al. (2005).

In the diagram, all Type 1 and Type 2 samples are plotted beyond the array, implying the subduction enrichment (Figure 4.14). It should be noted that, Type 1 samples show slightly higher Th/Yb values for a given Nb/Yb relative to Type 2 samples (Th/Yb for Type 1 = 0.12-1.77, ave. = 0.66; Th/Yb for Type 2=0.07-2.01, ave. = 0.42). This may mean that the contribution of the subduction component on Type 1 samples has been greater, in general. The relative Th/Yb enrichment may also signify crustal contamination, which will be discussed in Chapter 6. Additionally, Nb/Yb ratios of Type 1 are generally lower than the average N-MORB ratios (Nb/Yb for Type 1 = 0.16-1.23, ave. = 0.60, Nb/Yb for Type 2 = 0.20-2.09, ave. = 0.73, Nb/Yb ratio of N-MORB is 0.76; Sun and McDonough, 1989). This highlights once again the role of depleted mantle sources in the petrogenesis of the KM.

4.2.3 Melting Model

There are two main types of partial melting; fractional or rayleigh melting and equilibrium or batch melting. Batch melting will be considered hereafter because it may be a more common situation. As partial melting progresses, the mathematical explanation for batch melting is characterized by the existence of trace elements in the melt (Gast, 1968; Hanson and Langmuir, 1978; Hertogen and Gijbels, 1976; Minster and Allegre, 1978; Neumann et al., 1954; Shaw, 1970).

Different types of melt modelings were performed to understand i) source mineralogy (spinel- or garnet-bearing source), ii) degree of partial melting, and iii) nature of the source region (depleted or enriched source) in the following pages. Figure 4.15 displays chondrite-normalized REE patterns for a spinel lherzolite source and resulting batch partial melts over a range of melt fractions (F= 1% - 30%). This modeling was considered a first-order approach to get an idea regarding the melting characteristics of the investigated rock samples. The modeling uses Shaw's (1970) modal batch melting equations.

$$C^L = \frac{C_0}{[D_0 + F\text{-}(D_0F)]}$$

$$C^S = \frac{C_0 D_0}{[D_0 + F\text{-}(D_0F)]}$$

where:

C^L = concentration of the trace element in the partial melt

C^S = concentration of the trace element in the solid

C_0 = initial concentration of the trace element in the solid source (in this study this value is taken from (Workman and Hart, 2005)

F = weight fraction of melt produced (%)

D_0 = bulk partition coefficient at the onset of melting

P_0 = bulk distribution coefficient of the minerals which make up the melt (will be used in non-modal batch melting equation in the following section)

As shown in Figure 4.15, the smallest-degree partial melts (low F) are most enriched in the most incompatible elements, while higher-degree partial melts are similar to the source. In these REE diagrams, the most incompatible elements are situated on the left, while less incompatible elements are placed on the right. It should be noted that the left-hand side of the pattern, LREEs, are subduction mobile. Accordingly, these elements are affected by slab dehydration/melting. In contrast, the right-hand side of the pattern, HREEs, is not modified by such processes. Hence, they can provide insights into the partial melting of the source region. Besides, since HREEs are highly compatible with garnet, the existence of the residual garnet in the source would lead to depletion and fractionation in HREE in the resulting melts (Spath et al., 1996; Wilson, 1989). However, this case is not observed on the REE patterns of KM [$(Gd/Yb)_N$ = 0.66-1.12, ave. = 0.95 for Type 1; $(Gd/Yb)_N$ = 0.65-1.63, ave. = 1.15 for Type 2; OIB = 3.53; Sun and McDonough, 1989)]. The flat HREE patterns of the investigated rocks suggest derivation from a garnet-free source.

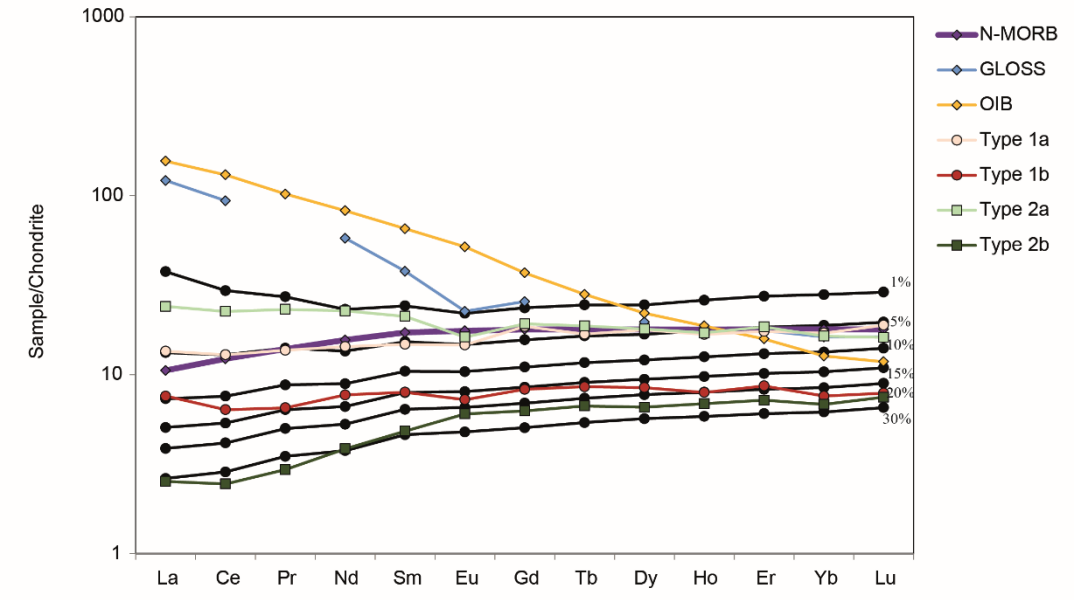


Figure 4.15. Chondrite-normalized spidergram showing modal batch melting of a spinel lherzolitic source and representative Kösdağ Metavolcanics. The spinel

lherzolitic source mode was presumed to be 0.57 olivine + 0.21 orthopyroxene + 0.20 clinopyroxene + 0.02 spinel.

In order to assess the results obtained from the preliminary approach, a ratio-based melt modeling was performed (Figure 4.16). The element pairs Lu/Hf vs. Nb/Yb diagram was used to determine the partial melting systematics of the KM. Since these elements are all subduction-immobile (e.g., Pearce and Stern, 2006), the modeling results are not affected by the addition of subduction components but reflect only the effects of partial melting and/or source mineralogy. The modeling (Figure 4.16) was conducted using the non-modal batch melting equations derived by Shaw (1970). In this respect, only the samples with $SiO_2 \leq 65.00$ wt.% were utilized to minimize the effects of fractional crystallization.

The partition coefficient data of Sayit et al., (2020) used in the modeling are presented in Table 4.5.

Table 4.5. Partition coefficients used in the melt modeling: [1]Kelemen et al. (1993); [2]McDade et al. (2003); [3]Salters et al. (2002); [4]Shaw (2006); and [5]McKenzie and O'nions (1991).

	Nb	*Yb*	*Hf*	*Lu*
olivine	0.0001 (1)	0.0305 (3)	0.001 (3)	0.0432 (3)
orthopyroxene	0.003 (1)	0.162 (3)	0.047 (2)	0.198 (3)
clinopyroxene	0.012 (1)	0.263 (3)	0.37 (2)	0.74 (2)
garnet	0.044 (3)	3.457 (3)	0.387 (3)	4.325 (3)
spinel	0.01 (1)	0.0045 (1)	0.05 (4)	0.01 (5)

Following non-modal batch melting equation was derived by Shaw (1970) to model batch melting:

$$C^L = \frac{C_0}{[D_0 + F(1 - P_0)]}$$

$$C^S = \frac{C_0 (D_0 - PF)}{(1-F) (D_0 + F(1 - P_0)}$$

Garnet lherzolite and spinel lherzolite are two different mantle mineral assemblages used in the modeling. It should be noted that Type 1 and Type 2

samples plot on different melting curves (Figure 4.16). While Type 2 samples plot on the spinel peridotite melt curve, Type 1 samples, on the other hand, are distributed on the pre-depleted spinel lherzolite (0.25%) curve. For a given Nb/Yb ratio, Type 1 samples have lower Lu/Hf ratios than Type 2 samples. This may indicate that the Type 2 samples may have been generated at a higher degree of partial melting relative to Type 1 from a spinel lherzolitic source (Lu/Hf for Type 1 = 0.12-0.48; Lu/Hf for Type 2 = 0.22-0.80). Although most Type 2 samples display generation under higher degrees of partial melting, Type 1 samples display a broader spectrum in Lu/Hf ratio. Accordingly, it can be suggested that Type 1 samples appear to have been derived from a more depleted source region due to their relatively lower Nb/Yb ratios (ave. Nb/Yb for Type 1 = 0.59; ave. Nb/Yb for Type 2 = 0.73). The compositions plotting to the left of the melting curve of DMM-type peridotite are represented by lower Nb/Yb ratios indicating more depleted geochemical signatures of those Type 1 samples. This relative depletion can be attributed to involvement of a more depleted mantle source than DMM, which may be explained by a previous melt-extraction. Indeed, it seems plausible and is confirmed by melt modeling, which suggests that more depleted sample compositions can be reproduced by partial melting of a DMM-like mantle source that has experienced 0.25% and 0.5% melt extraction. To test this, melt extraction curves were plotted in the same melt model (Figure 4.16).

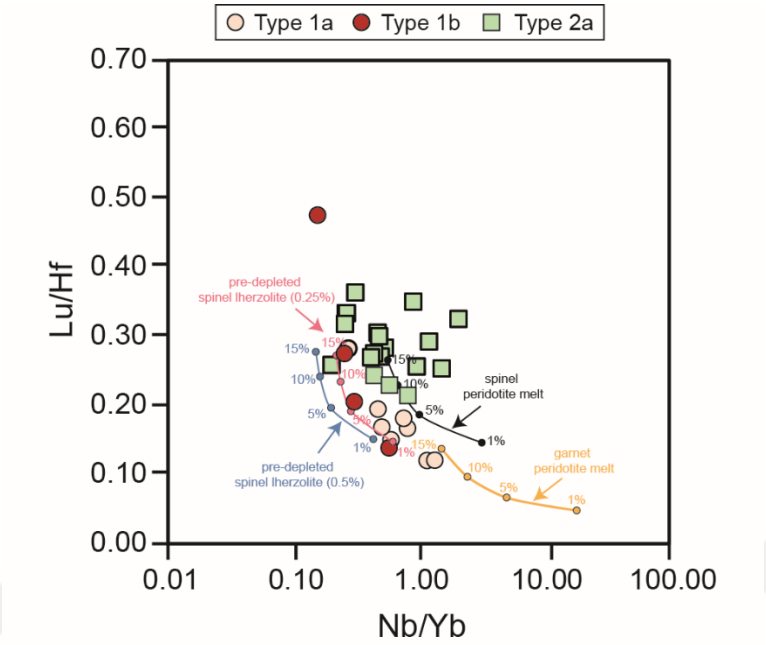


Figure 4.16. Melting model of the Kösdağ Metavolcanics. DMM composition of Workman and Hart (2005) was used for the "spi-peridotite" source The source mode was assumed to be 0.60 olivine + 0.24 orthopyroxene + 0.13 clinopyroxene + 0.03 spinel, which melts in the proportions 0.05 olivine + 0.07 orthopyroxene + 0.7 clinopyroxene + 0.18 spinel. The "pre-depleted spi-peridotite" source were generated by extracting 0.25% and 0.5% melts from DMM. The source mode of these source was presumed to be 0.606 olivine + 0.242 orthopyroxene + 0.124 clinopyroxene + 0.028 spinel, which melts in the proportions of 0.05 olivine + 0.07 orthopyroxene +0.70 clinopyroxene + 0.18 spinel. The grt-peridotite source is represented by the E-DMM composition of Workman and Hart (2005). The source mode was presumed to be 0.598 olivine + 0.211 orthopyroxene + 0.076 clinopyroxene + 0.115 garnet (McKenzie and O'Nions 1991), which melts in the proportions of 0.01 olivine + 0.04 orthopyroxene + 0.50 clinopyroxene + 0.45 garnet.

The modeling results demonstrate that the observed trace element ratios in the KM may not be explained only by different degrees of partial melting of a single DM-type source. As seen from Figure 4.16, samples plotted to the right of the melting curve of DMM-type spinel-lherzolite. Thus, this requires the involvement of additional mantle sources with distinct geochemical features. On the other hand, the samples with more enriched characteristics (i.e., higher Nb/Yb ratio) require another explanation.

On both global and local scales, isotope and trace element studies of oceanic basalts reveal that the Earth's mantle is heterogeneous (Gast et al., 1964; Hoffman, 1997; Zindler and Hart, 1986), and the most of the mantle sources are complex assemblages of two or more components with isolated long-term chemical evolution (Stracke, 2012). Eclogite/pyroxenite or metasomatized peridotite are lithologically representative of these recycled domains and describe enriched parts of the mantle. Thus, they are distinct from the adjacent dry, depleted peridotite with a higher solidus (e.g., Hirschmann and Stolper, 1996). Therefore, enriched, recycled domains may have contributed more to Type 2 samples, which have higher Nb/Yb ratios. An E-DMM-type garnet–peridotite, which is assumed to melt at greater depths due to its lower solidus, was used to test this scenario (e.g. Sayit, 2013). Then, the melts derived from this enriched peridotite and the melts of depleted spinel–lherzolite are mixed. In order to model the melt mixtures, the mixing arrays were constructed using a specific composition of garnet-facies melt with different degrees of melts of spinel–lherzolite (Figure 4.17). The modeled melt mixing region encompasses the enriched sample compositions (Figure 4.17).

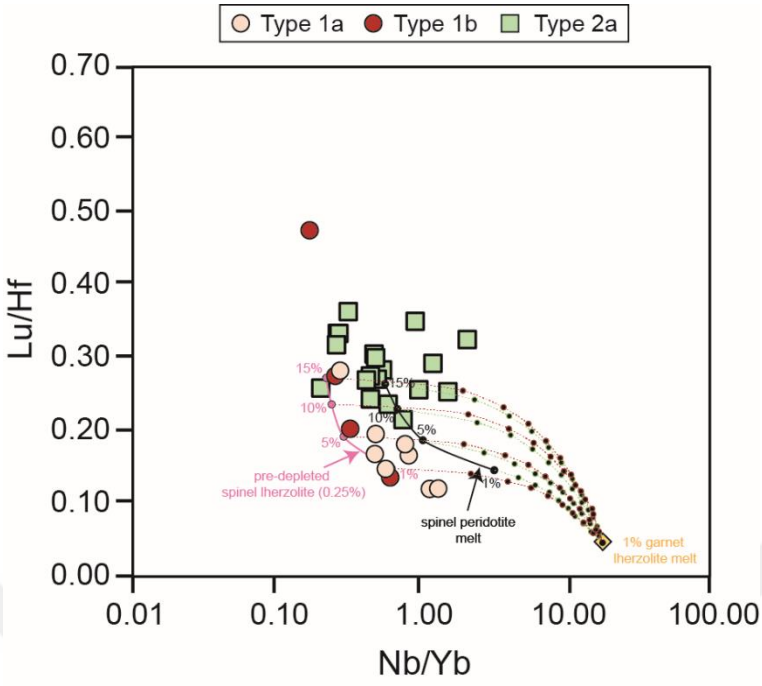


Figure 4.17. Melting model of the Kösdağ Metavolcanics regarding the "spi-peridotite" source, DMM composition of Workman and Hart (2005) was used. The source mode was assumed to be 0.60 olivine + 0.24 orthopyroxene + 0.13 clinopyroxene + 0.03 spinel, which melts in the proportions 0.05 olivine + 0.07 orthopyroxene + 0.70 clinopyroxene + 0.18 spinel. The "pre-depleted spi-peridotite" source was produced by extracting 0.25% melt from DMM. The source mode of this source was assumed to be 0.606 olivine + 0.242 orthopyroxene + 0.124 clinopyroxene + 0.028 spinel, which melts in the proportions of 0.05 olivine + 0.07 orthopyroxene + 0.70 clinopyroxene + 0.18 spinel. Tick marks were drawn to represent 1% melting intervals. Mixing arrays were constructed between 1% grt-peridotite melt and variable percents (1%, 5%, 10% and 15%) of spi-peridotite melt as well as between 1% grt-peridotite melt and variable percents (1%, 5%, 10% and 15%) of pre-depleted spi-peridotite. The grt-peridotite source was assumed to have E-DMM composition of Workman and Hart (2005). The source mode was taken as 0.598 olivine + 0.211 orthopyroxene + 0.076 clinopyroxene + 0.115 garnet (McKenzie and O'Nions, 1991), which melts in the proportions of 0.01 olivine + 0.04 orthopyroxene + 0.50 clinopyroxene + 0.45 garnet.

Boninitic Type 2b samples cannot be evaluated in the Lu/Hf vs. Nb/Yb diagram. Therefore, a different diagram including Sm absolute abundance and Sm/Yb ratio was plotted. The melt modeling shows that melting of asthenospheric N-MORB source cannot explain these highly depleted samples and that a previous melt extraction is required. According to the model of Sayit et al. (2016), this pre-depletion process can be accomplished by melting around 1-2% of the peridotite (Figure 4.18). If the pre-depleted source is then metasomatized by low-degree OIB-

type melts (1%), the observed compositions can be reproduced by melting the that source.

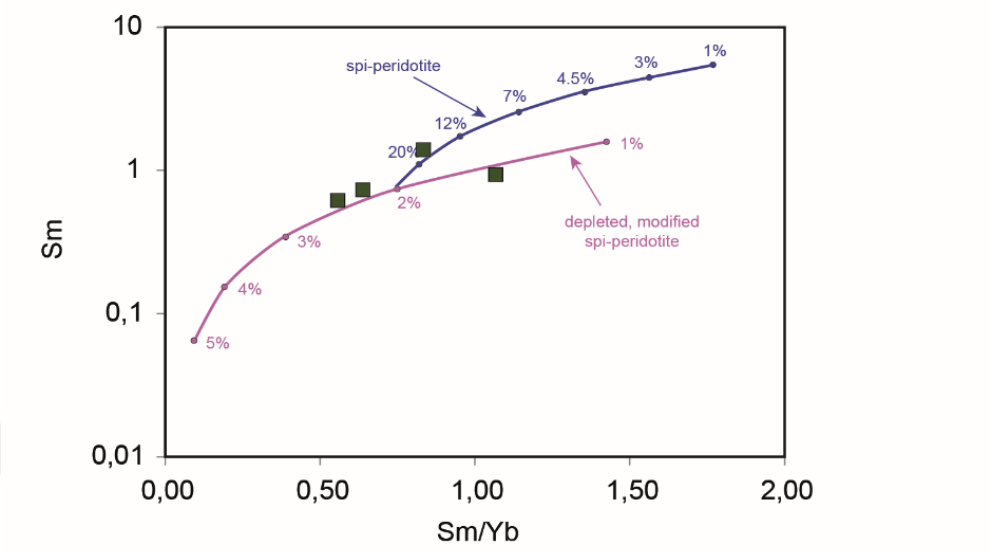


Figure 4.18. Melting model of the Type 2b (boninitic) samples. Spinel peridotite source has the mode of 0.565 olivine + 0.220 orthopyroxene + 0.180 clinopyroxene + 0.035 spinel, which melts in the proportions of 0.20 olivine + 0.15 orthopyroxene + 0.55 clinopyroxene + 0.10 spinel. The spi-peridotite and depleted, modified spi-peridotite curves from Sayit et al. (2016).

CHAPTER 5

GEOCHRONOLOGY

5.1 U-Pb Geochronology

This chapter includes U-Pb geochronology applied on selected six KM samples. The U-Pb geochronometers based on decay of U to Pb isotopes (^{238}U-^{206}Pb and ^{235}U-^{207}Pb) are among the most reliable radiometric techniques for revealing the crsystallization age of the igneous rocks. These chronometers have been used effectively to date igneous rocks that originated between a few million and billion years ago (e.g., Köksal et al., 2013; Schmidberger et al., 2005; Simonetti and Neal, 2010).

Zircon was chosen for geochronological research in this study owing to its resistance to secondary processes such as alteration and metamorphism. During magmatic crystallization, U is very compatible with zircon, however Pb is not. On the basis of this, Pb existing today may be considered to be the result of U decay, making zircon a robust geochronometer. Furthermore, zircon has a very high closure temperature (>900^{0}C) that allows best dating findings (Flowers et al., 2005). In addition, many significant U-bearing accessory minerals (apatite, baddeleyite, perovskite, titanite) have been utilized for in situ U-Pb dating (e.g., Bizzarro et al., 2002; Chen and Simonetti, 2014; Chen at al., 2013; Gumsley et al., 2015; Köksal et al., 2004; Rasmussen et al., 2013).

In-situ U-Pb dating of accessory minerals has recently become more commonly used approach in spite of the conventional single grain evaporation method, yielding significantly more accurate results (e.g., Hu et al., 2014). One argument is that ustilizing small laser spot sizes (e.g., ≤20 microns) different magmatic processes may be dated from the core/rims of the single mineral grains.

Furthermore, compared to Isotope Dilution Thermal Ionization Mass Spectrometry (ID-TIMS) and Secondary Ion Mass Spectrometry (SIMS), is cheaper and has a rapid analysis time with a simple sample preparation stage. Bulk zircon analysis, on the other hand, will lead to the masking of various magmatic and usual metamorphic details provided at the micronscale.

In a total of six samples from Type 1 and Type 2 groups were examined for geochronological studies. After sample separation including heavy mineral separation and hand picking of crystals using a stereo microscope, a hundred thirty-one zircon grains were obtained for in-situ U-Pb analysis. However, ninety-two zircon grains could be examined due to the loss of several zircon grains during the mounting step. The U-Pb analysis results are listed in Table 5.1.

Table 5.1. Age data and number of zircon grains

Chemical Type	*Coordinates*	*Lithology*	*Sample Number*	*Number of Zircon Grains*	*Number of Spots*	*Age*
Type 1	$40^0$58’19.89” N $34^0$04’59.43” E	Meta-rhyolite	197	4	10	94.7 ± 1.8 Ma
Type 1	$40^0$58’27.40” N $34^0$04’46.49” E	Meta-rhyolite	YD-1-18	4	11	93.7 ± 1.2 Ma
Type 1	$41^0$03’04.83”N $34^0$22’05.62”E	Meta-andesite	AB-6-17	19	30	95.38 ± 0.81 Ma
Type 2	$41^0$01’19.71” N $34^0$17’19.91” E	Meta-rhyolite	OR-4-18	20	35	94.89 ± 0.81 Ma
Type 2	$41^0$02’00.40” N $34^0$17’18.13” E	Meta-rhyolite	KR-5-18	38	38	96.9 ± 1.3 Ma
Type 2	$41^0$02’16.17” N $34^0$17’58.67” E	Meta-andesite	KR-13-17	7	7	95.8 ± 5.9 Ma

Furthermore, during the analytical sessions, two well-established and verified zircon standards, Plesovice and GJ-1 were analyzed to confirm and ensure the accuracy of the in-situ U-Pb data presented here. U-Pb data was evaluated by ISOPLOT v.3 (Ludwig, 2003), Microsoft Excel plug-in.

5.1.1 Meta-felsic Lithologies

The findings of zircon grains analyzed from four meta-felsic samples (197, YD-1-18, OR-4-18, KR-5-18) within the KM are displayed on concordia ($^{206}Pb/^{238}U$ vs. $^{207}Pb/^{235}U$) diagrams (Figures 5.1, 5.2, 5.3, 5.4, 5.6, 5.7, 5.8, 5.9). Four similar Late Cretaceous ages of 94.5 ± 1.8 Ma for 197 (concordia age), 93.7 ± 1.2 Ma for YD-1-18 (concordia age), 94.89 ± 0.81 Ma for OR-4-18 (concordia age) and 96.9 ± 1.3 Ma for KR-5-18 (weighted mean $^{206}Pb/^{238}U$ age) were revealed. The results given in Appendices B and C provide comprehensive U-Pb data as well as the location of the laser ablation spots.

Four of the ten zircons analyzed in sample 197 (Figure 5.1) gave concordant dates. Colorless zircons in 197 are euhedral to subhedral, with elongate to stubby grains. They are typically transparent, colorless to gray, and exhibit wide magmatic oscillatory zoning in CL images (Appendices C), implying an origin from a mafic magma. Th/U ratios in zircon are widely used to distinguish between metamorphic (Th/U<0.1) and magmatic (Th/U>0.1) origin for zircon overgrowths. The U and Th concentrations range from 97.1 to 109.6 ppm and 60.8–72.1 ppm, respectively. The Th/U ratios of zircons in 197 range from 0.63 to 0.73 with a mean of 0.67, which supports their magmatic origin (Hoskin and Black, 2000). Therefore, zircons can reflect the crystallization age of the investigated rocks. Figure 5.1 shows the U-Pb concordia diagrams for 197. The weighted mean $^{206}Pb/^{238}U$ age for 197 is 94.7 ± 1.8 Ma (2σ, MSWD = 1.20) (Figure 5.2).

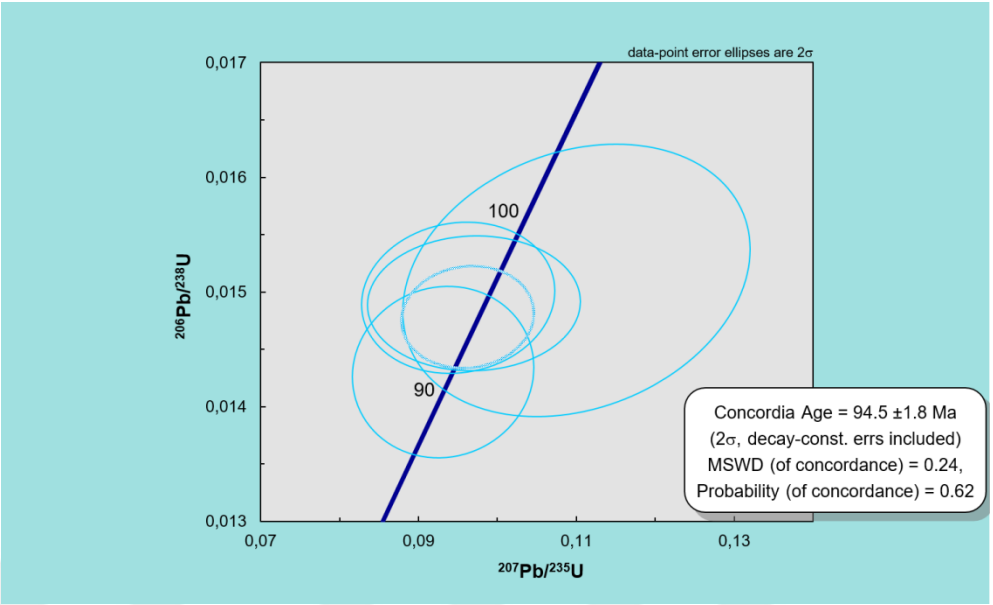


Figure 5.1. $^{206}Pb/^{238}U$ vs. $^{207}Pb/^{235}U$ diagram and concordia age for 197.

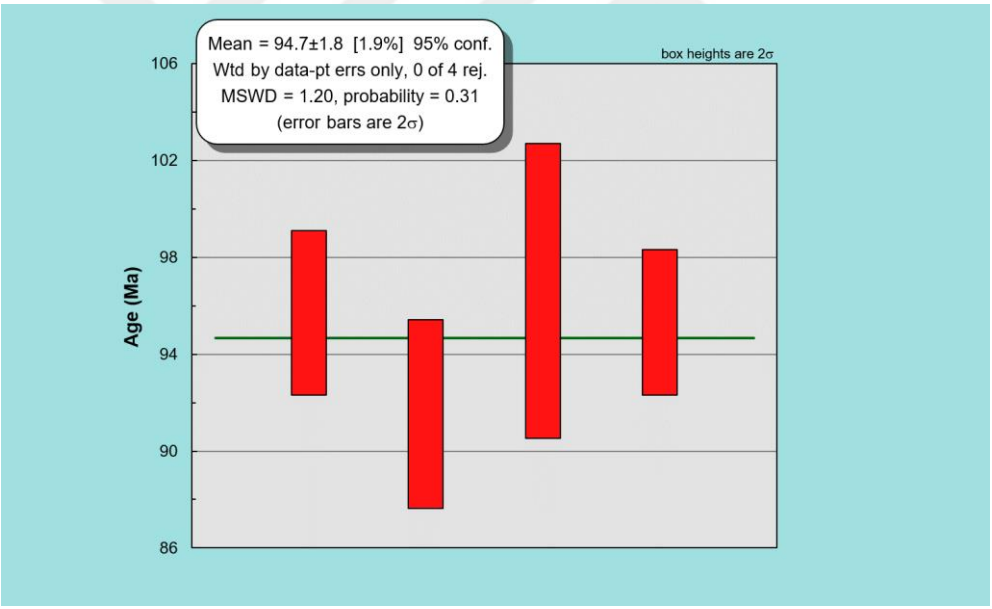


Figure 5.2. $^{206}Pb/^{238}U$ (weighted mean age) data for 197.

A total of eleven zircon analyses were carried out, of which seven were discarded owing to poor analyses in sample YD-1-18. Colorless zircons in YD-1-18 are euhedral to subhedral, with elongate to stubby grains. It is usual to see concentrated zoning and typical magmatic oscillatory zonation, indicating a magmatic origin of the zircon grains. The U and Th concentrations range from 113.3 to 697 ppm and 78.7–981.7 ppm, respectively. The Th/U ratios of zircons in YD-1-18 range from

0.69 to 1.41 (mean = 1.08), supporting their magmatic origin. Therefore, zircons can reflect the crystallization age of the investigated rocks. Figure 5.3 shows the U-Pb concordia diagrams for YD-1-18. The weighted mean $^{206}Pb/^{238}U$ age for YD-1-18 is 93.6 ± 1.2 Ma (2σ, MSWD = 1.14) (Figure 5.4).

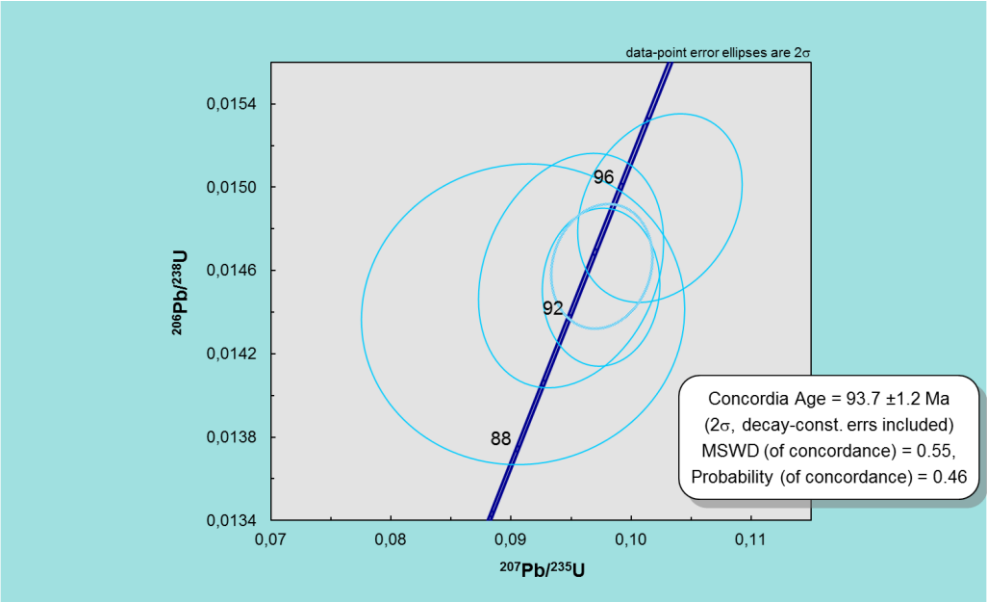


Figure 5.3. $^{206}Pb/^{238}U$ vs. $^{207}Pb/^{235}U$ diagram and concordia age for YD-1-18.

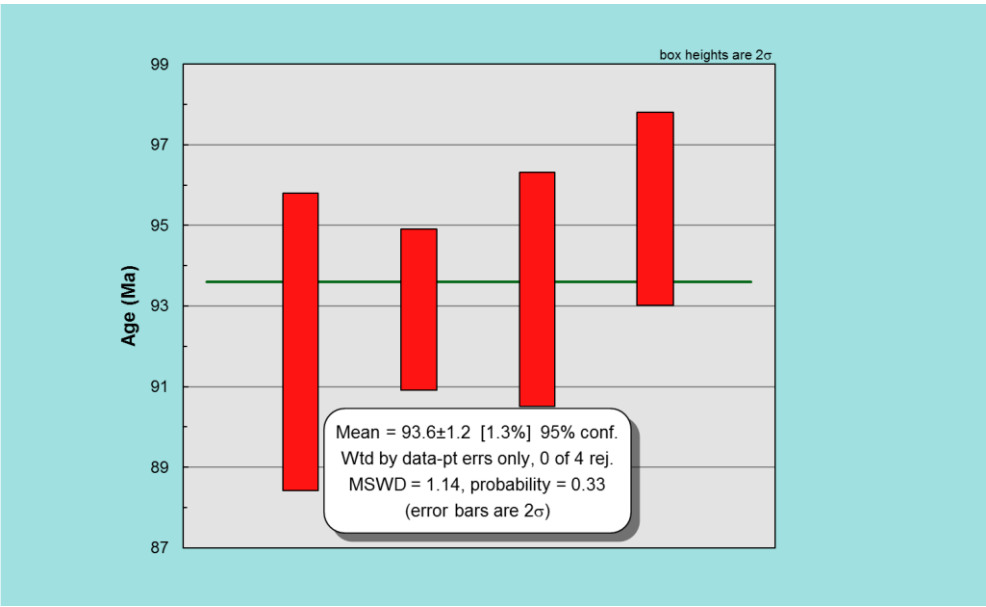


Figure 5.4. $^{206}Pb/^{238}U$ (weighted mean age) data for YD-1-18.

A total of thirty-five zircon analyses were performed, of which fifteen were discarded owing to poor analyses in OR-4-18. Colorless zircons in OR-4-18 are

euhedral to subhedral in shape, with elongate to stubby grains, colorless and transparent. Concentration zoning and oscillatory zonation are common. The U and Th concentrations range from 91.1 to 1192 ppm and 53.6–2140 ppm, respectively. The Th/U ratios of zircons in OR-4-18 range from 0.48 to 1.80 (mean = 0.98), indicative of originally having an igneous derivation. Figure 5.5 shows the U-Pb concordia diagrams for OR-4-18. The weighted mean $^{206}Pb/^{238}U$ age for OR-4-18 is 94.6 ± 1.2 Ma (2σ, MSWD = 4.5) (Figure 5.6).

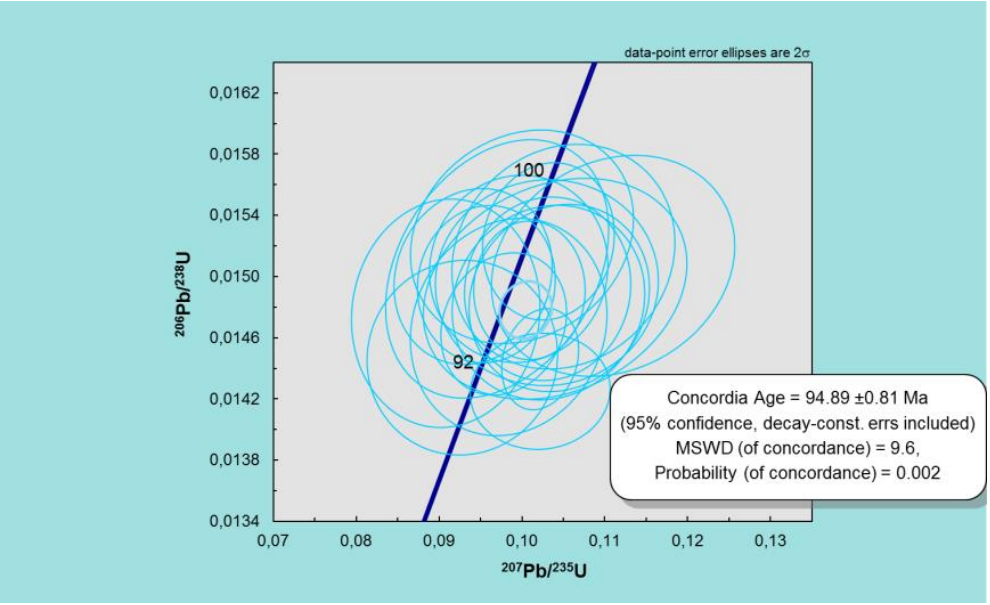


Figure 5.5. $^{206}Pb/^{238}U$ vs. $^{207}Pb/^{235}U$ diagram and concordia age for OR-4-18.

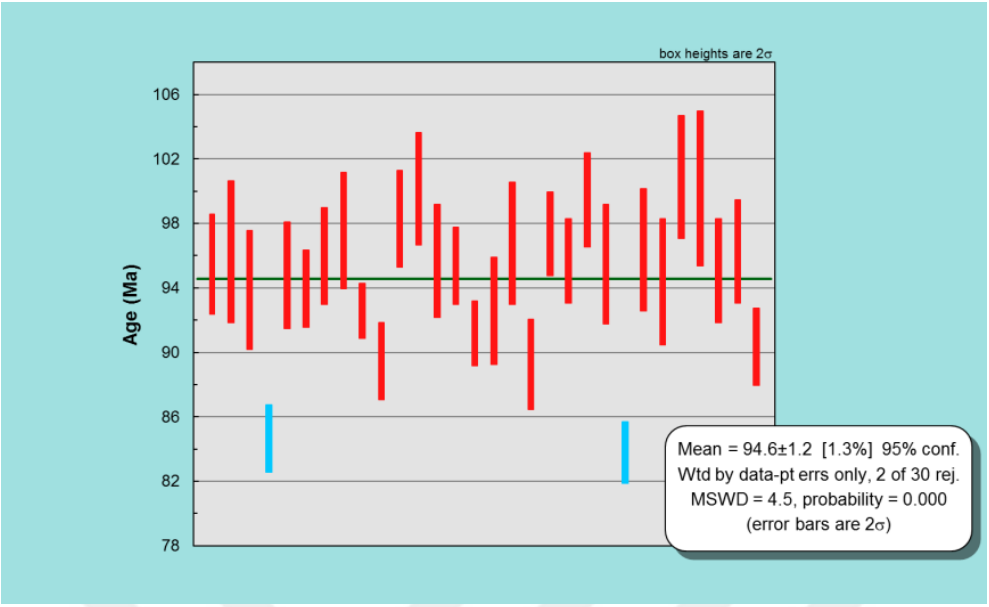


Figure 5.6. $^{206}Pb/^{238}U$ (weighted mean age) data for OR-4-18.

All of the thirty-eight zircon analyses were conducted in KR-5-18. Colorless zircons in KR-5-18 are euhedral to subhedral, with elongate to stubby grains. Concentration zoning and oscillatory zonation are common. The U and Th concentrations range from 59.5 to 2935 ppm and 23.2–7975 ppm, respectively. The Th/U ratios of zircons in KR-5-18 range from 0.39 to 2.94 (mean = 1.34), implying a magmatic origin. It should be emphasized that low-grade metamorphism and hydrothermal alteration may result in partial radiogenic Pb-loss within zircon grains leading to discordant data plotting below the concordia curve (Figure 5.7). The weighted mean $^{206}Pb/^{238}U$ age for KR-5-18 is 96.9 ± 1.3 Ma (2σ, MSWD = 4.5) (Figure 5.8).

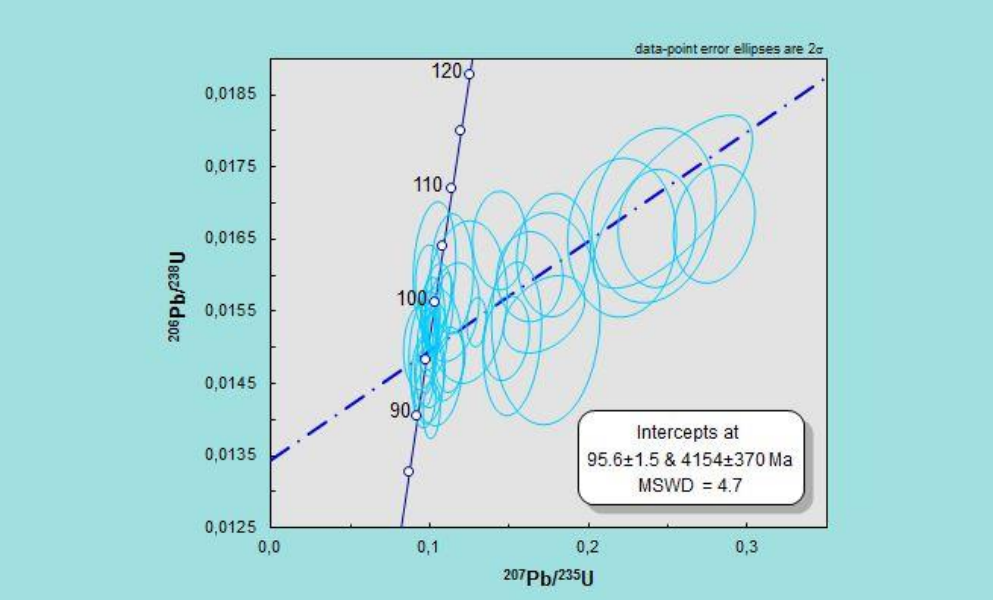


Figure 5.7. $^{206}Pb/^{238}U$ vs. $^{207}Pb/^{235}U$ diagram and lower intercept age for KR-5-18.

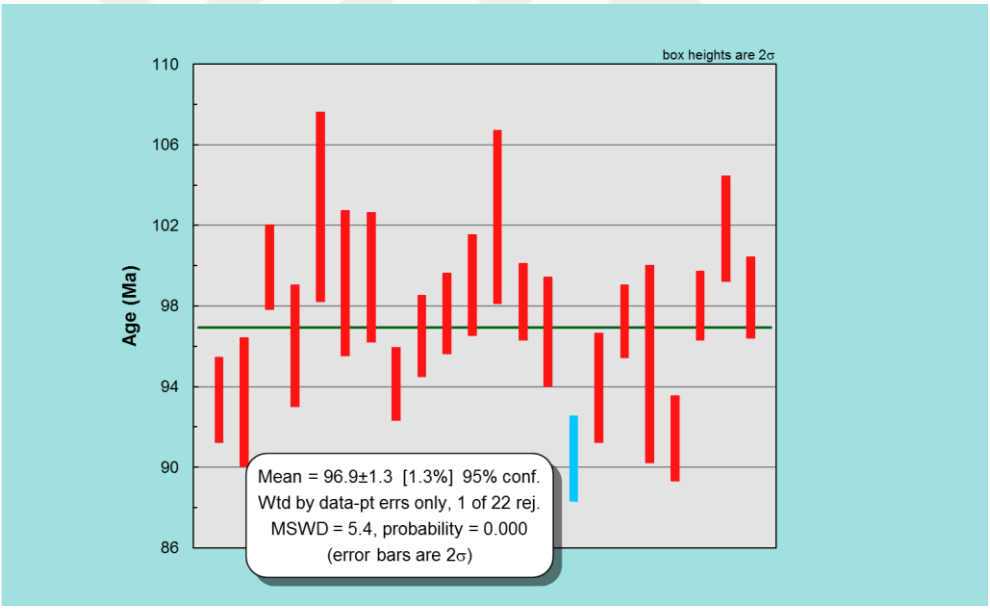


Figure 5.8. $^{206}Pb/^{238}U$ (weighted mean age) data for KR-5-18.

5.1.2 Meta-intermediate Lithologies

The findings of zircon grains analyzed from two meta-intermediate samples (AB-6-17, KR-13-17) within the KM are shown on concordia ($^{206}Pb/^{238}U$ vs $^{207}Pb/^{235}U$) diagrams (Figures 5.9, 5.10, 5.11). Two similar Late Cretaceous ages of 95.4 ± 0.8

Ma for AB-6-17 (concordia age), 95.8 ± 5.9 Ma for KR-13-17 (weighted mean age) were determined. The results are given in Appendices B and C provide comprehensive U-Pb data as well as the location of the laser ablation spots.

A total of thirty zircon analyses were performed, of which eleven were discarded owing to poor analyses in AB-6-17. Colorless zircons in AB-6-17 are euhedral to subhedral, with elongate to stubby grains. Concentration zoning and oscillatory zonation are common. The U and Th concentrations range from 86.4 to 1546 ppm and 56.2–2660.5 ppm, respectively. The Th/U ratios of zircons in AB-6-17 range from 0.65 to 1.72 (mean = 1.04), which are typical features of magmatic zircon. Figure 5.9 shows the U-Pb concordia diagrams for AB-6-17. The weighted mean $^{206}Pb/^{238}U$ age for AB-6-17 is 95.12 ± 0.8 Ma (2σ, MSWD = 1.5) (Figure 5.10).

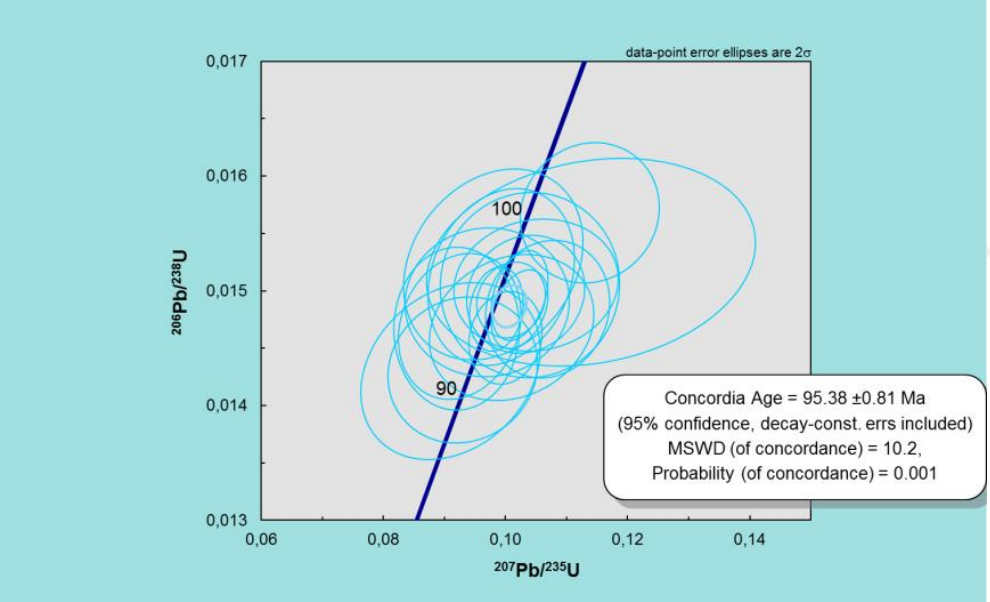


Figure 5.9. $^{206}Pb/^{238}U$ vs. $^{207}Pb/^{235}U$ diagram and concordia age for AB-6-17.

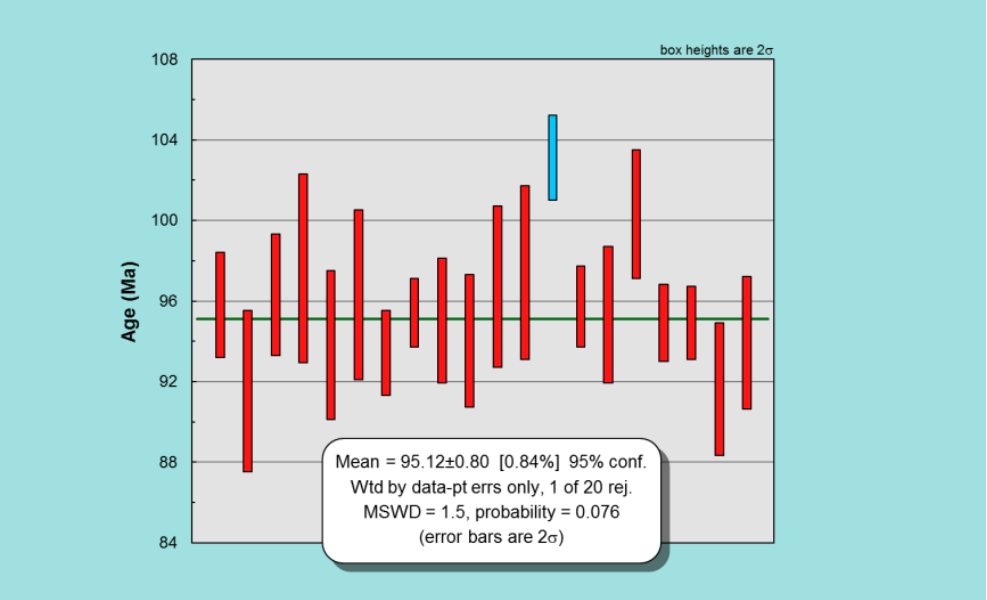


Figure 5.10. $^{206}Pb/^{238}U$ (weighted mean age) data for AB-6-17.

All of the seven zircon analyses were carried out in KR-13-17 sample. Colorless zircons in KR-13-17 are euhedral to subhedral, with elongate to stubby grains. concentration zoning and oscillatory zonation are common. The U and Th concentrations range from 47.9 to 2200 ppm and 22.3–964.4 ppm, respectively. The Th/U ratio of the analyzed zircons in KR-13-17 varies between 0.39 and 1.38 (mean = 0,87), consistent with a magmatic origin. The weighted mean $^{206}Pb/^{238}U$ age for KR-13-17 is 95.8 ± 5.9 Ma (2σ, MSWD = 9.8) (Figure 5.11).

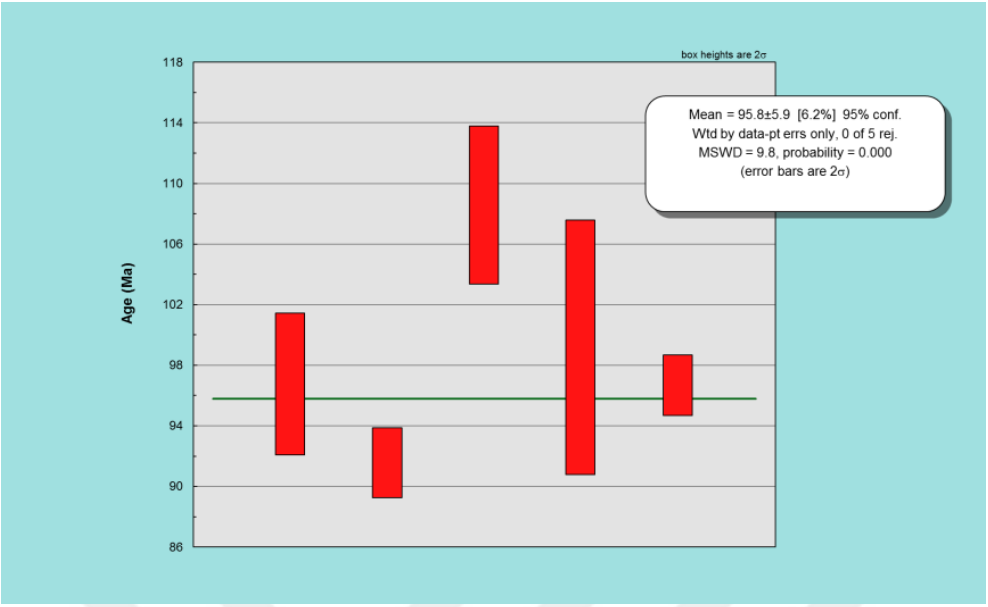


Figure 5.11. $^{206}Pb/^{238}U$ (weighted mean age) data for KR-13-17.

The age results for the meta-felsic and meta-intermediate samples within the KM indicate the crystallization age for the unit as early Late Cretaceous, ranging from 96.9 ± 1.3 Ma to 93.7 ± 1.2 Ma.

CHAPTER 6

DISCUSSION

This chapter gives a summary of all the provided data consisting of field and petrographic observations, as well as evaluations of analytical results obtained using whole-rock elemental and isotope geochemistry to make interpretations regarding the petrogenetic history of the KM. The geological, petrographical, and geochemical characteristics of the KM will be examined in this chapter to provide insights into their geodynamic evolution and relationship with the surrounding units. Furthermore, previous studies were also considered to reveal all of these features in more detail, and the KM were correlated with other Late Cretaceous arc basalts cropping out within the IAESZ. Combining this with the new findings presented here, it has been contributed to the studies on geodynamic evolution of the northern (IAE) branch of Neotethys Ocean.

6.1 Field Observations

The KM are represented by metavolcanic rocks, including meta-basics, meta-intermediates, and meta-felsics that have undergone low-grade metamorphism and varying degrees of mylonitic deformation. Meta-felsics are characterized by their white, greenish, and light brownish color in the field. Meta-intermediates are fine-grained and display greenish colors indicative of low-grade metamorphism. Meta-basic lithologies are represented by meta-basalts and meta-diabases. These lithologies are distinct by their dark color from meta-felsics and meta-intermediates. The most common lithologies of these volcanic rocks within the KM are meta-felsics and meta-andesites. The meta-basics are rarely found relative to other members. It is a robust observation that the Kösdağ meta-basics cross-cut the KM meta-dacites. The KM are steeply inclined due to the tectonism that affected

the region. The presence of dynamic metamorphism is the main difference between KM and other metamorphic units encountered in the region. In the study area, the members of the KM display cross-cut relationships. There is no systematic or geographic control on the distribution of the KM in the field. In addition to volcanic and subvolcanic members of the KM, volcaniclastic and sedimentary lithologies such as pelagic limestone, chert, and mudstone coexist with the volcanic-derived rocks. These sedimentary lithologies are interbedded within the metavolcanic rocks. An active splay of the North Anatolian Shear Zone (NASZ) constitutes the northern boundary of the KM. The presence of shear zones with highly mylonitized metavolcanic lithologies demonstrates the influence of faulting in the study area. On the other hand, the KM are stratigraphically overlain by the recrystallized limestones of the Dikmen Formation.

6.2 Petrographical Examinations

The KM are petrographically classified as meta-felsic lithologies (meta-dacites, meta-rhyolites), meta-intermediate lithologies (meta-andesites), and meta-basic lithologies (meta-basalts, meta-diabases) based on their texture and mineral composition. Porphyritic texture , is a typical feature of the KM. While quartz, K-feldspar, and plagioclase are the primary mineral phases of the meta-felsics, plagioclase and clinopyroxene constitute the primary mineral phases of meta-basics. Plagioclase is the main component of the meta-intermediates. Chlorite, epidote, sericite, and calcite are common secondary mineral phases in all lithologies. Actinolite is restricted only to meta-basics. On the basis of secondary mineral assemblages, such as calcite, chlorite and epidote, these lithologies have all been influenced by hydrothermal alteration and low-grade metamorphism. The assemblage including chlorite + albite + quartz + epidote + actinolite is produced from wairikite decomposition at low-P (<200 MPa) and pumpelleyite decomposition at higher P (<200 MPa). This assemblage represent typical greenschist facies mineralogy at about $320^0C \pm 30^0C$ (Bucher and Graphes, 2011). Opaques are observed in all members of the KM. On the other hand, apatite and zircon represent the most widespread accessory mineral phases in the meta-felsics

and meta-intermediates. Meta-felsics and meta-andesites typically show foliation, whereas meta-basics have both foliated and non-foliated varieties. Diabases commonly occur as dykes and cross-cut the meta-dacites in the field.

6.3 Geochemical Investigations

Variably metamorphosed 67 rock samples were investigated using various geochemical diagrams including harker, multi-element, binary and tectonomagmatic discrimination. The examined rock samples exhibit a broad range of primitive and evolved products, including basalt, andesite, and dacite, with SiO_2 contents between 44.95-84.66 wt.%. This significant range observed on SiO_2 is controlled by magmatic processes as evidenced by the linear trends in Zr vs. SiO_2 (Figure 4.9), reflecting relatively immobile behavior of the SiO_2 during secondary events. The studied rock samples display variable LOI values ranging from 0.9 to 10.4 weight wt.% suggesting the probable effect of post-magmatic processes such as hydrothermal alteration and low-grade metamorphism. This idea is supported by petrographic investigations, reflecting the secondary mineral assemblages such as calcite, chlorite and epidote.

Geochemically, KM is divided into two groups with subalkaline affinity as Type 1 and Type 2 based on trace elements that are thought to behave immobile. The presence of depletion in Zr-Hf in Type 2 samples appears to be a primary difference between the two types. Type 1 is characterized by slightly or no depletion in Zr, whereas Type 2 shows depletion in Zr with regard to Nd (ave. $[Nd/Zr]_N = 1.10$ for Type 1; ave. $[Nd/Zr]_N = 2.12$ for Type 2; where "N" denotes N-MORB normalized). On the basis of absolute Ce (ppm) abundances, Ce/Ti ratio, and the presence of negative Ti anomaly, Type 1 samples can be classified as Type 1a and Type 1b. Type 2 samples are relatively depleted compared to Type 1, but still enriched in terms of Th content when compared to N-MORB. Type 2 samples were subdivided into two main groups as Type 2a and Type 2b based on the Sm/Ti ratio. Type 2a samples have greater Sm/Ti relative to Type 2b samples. Type 2b differs from Type 2a with its more depleted, boninitic nature. Type 2b samples also

have geochemical features similar to boninitic rocks, such as high SiO_2 (51.59-59.22 wt.%) and MgO (8.40-11.81 wt.%) concentrations. Type 2b samples might be the fractionated products of boninitic-like melts.

Type 1 samples are highly enriched in LREE and show relatively fractionated HREE patterns, whereas Type 2 samples exhibit moderate enrichment in LREE. Furthermore, major oxide and trace element variation diagrams imply that olivine, pyroxene, plagioclase, and Fe-Ti oxides fractionation have played a crucial role in the magmatic evolution of the KM.

The KM display high Zr/Nb ratios (Zr/Nb ratio for Type 1 = 37.1-77.5; Zr/Nb ratio for Type 2 = 3.25-85.75), similar to that of N-MORBs, implying derivation from depleted sources. Based on their geochemical features (low Zr/Nb ratio, SiO_2: 51.59-59.22 wt.% and MgO: 8.40-11.81 wt.%), Type 2b samples may have been produced by hydrous melting of ultra-depleted harzburgites (Crawford et al., 1989). The low Zr/Y ratios of both types (1.11-6.89 and 0.6-2.44 for Type 1 and Type 2, respectively) also indicate that the KM mostly tapped depleted mantle source domains. However, Type 1 samples with lower Nb/Y ratios can be indicative of greater contributions from depleted mantle sources, while the samples with higher Nb/Y ratios can be linked to the addition of enriched mantle sources (N-MORB Nb/Y = 0.08, OIB Nb/Y = 1.65; Sun and McDonough, 1989). The low Nb/Y ratios of both types (0.02-0.19) further reinforce the results above, indicating the dominant involvement of a depleted source for the KM.

Negative anomalies of Nb (and Ta) are diagnostic of magma chemistry controlled by residual rutile in subduction zones (Pearce and Peate, 1995). They are also a feature of magmas that have been contaminated by continental crust (Wilson, 1989). Continental rocks are highly differentiated, and so the continental crust is enriched in incompatible elements compared to the upper mantle (e.g., Rudnick, 1995). For example, high Th content is a typical feature of continental arcs (ave. Th content of Aeolian arc = 4.35). However, this case is not observed on the KM samples (ave. Th content of the KM = 1.35). Moreover, continental material with a low time-integrated Sm/Nd ratio (i.e. negative εNd values; DePaolo, 1988) does

not appear to have made an important contribution to the KM samples. The KM conversely show a significant contribution from the depleted mantle (positive ƐNd values from +2.9 to +6.5). Lastly, if the contamination was present, a positive correlation between fractionation index (SiO_2, MgO, Ni, and Co) and ƐNd would be expected; however, there is no clear trend suggesting the investigated rock samples have not experienced any significant crustal contamination (Figure 6.1).

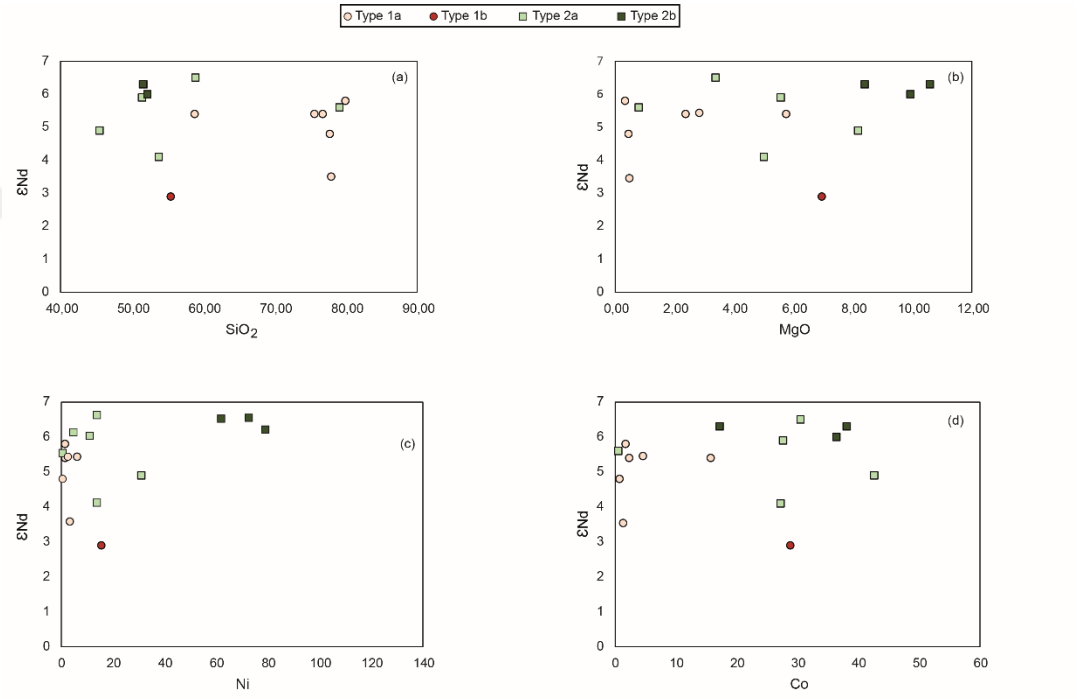


Figure 6.1. ƐNd value vs. major and trace elements as fractionation index.

6.3.1 Tectonomagmatic Discrimination of the Kösdağ Metavolcanics

Using tectonomagmatic discrimination diagrams is a popular method to understand the tectonic settings of igneous-derived lithologies. However, these diagrams involve only a few elements, somewhat limiting the extent of petrogenetic information that can be extracted. Thus, multielement variation diagrams (Figure 4.3) were primarily preferred here, on which the relationships between many elements can be examined together.

As mentioned before, the KM exhibit pronounced negative Nb anomalies, suggesting the existence of a mantle source metasomatized by subduction-derived

fluids/melts. Due to the lack of this signature in mid-ocean ridge and within-plate (OIB) environments, these tectonic environments cannot be possible candidates for the origin of KM. While subduction-related features are common in subduction zones, they have also been documented in continental rift environments (e.g. the Rio Grande Rift), though in a lesser amount (Gibson et al., 1993). However, even if the negative Nb anomalies can be observed in the rift settings, the level of enrichment is higher in rift environments than that of KM (Figure 6.2). Th_N (N-MORB normalized) values of the volcanics from the Rio Grande Rift vary between 20 and 800, whereas Nb_N values change between 3 and 40. On the other hand, Th_N values of the representative KM samples range from 2 to 20, while Nb_N changes between 0.2 and 1. Therefore, it does not seem likely that the KM were generated in a rift environment.

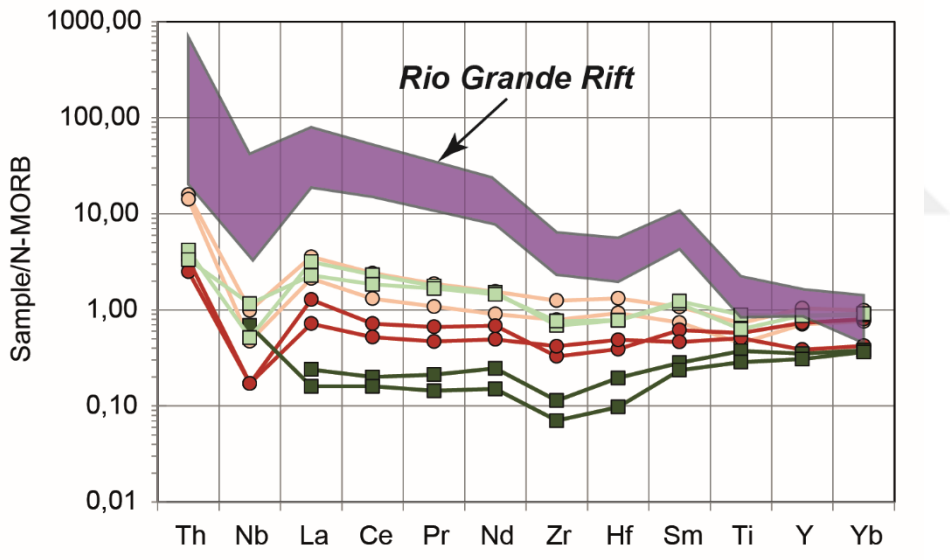


Figure 6.2. N-MORB multi-element variation diagrams with a comparison between the Kösdağ Metavolcanics and Rio Grande Rift. Flank and shoulder samples were used for Rio Grande Rift from Gibson et al. (1993).

Rather, an arc setting appears to be the most suitable tectonic setting for the petrogenesis of the KM, which is confirmed by a variety of parameters. First, the saw-teeth pattern on the spidergram could indicate an arc-like tectonic environment (Figure 4.3). Arc-related volcanics are characterized by low HFSE abundances compared to LILE and LREE (Stolz et al., 1996), suggesting that their mantle sources have been modified during subduction. Both Type 1 and Type 2 samples

display relative Th and La enrichment, indicating their arc-related affinity. This idea is supported by the Th/Yb-Nb/Yb diagram (after Pearce and Peate, 1995) where all the Kösdağ samples plot within the fields characterized by arc volcanics (Figure 4.14). In addition, tectonomagmatic diagrams also support the idea that the KM are arc-related. In the Th-Nb plot of Saccani (2015) (Figure 6.3), the samples fall in the subduction-related settings, including fore-arc, intraarc, back-arc, continental margin volcanic arc & polygenetic crust island arc. The trace element evidence suggests that the KM have been generated above a subduction zone.

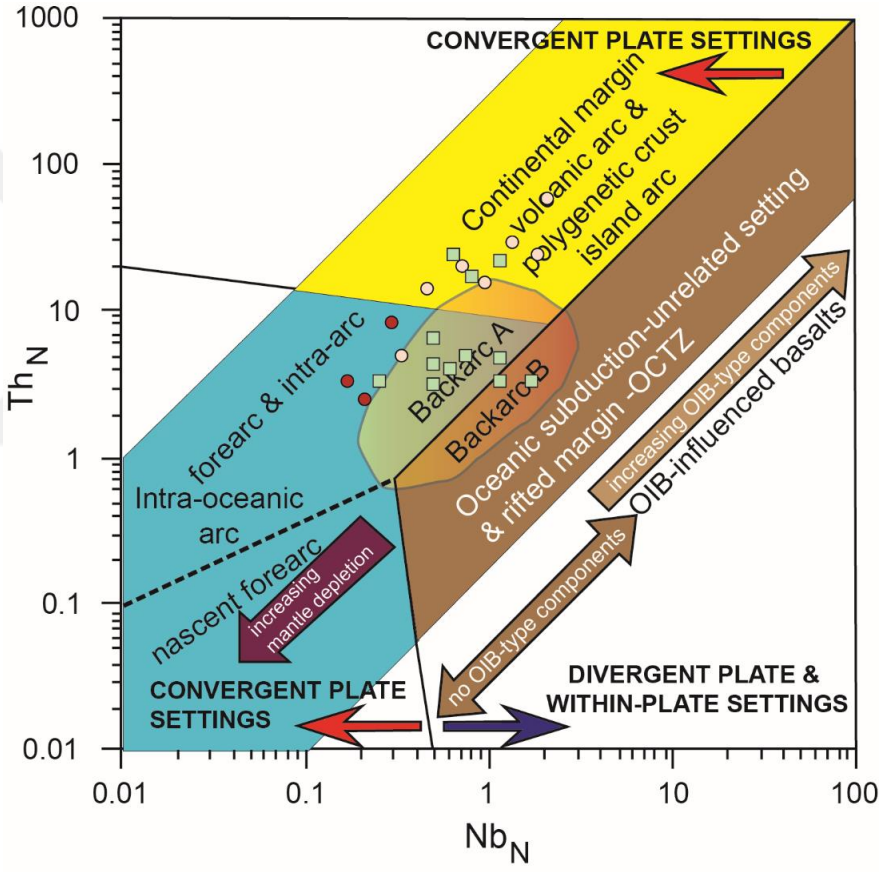


Figure 6.3. Tectonomagmatic discrimination of the Kösdağ Metavolcanics (Saccani, 2015).

It must be noted, however, that subduction processes may be continental or oceanic depending on the nature of the overriding lithosphere (e.g., Stern, 2010). The general mechanism is the same in both continental and oceanic arc environments. However, with the involvement of continental crust/lithosphere providing incompatible element enrichment, continental arcs can be distinguished from

oceanic ones. The amount of enrichment in LILE and HFSE is higher in continental arcs than in oceanic arcs. Compared to oceanic arcs, continental ones have higher Ta, Nb, Zr, and Hf values, which may be due to the contribution of continental crust and/or subcontinental lithospheric mantle (SCLM) (e.g., Pearce, 1983; Wilson, 1989). In order to gather more information regarding the tectonic affinity of the Kösdağ magmatism, the investigated rock samples were compared with those from the modern continental (Aeolian, Andes) and oceanic (Greater Antilles, Lesser Antilles, Mariana, South Sandwich, Vanuatu) arc settings (Figure 6.4). This correlation also supports the relationship between KM and arc settings. The samples with $SiO_2 \leq 65.00$ wt.% were taken into consideration to avoid the effect of fractional crystallization (Figure 6.4).

The Aeolian and Andes arcs display negative Nb anomalies similar to the Kösdağ samples. However, these continental arcs have higher Th concentrations relative to the Kösdağ samples, which may imply the role of the continental lithosphere in the Aeolian and Andes. Although the general pattern of the Aeolian and Andes arcs shows resemblance to the Kösdağ samples, the Aeolian and Andes are characterized by a higher level of enrichment. Also, the concentrations of incompatible elements (e.g. Th, Nb, La, Ce and Nd) in the Aeolian arc are even higher than the evolved products of the KM. Moreover, the KM include boninitic varieties with highly depleted concentrations of Zr, Hf, and Sm, which are not found in the continental arc system. Therefore, based on these geochemical characteristics, a continental arc origin seems not likely for the KM.

Oceanic arcs have low Nb/Yb ratios (ave. Greater Antilles Nb/Yb = 0.97: Jolly et al., 1998; Jolly, 2001; ave. Lesser Antilles Nb/Yb = 1.91: Turner et al., 1996; ave. Mariana Nb/Yb = 1.28: Pearce et al., 2005; ave. Vanuatu Nb/Yb = 0.90: Peate et al., 1997; ave. South Sandwich Nb/Yb=0.97: Pearce et al., 1995) (Figure 4.14), while in the continental arcs, this ratio attains higher values (ave. Andes Nb/Yb = 3.2 (Winter, 2001); ave. Aeolian Nb/Yb = 4.52 Calanchi et al., 2002). The KM show low Nb/Yb ratios (ave. = 0.68), suggesting an oceanic arc affinity. The Zr/Nb ratio also supports this idea. High values of Zr/Nb are typical for oceanic arcs, which is due to their derivation primarily from the depleted mantle sources. In

contrast, the continental arcs show relatively lower values (ave. Greater Antilles Zr/Nb = 48.62: Jolly et al., 1998; Jolly, 2001; ave. Lesser Antilles Zr/Nb = 21.98: Turner et al., 1996; ave. Mariana Zr/Nb = 39.13: Pearce et al., 2005; ave. Vanuatu Zr/Nb=49.60: Peate et al., 1997; ave. South Sandwich Zr/Nb = 79.33: Pearce et al., 1995; ave. Andes Zr/Nb = 30.8: Winter, 2001; ave. Aeolian Zr/Nb = 8.81: Calanchi et al., 2002) (Figure 4.10). The Kösdağ samples have an average Zr/Nb value of 40.5, implying an oceanic arc origin rather than a continental arc.

The similarity of the KM to the modern ocean arcs is also reinforced by the multi-element patterns. However, some differences exist, which can be mainly attributed to the nature of the mantle wedge underlying the arcs. The KM display a relatively wider spectrum than the South Sandwich arc. While Type 1a and Type 2a samples are relatively more enriched than the South Sandwich, the Type 2b samples are apparently more depleted (except for Nb). Type 1b samples, however, are akin to the South Sandwich in terms of multi-element systematics. The KM also share similarities with the Lesser and Greater Antilles, particularly in terms of Type 1a and 2a samples. The Vanuatu arc shows a wider level of enrichment relative to the Lesser and Greater Antilles, and except for Type 2b, it reflects similar characteristics to the KM. Thus, it is clear that the KM reflect multi-element systematics akin to the modern oceanic arcs, thus further supporting its oceanic affinity.

The geological observations presented here are consistent with the results obtained from geochemistry. The volcanics and volcaniclastics are observed to alternate with chert, mudstone, and pelagic limestone. Accordingly, it can be inferred that the KM was formed in a relatively deep marine environment in which cherts and pelagic limestones deposited. Besides, no continent-derived sediment was observed within the KM. In conclusion, both geological and geochemical evidence suggests melt generation from a metasomatized, heterogeneous mantle source in an intra-oceanic arc rather than a continental arc.

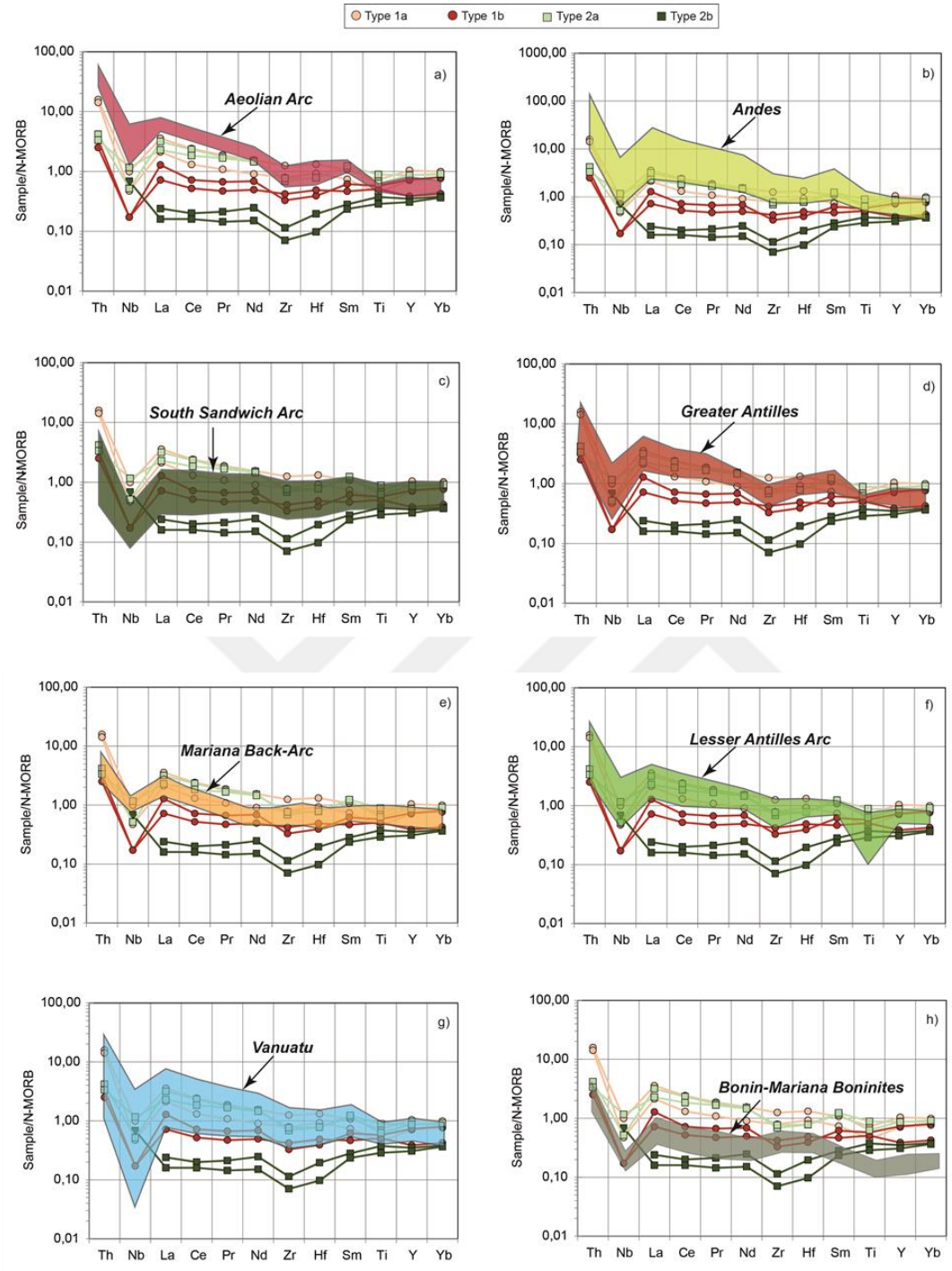


Figure 6.4. N-MORB multi-element variation diagrams showing a comparison between the Kösdağ Metavolcanics and modern continental and intra-oceanic arc environments. Aeolian from Calanchi et al. (2002); Andes from Winter, (2001); South Sandwich from Pearce et al. (1995); Greater Antilles from Jolly et al., (1998); Jolly, (2001); Mariana from Pearce et al. (2005); Lesser Antilles from Turner et al. (1996); Vanuatu from Peate et al. (1997); Bonin Mariana Boninites from Pearce et al. (1992).

Continental arcs also differ from oceanic arcs in terms of their isotopic characteristics, which can be attributed to the involvement of the continental lithosphere. In general, intra-oceanic arc settings display positive $\varepsilon_{Nd,}$ whereas continental arcs are characterized negative ε_{Nd} values (Figure 6.5). Isotope ratios of samples from the Aeolian continental arc range from 0.51257 to 0.51284, which correspond to ε_{Nd} values between – 1.52 and + 3.88 (Calanchi et al., 2002). $^{143}Nd/^{144}Nd$ ratios range from 0.512968 to 0.513140, ε_{Nd} values vary between + 5.48 and + 9.79 (Pearce et al., 1995). Although not common, negative ε_{Nd} values were also reported in some intra-oceanic arcs such as Lesser Antilles and Vanuatu, and have been ascribed to the sediment addition (Peate et al., 1997; Turner et al., 1996). On $^{143}Nd/^{144}Nd$ vs. $^{87}Sr/^{86}Sr$ plot, samples possess low $^{143}Nd/^{144}Nd$ and high $^{87}Sr/^{86}Sr$ fall within the field of local sediments (Turner et al., 1996). It is apparent from Figure 6.5 that the KM display positive ε_{Nd} values similar to that of oceanic arcs (Mariana, South Sandwich, Lesser Antilles, Greater Antilles, Vanuatu) rather than continental arcs (e.g. Andes and Aeolian).

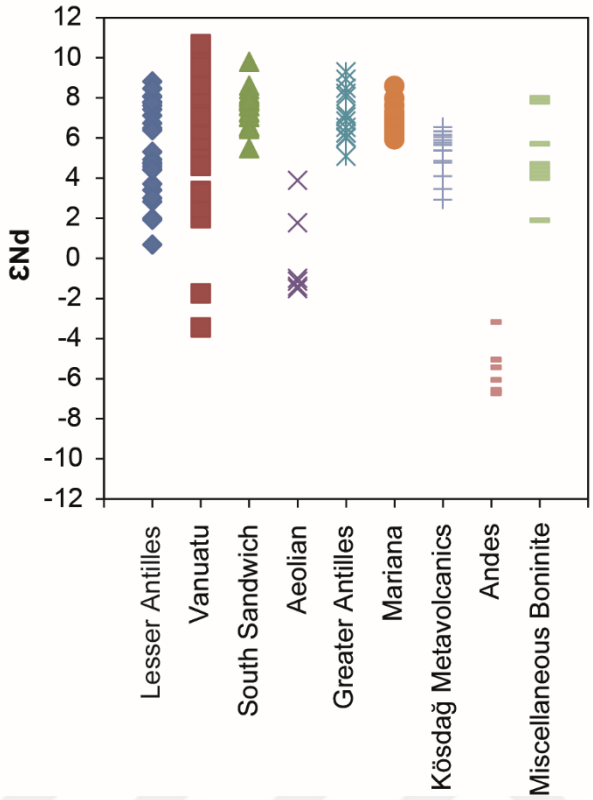


Figure 6.5. Radiogenic isotope data for Misc. Boninite from Cameron et al. (1983); South Sandwich from Pearce et al. (1995); Lesser Antilles from Turner et al. (1996); Vanuatu from Peate et al. (1997); Aeolian from Calanchi et al. (2002); Mariana from Pearce et al. (1997); Aeolian from Calanchi et al. (2002); Mariana from Pearce et al. (2005); Greater Antilles from Jolly et al. (2008).

6.3.2 Magma Generation At Convergent Margins

On the basis of geological and geochemical evidence, it can be inferred that the KM formed in an oceanic arc environment. The origin of arc magmas have been the focus of lengthy and ongoing discussions for decades. Compared to other oceanic magmas generated at ridges or within oceanic plates, arc magmas may require a more complex mixture of seawater, altered oceanic crust, and depleted mangle wedge (Wilson, 1989).

Seawater is the primary source accounting for most of the H_2O content in arc magmas. It is contained in pore spaces of seafloor sediment and it is integrated into the oceanic crust during metamorphism, then subducted with the oceanic crust. Altered oceanic crust consists of basalt, gabbro, and sediments including clays,

carbonates, and chert (Wilson, 1989). Subducted oceanic crust could be melted at depth, or the oceanic crust on which the arc volcano is built could melt as magmas pass through it. The cold crust is heated by the mantle during subduction and possibly also by heat generation at the surface of the slab. The depleted mantle wedge above the subducted slab consists of two components. One of them is the lithosphere of the mantle, which has 40-70 km thickness (Wilson, 1989). Since MORB melts have already been extracted, it is depleted in some components. Such depleted rocks are unlikely to melt readily. The other component is the asthenospheric mantle, consisting of lherzolites likely to be more fertile compared to those in the lithosphere. These lithologies can melt if they interact with fluids released by the subducting slab.

It must be noted that the geochemistry of arc-related magmas depends on both the mantle composition and the characteristics of the subduction components derived from the subducted slab (Langmuir et al., 2006; Pearce and Peate, 1995; Pearce and Stern, 2006). Numerous isotope and trace element measurements of oceanic basalts indicate that the Earth's mantle is heterogeneous (e.g., Allègre, 1982; Gast et al., 1964; Hart et al., 1973; Hedge, 1966; Hofmann, 1997; Stracke et al., 2005; Tatsumoto, 1966; Tatsumoto et al., 1965; White, 1985; White and Schilling, 1978; Zindler and Hart, 1986). Therefore, in the following sections, the mantle wedge composition of the KM will be explored, with a particular emphasis on subduction components.

6.3.2.1 Subduction-derived components

The enrichment of LILE and LREE compared to HFSE, combined with negative Nb anomalies on the KM imply that the mantle source of these lithologies might have been variably experienced by metasomatic agents enriched in LILE and LREE.

Subduction-related components include subducted sediments and sediment-derived melts or hydrous fluids. Subduction-derived fluids and melts modify the mantle source region at various scales based on their physical features. In the following

section, the processes and nature of the metasomatizing agents most likely derived from subducting slab, which contribute to the petrogenetic evolution of the KM, will be evaluated.

6.3.2.1.1 Slab-derived fluids

It is well known that LILE and LREE appear to be mobile relative to HFSE and HREE in hydrous melts (Brenan et al. 1995; Tatsumi et al., 1986). Thus, slab-derived hydrous melts become enriched in fluid-mobile elements such as Rb, K, Ba, Sr, and U, but have low concentrations of HFSE and Th due to their low solubility in hydrous melts (e.g., Elliott, 2003; Spandler and Pirard, 2013; Weaver, 1991). For this reason, a mantle enriched by slab-derived agents is represented by high U content, high Rb/Sr ratios, moderately Sm/Nd ratios, and depletion in HFSE (Hawkesworth et al., 1997). Due to their low solubility in hydrous fluids, the addition of significant quantities of HFSE by a fluid phase is usually unexpected (Stolz et al., 1996). According to the preceding discussion, several geochemical features of the KM, such as depletion in Nb, high LILE/HFSE, and LILE/LREE can be accepted as definitive proof for the existence of slab-derived fluid metasomatism. In this regard, ratio-ratio diagrams such as Ba/La vs. Th/Yb can provide valuable insights into the involvement of hydrous fluids (Figure 6.6). In the plot, variations in melt- versus fluid-related enrichments in the source region can be observed (Figure 6.6). Most of the KM are positioned along the fluid-related enrichment line in this diagram with relatively high Ba/La ratios.

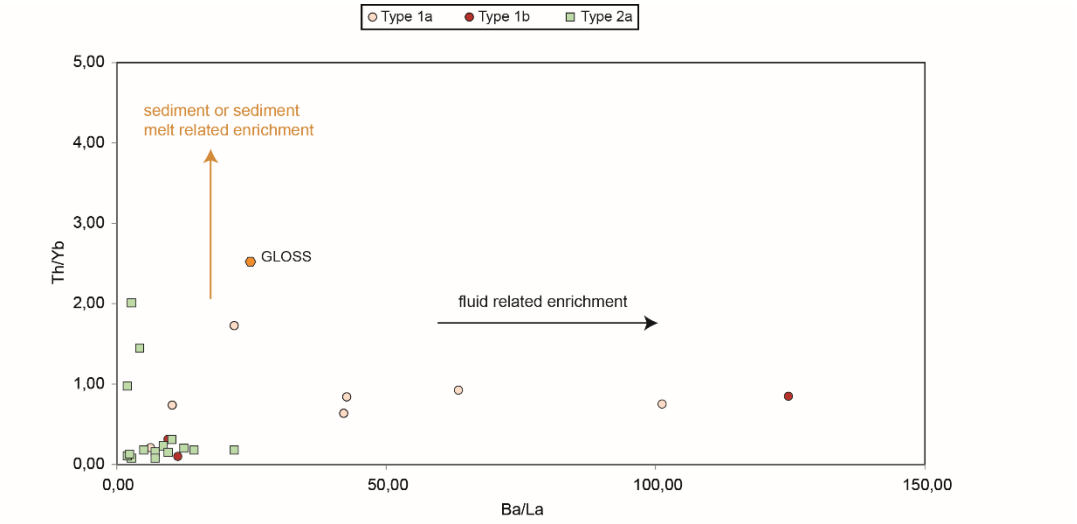


Figure 6.6. Ba/La vs. Th/Yb plot for the investigated Kösdağ Metavolcanics. High Ba/La ratios of the Kösdağ Metavolcanics can be attributed to fluid-related enrichment.

Type 1 samples generally plot toward high Ba/La ratios, indicating that fluid-related enrichment is dominant (Gill, 1981; McCulloch and Gamble, 1991). On the other hand, Type 2 samples show both sediment melt- and fluid-related enrichment, but the influence of sediment melt is more dominant. To sum up, the mantle source enrichment of the KM is controlled by subduction-related aqueous fluids and sediments, with variable concentrations of fluid-mobile elements (LILE and LREE) in the mantle source region rather than HFSE. It is significant that the compositions of slab-derived fluids vary considerably during the subduction process (Cao et al., 2017; Du et al., 2018, 2019; Moriguti et al., 2004; Walker et al., 2009). In this regard, the slab-derived fluid is highly aqueous beneath the forearc, becoming less aqueous with increasing depth.

H_2O-rich fluids play a significant role on the degree of mantle melting (Davies and Bickle, 1991; Langmuir et al., 2006; Stolper and Newman, 1994; Taylor and Martinez, 2003). The source of H_2O for arc magmas is hydrous minerals that are transported into Earth's interior by the subducting slab. Such minerals dehydrate and release their bound H_2O into overlying mantle wedge where melting initiates and continues as buoyant hydrous magmas rise and progressively hotter conditions are encountered (Grove et al., 2012). Therefore, the varying degrees of partial

melting observed in Type 1 and Type 2 may have resulted from the variable effects of water derived from the subduction events.

6.3.2.1.2 Sediment addition

Sea-floor sediments may be scraped off the subducting plate or accompany it into the mantle wedge at ocean trenches. Some of the subducted sediment may then be recycled to the arc crust by magmatism; the rest may be recycled into the mantle and contribute to the mantle heterogeneity (Plank and Langmuir, 1993). As stated before, LREE and Th are considered to be less mobile in aqueous fluids relative to the LILE. Therefore, their abundances in the source region are assumed to be derived from either by bulk addition of the sediments or by melt (Leat et al., 2000). Therefore, Th/Yb can be used as an indicator of sediment addition to the magma source (Handley et al., 2007). The KM are represented by high and variable Th/Yb (0.07-2.01) ratios, which can be explained by the sediment addition to the mantle source. Hence, it can be proposed that sediment addition has played a significant role in the petrogenesis of the KM.

The composition of subducted sediment packages can differ greatly from arc to arc (Plank and Langmuir, 1998). In an arc magma source, the abundance of subduction-mobile elements, such as Ba, Th and La, are strongly affected by even a small amount of sediment. On the other hand, the presence of some mineral phases in the subducting slab strongly fractionate HFSE and HREE (rutile, garnet; Class et al., 2000; Elliott et al., 1997). Accordingly, Nb and Yb are retained in the slab, whereas Th, La, and LILE leave the slab, thus regarded as subduction mobile (Pearce and Stern, 2006). The difference in elemental concentrations between mantle and sediment decreases towards the right of the spidergram, and so the relative effect of the sediment on the budget of these elements in the arc magma source considerably reduces. A reasonable selection of trace elements can give valuable information regarding the arc-related magmatism.

As mentioned before, Zr-Hf depletion is observed in some KM samples. If the sediments from the modern arc environments are examined, it is observed that

sediments from Tonga, Sunda, Mariana, and Kurile arcs have Zr-Hf depletion, others (Vanuatu, Kamchatka, Aleutian, and South Sandwich) have no depletion (Figure 6.7). This feature appears to be related to the composition of the sediments rather than the absence or presence of sediment addition during the evolution of the investigated rocks (Plank and Langmuir, 1998). In brief, it can be deduced that Zr-Hf depletion can be attributed to sediment composition.

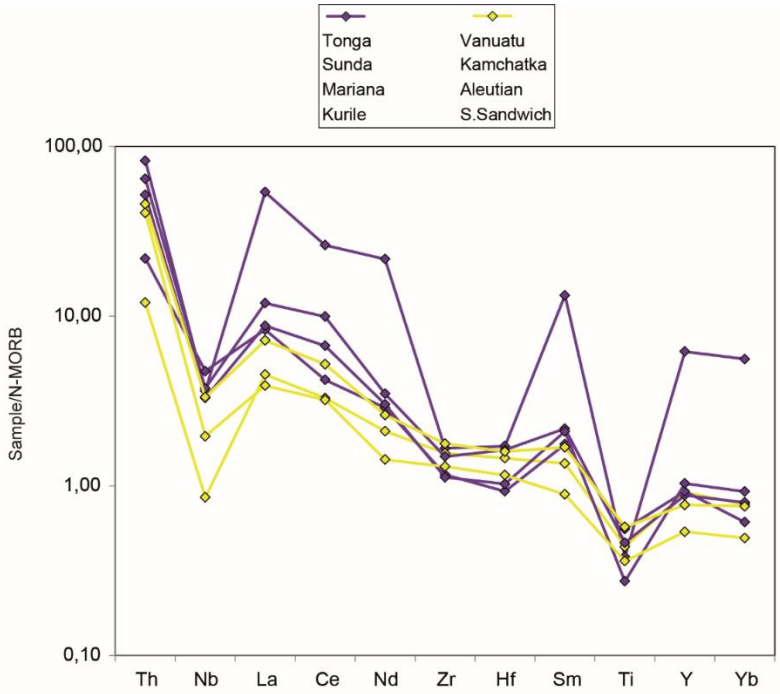


Figure 6.7. Multi-element variation patterns of the sediment samples from modern arcs. (Normalization values for N-MORB from Sun and McDonough (1989), trench samples taken from Plank and Langmuir, 1998).

Slab-derived fluids and sediment melts are two primary elements originating from the slab and contribute to the overlying mantle wedge where they contribute to the generation of subduction zone magmas (e.g., Elliott et al., 1997; Gill, 1981; Hawkesworth et al., 1993; Plank and Langmuir, 1998). In some cases, the influence of sediment melt dominates over slab-derived fluids, while in others, the reverse is valid (e.g. Woodhead et al., 2001). This variability modifies the mantle wedge, which is the primary source for arc magmas. Thus, at this point, it is important to reveal which slab-derived component could have been more influential for the genesis of KM, slab-derived fluids or sediments/sediment melts? To address this

question, some binary plots, including Ba/Yb vs. Nb/Yb and Ba/Nb vs. Th/Nb were used to find out the dominant component (Figure 6.8).

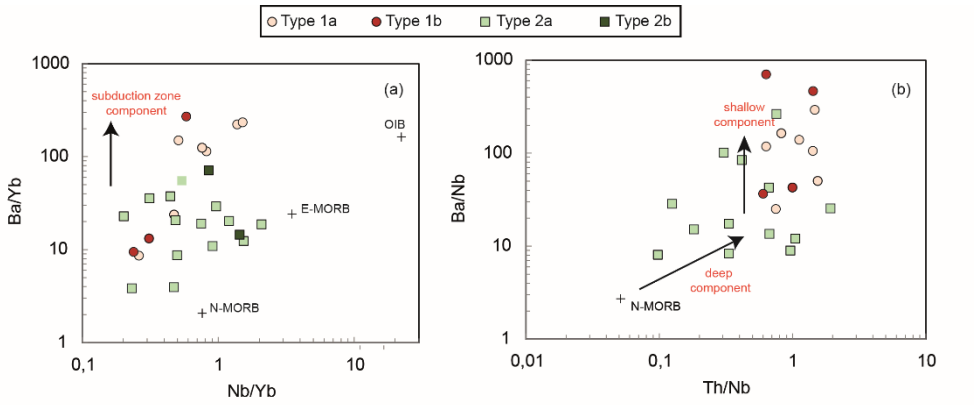


Figure 6.8. Ba/Yb-Nb/Yb and Ba/Nb-Th/Nb plots (based on Pearce et al. 2005), implying the effects of subduction zone components on the KM. It can also be noticed in the diagram that DMM is a probable mantle endmember for the origin of KM. Average N-MORB, E-MORB and OIB are from Sun and McDonough, (1989).

Interpretation of trace element concentrations in slab-derived fluids is not easy due to the altered nature of the subduction-related magmas. As mentioned before, LILE (except Th) are considered fluid-mobile. For this reason, aqueous fluids released from subducting slab at low temperatures can transport LILE to the overlying mantle wedge (e.g., Pearce and Peate, 1995; Pearce and Stern, 2006). Subduction-mobile elements (e.g., LILE, LREE, Th, U, Pb), on the other hand, reflect the influence of sediment melt (or bulk sediment) formed at high temperatures (e.g., Elliot et al., 1997; Pearce and Stern, 2006; Woodhead et al., 2001). Since Ba, Th, and Nb have similar partition coefficients during mantle melting and fractional crystallization processes, their elemental ratios can be used to infer the source composition (Pearce and Stern, 2006; Pearce et al., 2005). Furthermore, Ba, but not Th, is considerably mobile in aqueous fluids released from the subducted slab, while both Ba and Th can be considered mobile in siliceous melts (Keppler, 1996; Johnson and Plank, 1999). On the other hand, Nb behaves relatively immobile in slab melts at high temperatures (Ayers and Watson, 1993; Brenan et al., 1994; Ryerson and Watson, 1987). Accordingly, while Ba/Th ratios can be used as a

proxy for the shallow subduction component associated with aqueous fluids generated at low temperatures, Th/Nb ratios depict a deep subduction component associated with sediment-derived melt (or bulk sediment) generated at high temperatures. Therefore, Ba/Nb is a suitable proxy for the total addition of subduction components. It should be noted that both Nb and Yb are subduction immobile. Thus, Nb/Yb ratio is used here as a robust proxy for mantle fertility and degree of partial melting (e.g., Gribble et al., 1998; Pearce, 1983; Pearce and Parkinson, 1993).

The Kösdağ samples have higher Ba/Yb ratios than average N-MORB (Figure 6.8a). This may indicate variable influence of subduction component. Ba/Nb vs. Th/Nb diagram shows that samples of subduction zone are moved to significantly higher Th/Nb and Ba/Nb than N-MORB (Figure 6.8b). This suggests the involvement of deep subduction component during the genesis of those samples. Furthermore, this plot also demonstrates the effect of shallow subduction component. This idea is also supported by the Th/Nb vs. Nb/Sm diagram (Figure 6.9), in which the KM samples show a well-defined trend towards the sediment compositions characterized by global subducting sediment (GLOSS; Plank and Langmuir, 1998) and the sediment melt (Hochstaedter et al., 2001). Since Th values of Type 2b samples remain below the detection limit, those samples could not be plotted on this diagram.

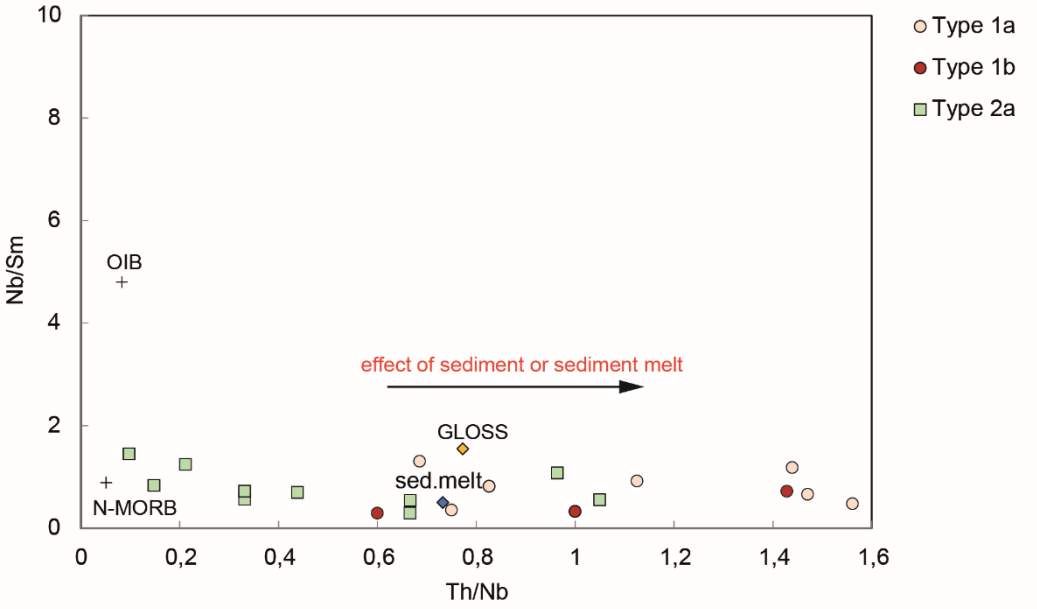


Figure 6.9. Nb/Sm vs. Th/Nb plot, displaying that enriched (plume-related) component shown by OIB-type samples has no effect on the KM. Conversely, the Kösdağ samples seem to include considerable sediment component, as shown by relatively high Th/Nb ratios. GLOSS from Plank and Langmuir, (1998). Sediment melt from Hochstaedter et al. (2001). N-MORB from Sun and McDonough, (1989).

6.4 Mantle Wedge Modeling

In order to reveal the contribution of subduction materials in the petrogenesis of KM, a mantle wedge modeling was performed, including subduction-mobile elements Th and La. The results of the modeling are shown in Figures 6.10, 6.11, 6.12, 6.13. In the modeling, it is assumed that the mantle wedge has first been modified by the addition of sediment-derived melts and then modified further by the addition of AOC fluid. The observed Th and La concentrations of the KM match the results of 10%–25% melting of the modified mantle wedge source (F = 0.1-0.25) (Figures 6.10, 6.11). The melt models based on REE and Lu/Hf vs. Nb/Yb, using the same end-members, mineral compositions, and degrees of partial melting and mixing, also show good agreement with the results of wedge modeling. As seen in Figure 4.15, the REE patterns of the calculated values and measured data for the KM fit consistently, indicating assumptions outlined above are quite plausible.

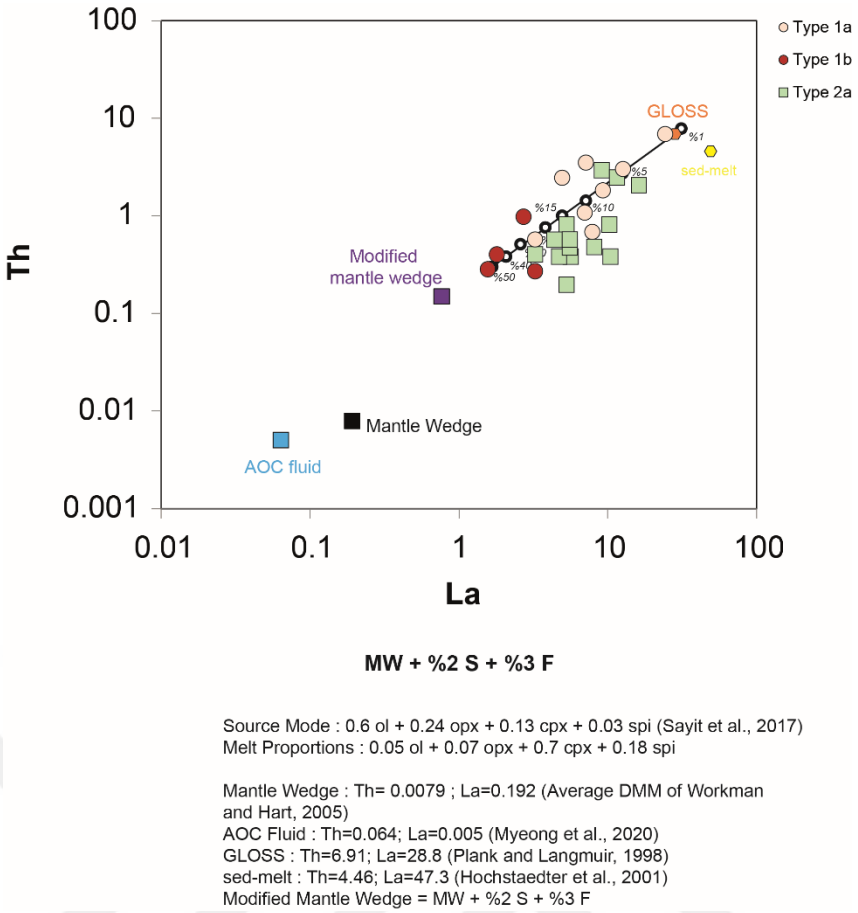


Figure 6.10. Mantle wedge modeling based on Th and La concentrations (MW + %2 S + %3 F).

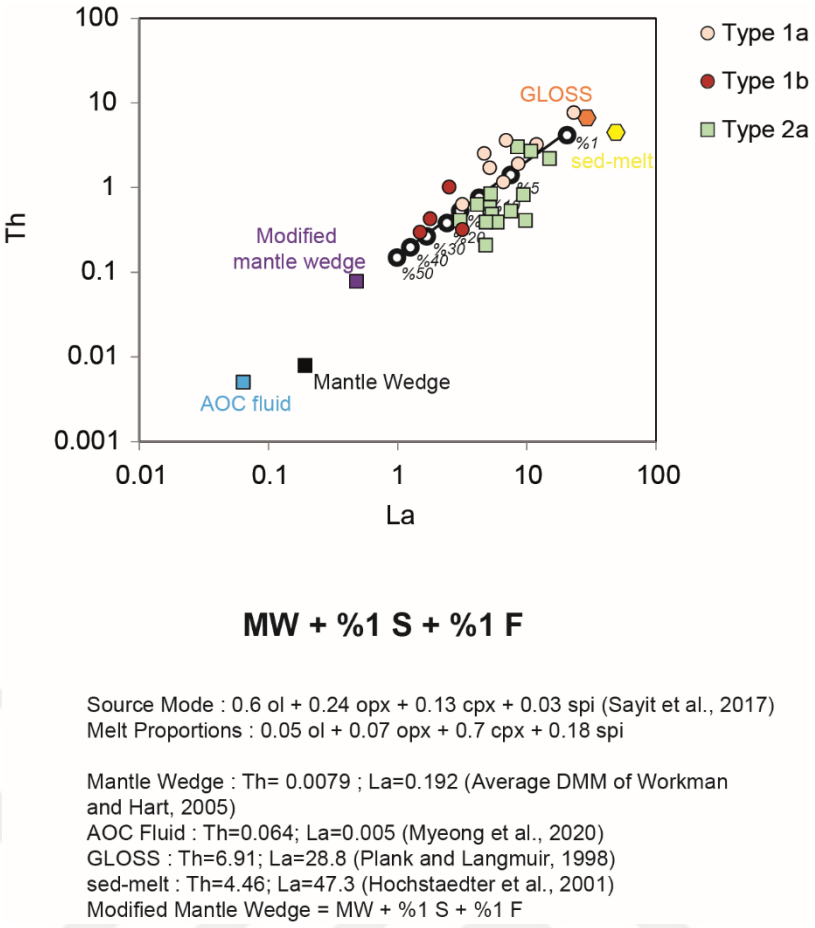


Figure 6.11. Mantle wedge modeling based on Th and La concentrations (MW + %1 S + %1 F).

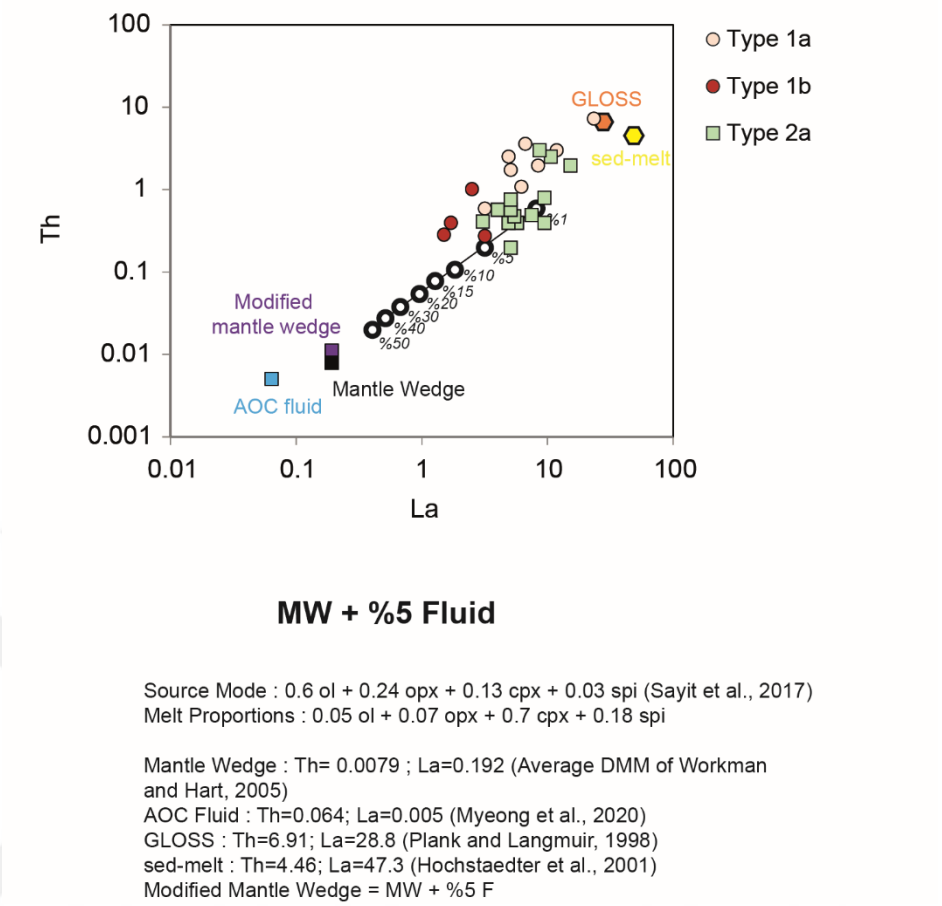
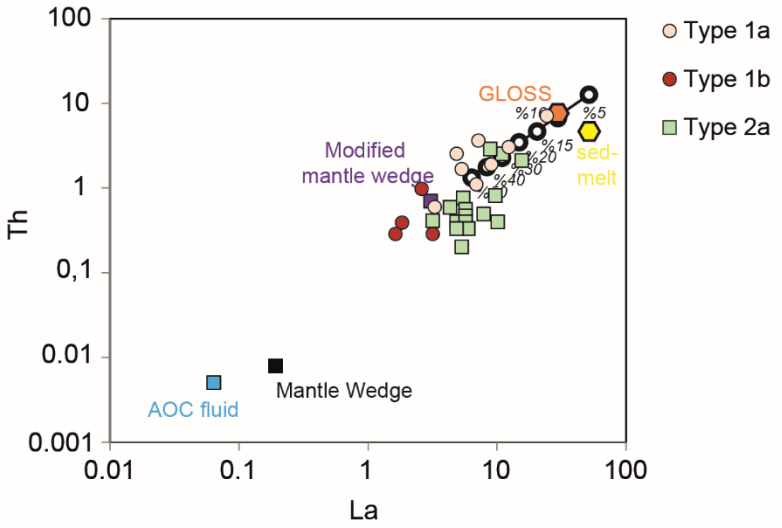


Figure 6.12. Mantle wedge modeling based on Th and La concentrations (MW + %5 F).



MW + %10 Sediment

Source Mode : 0.6 ol + 0.24 opx + 0.13 cpx + 0.03 spi (Sayit et al., 2017)
Melt Proportions : 0.05 ol + 0.07 opx + 0.7 cpx + 0.18 spi

Mantle Wedge : Th= 0.0079 ; La=0.192 (Average DMM of Workman and Hart, 2005)
AOC Fluid : Th=0.064; La=0.005 (Myeong et al., 2020)
GLOSS : Th=6.91; La=28.8 (Plank and Langmuir, 1998)
sed-melt : Th=4.46; La=47.3 (Hochstaedter et al., 2001)
Modified Mantle Wedge = MW + %10 GLOSS

Figure 6.13. Mantle wedge modeling based on Th and La concentrations (MW + %10 S).

The modeling plots suggest that the source region appears to be a three-component mixture including sediment, altered oceanic crust, and mantle wedge. The modelling of MW + %2 S + %3 F and MW + %1 S + %1 F are able to reproduce the observed values for the KM. On the other hand, MW + %5 F and MW + %10 S seem unrealistic for generating KM due to very high degrees of partial melting.

6.5 Age of the Kösdağ Metavolcanics

There has been no consensus on the age of the KM in previous studies. Hakyemez et al. (1986) proposed a deposition throughout the Malm-Neocomian based on fossil data from the Yaylacık Formation, which is equivalent to the Dikmen Formation. On the basis of regional correlation, Yılmaz and Tüysüz (1988)

suggested Liassic or pre Liassic age for the unit. Berber et al. (2014) assigned a Lower-Middle Jurassic age to the volcanism. The first reliable geochronological evidence (Aygül et al., 2015) revealed that the KM formed in the Late Cretaceous (93.8 ± 1.9 and 94.4 ± 1.9 Ma), which was also supported by 94.64 ± 0.77 Ma and 113.2 ± 2.3 Ma U-Pb zircon ages of Berber et al. (2021). Both geochemical groups (Type 1 and Type 2) were aged in this thesis study. These obtained ages ranging from 96.9 ± 1.3 Ma to 93.7 ± 1.2 Ma support the previous geochronological ages provided by Aygül et al. (2015) and Berber et al. (2021).

6.6 Geodynamic Implications

While there is a consensus on the presence of the IAE Ocean, the age and process of its opening (whether it began as a back-arc rift or involved a mantle-plume) are hotly debated. Some authors (Görür et al., 1983, 1984; Moix et al., 2008; Rojay, 2013; Rojay et al., 2001a,b, 2004; Şengör, 1979; Şengör and Yılmaz, 1981) suggest that it opened during the Early Jurassic, whereas the others (Balcı and Sayit, 2020; Göncüoğlu et al., 2003, 2010; Sayit et al., 2015, 2017; Tekin and Göncüoğlu, 2007, 2009; Tekin et al., 2002, 2016) believe that its opening occurred during the Late Triassic or earlier. Concerning the evolution of the IAESZ, studies indicate that its mélange complexes were produced during the closure of IAE Ocean in the Late Cretaceous (e.g., Göncüoğlu et al., 2010). The mélange complexes are made up of numerous slide-blocks, including radiolarian cherts and/or pelagic limestones in association with pillow lavas. The ophiolitic mélange representing the IAESZ contains several subduction-related fragments. On the other hand, few partially preserved oceanic arc sequences, such as volcaniclastics, lava flows, and associated marine sediments, are also contained within the IAESZ. These oceanic arc sequences are unique tectonic slices which are not part of the IAESZ. One of these sequences is the KM.

Late Cretaceous magmatism is widespread in the Central Pontides (Aygül et al., 2015; Berber et al., 2014, 2021; Sayit et al., 2022; Tüysüz, 1990; Tüysüz et al., 1995). The KM is considered to be one of the products of this magmatism. The

trace element systematics, characterized by relative enrichment in Th and La coupled with N-MORB-like HFSE abundances, indicate that the KM were produced above an intra-oceanic subduction zone (Figure 6.14). High Zr/Nb, low Zr/Y and Nb/Y ratios, positive ε_{Nd} values of the KM suggest that an oceanic arc origin is more appropriate than a continental arc for their genesis. The idea of oceanic arc is also in accordance with the previous studies on the KM as well as its equivalents in northern Turkey (Aygül et al., 2015; Berber et al., 2014, 2021; Sayit et al., 2022; Tüysüz, 1990; Tüysüz et al., 1995). In detail, geochemical characteristics of the KM is consistent with that of the Late Cretaceous Yaylaçayı Volcanics of Tüysüz et al. (1995) and Kösdağ Formation of Aygül et al. (2015) (Figure 6.14).

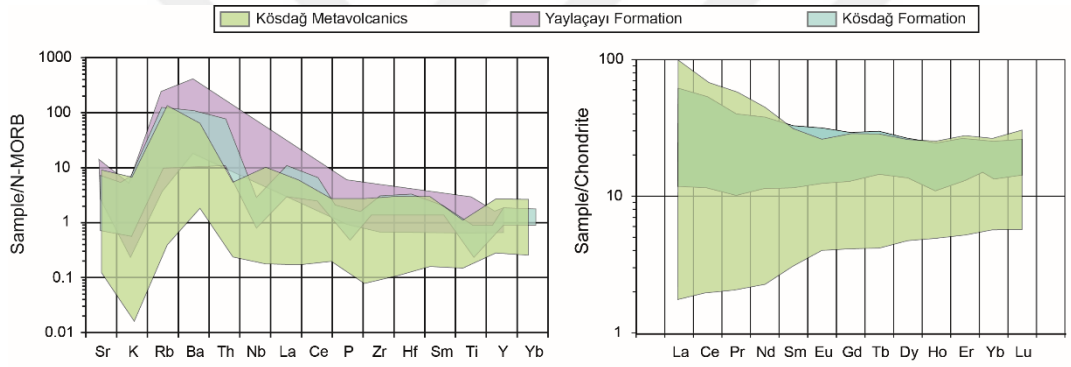


Figure 6.14. N-MORB normalized multi-element and Chondrite-normalized REE spidergrams of the Kösdağ Metavolcanics, Yaylaçayı Formation and Kösdağ Formation (normalization values for both N-MORB and Chondrite from Sun and McDonough, 1989). Yaylaçayı Formation data from Tüysüz et al. (1995); Kösdağ Formation data from Aygül et al. (2015).

Both KM and volcanics of the Kösdağ Formation exhibit relative enrichment in LREE compared to HREE, though the KM also show LREE-depleted characteristics as revealed by this study. Although the volcanic rocks of the Yaylaçayı unit were not examined on the REE diagrams owing to lack of REE analytical data in Tüysüz et al. (1995), their tectonomagmatic characteristics are somewhat similar. Tüysüz et al. (1995) proposed arc-related characteristics for the Yaylaçayı Formation. However, they also mentioned the existence of OIB-like signatures within the volcanics, which contrast with the arc-related signatures of the KM (Figure 6.14).

Recently, Sayıt et al. (2022) identified the Yerkuyu Unit around the Ilgaz district, which can be equivalent to the KM. The Yerkuyu Unit is characterized by a volcanic complex including an assemblage of basalt, basaltic andesite, and dacite flows cut by subordinate basaltic dykes (Sayit et al., 2022). The tectono-metamorphic evolution of the Kösdağ and Yerkuyu Units is distinct. While the KM are affected by low-grade metamorphism and ductile deformation, the Yerkuyu Unit does not reflect any metamorphic overprint associated with dynamic metamorphism (Sayit et al., 2022). Both the KM and Yerkuyu Unit have negative Nb anomalies and include HFSE-depleted members (Figure 6.15).

In the chondrite-normalized REE diagram both the KM and Yerkuyu Unit samples display relatively flat HREE patterns (Figure 6.15). Type 1a and Type 2a samples of the KM exhibit nearly flat REE patterns, whereas Type 1b and Type 2b samples have LREE-depleted REE patterns. On the other hand, while the primitive members of the Yerkuyu Unit show relatively flat REE patterns, the evolved members display LREE enrichment.

Both the KM and the Yerkuyu Unit samples are represented high Zr/Nb ratios (KM ave. Zr/Nb = 40.5; Zr/Nb for the Yerkuyu Unit = 17.34-35.3), implying that the DM is the main component. The multi-element systematics suggest that the volcanic rocks of the Yerkuyu Unit were formed in an oceanic arc similar to the KM. Unlike the KM, the age of the Yerkuyu Unit remains unclear. Sayit et al. (2022) stated that the Yerkuyu Unit is a probable equivalent of the KM based on geological observations and geochemical evidence. Thus, the age of the Yerkuyu Unit can also be Late Cretaceous.

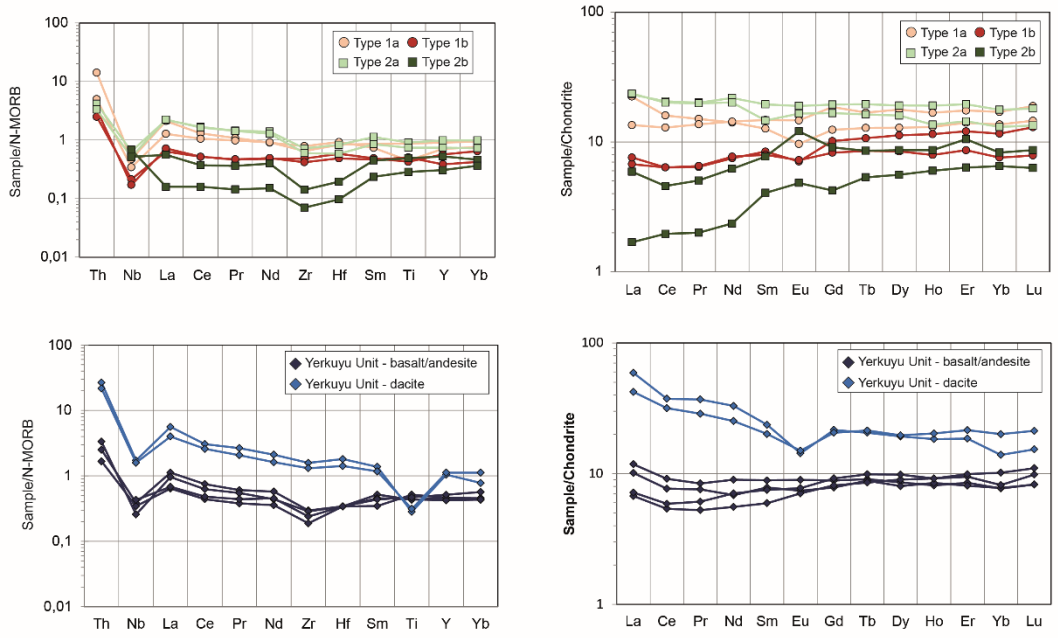


Figure 6.15. N-MORB normalized multi-element and Chondrite-normalized REE spidergrams of the Kösdağ Metavolcanics and Yerkuyu Unit (normalization values for both N-MORB and Chondrite from Sun and McDonough, 1989). Yerkuyu Unit data from Sayit et al. (2022).

The Tafano Unit is another product of the Late Cretaceous magmatism in the Central Pontides (Ellero et al., 2015b). It is composed of non-metamorphic volcanic rocks and a sedimentary sequence. The volcanic rocks are mostly basalts and basaltic andesites associated with a volcaniclastic formation composed of breccias and sandstones which is stratigraphically overlain by a Marly-calcareous turbidite formation. On the other hand, the KM is composed of meta-dacites, meta-andesites, and meta-basalts interbedded with pelagic limestone, mudstone, and chert. Like the KM, the Tafano volcanics are characterized by negative Nb anomalies (Figure 6.16). However, the KM samples are more depleted relative to the Tafano samples.

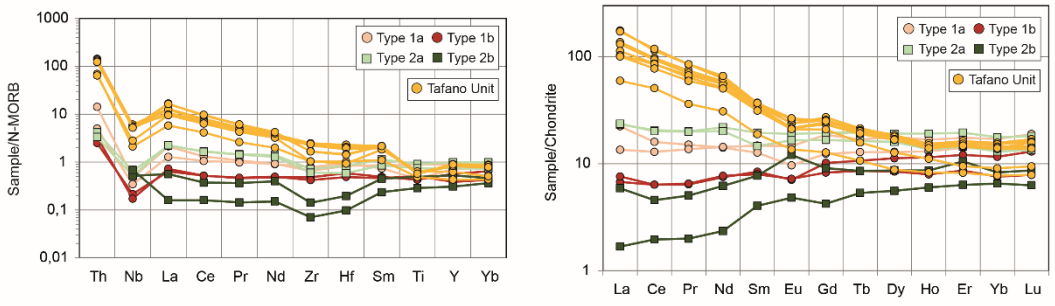


Figure 6.16. N-MORB normalized multi-element and Chondrite-normalized REE spidergrams of the Kösdağ Metavolcanics and Tafano Unit (normalization values for both N-MORB and Chondrite from Sun and McDonough, 1989). Tafano Unit data from Ellero et al. (2015b).

The KM and the Tafano Unit samples have somewhat flat HREE patterns in the chondrite-normalized REE diagram (Figure 6.16). However, the Type 1b and Type 2b samples of the KM have flat or depleted LREE patterns, whereas Type 1a and Type 2a samples are LREE-enriched. On the other hand, all of the Tafano Unit samples have LREE enrichment.

The KM samples show high Zr/Nb (ave. Zr/Nb = 40.5) and low Nb/Yb ratios (ave. Nb/Yb = 0.68), implying that the DM component may have played a significant role. On the other hand, the lower Zr/Nb (ave. Zr/Nb = 12.7) and higher Nb/Yb ratios (ave. Nb/Yb = 4.9) of the Tafano Unit samples suggest a lesser contribution from DM. This could imply that the petrogenesis of the Tafano Unit samples was dominated by the enriched components. Strong Nb anomalies and LILE enrichment relative to HFSE indicate that both the KM and Tafano Unit generated above a subduction zone. The Kösdağ samples have an average Zr/Nb value of 40.5, implying an oceanic arc origin rather than a continental arc, whereas the Tafano Unit have relatively enriched signatures (lower Zr/Nb, higher Nb/Yb ratios) which are typical characteristics of magmas generated at continental arc environment (Ellero et al., 2015b). The LA-ICP-MS zircon dating suggests that the crystallization age of the KM is early Late Cretaceous, ranging from 96.9 ± 1.3 Ma to 93.7 ± 1.2 Ma in this study. Ellero et al., (2015b) suggested a late Santonian to middle Campanian age for the Tafano Unit.

The Late Cretaceous subduction-related magmatism is also known in the southern branch of Neotethys (Akgül, 1993; Aktaş and Robertson, 1990; Asutay, 1988; Bingöl, 1982, 1988; Parlak, 2006; Parlak et al., 2004; Rızaoğlu et al., 2006, 2009; Ural et al., 2015; Yazgan, 1972; Yılmaz et al., 1993). One of the products of this magmatism is the Yüksekova Comlex. The Yüksekova Complex comprises an assemblage of slide blocks varying sizes and lithologies. The blocks are made up of red-green limestones, shales, greywackes, tuffs, agglomerates, basalts, diabases, gabbros, and serpentinites (Ural et al., 2015). All samples have negative Nb anomalies, with high Th/Nb ratios and La/Nb ratios. Therefore, the rock samples of the Yüksekova Complex are represented by relative enrichments in Th and La over HFSE and HREEs, suggesting their origin from a subduction modified source region (Figure 6.17). In the chondrite-normalized REE diagram, all samples have relatively flat patterns. On the other hand, all Yüksekova Complex samples display LREE enrichment (Figure 6.17). Their positive $\varepsilon_{Nd(i)}$ values (+ 6.4 and + 7.2) imply a depleted mantle source for their origin, whereas their slightly radiogenic Pb values reflect a sedimentary involvement to the source of the rocks (Ural et al., 2021). The U-Pb data provided by Ural et al. (2021) suggest an 80-88 Ma lifespan for the felsic and intermediate volcanic rocks of the Yüksekova Complex. The overall geochemical features imply that they were formed in an oceanic arc environment during the Late Cretaceous.

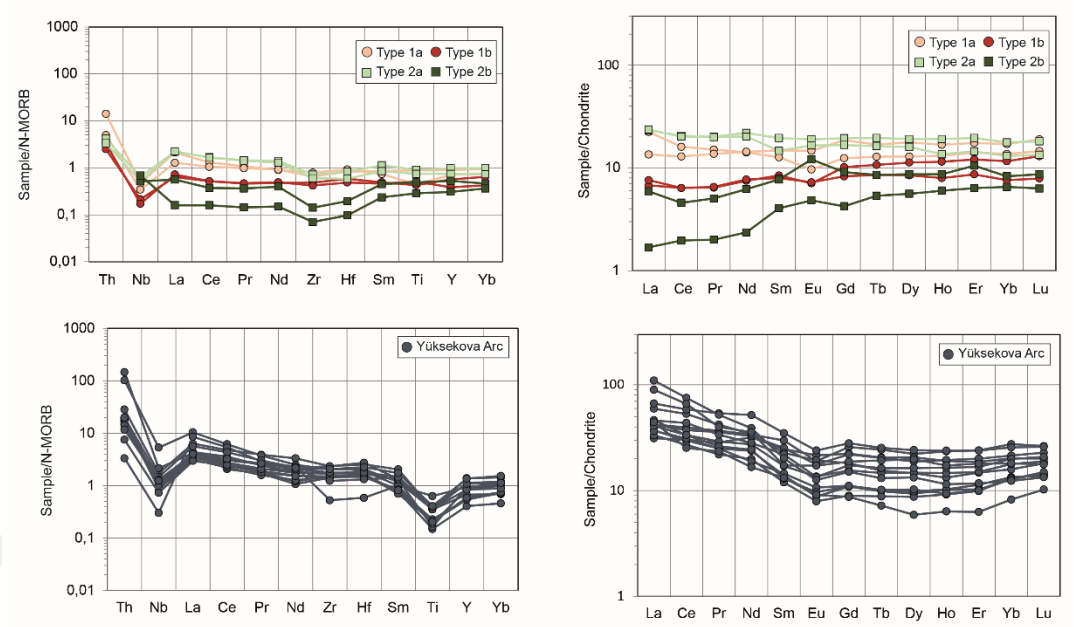


Figure 6.17. N-MORB normalized multi-element and Chondrite-normalized REE spidergrams of the Kösdağ Metavolcanics and Yüksekova Arc (normalization values for both N-MORB and Chondrite from Sun and McDonough, 1989). Yüksekova Arc data from Ural et al. (2021).

It is assumed that Eastern Pontides was a continental arc developed by subduction of northern Tethys oceanic plate towards Eurasian plate during the Mesozoic (Altherr et al., 2008; Okay and Şahintürk, 1997; Şengör and Yılmaz, 1981). Late Cretaceous volcanic rocks (92-72 Ma) in the region are represented mainly by calc-alkaline to high K calc-alkaline volcanics including the Çatak Formation, Kızılkaya Formation, Çağlayan Formation, Tirebolu Formation, and Cankurtaran Formation.

The Turonian Çatak Formation consisting of basaltic-andesitic volcanics interlayerd with sandstone and red-grey limestone, form the basement unit of the Upper Cretaceous volcano-sedimentary sequence in the Eastern Pontides (Güven, 1993; Kurt et al., 2006). The formation is overlain by the Kızılkaya Formation comprising pelagic carbonates interbedded with dacitic-rhyodacitic rocks and is Santonian in age. Both formations are conformably overlain by the Upper Santonian-Lower Campanian Çağlayan Formation (basaltic-andesitic volcanic rocks interlayered with tuffite, sandstone, claystone and micricit limestone) and the Campanian Tirebolu (or Çayırbağ) Formation (rhyolitic rocks interbedded with tuffite, sandstone, claystone and micritic limestone). The sequence ends with the

Cankurtaran Formation, which is mostly composed of calciclastic turbidites (Sofracıoğlu and Kandemir, 2013).

The mafic rocks of Çatak Formation and Çağlayan Formation are classified as subalkaline basalt, whereas the felsic samples of the Kızılkaya Formation and Tirebolu Formation plot in the andesite to dacite and rhyolite fields, respectively (Aydın et al., 2020). Enrichment of LILE and HFSE relative to the primitive mantle is observed in rock samples of all of these formations. All samples are characterized by negative Nb and Ta anomalies, typical of arc-type rocks. Asan et al. (2004) stated that the Hamsilos volcanics are mainly composed of basaltic lava flows, basalt dikes, brecciated volcaniclastics, agglomerates and tuffs. The Hamsilos volcanics exhibit high K calc-alkaline, shoshonitic and ultra-K characteristics. They are enriched in LILE and LREEs compared to HFSEs (Aydınçakır, 2016). The Kermutdere Formation is represented by a thick sedimentary sequence with interlayered felsic tuffs (Eyüboğlu et al., 2014). Felsic tuffs of the Kermutdere Formation have negative Nb, Ta, and Ti anomalies indicative of subduction-related magma (Gill, 1981). Their enrichment in LILE and LREE relative to HFSE and HREE, and strong Nb, Ta, and Ti anomalies are consistent with magmas generated above subduction zones. The felsic volcanic rocks of the Çayırbağ (or Tirebolu) Formation plot in the field of rhyolite on the TAS diagram (Eyüboğlu et al., 2014). They also plot in the field of typical arc volcanic rocks.

For all of these formations, the involvement of a subduction component in their petrogenesis is supported by the plot of Nb/Yb vs. Th/Yb (Pearce and Peate, 1995) (Figure 6.18). All of the samples plot above the MORB array, implying that variable subduction component have been added to their mantle sources. It should be noted that the Hamsilos Volcanics and Kızılkaya Formation show slightly higher Th/Yb values for a given Nb/Yb relative to others. This may mean that the contribution of the subduction component on the Hamsilos Volcanics has been greater, in general.

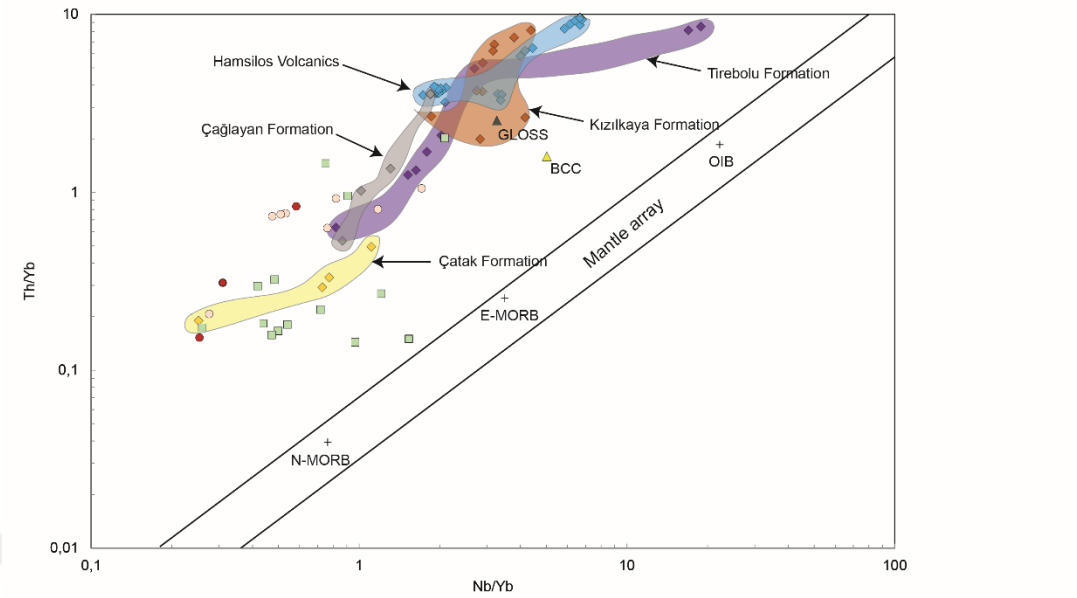


Figure 6.18. Th/Yb vs. Nb/Yb diagram (after Pearce and Peate, 1995). Average N-MORB, E-MORB and OIB values from Sun and McDonough (1989), BCC from Taylor and McLenan, (1985). Çağlayan Formation, Çatak Formation, Kızılkaya Formation, Tirebolu Formation from Aydın et al. (2020); Hamsilos Volcanics from Aydınçakır et al. (2016).

Berber et al. (2021) proposed a new geodynamic model to explain the formation of the KM (Figure 6.19). The IAE Ocean between the Tauride-Anatolide/Central Anatolian Units in the south and the SCT in the north was already shortening during the mid Cretaceous due to several subduction zones. During the Late Cretaceous, the northern subduction zone formed the Tafano continental arc (Ellero et al., 2015b) in the southern Central Pontides. Another subduction that produced Kösdağ island arc type volcanism (including the Yaylaçayı Volcanics of Tüysüz et al., 1995) most likely began earlier in the early Late Cretaceous. Further representatives of this arc, as well as fore-and-back-arc (SSZ) type oceanic lithosphere, may now be identified as large slideblocks within the Ankara Mélange and its extension to the east and west (e.g., Bortolotti et al., 2013, 2018; Göncüoğlu et al. 2010, 2015; Dangerfield et al., 2011). The final closure of the IAE Ocean in southern Central Pontides should have been later in the Early Eocene, as shown by youngest Middle Eocene overstep sequence spanning the key alpine tectonic units (Ottria et al., 2017). This study proposes that the KM is a remnant of an early Late Cretaceous intra-oceanic arc system.

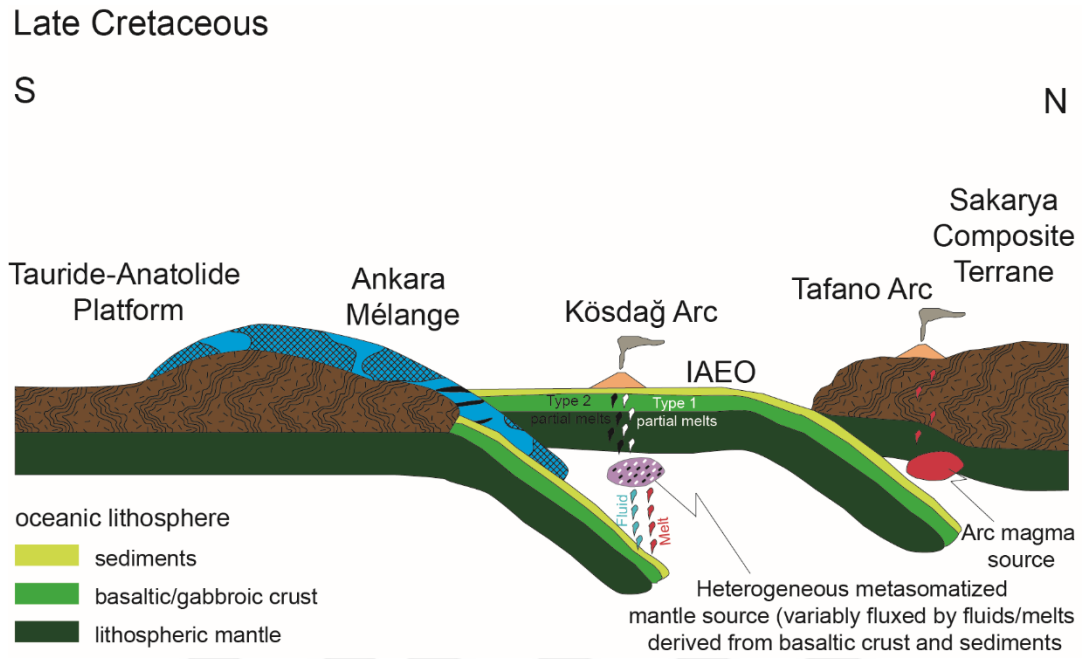


Figure 6.19. Simplified cartoon depicting the geodynamic scenario of the Kösdağ Metavolcanics (modified after Göncüoğlu, 2019; Yalınız et al., 1996).

Further east in the Alpine-Himalayan orogenic belt, remnants of Late Cretaceous intra-oceanic arcs have been identified. The Sabzevar region of NE Iran belongs to a belt of Neotethys-related HP/LT rocks that extend from Turkey to Tibet. The Sabzevar magmatic rocks have high LILEs and depletion in HFSEs, as well as Nd-Pb isotopic features, suggesting that the magmas were derived from a depleted MORB-type mantle influenced by subduction components. Several Sabzevar rocks (with the exception of OIB-type lavas) have greater Th/Yb ratios and plot away from the mantle array, making them similar to arc-related rocks. SSZ-type lavas exhibit positive ε_{Nd} values from + 5.4 to + 8.3 suggesting the presence of the depleted mantle source. Intra-oceanic subduction produced the SSZ-related magmas within the Sabzevar oceanic lithosphere, followed by the nucleation and development of a mature arc, as shown by thick granitic crust within the Sabzevar substratum (Moghadam et al., 2014).

Another Late Cretaceous arc setting example is the Kata-Rash arc fragment is located about Penjween, 100 km northeast of Sulymannia city of Iraq in the Kurdistan Region. The Kata-Rash arc fragment consists of massive volcanic rocks (Bolton, 1958), with alternation of limestone, phyllitic slates, and sandstone

(Smirnov and Nelidov, 1962). It is characterized by calc-alkaline andesite and basaltic-andesite, rhyodacite to rhyolite and intruded by granitic, granodioritic and dioritic dykes. The Kata-Rash samples exhibit typical arc-like signatures evidenced by Th/Yb vs. Nb/Yb diagram displaying that all Kata-Rash samples fall within the field of arc-related rocks above the MORB-OIB mantle array. The trace element patterns for the Kata-Rash samples demonstrate enrichment in LILEs and depletion in HFSEs, indicating subduction-related signature. SHRIMP zircon U-Pb dates for 108.1 ± 2.9 Ma (Harbar volcanic rocks) and 107.7 ± 1.9 Ma (Aulan intrusion) suggest an Albian age, which is regarded as the time of crystallization for the rocks. Ali et al. (2016) proposed that the Kata-Rash igneous rocks are interpreted as a part of the Late Cretaceous supra-subduction zone system that most likely generated within the Neotethys Ocean rather than a continental margin. Then, from the Late Cretaceous to the Paleocene, the arc was accreted to the northern boundary of the Arabian plate. On a greater scale, oceanic arc rocks of similar age may be found in the Himalayas and farther east in the Myanmar (Burma)-Assam area (Mitchell, 1993). This shows the presence of Cretaceous intra-oceanic subduction systems (>10.000 km) involved in consumption of the Neotethys Ocean (Ali et al., 2016).

CHAPTER 7

CONCLUSIONS

The KM is located between the IAESZ to the south and SCT to the north in the southern Central Pontides. The KM is represented by meta-felsic (meta-dacites, meta-rhyolites), meta-intermediate (meta-andesites) and meta-basic lithologies (meta-basalts, meta-diabases) interbedded with sedimentary lithologies as pelagic limestone, mudstone, and chert. All lithologies of the unit have been affected by hydrothermal and dynamic metamorphism. The KM is stratigraphically overlain by the carbonates of the Dikmen Formation.

Geochemically, there are two different chemical groups as Type 1 and Type 2 based on immobile trace element systematics. These groups are subdivided into two as Type 1a, Type 1b, Type 2a and Type 2b. The KM range from basalt to dacite with SiO_2 contents between 44.95-84.66 wt.%. This large variation can be attributed to fractional crystallization. The geochemistry of the investigated rock samples suggest subduction-related volcanism as indicated by enrichment in LILE coupled with depletion in HFSE. The high Zr/Nb, low Zr/Y, and Nb/Y ratios indicate that the KM have been derived from a depleted mantle source resembling N-MORB source. Type 2b samples might represent boninitic melts generated by hydrous melting of ultra-depleted harzburgites. This idea is supported by high SiO_2 (51.59-59.22 wt.%) and MgO (8.40-11.81 wt.%) concentrations of the Type 2b samples. The flat HREE patterns suggest the absence of garnet in the source region. According to melting models, KM have been derived from a spinel lherzolitic source.

The source region appears to be a three-component combination of sediment, altered oceanic crust, and mantle wedge. The KM may be produced by MW + %2 S + %3 F and MW + %1 S + %1 F based on the wedge modeling plots.

The ages of both geochemical groups were revealed by the geochronological investigations. Four meta-felsic samples yielded ages of, 96.9 ± 1.3 Ma, 94.89 ± 0.81 Ma, 94.7 ± 1.8 Ma, 93.7 ± 1.2 Ma, while two meta-intermediate samples provided ages of 95.8 ± 5.9 and 95.38 ± 0.81 Ma. Accordingly, geochronological findings suggest that the crystallization age for the KM is early Late Cretaceous ranging from 96.9 ± 1.3 Ma to 93.7 ± 1.2 Ma. Combined with geochemistry, these ages suggest that the KM reflects Cenomanian-Turonian oceanic arc magmatism within the IAE Ocean.

REFERENCES

Akgül, B., 1993. Petrographical and petrological features of magmatic rocks in the vicinity of Piran village (Keban-Elazığ) (PhD Thesis). Elazığ: Fırat University, Turkey, 1-125 (in Turkish with English abstract).

Akyürek, B., Akbaş, B., Hakyemez, Y., Yıldırım, H., Hepşen, N., Soysal, Y., and Dağer, Z. 1982. Ankara-Elmadağ-Kalecik dolayının jeolojisi. MTA Report, (7298).

Alan, İ., Balcı, V., Keskin, H., Altun, İ., Böke, N., Demirbağ, H., Arman, S., Elibol, H., Soyakıl, M., Kop, A., and Hanilçi, N. 2019. Tectonostratigraphic characteristics of the area between Çayeli (Rize) and İspir (Erzurum). Bulletin of the Mineral Research and Exploration, 158(158), 1-29.

Aldanmaz, E., Yaliniz, M.K., Guectekin, A., and Göncüoğlu, M.C. 2008. Geochemical characteristics of mafic lavas from the Neotethyan ophiolites in western Turkey: Implications for heterogeneous source contribution during variable stages of ocean crust generation. Geological Magazine, 145,1, 37-54.

Ali, S.A., Ismail, S.A., Nutman, A.P., Bennett, V.C., Jones, B.G., and Buckman, S. 2016. The intra-oceanic Cretaceous (~ 108 Ma) Kata–Rash arc fragment in the Kurdistan segment of Iraqi Zagros suture zone: Implications for Neotethys evolution and closure. Lithos, 260, 154-163.

Allègre, C.J. 1982.Chemical geodynamics Tectonophysics, 81, 109-132.

Altherr, R., Topuz, G., Marschall, H., Zack, T., and Ludwig, T. 2004. Evolution of a tourmaline-bearing lawsonite eclogite from the Elekdağ area (Central Pontides, N Turkey): Evidence for infiltration of slab-derived B-rich fluids during exhumation. Contributions to Mineralogy and Petrology, 148, 4, 409-425.

Asutay, H.J. 1988. Geology of the baskil (Elazığ) area and the petrology of baskil magmatics. Bulletin of the Mineral Research and Exploration, 107, 51-69.

Ayaroğlu, H. 1980. Tosya kuzeybatısının (Karadere) jeolojisi ve ekonomik olanakları. Jeoloji Mühendisliği, 10, 65-73, (In Turkish).

Aydin, F., Saka, S.O., Şen, C., Dokuz, A., Aiglsperger, T., Uysal, I., and Başer, R. 2020. Temporal, geochemical and geodynamic evolution of the Late Cretaceous subduction zone volcanism in the eastern Sakarya Zone, NE Turkey: Implications for mantle-crust interaction in an arc setting. Journal of Asian Earth Sciences, 192, 104217.

Aydın, M., Demir, O., Özçelik, Y., Terzioğlu, N., and Satır, M. 1995. Geological revision of İnebolu, Devrekani, Ağlı and Küre areas: New observations in Paleo-Tethys–Neo-Tethys sedimentary successions A. Erler, T. Ercan, E. Bingöl, S. Örçen (Eds.), Geology of the Black Sea Region, MTA/JMO, 33-38.

Aydın, M., Şahintürk, Ö., Serdar, H.S., Özçelik, Y., Akarsu, İ., Üngör, A., Çokuğraş, R., and Kasar, S. 1986. Ballıdağ-Çangaldağı (Kastamonu) arasındaki bölgenin jeolojisi, TJK Bülteni, 29, 1-16.

Aydınçakır, E. 2016. Subduction-related Late Cretaceous high-K volcanism in the Central Pontides orogenic belt: Constraints on geodynamic implications. Geodinamica Acta, 28(4), 379-411.

Ayers, J.C., and Watson, B. 1993. Rutile solubility and mobility in supercritical aqueous fluids. Contrib. Mineral. Petrol, 114, 321-330.

Aygül, M., and Oberhänsli, R. 2017. Tectonic stacking of HP/LT metamorphic rocks in accretionary wedges and the role of shallowing slab-mantle decoupling Tectonics, 36, https://doi.org/10.1002/2017TC004689

Aygül, M., Okay, A.I., Oberhansli, R., Schmidt, A., and Sudo, M. 2015. Late Cretaceous infant intra-oceanic arc volcanism, the Central Pontides, Turkey: Petrogenetic and tectonic implications. Journal of Asian Earth Sciences.

Aygül, M., Okay, A.I., Oberhänsli, R., and Sudo M. 2016. Pre-collisional accretionary growth of the southern Laurasian active margin, Central Pontides, Turkey Tectonophysics, 671, 218-234.

Aysal, N., Ustaömer, T., Öngen, S., Keskin, M., Köksal, S., Peytcheva, I., and Fanning, M. 2012. Origin of the Early-Middle Devonian magmatism in the Sakarya Zone, NW Turkey: geochronology, geochemistry and isotope systematics. Journal of Asian Earth Sciences, 45, 201-222.

Baier, J., Audétat, A., and Keppler, H. 2008. The origin of the negative niobium tantalum anomaly in subduction zone magmas. Earth and Planetary Science Letters, 267:1-2, 290-300.

Bard, J.P. 1986. Microtextures of igneous and metamorphic rocks (Vol. 1). Springer Science & Business Media.

Barka, A.A. 1992. The north Anatolian fault zone. Annales tectonicae. Vol, 6. 164-195.

Bedard, J.H. 1999. Petrogenesis of Boninites from the Betts Cove Ophiolite, Newfoundland, Canada: identification of subducted source components. J Petrol, 40,1853-1889.

Berber, F. 2015. Geology and petrology of the kösedağ metavolcanic rocks to the south of Tosya (Master's thesis).

Berber, F., Göncüoğlu, M.C., and Sayit, K. 2014. Geochemistry and Tectonic Significance of the Kösedağ Metavolcanic Rocks from the Sakarya Zone, Northern Turkey. In: Proceedings of 20th CBGA Congress, Abstract Book, vol.1, 161-163, Tirana, Albania.

Berber, F., Göncüoğlu, M.C., Sayit, K., and Crowley, Q. 2016. Geochemistry, Geochronology and Petrology of the Kösedağ Metavolcanic Rocks to the South of Tosya (Central Pontides) In: Proceedings 69th. Geological Congress of Turkey, 266-267.

Berber, F., Sayit, K., and Goncuoglu, M.C. 2021. Geochemistry and U-Pb ages from the Kosdag Metavolcanics in the southern Central Pontides (Turkey):

Complementary data for early Late Cretaceous island arc development in the Northern Neotethys. Turkish Journal of Earth Sciences, 30:1, 59-80.

Bingöl, A.F., 1982. Petrographic and petrological investigation of volcanic rocks between Elazığ-Pertek-Kovancılar. Fırat University, Journal of Science Faculty, 1, 9-21.

Bingöl, A.F., 1988. Petrographical and petrological features of intrusive rocks of Yüksekova Complex in the Elazığ region (eastern Taurus-Turkey). The Journal of Science and Engineering of Fırat University, 3:2, 1-17.

Bingöl, E., Akyürek, B., and Korkmazer, B. 1973. Biga Yarımadasının jeolojisi ve Karakaya Formasyonunun bazı özellikleri [Geology of the Biga Peninsula and some characteristics of the Karakaya Formation]. Cumhuriyetin 50. Yılı Yerbilimleri Kongresi, Tebliğer, MTA Enstitüsü [Congress on Earth Sciences for the 50th Anniversary of Republic of Turkey, Abstracts], p. 70–77 [in Turkish with English abstract].

Bizzarro, M., Simonetti, A., Stevenson, R.K., and David, J., 2002. Hf isotope evidence for a hidden mantle reservoir. Geology, 30, 771-774.

Blumental, M. 1939. Über den stand der geologischen aufnahmen im Ilgaz Dağ. Maden Tetkik Arama Genel Müdürlüğü Rapor No: 842, pp, 35. Ankara (unpublished).

Blumental, M. 1948. Bolu civarı ile Aşağı Kızılırmak arasındaki Kuzey Anadolu Silsilelerinin jeolojisi. Ankara MTA Yayınları. Seri B, No: 13, 71-119

Blumental, M. 1950. Orta ve Aşağı Yeşilırmak Bölgelerinin Jeolojisi, Ankara MTA Yayınları Seri: D, No:4.

Bolton, C.M.G. 1958. The geology of the Ranya area. Site Inv. Co. Report, SOM Library, No. 271, Baghdad.

Bortolotti, V., Chiari, M., Göncüoğlu, M.C., Marcucci, M., Principi, G., Tekin, U. K., Saccani, E., and Tassinari, R. 2013. Age and geochemistry of basalt-

chert associations in the ophiolites of the Izmir-Ankara Mélange, east of Ankara, Turkey: Preliminary data. Ofioliti 38, 2, 157-173.

Bortolotti, V., Chiari, M., Göncüoğlu, M.C., Principi, G., Saccani, E., Tekin, U.K., and Tassarini, R. 2018. The Jurassic–Early Cretaceous basalt–chert association in the ophiolites of the Ankara Mélange east of Ankara, Turkey: age and geochemistry Geological Magazine, 155,451-478.

Bowen, N. L. 1928. The Evolution of the Igneous Rocks, Princeton, Univ. Press-1928.

Bozkaya, Ö., Yalçın, H., and Göncüoğlu, M.C. 2012. Mineralogic evidences of a mid-Paleozoic tectono-thermal event in the Zonguldak terrane, northwest Turkey: implications for the dynamics of some Gondwana-derived terranes during the closure of the Rheic Ocean. Canadian Journal of Earth Sciences, 49:4, 559-575.

Boztuğ, D. 1983. Daday-Devrakani masifikuzeyindeki Büyükçay-Elşmalıçay granitik sokulumu, Yüksek Müh. Tezi, Hacettepe Üniversitesi.

Boztuğ, D. 1988. Daday-Devrakani masifi güneybatı kesiminin mineralojik-petrografik ve jeokimyasal incelenmesi, Doktora Tezi, Hacettepe Üniversitesi.

Boztuğ, D. 1992a. Lithostratigraphic units and tectonics of the southwestern part of DadayDevrekani massif, western Pontides, Turkey, MTA Bullettin, 114, 1-22.

Boztuğ, D. 1992b. Orta-Batı Pontidlerdeki Küre yöresi (K Kastamonu) magmatitinetanorfitlerinin petrografisi ve magmatitlerin ana element jeokimyası, Cunhuriyet Üniversitesi Müh. Fak. Dergisi, Seri-A, Yerbilimleri, 9:1, 75-106.

Boztuğ, D., Debon, F., Le Fort, P., and Yılmaz, O. 1995. High compositional diversity of the Middle Jurassic Kastamonu Plutonic Belt, northern Anatolia, Turkey Turkish Journal of Earth Sciences, 4, 67-86.

Boztuğ, D., and Yılmaz, O. 1983. Mineralogical-petrographic and geochemical study of the Büyükçay-Elmalıçay granitoid (Kastamonu) and its country rocks. Yerbilimleri, 10, 71-88.

Boztuğ, D., and Yılmaz, O. 1995. Daday-Devrekani masifi metamorfizması ve jeolojik evrimi, Kastamonu bölgesi, Batı Pontidler, Türkiye TJK Bülteni, 38, 33-52 (in Turkish).

Brenan, J. M., Shaw, H.F., Phinney, D.L., and Ryerson, F.J. 1994. Rutile-aqueous fluid partitioning of Nb, Ta, Hf, Zr, U and Th: implications for high field strength element depletions in island-arc basalts. Earth and Planetary Science Letters, 128:3-4, 327-339.

Brenan, J. M., Shaw, H.F., Ryerson, F.J., and Phinney, D.L. 1995. Mineral-aqueous fluid partitioning of trace elements at 900 C and 2.0 GPa: Constraints on the trace element chemistry of mantle and deep crustal fluids. Geochimica et Cosmochimica Acta, 59:16, 3331-3350.

Bucher, K., and Graphes, R. 2011. Petrogenesis of Metamorphic Rocks.

Calanchi, N., Peccerillo, A., Tranne, C.A., Lucchini, F., Rossi, P.L., Kempton, P., Barbieri, M., and Wu, T.W. 2002. Petrology and geochemistry of volcanic rocks from the island of Panarea: implications for mantle evolution beneath the Aeolian island arc (southern Tyrrhenian sea). Journal of Volcanology and Geothermal Research,115, 367–395.

Cameron, W.E., Culloch, M.T., and Walker, D.A. 1983. Boninite petrogenesis: Chemical and Nd-Sr isotopic constraints. Earth Planet Sci Lett,65,75–89.

Cao, Y-T., Liu, L., Chen, D-L., Wang, C., Yang, W-Q., Kang, L., and Zhu, X-H. 2017. Partial melting during exhumation of Paleozoic retrograde eclogite in North Qaidam, western China. Journal of Asian Earth Science, 148: 223-240. https://doi.org/10.1016/j.jseaes.2017.09.009

Chen, W., and Simonetti, A. 2014. Evidence for the multi-stage petrogenetic history of the Oka carbonatite complex (Quebec, Canada) as recorded by perovskite and apatite Minerals, 4, 437-476.

Chen, W., Simonetti, A., and Burns, P.C., 2013. A combined geochemical and geochronological investigation of niocalite from the Oka carbonatite complex, Canada. The Canadian Mineralogist, 51, 785-800.

Crawford, A.J., Falloon, T.J., and Green, D.H. 1989. Classification, petrogenesis and tectonic setting of boninites.

Çelik, Ö.F., Chiaradia, M., Marzoli, A., Billor, Z., and Marschik, R. 2013. The Eldivan ophiolite and volcanic rocks in the İzmir–Ankara–Erzincan suture zone, Northern Turkey: Geochronology, whole-rock geochemical and Nd–Sr–Pb isotope characteristics. Lithos, 172:173, 31–46.

Çelik, Ö.F., Chiaradia, M., Marzoli, A., Özkan, M., Billor, Z., and Topuz, G. 2016. Jurassic metabasic rocks in the Kızılırmak accretionary complex (Kargı region, Central Pontides, Northern Turkey) Tectonophysics, 672, 34-49.

Çelik, Ö.F., Marzoli, A., Marschik, R., Chiaradia, M., Neubauer, F., and Öz, İ. 2011. Early–middle Jurassic intra-oceanic subduction in the İzmir-Ankara-Erzincan Ocean, northern Turkey. Tectonophysics, 509:1-2, 120-134.

Çimen, O. 2020. Geochemical characteristics of the adakite-like Dodurga Pluton (Central Pontides, N Turkey): implications for Middle Triassic continental arc magmatism in southern Black Sea region. International Journal of Earth Sciences, 109:3.

Çimen, O., Göncüoğlu, M.C., and Sayit, K. 2016. Geochemistry of the meta-volcanic rocks from the Çangaldağ Complex in Central Pontides: implications for the Middle Jurassic arc–back-arc system in the Neotethyan Intra-Pontide Ocean Turkish Journal of Earth Sciences, 25, 491-512.

Çimen, O., Göncüoğlu, M.C., Simonetti, A., and Sayit, K. 2017. Whole rock geochemistry, zircon U-Pb and Hf isotope systematics of the Çangaldağ pluton: evidences for middle Jurassic Continental Arc magmatism in the central Pontides, Turkey Lithos, 290, 136-158.

Çimen, O., Göncüoglu, M.C., Simonetti, A., and Sayit, K. 2018. New zircon U-Pb LA-ICP-MS ages and Hf isotope data from the Central Pontides: geological and geodynamic constraints Journal of Geodynamics, 116, 23-36.

Dangerfield, A., Harris, R., Sarifakioglu, E., and Dilek, Y. 2011. Tectonic evolution of the Ankara Mélange and associated Eldivan ophiolite near Hançili, central Turkey. Geological Society of America Special Papers, 480, 143-169.

Davies, J.H., and Bickle, M.J. 1991. A physical model for the volume and composition of melt produced by hydrous fluxing above subduction zones. Philosophical Transactions of the Royal Society of London. Series A: Physical and Engineering Sciences, 335 (1638), 355-364.

Deer, W.A., Howie, R.A., and Zussman, J. 1992. An Introduction to the rock forming minerals, 2nd edn. Longman, London, 696 pp.

Defant, M.J., and Drummond, M.S. 1990. Derivation of some modern arc magmas by melting of young subducted lithosphere. nature, 347(6294), 662-665.

DePaolo, D.J., and Wasserburg, G.J. 1976. Nd isotopic variations and petrogenetic models. Geophysical Research Letters, 3(5), 249-252.

Dewey, J.F., Hempton, M.R., Kidd, W. S.F., Saroglu, F., and Şengör, A.M.C. 1986. Shortening of continental lithosphere: the neotectonics of Eastern Anatolia-a young collision zone. Geological Society, London, Special Publications, 19(1), 1-36.

Dilek, Y., and Moores, E. M. 1990. Regional tectonics of the eastern Mediterranean ophiolites
J. Malpas, E. Moores, A. Panayiotou, C. Xenophontos (Eds.), Ophiolites,Oc eanicCrustal Analogues: Proceedings of the Symposium "Troodos 1987", Geological Survey Department, Nicosia, 295-309.

Du, L., Long, X., Yuan, C., Zhang, Y., Huang, Z., Sun, M., and Xiao, W. 2018. Petrogenesis of Late Paleozoic diorites and A-type granites in the central

Eastern Tianshan, NW China: Response to post-collisional extension triggered by slab breakoff. Lithos, 318-319, 47- 59. https://doi.org/10.1016/j.lithos.2018.08.006

Du, L., Zhang, Y., Huang, Z., Li, X-P., Yuan, C., Wu, B., and Long, X. 2019. Devonian to carboniferous tectonic evolution of the Kangguer Ocean in the Eastern Tianshan, NW China: Insights from three episodes of granitoids. Lithos: 105243. http://doi.org/10.1016/j.lithos.2019.105243

Ellam, R.M., Menzies, M.A., Hawkesworth, C.J., Leeman, W.P., Rosi, M., and Serri, G. 1988. The transition from calc-alkaline to potassic orogenic magmatism in the Aeolian Islands, Southern Italy. Bulletin of Volcanology, 50(6), 386-398.

Ellero, A., Ottria, G., Marroni, M., Pandolfi, L., and Göncüoğlu, M.C. 2015a. Analysis of the North Anatolian Shear Zone in Central Pontides (northern Turkey): insight for geometries and kinematics of deformation structures in a transpressional zone Journal of Structural Geology, 72, 124-141.

Ellero, A., Ottria, G., Sayit, K., Catanzariti, C., Frassi, C., Göncüoğlu, M.C., Marroni, M., and Pandolfi, L. 2015b. Geological and geochemical evidence for a Late Cretaceous continental arc in the Central Pontides, northern Turkey Ofioliti, 40, 73-90.

Elliott, T. 2003. Tracers of the slab Geophysical Monograph, 138, 23-45.

Elliott, T., Plank, T., Zindler, A., White, W., and Bourdon, B. 1997. Element transport from slab to volcanic front at theMariana arc. J. Geophys. Res. 102:14,991–15,019.

Elmas A, Yiğitbas¸ E. 2001. Ophiolite emplacement by strike-slip tectonics between the Pontide Zone and the Sakarya Zone in northwestern Anatolia, Turkey. Int J Earth Sci 90,257–269.

Erlank, A.J., and Kable, E.J.D. 1976. The significance of incompatible elements in Mid-Atlantic Ridge basalts from 45 N with particular reference to Zr/Nb. Contributions to Mineralogy and Petrology, 54(4), 281-291.

Ewart, A., Marsh, J. S., Milner, S. C., Duncan, A. R., Kamber, B. S., and Armstrong, R. A. 2004. Petrology and geochemistry of Early Cretaceous bimodal continental flood volcanism of the NW Etendeka, Namibia. Part 1: Introduction, mafic lavas and re-evaluation of mantle source components. Journal of Petrology, 45(1), 59-105.

Eyüboğlu, Y. (2015). Petrogenesis and U–Pb zircon chronology of felsic tuffs interbedded with turbidites (Eastern Pontides Orogenic Belt, NE Turkey): Implications for Mesozoic geodynamic evolution of the eastern Mediterranean region and accumulation rates of turbidite sequences. Lithos, 212, 74-92.

Eyüboğlu, Y., Santosh, M., Yi, K., Tuysuz, N., Korkmaz, S., Akaryali, E., and Bektas, O. 2014. The Eastern Black Sea-type volcanogenic massive sulfide deposits: Geochemistry, zircon U–Pb geochronology and an overview of the geodynamics of ore genesis. Ore Geology Reviews, 59, 29-54.

Flowers, R.M., Bowring, S.A., Tulloch, A.J., and Klepeis, K.A., 2005. Tempo of burial and exhumation within the deep roots of a magmatic arc, Fiordland, New Zealand: Geology, 33, 17-20.

Floyd, P.A., Göncüoğlu, M.C., Winchester, J.A., and Yaliniz, M.K. 2000. Geochemical character and tectonic environment of Neotethyan ophiolitic fragments and metabasites in the Central Anatolian Crystalline Complex, Turkey. Geological Society, London, Special Publications, 173(1), 183-202.

Floyd, P.A., and Winchester, J.A. 1978. Identification and discrimination of altered and metamorphosed volcanic rocks using immobile elements, 21, 291-306.

Frassi, C., Göncüoğlu, M.C., Marroni, M., Pandolfi, L., Ruffini L., Ellero, A., Ottria, G., and Sayit, K. 2016. The Intra-Pontide suture zone in the Tosya-Kastamonu area, Northern Turkey Journal of Maps, 12, 211-219.

Frassi, C., Marroni, M., Pandolfi, L., Göncüoğlu, M.C., Ellero, A., Ottria, G., Sayit, K., Mcdonald, C.S., Balestrieri M.L., and Malasoma, A. 2017. Burial and exhumation history of the Daday Unit (Central Pontides, Turkey): implications for the closure of the Intra-Pontide oceanic basin Geological Magazine, 10.1017/S0016756817000176

Frassi, C., Marroni, M., Pandolfi, L., Göncüoğlu, M.C., Ellero, A., Ottria, G., Sayit, K., McDonald, C.S., Balestrieri, M.L., and Malasoma, A. 2018. Burial and exhumation history of the Daday Unit (Central Pontides, Turkey): implications for the closure of the Intra-Pontide oceanic basin Geol. Mag., 155, 356-376.

Frassi, C., Rebay, G., Marroni, M., Sayit, K., Göncüoğlu, M.C., Ellero, A., and Pandolfi, L. 2020. Metamorphic imprint of ridge subduction on the Neo-Tethyan ophiolites from the Saka Unit (Central Pontides, northern Turkey). Journal of Asian Earth Sciences, 200, 104468.

Gast, P. W. 1968. Trace element fractionation and the origin of tholeiitic and alkaline magma types. Geochimica et Cosmochimica Acta, 32(10), 1057-1086.

Gast, P. W., Tilton, G. R., and Hedge, C. 1964. Isotopic composition of lead and strontium from Ascension and Gough Islands. Science, 145(3637), 1181-1185.

Genç, Ş.C., and Tüysüz, O. 2010. Tectonic setting of the Jurassic bimodal magmatism in the Sakarya Zone (Central and Western Pontides), Northern Turkey: a geochemical and isotopic approach. Lithos, 118, 95-111.

Gibson, S.A., Thompson, R.N., Leat, P.T., Morrison, M.A., Hendry, G.L., Dickin, A.P., and Mitchell, J.G., 1993. Ultrapotassic magmas along the flanks of the Oligo-Miocene Rio Grande Rift, USA: monitors of the zone of lithospheric mantle extension and thinning beneath a continental rift. Journal of Petrology 34, 187–228.

Gill, J.B. 1981. Orogenic Andesites and Plate Tectonics, Springer-Verlag, 330 pp.

Goscombe, B.D., Passchier, C.W., and Hand, M. 2004. Boudinage classification: end-member boudin types and modified boudin structures. Journal of structural Geology, 26(4), 739-763.

Göncüoglu, M.C. 2010. Introduction to the geology of Turkey: Geodynamic evolution of the pre-Alpine and Alpine terranes. Mineral Research and Exploration Monography Series 6, 1–66.

Göncüoğlu, M.C. 2019. A review of the geology and geodynamic evolution of tectonic terranes in Turkey Mineral Resources of Turkey, Springer, Cham, 19-72.

Göncüoglu, M.C., Dirik, K., and Kozlu, H. 1997. General characteristics of pre-Alpine and Alpine Terranes in Turkey: explanatory notes to the terrane map of Turkey, 515-537.

Göncüoğlu, M.C., and Erendil, M. 1990. Pre-Late Cretaceous tectonic units of the Armutlu Peninsula. In: Proceedings of 8th Turkish petroleum congress, vol 8, 161-168.

Göncüoğlu, M.C., Erendil, M., Tekeli, O., Aksay, A., Kuscu, A., and Urgun, B. 1987. Geology of the Armutlu Peninsula. IGCP-5 Guide Book 5, 12–18.

Göncüoğlu M. C., Gürsu S, Tekin U.K., Koksal, S. 2008. New data on the evolution of the Neotethyan oceanic branches in Turkey: late Jurassic ridge spreading in the Intra-Pontide branch. Ofioliti 33,153–164.

Göncüoglu, M.C., Marroni, M., Pandolfi, L., Ellero, A., Ottria, G., Catanzariti, R., Tekin, U.K., Sayit, K. 2014. The Arkot Dağ Mélange in Araç area, central Turkey: Evidence of its origin within the geodynamic evolution of the Intra-Pontide suture zone. Journal of Asian Earth Sciences, 85, 117-139.

Göncüoglu, M.C., Marroni, M., Sayit, K., Tekin, U.K., Ottria, G., and Pandolfi, L. 2012. The Ayli dag ophiolite sequence (central Northern Turkey): a fragment of middle jurassic oceanic lithosphere within the intra-pontide suture zone. Ofioliti, 37.2, 77-92.

Göncüoglu, M.C., Sayit, K., and Tekin, U.K. 2010. Oceanization of the northern Neotethys: geochemical evidence from ophiolitic melange basalts within the Izmir– Ankara suture belt, NW Turkey. Lithos, 116.1, 175-187.

Göncüoğlu, M.C., Tekin, U.K., Sayit, K., Bedi, Y., and Uzuncimen, S. 2015. Opening, evolution and closure of the Neotethyan oceanic branches in Anatolia as inferred by radiolarian research Radiolaria, 35, 88-90.

Göncüoğlu, M.C., Toprak, V., Erler, A., and Kuşçu, İ. 1991. Orta Anadolu Masifinin Batı Bölümünün Jeolojisi, Bölüm 1, Güney Kesim TPAO Rap no: 2909, pp.176.

Göncüoğlu, M.C., Turhan, N., Şentürk, K., Özcan, A., Uysal, Ş., and Yaliniz, M.K. 2000. A geotraverse across northwestern Turkey: tectonic units of the Central Sakarya region and their tectonic evolution. Geological Society of London, Special Publications, 173, 139-161.

Göncüoglu, M.C., Yaliniz, M.K., and Tekin, U.K. 2006. Geochemistry, tectono-magmatic discrimination and radiolarian ages of basic extrusives within the Izmir-Ankara suture belt (NW Turkey); time constraints for the Neotethyan evolution. Ofioliti, 31, 25-38.

Görür, N., Monod, O., Okay, A.I., Sengör, A.M.C., Tüysüz, O., Yiğitbas, E., Sakinc, M., and Akkök, R. 1997. Palaeogeographic and tectonic position of the Carboniferous rocks of the western Pontides (Turkey) in the frame of the Variscan belt. Bull Soc Géol France, 168,197–205.

Görür, N., Şengör, A.M.C., Akkök, R., and Yilmaz, Y. 1983. Sedimentological evidence for the opening of the northern branch of Neo-Tethys in the Pontides. Bull. Geol. Soc. Turk, 26, 11–20 (in Turkish with English abstract).

Gribble, R.F., Stern, R.J., Newman, S., Bloomer, S.H., and O'Hearn, T. 1998. Chemical and isotopic composition of lavas from the Northern Mariana Trough: implications for magmagenesis in back-arc basins. Journal of Petrology, 39, 125–154.

Grove, T.L., Till, C.B., and Krawczynski, M.J. 2012. The role of H2O in subduction zone magmatism. Annual Review of Earth and Planetary Sciences, 40, 413-439.

Gumsley, A., Olsson, J., Söderlund, U., Kock, M. Hofmann, A., and Klausen, M. 2015. Precise U-Pb baddeleyite age dating of the Usushwana Complex, southern Africa - Implications for the Mesoarchaean magmatic and sedimentological evolution of the Pongola Supergroup, Kaapvaal Craton. Precambrian Research, 267, 17-185.

Gücer, M.A., Arslan, M., Sherlock, S., and Heaman, L.M. 2016. Permo-Carboniferous granitoids with Jurassic high temperature metamorphism in Central Pontides, Northern Turkey Mineralogy and Petrology, 110, 943-964.

Günay, K., Dönmez, C., Uysal, İ., Yıldırım, N., Şahin, M.B., Yıldırım, E., Tablacı, A., Kang, J., and Lee, I. 2016. Chrome spinel geochemistry of ultramafic rocks from the Elekdağ metaophiolite (Northern Turkey): implications for greenschist to mid-amphibolite facies metamorphism Neues Jahrbuch für Mineralogie (Abhandlungen), 193, 1-16.

Gündogdu-Atakay, E. 2009. Geological and petrological characteristics of volcanic rocks at soutwest of Çorum and geoarcheological studies at Alaca höyük excavation site (Doctoral dissertation, PhD Thesis, Ankara University, Ankara, Turkey, 194.

Güven, İ.H. 1993. 1:25.000-Scale Geological and Metallogenical Map of the Eastern Black Sea Region (in Turkish). Mineral Research and Exploration Institute of Turkey (MTA) Publications, Ankara, Turkey, pp. 98.

Hakyemez, Y., Barkurt, M.Y., Bilginer, E., Pehlivan, Ş., Can, B., Dağer, Z., ve Sözeri, B. 1986. Yapraklı-llgaz-Çankırı-Çandır dolayının jeolojisi: MTA Enst. Rap. 7966.

Hanan, B.B., Blichert-Toft, J., Hemond, C., Sayit, K., Agranier, A., Graham, D.W., and Albarède, F. 2013. Pb and Hf isotope variations along the Southeast Indian Ridge and the dynamic distribution of MORB source domains in the upper mantle. Earth and Planetary Science Letters 375, 196–208.

Handley, H., Macpherson, C., Davidson, J., Berlo, K., and Lowry, D. 2007. Constraining fluid and sediment contributions to subduction-related magmatism in Indonesia, Ijen Volcanic Complex Journal of Petrology, 48, 1155-1183.

Hanson, G.N., and Langmuir, C.H. 1978. Modelling of major elements in mantle-melt systems using trace element approaches. Geochimica et Cosmochimica Acta, 42(6), 725-741.

Harker, A. 1909. The natural history of igneous rocks. Methuen and Company.

Hart, S.R., Schilling, J.G., and Powell, J.L. 1973.Basalts from Iceland and along the Reykjanes Ridge: Sr isotope geochemistry Nature, 246, 104-107.

Hastie, A.R., Kerr, A.C., Pearce, J.A., and Mitchell, S.F. 2007. Classification of altered volcanic island arc rocks using immobile trace elements: development of the Th-Co discrimination diagram. J. Geol., 48: 2341-2357.

Hawkesworth, C.J., Gallagher, K., Hergt, J.M., and McDermott, F. 1993. Mantle and slab contributions in arc magmas. Annual Review of Earth and Planetary Sciences, 21(1), 175-204.

Hawkesworth, C.J., O'nions, R.K., Pankhurst, P.J., Hamilton, P.J., and Evensen, N.M. 1977. A geochemical study of island arc and back arc tholeiites from Scotia Sea. Earth Planet. Sci. Lett., 36, 253-62.

Hawkesworth, C.J., Turner, S., Peate, D., McDermott, F., and Van Calsteren, P. 1997. Elemental U and Th variations in island arc rocks: implications for U-series isotopes. Chemical Geology, 139(1-4), 207-221.

Hedge, C.E. 1966. Variations in radiogenic strontium found in volcanic rocks. Journal of Geophysical Research, 71(24), 6119-6126.

Hertogen, J., and Gijbels, R. 1976. Calculation of trace element fractionation during partial melting. Geochimica et Cosmochimica Acta, 40(3), 313-322.

Hey, M.H. 1954. A new review of the chlorites. Mineralogy Mag. 30, 277-292.

Hirschmann, M.M., and Stolper, E.M. 1996. A possible role for garnet pyroxenite in the origin of the "garnet signature" in MORB. Contributions to Mineralogy and Petrology 124, 185–208.

Hochstaedter, A., Gill, J., Peters, R., Broughton, P.,Holden, P., and Taylor, B. 2001. Across-arc geochemical trends in the Izu-Bonin arc: contributions from the subducting slab. Geochem. Geophys. Geosyst. 2:2000GC000105.

Hoernle, K., Hauff, F., Kokfelt, T.F., Haase, K., Garbe-Schönberg, D., Werner, R. 2011. Onand off-axis chemical heterogeneities along the South Atlantic Mid-Ocean-Ridge (5–11° S): shallow or deep recycling of ocean crust and/or intraplate volcanism? Earth and Planetary Science Letters 306, 86-97.

Hofmann, A.W. 1997. Mantle geochemistry: the message from oceanic volcanism, Nature, 385,219-229.

Hofmann, A.W., and White, W.M. 1982. Mantle plumes from ancient oceanic crust. Earth and Planetary Science Letters, 57, 421–436.

Hoskin, P.W.O., and Black, L.P. 2000. Metamorphic zircon formation by solid-state recrystallization of protolith igneous zircon. Journal of metamorphic Geology, 18(4), 423-439.

Hu, J., Gong, W., Wu, S., Liu, Y., and Liu, S. 2014. LA-ICP-MS zircon U–Pb dating of the Langshan Group in the northeast margin of the Alxa block, with tectonic implications. Precambrian Research, 255, 756-770.

Humphris, S.E., and Thompson, G., 1978. Trace element mobility during hydrothermal alteration of oceanic basalts. Geochimica et Cosmochimica Acta 42, 127-136.

Irving, A.J., and Frey, F.A. 1978. Distribution of trace elements between garnet megacrysts and host volcanic liquids of kimberlitic to rhyolitic composition. Geochimica et Cosmochimica Acta, 42(6), 771-787.

İlbeyli, N., Demirbilek, M., and Kibici, Y. 2015. Geochemistry and petrogenesis of the Late Paleozoic magmatism in the Sakarya Zone (NW Turkey) Neues Jb. Mineral. Abh., 192, 177-194.

Jackson, J., and McKenzie, D. 1988. The relationship between plate motions and seismic moment tensors, and the rates of active deformation in the

Mediterranean and Middle East. Geophysical Journal International, 93(1), 45-73.

Jacobsen, S.B., and Wasserburg, G.J. 1980. Sm-Nd isotopic evolution of chondrites. Earth and Planetary Science Letters, 50(1), 139-155.

Johnson, M.C., and Plank, T. 1999. Dehydration and melting experiments constrain the fate of subducted sediments, Geochemistry Geophysics Geosystems., 1-1, 1-26.

Jolly, W.T., Lidiak, E.G., and Dickin, A.P. 2008. The case for persistent southwest-dipping Cretaceous convergence in the northeast Antilles: geochemistry, melting models, and tectonic implications. Geol. Soc. Am. Bull. 120:1036–1052.

Jolly, W.T., Lidiak, E.G., Dickin, A.P., and Wu, T.W. 1998. Geochemical diversity ofMesozoic island arc tectonic blocks in eastern Puerto Rico. Geological Society of America, 322, pp.67.

Jolly, W. T., Lidiak, E.G., Dickin, A.P., and Wu, T.S. 2001. Secular geochemistry of central Puerto Rican island arc lavas: Constraints on Mesozoic tectonism in the eastern Greater Antilles.Journal of Petrology, 42.12, pp. 2197- 2214.

Kandemir, Ö., Akbayram, K., Çobankaya, M., Kanar, F., Pehlivan, Ş., Tok, T., and Temiz, U. (2019). From arc evolution to arc-continent collision: Late Cretaceous–middle Eocene geology of the Eastern Pontides, northeastern Turkey. Bulletin, 131(11-12), 1889-1906.

Kaygusuz, A., and Eker, Ç.S. 2021. Geochemical features and petrogenesis of Late Cretaceous subduction-related volcanic rocks in the Değirmentaşı (Torul/Gümüşhane) area, Eastern Pontides (NE Turkey). Journal of Engineering Research and Applied Science, 10(1), 1689-1702.

Kelemen, P.B., Shimizu, N., and Dunn, T. 1993. Relative depletion of niobium in some arc magmas and the continental crust: partitioning of K, Nb, La and Ce during melt/ rock reaction in the upper mantle. Earth and Planetary Science Letters 120, 111–134.

Keppler, H. 1996. Constraints from partitioning experiments on the composition of subduction-zone fluids, Nature, 380, 237-240.

Keskin, M., Genç, Ş.C., and Tüysüz, O. 2008. Petrology and geochemistry of post-collisional Middle Eocene volcanic units in North-Central Turkey: evidence for magma generation by slab breakoff following the closure of the Northern Neotethys Ocean. Lithos, 104(1-4), 267-305.

Ketin, İ. 1962. 1:500.000 ölçekli Türkiye Jeoloji Haritası-Sinop. M.T.A Yayınları, Ankara.

Koçyiğit, A., Yılmaz, A., Adamia, S., and Kuloshvili S. 2001. Neotectonic of East Anatolian Plateau (Turkey) and Lesser Caucasus: implication for transition from thrusting to strike-slip faulting Geodin. Acta, 14, 177-195.

Kozur, H., Aydın, M., Demir, O., Yakar, H., Göncüoğlu, M.C., and Kuru, F. 2000. New stratigraphic results from the Paleozoic and Early Mesozoic of the Middle Pontides (Northern Turkey) Geologia Croatica, 53, 209-268.

Köksal, S., Romer, R. L., Göncüoglu, M.C., and Toksoy-Köksal, F. 2004. Timing of post-collisional H-type to A-type granitic magmatism: U-Pb titanite ages from Alpine central Anatolian Granitoids (Turkey). International Journal of Earth Science, 93, 974-989.

Köksal, S., Toksoy-Köksal, F., Göncüoğlu, M.C., Möller, A., Gerdes, A., and Frei, D., 2013. Crustal source of the Late Cretaceous Satansarı monzonite stock (central Anatolia -Turkey) and its significance for the Alpine geodynamic evolution. Journal of Geodynamics, 65, 82-93.

Kurt, İ., Özkan, M., Karslı, Ş., Çolak, T., Topçu, T. 2006. Doğu Karadeniz Bölgesi'nin Jeodinamik ve Metalojenik evrimi (Keşap, Giresun-Çarşıbaşı, Trabzon-Torul, Gümüşhane arasının jeolojisi). MTA Genel Müd. Project no: 10875.

Langmuir, C.H., Bezos, A., Escrig, S., and Parman, S.W. 2006. Chemical systematics and hydrous melting of the mantle in back-arc basins. Geophysical Monograph-American Geophysical Union, 166, 87.

Lapierre, H., Samper, A., Bosch, D., Maury, R.C., Béchennec, F., Cotten, J., Demant, A, Brunet, P., Keller, F., and Marcoux, J. 2004. The Tethyan plume: geochemical diversity of middle Permian basalts from the Oman rifted margin. Lithos, 74, 167–198.

Leat, P.T., Livermore, R.A., Millar, I.L., and Pearce, J.A., 2000. Magma supply in back-arc spreading centre segment E2, East Scotia Ridge. Journal of Petrology, 41, 845–866.

Le Bas, M.J., Le Maitre, R.W., Streckeisen, A., and Zanettin, B. 1986. A Chemical Classification of Volcanic Rocks Based on the Total Alkali-Silica Diagram. Journal of Petrology, 27, 3, 745-750.

Le Roex, A.P., Dick, H.J.B., Erlank, A.J., Reid, A.M., Frey, F.A., and Hart, S.R. 1983. Geochemistry, mineralogy and petrogenesis of lavas erupted along the Southwest Indian Ridge between the Bouvet triple junction and 11 degrees east. Journal of Petrology, 24(3), 267-318.

Leterrier, J., Maury, R.C., Thonon, P., Girard, D., and Marchal, M. 1982. Clinopyroxene composition as a method of identification of the magmatic affinities of paleo-volcanic series. Earth and Planetary Science Letters, 59(1), 139-154.

Ludwig, K.R. 2003. User's manual for IsoPlot 3.0. A geochronological toolkit for Microsoft Excel, 71.

Manav, H., Gültekin, A.H., and Uz, B. 2004. Geochemical evidence for the tectonic setting of the Harmancik ophiolites, NW Turkey. Journal of Asian Earth Sciences, 24(1), 1-9.

Marroni, M., Göncüoğlu, M.C., Frassi, C., Sayit, K., Pandolfi, L., Ellero, A., and Ottria, G. 2020. The Intra-Pontide ophiolites in Northern Turkey revisited: from birth to death of a Neotethyan oceanic domain Geosci. Front., 11, 129-149.

Marroni, M., Frassi, C., Göncüoğlu, M.C., Di Vincenzo, G., Pandolfi, L., Rebay. G., Ellero, and A., Ottria, G. 2014. Late Jurassic amphibolite-facies metamorphism in the Intra-Pontide Suture Zone (Turkey): an eastward extension of the Vardar Ocean from the Balkans into Anatolia, J Geol. Soc. 171, 605-609.

Maury, R.C., Bechennec, F., Cotten, J., Caroff, M., Cordey, F., and Marcoux, J. 2003. Middle Permian plume-related magmatism of the Hawasina Nappes and the Arabian Platform: implications on the evolution of the Neotethyan margin in Oman. Tectonics, 22(6), 1073-1085.

McCulloch, M.T., and Gamble, J.A. 1991. Geochemical and geodynamical constraints on subduction zone magmatism. Earth and Planetary Science Letters, 102, 358-374.

McDade, P., Blundy, J.D., and Wood, B.J. 2003. Trace element partitioning on the Tinaquillo Lherzolite solidus at 1.5 GPa. Phys. Earth Planet. Inter., 139,129-147.

McDougall, I., and Lovering, J.F. 2007. Fractionation of chromium, nickel, cobalt and copper in a differentiated dolerite-granophyre sequence at Red Hill, Tasmania. Journal of the Geological Society of Australia, 10.2, 325-338.

McKenzie, D. 1976. The East Anatolian Fault: a major structure in eastern Turkey. Earth and Planetary Science Letters, 29(1), 189-193.

McKenzie, D., and O'Nions, R.K. 1983. Mantle reservoirs and ocean island basalts. Nature, 301, 229–231.

McKenzie, D., and O'nions, R.K. 1991. Partial melt distributions from inversion of rare earth element concentrations. Journal of Petrology, 32, 1021-1091.

Meyer, C., and Hemley, J.J. 1967. Wall rock alterations, 166–235. Geochemistry of hydrothermal ore deposits (HG Barnes, ed.), Winston Inc. New York, 670.

Minster, J.F., and Allegre, C.J. 1978. Systematic use of trace elements in igneous processes. Contributions to Mineralogy and Petrology, 68(1), 37-52.

Mitchell, A.H.G. 1993. Cretaceous–Cenozoic tectonic events in the western Myanmar (Burma)–Assam region: Journal of the Geological Society of London, v. 150, no. 6.

Moghadam, H.S., Corfu, F., Chiaradia, M., Stern, R.J., and Ghorbani, G. 2014. Sabzevar Ophiolite, NE Iran: Progress from embryonic oceanic lithosphere into magmatic arc constrained by new isotopic and geochemical data. Lithos, 210, 224-241.

Moix, P., Beccaletto, L., Kozur, H.W., Hochard, C., Rosselet, F., and Stampfli, G.M., 2008. A new classification of the Turkish terranes and sutures and its implication for the paleotectonic history of the region. Tectonophysics 451, 7-39.

Moriguti, T., Shibata, T., and Nakamura, E. 2004. Lithium, boron and lead isotope and trace element systematics of Quaternary basaltic volcanic rocks in northeastern Japan: mineralogical controls on slab-derived fluid composition. Chemical Geology, 212(1-2), 81-100.

Morimoto, N., Fabries, J., Ferguson, A.K., Ginzburg, I.V., Ross, M., Seifert, F.A., Zussman, J., Aoki, K., and Gottardi, G. 1988. Nomenclature of pyroxenes. Mineral Mag., 52, 535-550.

Myeong, B., Kim, J., Kim, J.H., and Jang, Y.D. 2020. Petrogenesis of subduction-related lavas from the southern Tonga arc. Journal of Asian Earth Sciences, 188, 104089.

Neumann, H., Mead, J., and Vitaliano, C.J. 1954. Trace element variation during fractional crystallization as calculated from the distribution law. Geochimica et Cosmochimica Acta, 6 (2-3), 90-99.

Nisbet, E.G., and Pearce, J.A. 1977. Clinopyroxene composition in mafic lavas from different tectonic settings. Contributions to mineralogy and petrology, 63(2), 149-160.

Nzegge, O. 2008. Petrogenesis and Geochronology of the Deliktaş, Sivrikaya and Devrekani Granitoids and Basement, Kastamonu Belt-Central Pontides (NW Turkey): Evidence for Late Paleozoic–Mesozoic Plutonism, and Geodynamic Interpretation (PhD Thesis) p. 177.

Nzegge, O.M., Satir, M., Siebel, W., and Taubald, H. 2006. Geochemical and isotopic constraints on the genesis of the Late Palaeozoic Deliktas and Sivrikaya granites from the Kastamonu granitoid belt (Central Pontides, Turkey). Neues Jahrbuch fur Mineralogie-Abhandlungen, 183(1), 27-40.

Okay, A.İ. 1989. Tectonic units and sutures in the Pontides, northern Turkey, A.M.C. Şengör (Ed.), Tectonic Evolution of the Tethyan Region, Kluwer Academic Publ. 109-116.

Okay, A.I. 2000. Was the Late Triassic orogeny in Turkey caused by the collision of an oceanic plateau?, in Bozkurt, E., et al., (eds)., Tectonics and magmatism in Turkey and surrounding area: Geological Society [London] Special Publication 173, p. 25–41.

Okay, A.I., Altıner, D., and Kılıç, A. 2015. Triassic limestone, turbidites and serpentinite–the Cimmeride orogeny in the Central Pontides. Geological Magazine, 152.3, 460-479.

Okay, A.I., Altıner, D., and Kylander-Clark, A.R. 2019. Major Late Cretaceous mass flows in Central Turkey recording the disruption of the Mesozoic continental margin Tectonics, 38 (3), 960-989.

Okay, A.I., and Göncüoğlu, M.C. 2004. The Karakaya Complex: a review of data and concepts. Turkish Journal of Earth Sciences, 13.2, 75-95.

Okay, A.I., Gürsel, S., Tüysüz, O., Sherlock, S., Keskin, M., and Kylander-Clark, A.R.C. 2014. Low-pressure–high-temperature metamorphism during extension in a Jurassic magmatic arc, Central Pontides, Turkey Journal of Metamorphic Geology, 32,49-69.

Okay, A.I., and Nikishin, M.A. 2015. Tectonic evolution of the southern margin of Laurasia in the Black Sea region International Geology Review. 1-26.

Okay, A.I., Sengor, A.M.,C., and Görür, N. 1994. Kinematic history of the opening of the Black Sea and its effect on the surrounding regions. Geology, 22(3), 267-270.

Okay, A.I., Sunal, G., Sherlock, S., Altıner, D., Tüysüz, O., Kylander-Clark, A.R.C., and Aygül, M. 2013. Early Cretaceous sedimentation and orogeny on the active margin of Eurasia: Southern Central Pontides, Turkey. Tectonics, 32.5, 1247-1271.

Okay, A.I., and Tüysüz, O. 1999. Tethyan sutures of northern Turkey, in The Mediterranean Basins: Tertiary Extension Within the Alpine Orogen, vol. 156, Geological Society, London, Special Publication, pp. 475-515, Oxford, UK.Allmendinger, R. W.1999. Introduction to Structural Geology. Lecture notes. 279 p.

Okay, A.I., Tüysüz, O., and Kaya, Ş. 2004. From transpression to transtension: changes in morphology and structure around a bend on the North Anatolian Fault in the Marmara region. Tectonophysics, 391(1-4), 259-282.

Okay, A.I., Tüysüz, O., Satır, M., Altıner, S.Ö., Altıner, D., Sherlock, S., and Eren, R.H. 2006. Cretaceous and Triassic subduction-accretion, high-pressure–lowtemperature metamorphism, and continental growth in the Central Pontides, Turkey. Geological Society of America Bulletin, 118.9-10, pp. 1247-1269.

Okuyucu, C., Dimitrova, T.K., Göncüoğlu, M.C., and Gedik, I. 2017. Late Permian (Tatarian) fluvio-lacustrine successions in NW Anatolia (Zonguldak terrane, Turkey): Palaeogeographic implications Geological Magazine, 154, 1073-1087.

Ottria, G., Pandolfi, L., Catanzariti, R., Da Prato, S., Ellero, A., Frassi, C., and Göncüoğlu M.C. 2017. Evolution of an early Eocene pull-apart basin in the central Pontides (northern Turkey): new insights into the origin of the north Anatolian shear zone Terra Nova, 29, 392-400.

Önen, A.P., and Hall, R. 1993. Ophiolites and related metamorphic rocks from the Kütahya region, north-west Turkey. Geological Journal, 28(3-4), 399-412.

Özcan, E., Less, G., and Kertesz, B. 2007. Late Ypresian to middle Lutetian Orthophragminid record from central and northern Turkey: taxonomy and remarks on zonal scheme, Turkish. J. Earth Sc., 16, 281–318.

Özdamar, Ş. 2016. Geochemistry and geochronology of late Mesozoic volcanic rocks in the northern part of the Eastern Pontide Orogenic Belt (NE Turkey): Implications for the closure of the Neo-Tethys Ocean. Lithos, 248, 240-256.

Özgül, N. 2012. Stratigraphy and some structural features of the İstanbul Paleozoic Turkish Journal of Earth Sciences, 21, 817-866.

Özkan, M., Çelik, Ö.F., Soycan, H., Çörtük, R.M., and Marzoli, A. 2020. The Middle Jurassic and Early Cretaceous basalt-radiolarian chert association from the Tekelidağ Melange, eastern Izmir-Ankara-Erzincan suture zone (northern Turkey). Cretaceous Research: 107:104280.

Parlak, O. 2006. Geodynamic significance of granitoid magmatism in the southeast Anatolian orogen: Geochemical and geochronogical evidence from Göksun–Afşin (Kahramanmaraş, Turkey) region. International Journal of Earth Sciences, 95(4), 609-627.

Parlak, O., Çolakoğlu A., Dönmez, C., Sayak, H., Yıldırım, N., Türkel, A., and Odabaşı, İ., 2013. Geochemistry and tectonic significance of ophiolites along the İzmir-Ankara-Erzincan Suture Zone in northeastern Anatolia. Geological Society, London, 372, 75-105.

Parlak, O., Höck, V., Kozlu, H., and Delaloye, M. 2004. Oceanic crust generation in an island arc tectonic setting, SE Anatolian orogenic belt (Turkey). Geological Magazine, 141(5), 583-603.

Parlak, O., Karaoğlan, F., Rızaoğlu, T., Klötzli, U., Koller, F., and Billor, Z. 2013. U–Pb and 40A-39Ar geochr onology of the ophiolites and granitoids from the Tauride belt: implications for the evolution of the Inner Tauride suture Journal of Geodynamics, 65,22-37.

Parlak, O., Karaoğlan, F., Rızaoğlu, T., Nurlu, N., Bağcı, U., Höck, V., Önal, A., Kürüm, S., and Topak, Y. 2012. Petrology of the İspendere (Malatya) Ophiolite From the Southeast Anatolia: Implications for the Late Mesozoic Evolution of the Southern Neotethyan Ocean Geological Society, London, 219-247, Special Publications 372.

Passchier, C.W., and Trouw, R.A.J. 2005. Microtectonics. Springer, Berlin, New York, 16, p. 366.

Pearce, J.A. 1982. The trace element characteristics of lavas from destructive plate boundaries. In: Thorpe, R.S., (ed.), Andesites, 525-548. New York: John Wiley and Sons.

Pearce, J.A. 1983. Role of the subcontinental lithosphere in magma genesis at active continental margins, 230-249.

Pearce, J.A., Arculus, R.J., Murton, B.J., Ishci, T., Peate, D.W., and Parkinson, T. 1992. Boninite and harzburgite from Leg. 125 (Bonin-Mariana forearc): a case study of magma genesis during the initial stages of subduction Proc. Ocean Drilling Program Sci. Res., 125, 623-659.

Pearce, J.A., Baker, P.E., Harvey, P.K., and Luff, I.W., 1995. Geochemical evidence for subduction fluxes, mantle melting and fractional crystallization beneath the South Sandwich island arc. Journal of Petrology 36, 1073–1109.

Pearce, J.A., Bender, J.F., De Long, S.E., Kidd, W.S.F., Low, P. J., Güner, Y., and Mitchell, J.G. 1990. Genesis of collision volcanism in Eastern Anatolia, Turkey. Journal of Volcanology and Geothermal Research, 44(1-2), 189-229.

Pearce, J.A., and Cann, J.R. 1973. Tectonic setting of basic volcanic rocks determined using trace element analyses. Earth and planetary science letters,19.2, 290-300.

Pearce J.A., Ernewein, M., Bloomer, S.H., Parson, L.M., Morton, B.J., and Johnson, L.E. 1994. Geochemistry of Lau Basin volcanic rocks: influence of ridge segmentation and arc proximity. In: Smellie JL (ed) Volcanism associated with extension at consuming plate margins. Geological Society Special Publications, vol 81.

Pearce, J.A., and Norry, M.J. 1979. Petrogenetic implications of Ti, Zr, Y, and Nb variations in volcanic rocks. Contributions to mineralogy and petrology, 69(1), 33-47.

Pearce, J.A., and Parkinson, I.J. 1993. Trace element models for mantle melting: application to volcanic arc petrogenesis. Geological Society, London, Special Publications, 76(1), 373-403.

Pearce, J.A., and Peate, D.W. 1995. Tectonic implications of the composition of volcanic arc magmas. Annual Review of Earth and Planetary Sciences, 23, 251- 286.

Pearce, J.A., and Stern, R.J. 2006. Origin of back-arc basin magmas: trace element and isotope perspectives. In: Christie D (ed) Back-arc spreading systems: geological, biological, chemical and physical interactions. AGU Geophysical Monograph Series, vol 166, pp 63–8.

Pearce, J.A., Stern, R.J., Bloomer, S.H., and Fryer, P. 2005. Geochemical mapping of the Mariana arc-basin system: Implications for the nature and distribution of subduction components. Geochemistry, Geophysics, Geosystems. v6.7.

Peate, D. W., Pearce, J.A., Hawkesworth, C.J., Colley, H., Edwards, C.M., and Hirose, K. 1997. Geochemical variations in Vanuatu arc lavas: the role of subducted material and a variable mantle wedge composition. Journal of Petrology, 38(10), 1331-1358.

Pickett, E.A., and Robertson, A.H. 2004. Significance of the volcanogenic Nilüfer Unit and related components of the Triassic Karakaya Complex for Tethyan subduction/accretion processes in NW Turkey. Turkish Journal of Earth Sciences, 13(2), 97-143.

Pilz, R. 1937. Kastamonu ve Sinop vilayetlerindeki çeşitli mineral yataklarının tetkiki. Ankara MTA Raporu.

Piper, J.D.A., Gürsoy, H., Tatar, O., Beck, M.E., Rao, A., Koçbulut, F., Mesci, B.L. 2010. Distributed neotectonic deformation in the Anatolides of Turkey: a palaeomagnetic analysis. Tectonophysics 488, 31-50.

Plank, T., and Langmuir, C.H. 1998. The chemical composition of subducting sediment and its consequences for the crust and mantle. Chemical geology, 145(3-4), 325-394.

Rasmussen, B., Fletcher, I.R., and Muhling, J.R. 2013. Dating deposition and low-grade metamorphism by in situ UPb geochronology of titanite in the Paleoproterozoic Timeball Hill Formation, southern Africa. Chemical Geology, 351, 29-39.

Reilinger, R.E., McClusky, S.C., Oral, M.B., King, R.W., Toksoz, M.N., Barka, A. and Sanli, I. 1997. Global Positioning System measurements of present-day crustal movements in the Arabia-Africa-Eurasia plate collision zone. Journal of Geophysical Research: Solid Earth, 102(B5), 9983-9999.

Rızaoğlu, T., Parlak, O., Höck, V., Koller, F., Hames, W.E., and Billor, Z. 2009. Andean-type active margin formation in the eastern Taurides: Geochemical and geochronogical evidence from the Baskil granitoid (Elazığ, SE Turkey). Tectonophysics, 473(1-2), 188-207.

Rice, S.P., Robertson, A.H.F., and Ustaömer, T. 2006. Late Cretaceous-Early Cenozoic tectonic evolution of the Eurasian active margin in the Central and Eastern Pontides, northern Turkey. In: Robertson AHF (ed) Tectonic development of the Eastern Mediterranean Region. Geological Society Special Publications, vol 260, pp 413–445.

Rizaoğlu, T., Parlak, O., Hoeck, V., and İşler, F. 2006. Nature and significance of Late Cretaceous ophiolitic rocks and their relation to the Baskil granitic intrusions of the Elazığ region, SE Turkey. Geological Society, London, Special Publications, 260(1), 327-350.

Robertson, A.H.F., Dixon, J.E., Brown, S., Collins, A., Morris, A., Pickett., E., Sharp, I., and Ustaömer, T. 1996. Alternative tectonic models for the Late Palaeozoic-Early Tertiary development of Tethys in the Eastern Mediterranean region. Geological Society, London, Special Publications, 105.1, 239-263.

Robertson, A.H.F., and Ustaömer, T., 2004. Tectonic evolution of the intra-pontide suture zone in the Armutlu peninsula, NW Turkey Tectonophysics, 381, 175-209.

Robertson, A.H.F., Ustaömer, T., Pickett, E.A., Collins, A.S., Andrew, T., Dixon, J.E. 2004. Testing models of Late Palaeozoic–Early Mesozoic orogeny in Western Turkey: support for an evolving open-Tethys model. Journal of the Geological Society, 161.3, 501-511.

Rollinson, H.R. 1993. Discriminating between tectonic environments using geochemical data. In: H.R. Rollinson (Ed.), Using geochemical data: Evaluation, presentation, interpretation Longman Sci. Techn., Essex, UK, p. 171-214.

Rotstein,Y. 1984. Counterclockwise rotation of the Anatolian block. Tectonophysics, 108(1-2), 71-91.

Rotstein, Y., and Kafka, A.L. 1982. Seismotectonics of the southern boundary of Anatolia, eastern Mediterranean region: Subduction, collision, and arc jumping. Journal of Geophysical Research: Solid Earth, 87(B9), 7694-7706.

Ryerson, F.J., and Watson, E.B., 1987. Rutile saturation in magmas: implications for Ti–Nb–Ta depletion in island-arc basalts. Earth and Planetary Science Letters,86, 225-239.

Saccani, E. 2015. A new method of discriminating different types of post-Archean ophiolitic basalts and their tectonic significance using Th-Nb and Ce-Dy-Yb systematics. Geosci. Front, 6, 481-501.

Sahin, S. Y., Güngör, Y., Aysal, N., and Öngen, S. 2009. Geochemistry and SHRIMP zircon U–Pb dating of granitoids within the Strandja and Istanbul Zones (NW Turkey). In Abstracts, 62nd Geological Congress of Turkey, Ankara, 598-599.

Salters, V.J.M., and Longhi, J. 1999. Trace element partitioning during the initial stages of melting beneath mid-ocean ridges. Earth and Planetary Science Letters, 166 (1-2), 15-30.

Salters, V.J.M., Longhi, J., and Bizimis, M., 2002. Near mantle solidus trace element partitioning at pressures up to 3.4 GPa. Geochemistry, Geophysics, Geosystems 3 (6). http://dx.doi.org/10.1029/2001GC000148

Sarıfakıoğlu, E., Özen, H., Çolakoğlu, A., and Sayak, H. 2010. Petrology, mineral chemistry, and tectonomagmatic evolution of Late Cretaceous suprasubduction-zone ophiolites in the İzmir–Ankara–Erzincan suture zone, Turkey. International Geology Review, 52(2-3), 187-222.

Sayit, K., Bedi, Y., Tekin, U.K., and Göncüoğlu, M.C. 2017. Middle Triassic back-arc basalts from the blocks in the Mersin Mélange, southern Turkey: Implications for the geodynamic evolution of the northern Neotethys Lithos, 268, 102-113.

Sayit, K., and Göncüoglu, M.C. 2009. Geochemistry of mafic rocks of the Karakaya Complex, Turkey: evidence for plume-involvement in the Palaeotethyan extensional regime during the Middle and Late Triassic. International Journal of Earth Sciences, 98.2, 367-385.

Sayit, K., and Göncüoglu, M.C. 2013. Geodynamic evolution of the Karakaya Mélange Complex, Turkey: A review of geological and petrological constraints. Journal of Geodynamics, 65, 56-65.

Sayit, K., Göncüoğlu, M.C., Ellero, A., Ottria, G., Frassi, C., Marroni, M., and Pandolfi, L. 2021. Late cretaceous arc magmatism in the southern central pontides: Constraints for the closure of the northern neotethyan branches. Ofioliti, 47(1).

Sayit, K., Göncüoğlu, M.C., and Furman, T. 2010. Petrological reconstruction of Triassic seamounts/oceanic islands within the Palaeotethys: geochemical implications from the Karakaya subduction/accretion Complex, Northern Turkey Lithos, 119, 501-511.

Sayit, K., Göncüoglu, M.C., and Tekin, U.K. 2015. Middle Carnian arc-type basalts from the Lycian Nappes, southwestern Anatolia: early Late Triassic subduction in the northern branch of Neotethys. Journal of Geology, 123, 561–579.

Sayit, K., Göncüoğlu, M.C., Ellero, A., Ottria, G., Frassi, C., Marroni, M., and Pandolfi, L. 2022. Late Cretaceous Arc Magmatısm In The Southern Central Pontıdes: Constraınts For The Closure Of The Northern Neotethyan Branches. Ofioliti, 47(1).

Sayit, K., Marroni, M., Göncüoglu, M.C., Pandolfi, L., Ellero, A., Ottria, G., and Frassi, C. 2016. Geological setting and geochemical signatures of the mafic rocks from the Intra-Pontide Suture Zone: implications for the geodynamic reconstruction of the Mesozoic Neotethys. International Journal of Earth Sciences, 1-26.

Sayit, K., Tekin, U.K., and Göncüoglu, M.C. 2011. Early-middle Carnian radiolarian cherts within the Eymir Unit, Central Turkey: Constraints for the age of the Palaeotethyan Karakaya Complex. Journal of Asian Earth Sciences, 42.3, 398- 407.

Schmidberger, S.S., Heaman, L.M., Simonetti, A., Creaser, R.A., and Cookenboo, H.O. 2005. Formation of Paleoproterozoic eclogitic mantle, Slave Province (Canada): insights from in-situ Hf and U–Pb isotopic analyses of mantle zircons. Earth and Planetary Science Letters, 240(3-4), 621-633.

Sevin, M., and Uğuz, M.F. 2011. Çankırı-G32 paftasına ait rapor, No: 148. Maden Tetkik ve Arama Genel Müdürlüğü, Ankara.

Shaw, D.M. 1970. Trace element fractionation during anataxis. Geochimica et Cosmochimica Acta 34, 237–243.

Shervais, J.W., and Kimbrough, D.L. 1985. Geochemical evidence for the tectonic setting of the Coast Range ophiolite: A composite island arc–oceanic crust terrane in western California. Geology, 13(1), 35-38.

Simonetti, A., and Neal, C.R. 2010. In-situ chemical U–Pb dating and Hf isotope investigation of megacrystic zircons, Malaita (Solomon Islands): evidence for multiple stage alkaline magmatic activity beneath the Ontong Java Plateau Earth and Planetary Science Letters, 295, 251-261.

Sipahi, F. 2005. Zigana Dağı (Torul-Gümüşhane) volkanitlerindeki hidrotermal ayrışmaların mineraloji ve jeokimyası, Doktora Tezi, KTÜ Fen Bilimleri Enstitüsü, Trabzon.

Smirnov, V.A. and Nelidov, A.A., 1962. Report on 1:200,000 representing correlation of the Sulaimaniya, Choarta, Penjwin area carried out in 1961. Technoexport Rep., SOM Library No. 290, Baghdad.

Spandler, C., and Pirard, C. 2013. Element recycling from subducting slabs to arc crust: A review. Lithos, 170, 208-223.

Spath, A., Roex, A.P.L., and Duncan, R.A. 1996. The Geochemistry of Lavas from the Gomores Archipelago, Western Indian Ocean: Petrogenesis and Mantle Source Region Characteristics. Journal of Petrology, 37(4), 961-991.

Stampfli, G.M. 2000. Tethyan oceans. E. Bozkurt, J. Winchester, A. Piper (Eds.), Tectonics and Magmatism in Turkey and the Surrounding Area, vol. 173, Geological Society of London, Special Publications, 1-23.

Stampfli, G.M., and Borel, G.D. 2002. A plate tectonic model for the Paleozoic and Mesozoic constrained by dynamic plate boundaries and restored synthetic oceanic isochrons. Earth Planet. Sci. Lett, 196(1–2),17–33.

Stern, R.J. 2010. The anatomy and ontogeny of modern intra-oceanic arc systems. In: Kusky Tm, Zhai MG, Xiao W (eds) The evolving continents: understanding processes of continental growth. Geological Society of London Special Publications 338, 7-34.

Stolper, E., and Newman, S. 1994. The role of water in the petrogenesis of Mariana trough magmas. Earth and Planetary Science Letters, 121(3-4), 293-325.

Stolz, A.J., Jochum, K.P., Spettel, B., and Hofman, A.W. 1996. Fluid and melt related enrichemnt in the subarc mantle: evidence from Nb/Ta variations in island arc basalts. Geology; v.24; no 7; 587-590.

Stolz, A.J., Varne, R., Davies, G.R., Wheller, G.E., and Foden, J.D. 1990. Magma source components in an arc-continent collision zone: the Flores-Lembata sector, Sunda arc, Indonesia. Contributions to Mineralogy and Petrology, 105(5), 585-601.

Stracke, A., Hofmann, A.W., and Hart, S.R. 2005. FOZO, HIMU, and the rest of the mantle zoo. Geochemistry, geophysics, geosystems, 6(5).

Sun, S.S., and McDonough, W.F. 1989. Chemical and isotopic systematics of oceanic basalts: implications for mantle composition and processes. Geological Society, London, Special Publications, 42.1, 313-345.

Sunal, G. 2012. Devonian magmatism in the western Sakarya Zone, Karacabey region, NW Turkey. Geodin Acta 25:183–201.

Şengör, A.M.C. 1979. Mid-Mesozoic closure of PermoTriassic Tethys and its implications. Nature 279: 590–593.

Şengör, A.M.C. 1984. The Cimmeride orogenic system and the tectonics of Eurasia. Geological Society of America Special Papers, 195, 1-74.

Şengör, A.M.C., Altıner, D., Cin, A., Ustaömer, T., and Hsü, K.J. 1988. Origin and assembly of the Tethyside orogenic collage at the expense of Gondwana Land, Geological Society, London, Special Publications, 37, 119-181, https://doi.org/10.1144/GSL.SP.1988.037.01.09

Şengör, A.M.C., Burke, K., and Dewey, J.F. 1982. Tectonics of the North Anatolian Transform Fault. See Işıkara and Vogel, 1982, 3–22.

Şengör, A.M.C., Büyükaşikoğlu, S., and Canitez, N. 1983. Neotectonics of the Pontides: implications for 'incompatible'structures along the North Anatolian fault. Journal of Structural Geology, 5(2), 211-216.

Şengör, A.M.C., Görür, N., and Şaroğlu, F. 1985. Strikeslip faulting and related basin formation in zones of tectonic escape: Turkey as a case study. In Strike-slip Deformation, Basin Formation, and Sedimentation, Soc. Econ. Paleontol. Miner. Spec. Publ. 37 (in honor of J.C. Crowell), ed. KT Biddle, N Christie-Blick, 227–64.

Şengör, A.M.C., and Kidd, W.S.F. 1979. Post-collisional tectonics of the Turkish-Iranian plateau and a comparison with Tibet. Tectonophysics, 55(3-4), 361-376.

Şengör, A.M.C., Özeren, S., Genç, T., and Zor, E. 2003. East Anatolian high plateau as a mantle-supported, north-south shortened domal structure. Geophysical Research Letters, 30(24).

Şengör, A.M.C., Tüysüz, O., İmren, C., Sakınç, M., Eyidoğan, H., Görür, N., Pichon, X.L., and Rangin, C. 2005. The North Anatolian fault: A new look. Annu. Rev. Earth Planet. Sci. 33, 37-112.

Şengör, A.M.C. and Yılmaz, Y. 1981. Tethyan evolution of Turkey: A plate tectonic approach. Tectonophysics, 75, 181-241.

Şengör, A.M.C., Yılmaz, Y., and Ketin, I. 1980. Remnants of a pre-Late Jurassic ocean in northern Turkey: Fragments of Permian-Triassic Paleo-Tethys. Geological Society of America Bulletin, 91, 599-609.

Şengör, A.M.C., Yılmaz, Y., and Sungurlu, O. 1984. Tectonics of the Mediterranean Cimmerides: nature and evolution of the western termination of Paleo-Tethys. In: Dixon, J.E., and Robertson, A.H.F., (eds.), The Geological Evolution of the Eastern Mediterranean. Geological Society, London, Special Publications, 17, 77-112.

Şengün, M., Akçaöre, F., Keskin, H., Akat, U., Altun, İ.E., Deveciler, E., Sevin, M., Armağan, F., Erdoğan, K., Acar, Ş., and Gündüz, H. 1988. Daday-Kastamonuİnebolu yöresinin jeolojisi. MTA Raporu, No: 8994 (yayımlanmamış).

Tatsumi, Y., Hamilton, D.L., and Nesbitt, R.W. 1986. Chemical characteristics of fluid phase released from a subducted lithosphere and origin of arc magmas: evidence from high-pressure experiments and natural rocks. Journal of Volcanology and Geothermal Research, 29(1-4), 293-309.

Tatsumoto, M. 1966. Genetic relations of oceanic basalts as indicated by lead isotopes. Science, 153(3740), 1094-1101.

Tatsumoto, M., Hedge, C.E., and Engel, A.E.J. 1965. Potassium, rubidium, strontium, thorium, uranium, and the ratio of strontium-87 to strontium-86 in oceanic tholeiitic basalt. Science, 150(3698), 886-888.

Taylor, B., and Martinez, F. 2003. Back-arc basin basalt systematics. Earth and Planetary Science Letters, 210(3-4), 481-497.

Taylor, R.N., and Nesbitt, R.W. 1998. Isotopic characteristics of subduction fluids in an intra-oceanic setting, Izu–Bonin Arc, Japan. Earth and Planetary Science Letters, 164(1-2), 79-98.

Taylor, S.R., and McLennan, S.M. 1985. The continental crust. Its composition and evolution; an examination of the geochemical record preserved in sedimentary rocks. Blackwell, Oxford, 312.

Taylor, S.R., and McLennan, S.M. 1995. The geochemical evolution of the continental crust. Reviews of Geophysics, 33.2, 241-265.

Taymaz, T., Jackson, J. A., and McKenzie, D. 1991. Active tectonics of the north and central Aegean Sea. Geophysical Journal International, 106, 433–490.

Tekin, U.K., Bedi, Y., Okuyucu, C., Göncüoglu, M.C., Sayit, K. 2016b. Radiolarian biochronology of upper Anisian to upper Ladinian (Middle Triassic) blocks and tectonic slices of volcano-sedimentary successions in the Mersin Mélange, southern Turkey: new insights for the evolution of Neotethys. Journal of African Earth Sciences, 124, 409-426.

Tekin, U.K., and Göncüoglu, M.C. 2007. Discovery of the oldest (Upper Ladinian to Middle Carnian) radiolarian assemblages from the Bornova flysch zone in western Turkey: implications for the evolution of the Neotethyan Izmir-Ankara ocean. Ofioliti, 32(2), 131-150.

Tekin, U.K., Göncüoğlu, M.C., Pandolfi, L., and Marroni, M. 2012. Middle-Late Triassic radiolarian cherts from the Arkotdağ mélange in northern Turkey: implications for the life span of the northern Neotethyan branch. Geodinamica Acta, 25(3-4), 305-319.

Tekin U.K., Göncüoglu M.C. and Turhan N. 2002. First evidence of Late Carnian radiolarian fauna from the Izmir-Ankara Suture Complex, Central Sakarya, Turkey: Implications for the opening age of the Izmir-Ankara branch of Neotethys. Geobios, 35.1, 127-135.

Tekin, U.K., Okuyucu, C., Sayit, K., Bedi, Y., Noble, P. J., Krystyn, L., and Göncüoglu, M.C. 2019. Integrated radiolaria, benthic foraminifera and conodont biochronology of the pelagic Permian blocks/tectonic slices and geochemistry of associated volcanic rocks from the Mersin Mélange, southern Turkey: implications for the Permian evolution of the northern Neotethys. Island Arc 28:e12286.

Thompson, G. 1991. Metamorphic and hydrothermal processes: basalt—seawater interactions. In Oceanic basalts (148-173). Springer, Dordrecht.

Topuz, G., Altherr, R., Schwarz, W.H., Dokuz, A., and Meyer, H.P. 2007. Variscan amphibolite-facies rocks from the Kurtoğlu metamorphic complex (Gümüşhane area, Eastern Pontides, Turkey). International Journal of Earth Sciences, 96(5), 861-873.

Topuz, G., Altherr, R., Siebel, W., Schwartz, W.H., Zack, T., Hasözbek, A., Barth, B., Satır, M., and Sen, C. 2010. Carboniferous high-potassium I-type granitoid magmatism in the Eastern Pontides: the Gümüs¸hane pluton (NE Turkey). Lithos, 116,92-110.

Topuz, G., Göçmengil, G., Rolland, Y., Çelik, Ö.F., Zack, T., and Schmitt A.K. 2013. Jurassic accretionary complex and ophiolite from northeast Turkey: no evidence for the Cimmerian continent. Geology,41,255-258.

Treuil, M., and Varet, J. 1973. Criteres volcanologiques, petrologiques et geochimiques de la genese et de la differenciation des magmas basaltiques; exemple de l'Afar. Bulletin de la Société géologique de France, 7(5-6), 506-540.

Turhan, N., Okuyucu, C., and Göncüoğlu M.C. 2004. Autochthonous upper permian (midian) carbonates in the western sakaraya composite terrane. Geyve area, Turkey. Preliminary data. Turk J Earth Sci, 13,215–230.

Turner, S., Hawkesworth, C., Rogers, N., Bartlett, J., Worthington, T., Hergt, J., and Smith, I. 1997. 238U 230Th disequilibria, magma petrogenesis, and flux rates beneath the depleted Tonga-Kermadec island arc. Geochimica et Cosmochimica Acta, 61(22), 4855-4884.

Turner, S., Hawkesworth, C., Van Calsteren, P., Heath, E., Macdonald, R., and Black, S. 1996. U-series isotopes and destructive plate margin magma genesis in the Lesser Antilles. Earth and Planetary Science Letters, 142(1-2), 191-207.

Türkecan, A., Hepşen, N., Papak, I, Akbaş, B., Dinçel, A., Karataş, S., Özgür, İ, Akay, E., Bedi, Y., Sevin, M., Mutlu, G., Sevin, D., Ünay, E., and Saraç, G. 1991. Seben-Gerede (Bolu)-Güdül-Beypazarı (Ankara) ve Çerkeş-Orta-Kurşunlu (Çankırı) Yörelerinin (Köroğlu Dağları) Jeolojisi ve Volkanik Kayaçlarının Petrolojisi [Geology of Seben-Gerede (Bolu)-Güdül-Beypazarı (Ankara) ve Çerkeş-Orta Kurşunlu (Çankırı) Regions (Köroğlu Mountains) and Petrology of Volcanic Rocks]. Mineral Research and Exploration Institute of Turkey Report, No. 9193, 118 p [unpublished, in Turkish]

Tüysüz, O. 1985. Kargı Masifi ve dolayındaki tektonik birliklerin ayırdı ve araştırılması (petrolojik inceleme). Diss. PhD thesis, Istanbul University Institute of Science, 431 pp. (unpublished).

Tüysüz, O. 1990. Tectonic evolution of a part of the Tethyside orogenic collage: the Kargi Massif, northern Turkey. Tectonics, 9.1, 141-160.

Tüysüz, O. 1993. Karadeniz'den Orta Anadolu'ya bir jeotravers: kuzey Neo-Tetisin tektonik evrimi (A geotraverse from the Black Sea to the Central Anatolia: Tectonic evolution of the northern Neo-Tethys). TPJD Bülteni, Turkish Association of Petroleum Geologists Bulletin, 5, 1-33.

Tüysüz, O. 1999. Geology of the Cretaceous sedimentary basins of the Western Pontides Geological Journal, 34, 75-93.

Tüysüz, O., Dellaloğlu, A.A., and Terzioğlu, N. 1995. A magmatic belt within the Neo-Tethyan suture zone and its role in the tectonic evolution of northern Turkey. Tectonophysics, 243 (1-2), 173-191.

Tüysüz, O., and Tekin, U.K. 2007. Timing of imbrication of an active continental margin facing the northern branch of Neotethys, Kargı Massif, northern Turkey. Cretaceous Research, 28.5, 754-764.

Tüysüz, O., and Yiğitbaş, E. 1994. The Karakaya basin: a Palaeo-Tethyan marginal basin and its age of opening. Acta Geologica Hungarica, 37.3-4, 327-350.

Tüysüz, O., Yiğitbaş, E., and Serdar, H.S. 1988. Vezirkörpü-Boyabat dolayının jeolojisi. TPAO Rap.

Uğuz, M.F., and Sevin, M. 2007. Türkiye Jeoloji Haritaları, Kastamonu-E32 Paftası Jeoloji Etütleri Dairesi, 32 (in Turkish).

Ural, M., Arslan, M., Göncüoglu, M.C., Tekin, U.K., and Kürüm, S. 2015. Late Cretaceous arc and back-arc formation within the Southern Neotethys: whole-rock, trace element and Sr-Nd-Pb isotopic data from basaltic rocks of the Yüksekova Complex (Malatya-Elazığ, SE Turkey). Ofioliti, 40(1).

Ural, M., Sayit, K., Koralay, O.E., and Goncuoglu, M.C. 2021. Geochemistry and Zircon U-Pb Dates of Felsic-Intermediate Members of the Late Cretaceous Yüksekova Arc Basin: Constraints on the Evolution of the Bitlis–Zagros Branch of Neotethys (Elazığ, E Turkey). Acta Geologica Sinica-English Edition, 95(4), 1199-1216.

Ustaömer, T., and Robertson, A.H.F. 1993. A Late Palaeozoic-Early Mesozoic marginal basin along the actives sourthern continental margin of Eurasia: Evidence from the central Pontides (Turkey) and adjacent regions. Geological Journal, 28.3- 4, 219-238.

Ustaömer, T., and Robertson, A.H.F. 1994. Late Palaeozoic marginal basin and subduction-accretion: The Palaeotethyan Küre complex, central Pontides, northern Turkey. Journal of the Geological Society, 151(2), 291-305.

Ustaömer, T., and Robertson, A.H.F. 1997. Tectonic-sedimentary evolution of the north tethyan margin in the Central Pontides of northern Turkey. AAPG Mem 68, 255-290.

Ustaömer, T., and Robertson A.H.F. 1999. Geochemical evidence used to test alternative plate tectonic models for pre-Upper Jurassic (Palaeotethyan) units in the Central Pontides, N Turkey. Geol J, 34, 25-53.

Ustaömer, P.A., and Rogers, G. 1999. The Bolu Massif: remnant of a pre-Early Ordovician active margin in the west Pontides, northern Turkey. Geological Magazine, 136.5, 579-592.

Ustaömer, P.A., Ustaömer, T., and Robertson, A.H.F. 2012. Ion Probe U-Pb dating of the Central Sakarya Basement: a peri-Gondwana terrane intruded by Late Lower Carboniferous subduction/collision-related granitic rocks. Turkish Journal of Earth Sciences, 21.6, 905-932.

Ustaömer, T., Ustaömer, P.A., Robertson, A.H., and Gerdes, A. 2016. Implications of U–Pb and Lu–Hf isotopic analysis of detrital zircons for the depositional age, provenance and tectonic setting of the Permian–Triassic Palaeotethyan Karakaya Complex, NW Turkey. International Journal of Earth Sciences, 105(1), 7-38.

Üner, T., Çakır, U., Özdemir, Y., and Arat, I. 2014. Geochemistry and origin of plagiogranites from the Eldivan Ophiolite, Çankırı (Central Anatolia, Turkey). Geologica Carpathica, 65, 197-207.

Vernon, R.H. 2004. A Practical Guide to Rock Microstructure, Cambridge University Press.

Walker, J.A., Teipel, A.P., Ryan, J.G., and Syracuse, E. 2009. Light elements and Li isotopes across the northern portion of the Central American subduction zone. Geochemistry, Geophysics, Geosystems, 10(6). https://doi.org/10.1029/2009GC002414

Weaver, B.L. 1991. The origin of ocean island basalt end-member compositions: trace element and isotopic constraints Earth and Planetary Science Letters, 104, 381-397

White, W.M. 1985. Sources of oceanic basalts—radiogenic isotopic evidence Geology, 13, 115-118.

White, W.M., and Schilling, J.G. 1978. The nature and origin of geochemical variation in Mid-Atlantic Ridge basalts from the central North Atlantic. Geochimica et Cosmochimica Acta, 42(10), 1501-1516.

Wilson, M. 1989. Igneous Petrogenesis. London: Unwin Hyman, 466 pp.

Williams, P. F. (1972). Pressure shadow structures in foliated rocks from Bermagui, New South Wales. Journal of the Geological Society of Australia, 18(4), 371-377.

Winchester, J.A., and Floyd, P.A. 1977. Geochemical discrimination of different magma series and their differentiation products using immobile elements. Chemical geology, 20, 325-343.

Winter, J.D. 2001. An introduction to igneous and metamorphic petrology, 699 pp.

Wood, D.A., Gibson, I.L., and Thompson, R.N. 1976. Elemental mobility during zeolite facies metamorphism of the Tertiary basalts of eastern Iceland. Contributions to Mineralogy and Petrology, 55(3), 241-254.

Wood, S.D., Joron, J.J., Trueil, M., Norry, M., and Tarney, J. 1979. Elemental and Sr isotope variations in basic lavaş from Iceland and surrounding ocean floor. The nature of mantle source heterogeneities. Contributions to Mineralogy and Petrology 70, 319-340.

Woodhead, J.D., Hergt, J.M., Davidson, J.P., and Eggins, S.M. 2001. Hafnium isotope evidence for 'conservative'element mobility during subduction zone processes. Earth and Planetary Science Letters, 192(3), 331-346.

Workman, R.K., and Hart, S.R., 2005. Major and trace element composition of the depleted MORB mantle (DMM). Earth and Planetary Science Letters 231, 53–72.

Yalınız, M.K., Floyd, P.A., and Göncüoğlu, M.C. 1996. Supra-subduction zone ophiolites of central Anatolia: geochemical evidence from the Sarıkaraman ophiolite, Aksaray, Turkey Mineralogical Magazine, 60, 697-710.

Yanev, S., Göncüoğlu, M.C., Gedik, I., Lakova, I., Boncheva, I., Sachanski, V., and Saydam, G. 2006. Stratigraphy, correlations and palaeogeography of Palaeozoic terranes of Bulgaria and NW Turkey: a review of recent data. Geological Society, London, Special Publications, 260(1), 51-67.

Yazgan, E. (1972). Etude geologique et petrographique du complexe ophiolitique de la region situee au Sud-Est de Malatya (Taurus oriental, Turquie) et da sa couverture volcano-sedimentaire. (Phd thesis) Univ. De Geneve.

Yılmaz, O. 1980. Daday-Devrakani masifi kuzeydoğu kesimi litostratigrafi birimleri ve tektoniği. Yerbilimleri, 5, 101-135 (in Turkish).

Yılmaz, O. 1983. Çangal metaofiyolitinin mineralojik-petrografik incelenmesi ve metamorfizma koşulları. Yerbilimleri, 10, 45-58 (in Turkish).

Yılmaz, O. 1988. L'ensemble ophiolitique de Çangal (Turquie du Nord): Mise en évidence d'un métamorphisme océanique et d'un rétrométamorphisme cataclastique tardif. Geologie Alpine, 64, 113-132 (in French with abstract in English).

Yılmaz, O., and Bonhomme, M.G. 1991. K-Ar isotopic age evidence for a Lower to Middle Jurassic low-pressure and a Lower Cretaceous high-pressure metamorphic events in north-central Turkey. Terra Abstracts,3, 501.

Yılmaz, O, and Boztuğ, D. 1986. Kastamonu granitoid belt of northern Turkey: first arc plutonism product related to the subduction of the Paleo-Tethys Geology, 14, 179-183.

Yılmaz, O., and Boztuğ, D. 1987. Petrography, petrochemistry and solidification sequences of the Ağlı pluton from the Kastamonu granitoid belt, northern Turkey, Yerbilimleri, 14, 91-107.

Yılmaz, Y. 1990. Allochthonous terranes in the Tethyan Middle East, Anatolia and surrounding regions. PhilosTrans R Soc Lond A 331:611–624.

Yılmaz Y, Genc S. C., Yiğitbas¸ E., Bozcu, M., and Yilmaz, K. 1995. Geological evolution of the late Mesozoic continental margin of Northwestern Anatolia. Tectonophysics, 243,155-1.

Yılmaz, Y., and Şengör, A.M.C., 1985. Palaeo-Tethyan ophiolites in northern Turkey: Petrology and tectonic setting. Ofioliti, 10, 485-504.

Yılmaz, Y., and Tüysüz, O. 1984. Kastamonu-Boyabat-Vezirköprü-Tosya arasındaki bölgenin jeolojisi (Ilgaz-Kargı masiflerinin etüdü). MTA rapor No. 7838.

Yılmaz, Y., and Tüysüz, O. 1991. Geology of the Kargı massif, central pontides. Bull. Tech. Univ. Istanbul, 1(44), 279-299.

Yılmaz, Y., Tüysüz, O., Yiğitbas, E., Genç S.C, and Sengör A.M.C. 1997. Geology and tectonic evolution of the Pontides. In: Robinson AG (ed) Regional and Petroleum geology of the Black Sea and surrounding region. Bull Am Ass Petrol Geol 68:183–226.

Yılmaz Y., Yiğitbaş E., and Genç Ş.C. 1993. Ophiolitic and metamorphic assemblages of southeast Anatolia and their significance in the geological evolution of the orogenic belt Tectonics, 12, 1280-1297.

Yiğitbaş, E., Elmas, A., and Yilmaz, Y. 1999. Pre-Cenozoic tectono-stratigraphic components of the Western Pontides and their geological evolution. Geological Journal, 34(1-2), 55-74.

Yoldaş, R. 1982. Tosya (Kastamonu) ile Bayat (Çorum) arasındaki bölgenin jeolojisi: Ph.D. Thesis. İstanbul Üniversitesi, 311.

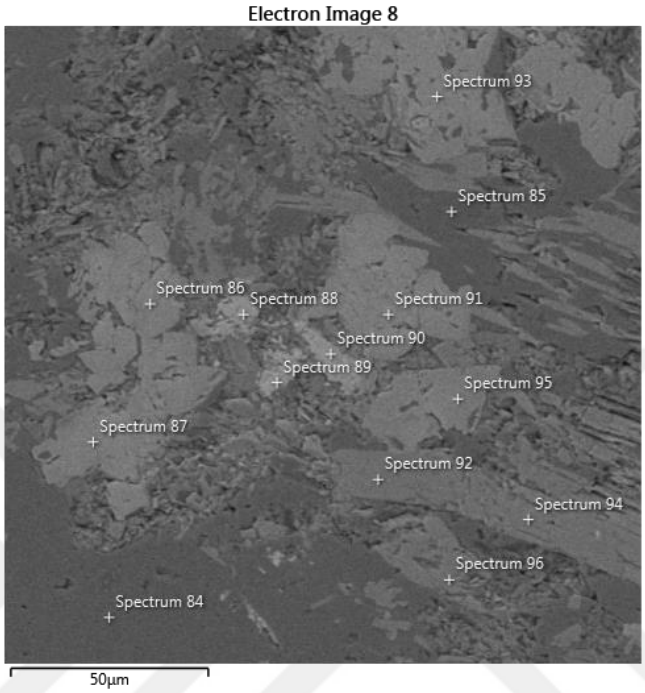
Yücel, C. 2017. Akçaabat (Trabzon) Güneyi ve Çevresindeki Kampaniyen Yaşlı Volkanik Kayaçların Petrografisi, Jeokimyası, Jeokronolojisi ve Petrojenezi. Gümüşhane Üniversitesi Fen Bilimleri Enstitüsü Dergisi, 7(1), 79-101.

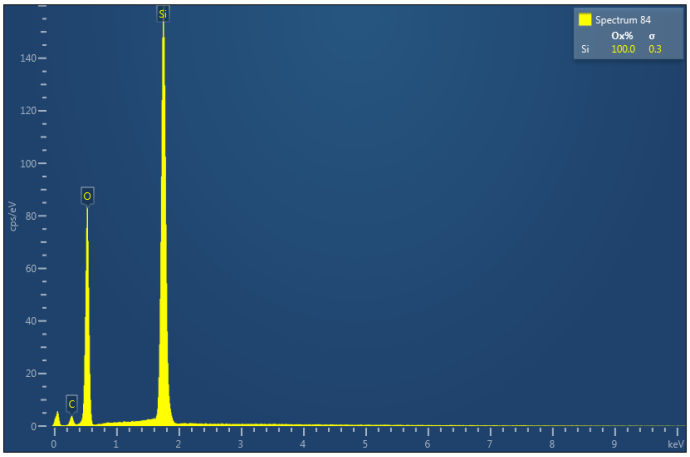
Zachariah, J.K., Balakrishnan, S., and Rajamani, V. 1997. Significance of Sm-Nd isotope systematics in crustal genesis: A case study of Archaean metabasalts of the eastern Dharwar Craton. Proceedings of the Indian Academy of Sciences-Earth and Planetary Sciences, 106(4), 361-367.

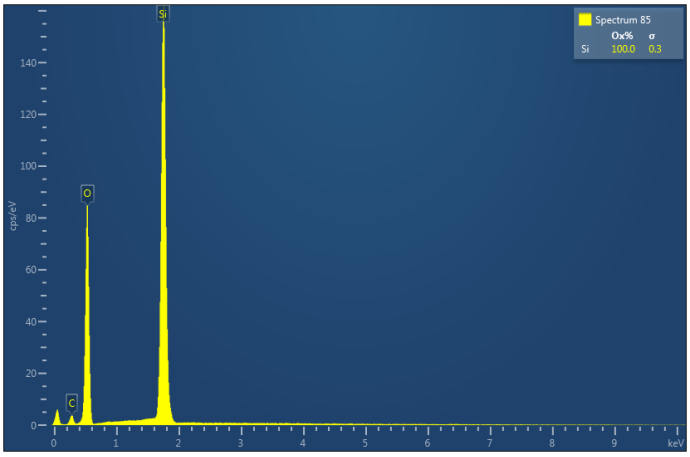
Zindler, A., and Hart, S. 1986. Chemical geodynamics. Annual Review of Earth and Planetary Sciences 14, 493–571.

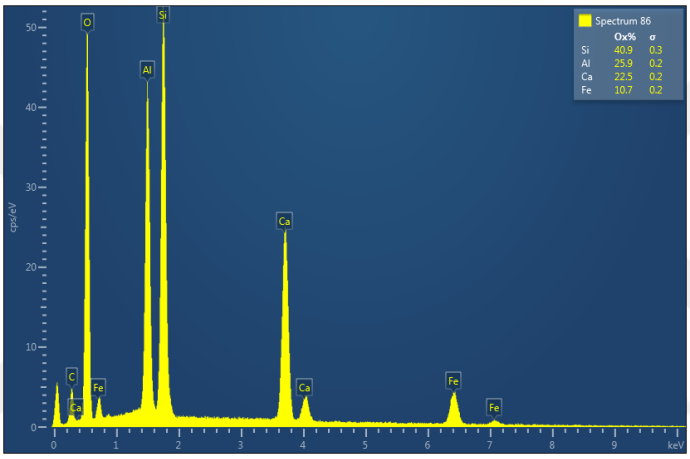
A. SEM-EDS Analysis

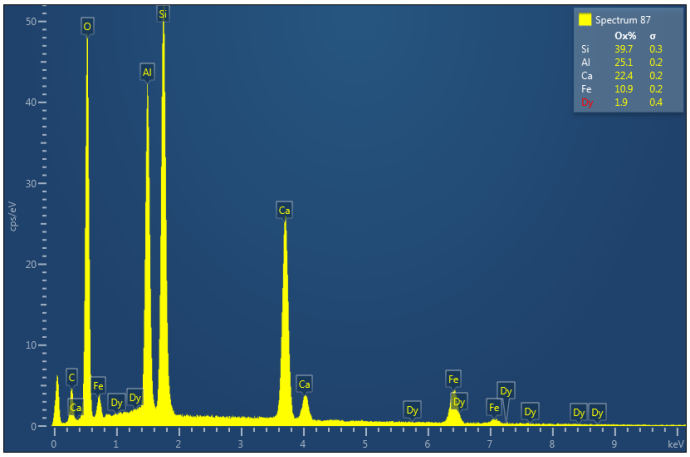
Sample AB-6-18

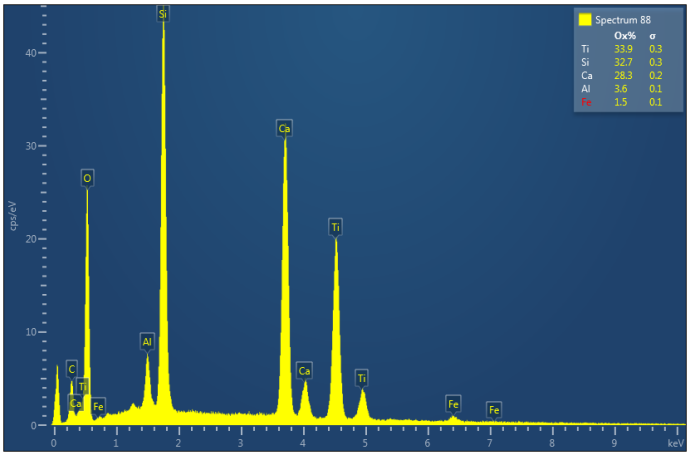


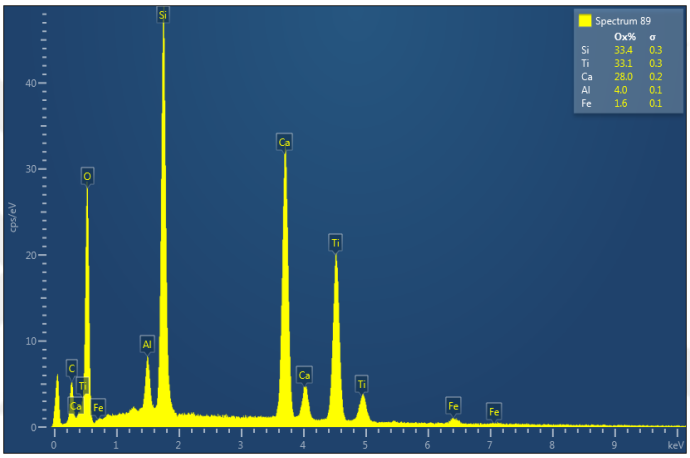


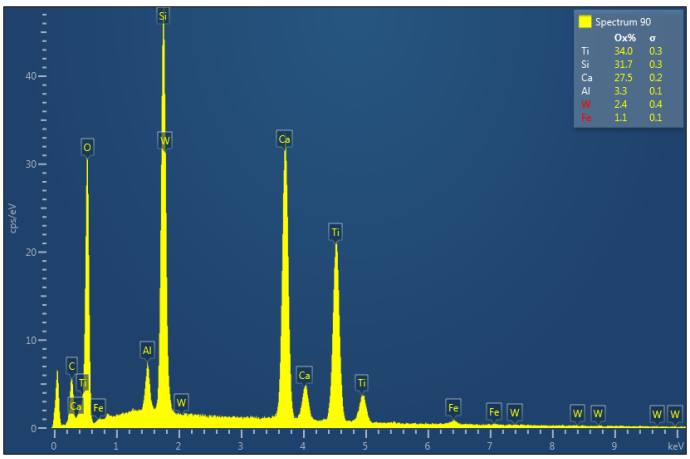

Spectrum 85
Ox%
σ
Si 100.0 0.3
Si
O
C
cps/eV
keV

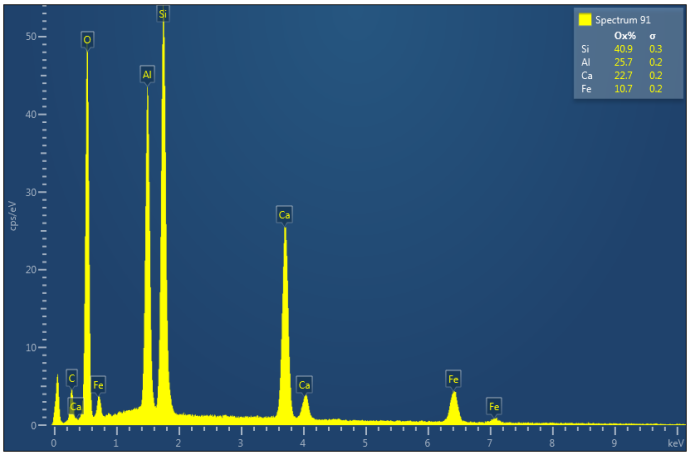

Spectrum 86
Ox%
σ
Si 40.9 0.3
Al 25.9 0.2
Ca 22.5 0.2
Fe 10.7 0.2
O
Si
Al
Ca
C
Fe
Ca
Fe
Fe
cps/eV
keV

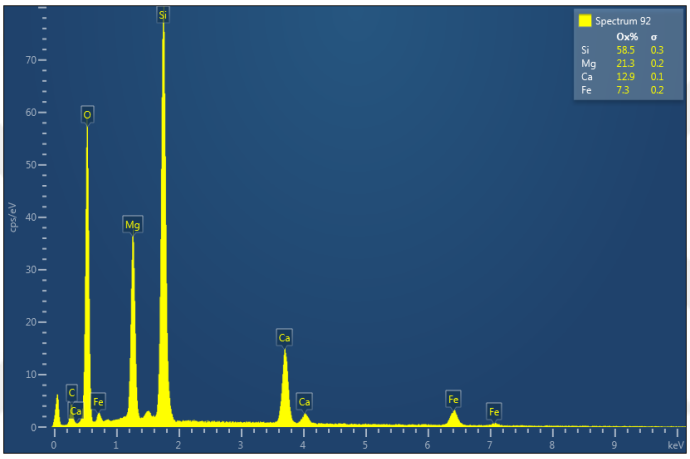

Spectrum 87
Ox%
σ
Si 39.7 0.3
Al 25.1 0.2
Ca 22.4 0.2
Fe 10.9 0.2
Dy 1.9 0.4
O
Si
Al
Ca
C
Fe
Ca
Dy
Dy
Dy
Fe
Dy
Fe
Dy
Dy
Dy
Dy
cps/eV
keV

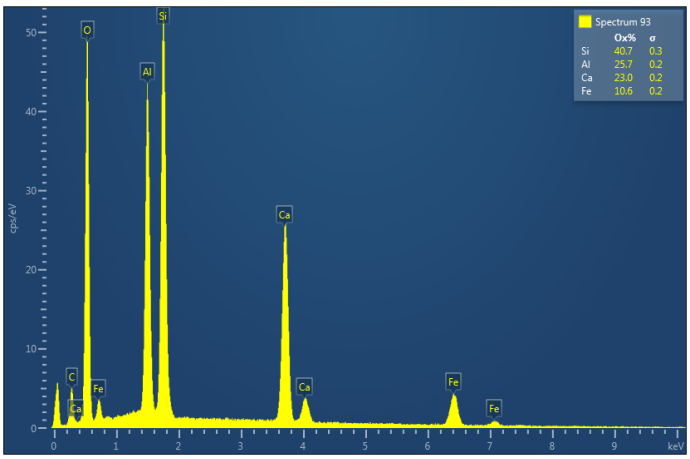

Spectrum 88
Ox%
σ
Ti 33.9 0.3
Si 32.7 0.3
Ca 28.3 0.2
Al 3.6 0.1
Fe 1.5 0.1
cps/eV
keV

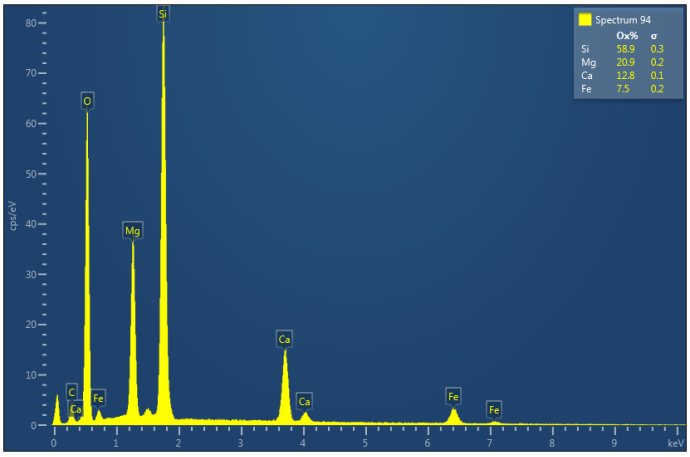

Spectrum 89
Ox%
σ
Si 33.4 0.3
Ti 33.1 0.3
Ca 28.0 0.2
Al 4.0 0.1
Fe 1.6 0.1
cps/eV
keV

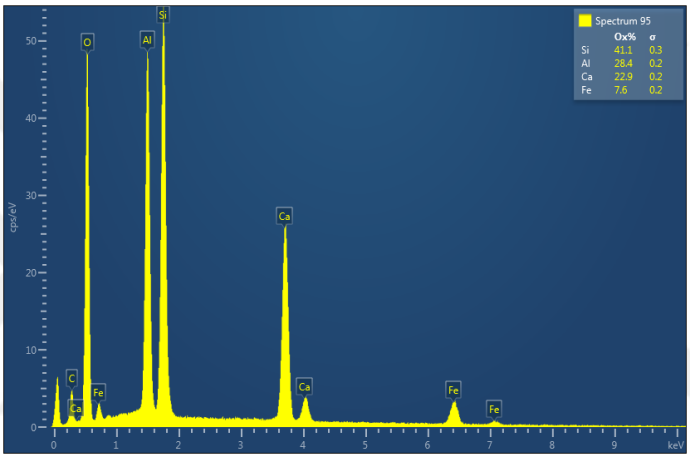

Spectrum 90
Ox%
σ
Ti 34.0 0.3
Si 31.7 0.3
Ca 27.5 0.2
Al 3.3 0.1
W 2.4 0.4
Fe 1.1 0.1
cps/eV
keV

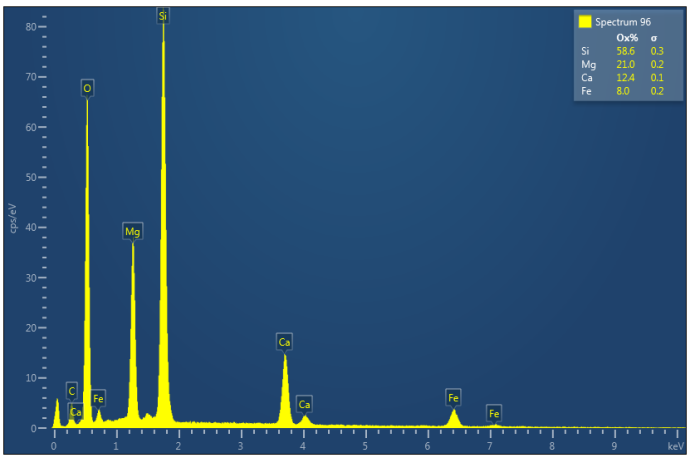

Spectrum 91
Ox%
σ
Si 40.9 0.3
Al 25.7 0.2
Ca 22.7 0.2
Fe 10.7 0.2
cps/eV
keV
O
Si
Al
Ca
C
Fe
Ca
Ca
Fe
Fe


Spectrum 92
Ox%
σ
Si 58.5 0.3
Mg 21.3 0.2
Ca 12.9 0.1
Fe 7.3 0.2
cps/eV
keV
O
Si
Mg
Ca
C
Fe
Ca
Ca
Fe
Fe

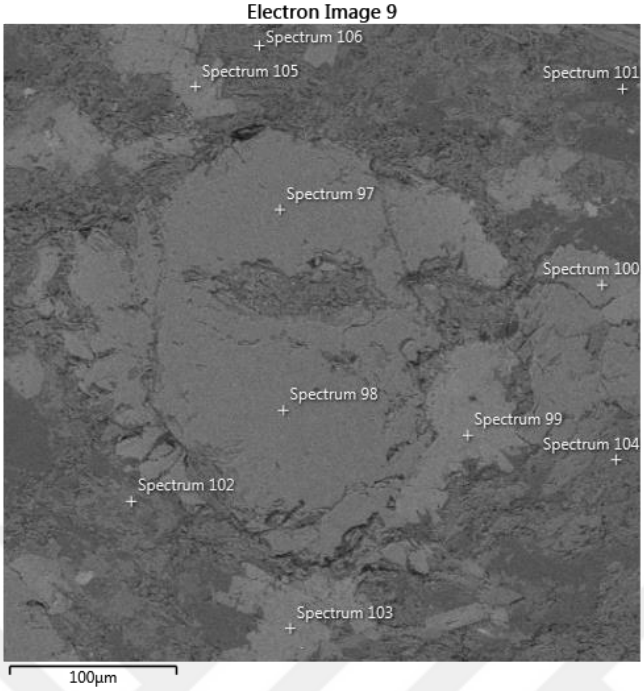

Spectrum 93
Ox%
σ
Si 40.7 0.3
Al 25.7 0.2
Ca 23.0 0.2
Fe 10.6 0.2
cps/eV
keV
O
Si
Al
Ca
C
Fe
Ca
Ca
Fe
Fe

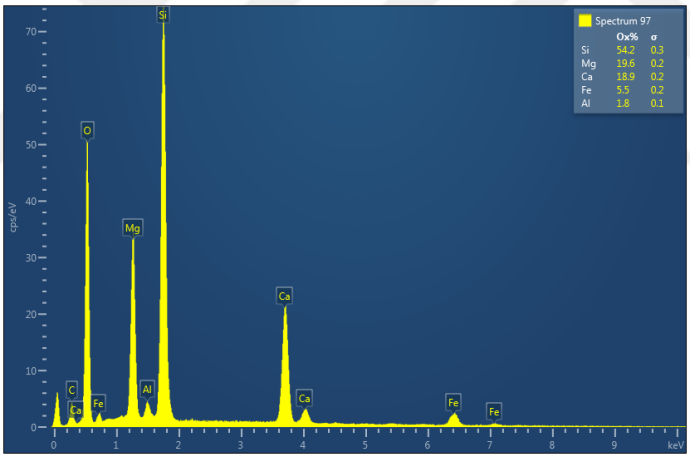

Spectrum 94
Ox%
σ
Si 58.9 0.3
Mg 20.9 0.2
Ca 12.8 0.1
Fe 7.5 0.2
cps/eV
keV
O
Si
Mg
Ca
C
Fe

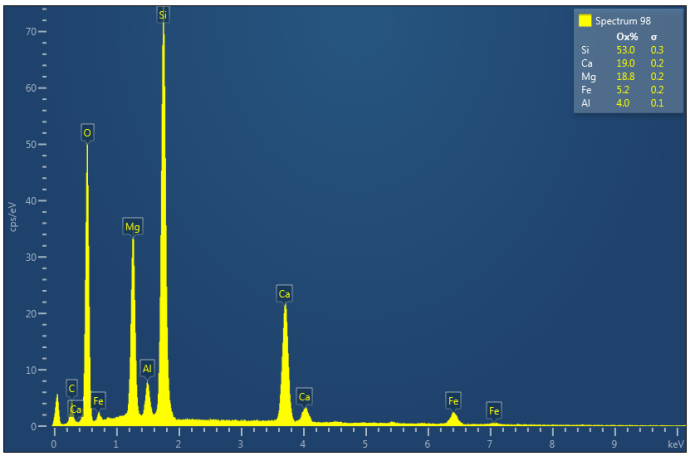

Spectrum 95
Ox%
σ
Si 41.1 0.3
Al 28.4 0.2
Ca 22.9 0.2
Fe 7.6 0.2
cps/eV
keV
O
Si
Al
Ca
C
Fe

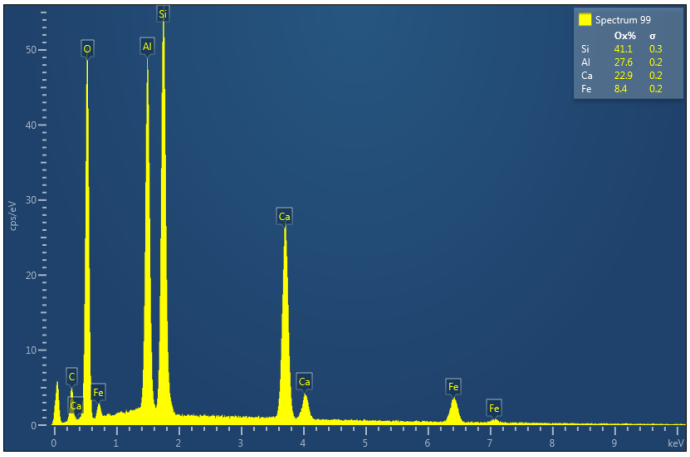

Spectrum 96
Ox%
σ
Si 58.6 0.3
Mg 21.0 0.2
Ca 12.4 0.1
Fe 8.0 0.2
cps/eV
keV
O
Si
Mg
Ca
C
Fe

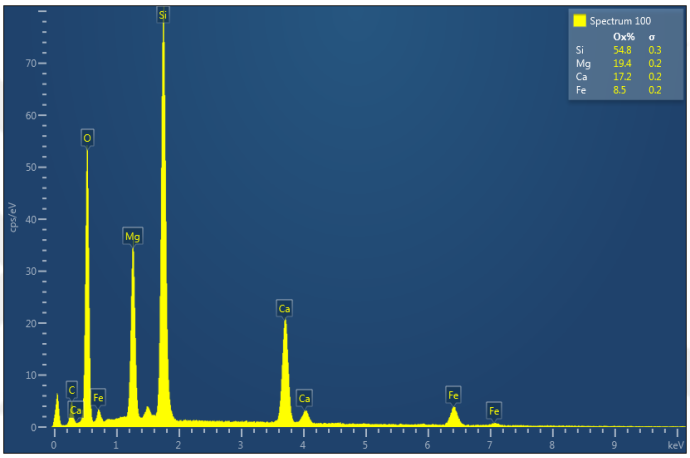
Electron Image 9

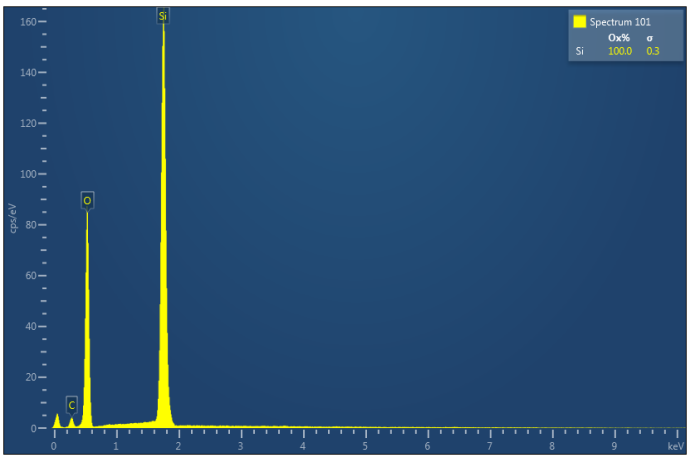


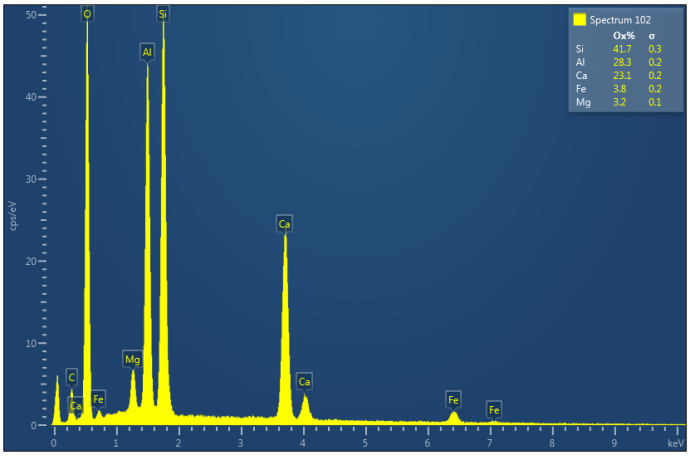


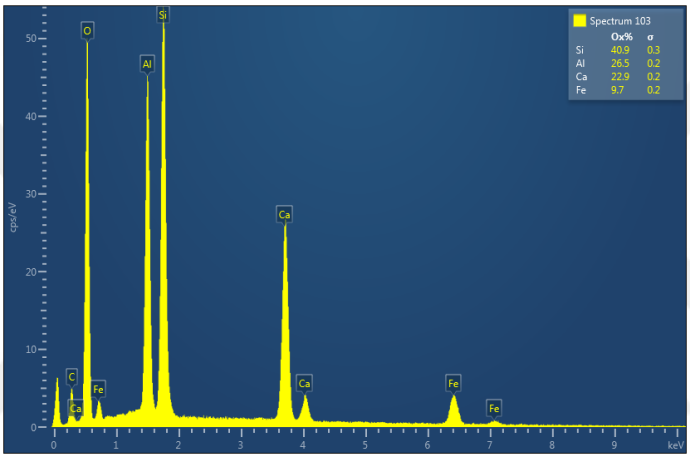


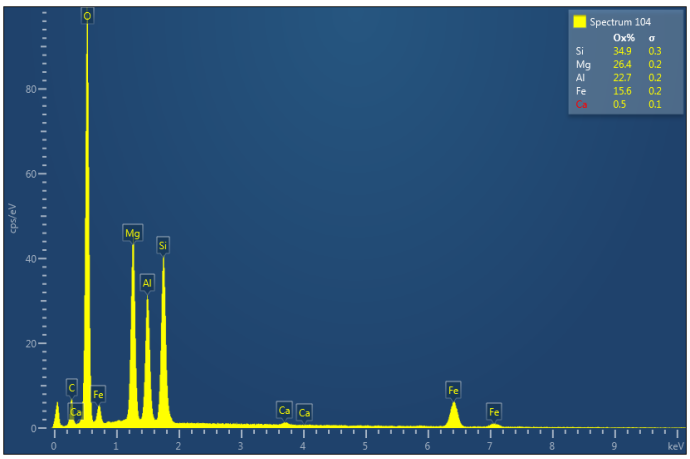

Spectrum 99
Ox% σ
Si 41.1 0.3
Al 27.6 0.2
Ca 22.9 0.2
Fe 8.4 0.2
cps/eV
keV
O
Si
Al
Ca
C
Fe

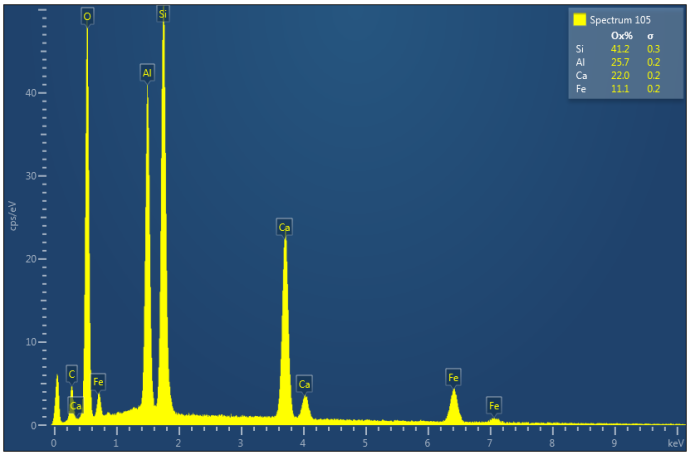

Spectrum 100
Ox% σ
Si 54.8 0.3
Mg 19.4 0.2
Ca 17.2 0.2
Fe 8.5 0.2
cps/eV
keV
O
Si
Mg
Ca
C
Fe

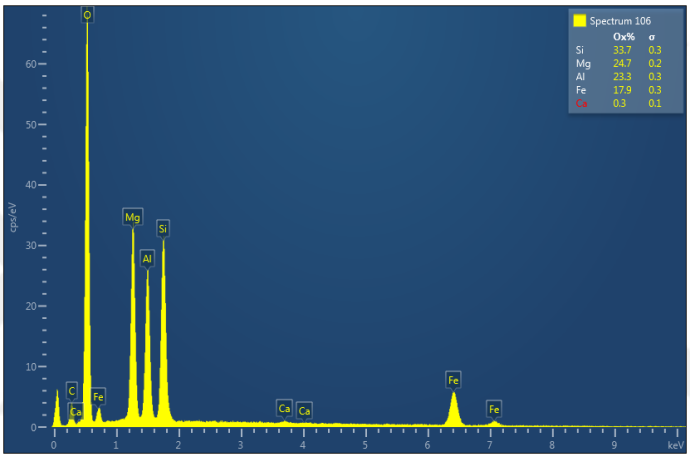

Spectrum 101
Ox% σ
Si 100.0 0.3
cps/eV
keV
O
Si
C

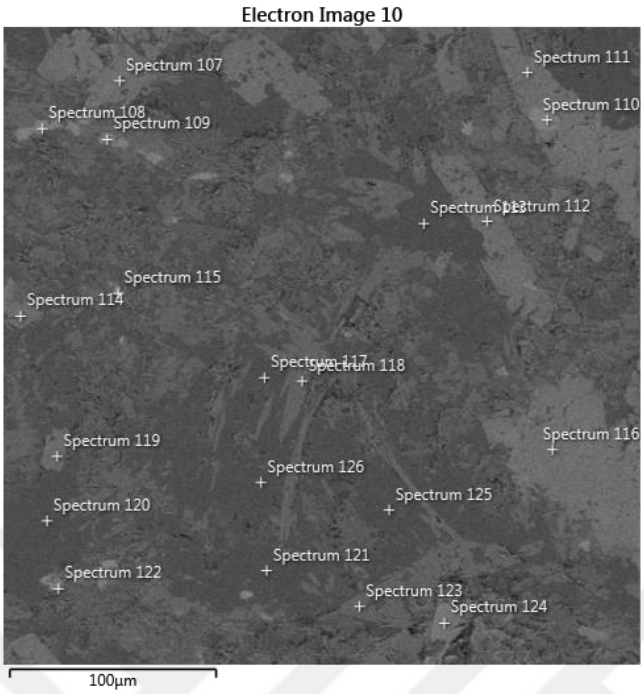

Spectrum 102
Ox% σ
Si 41.7 0.3
Al 28.3 0.2
Ca 23.1 0.2
Fe 3.8 0.2
Mg 3.2 0.1
O
Si
Al
Mg
C
Ca
Fe
cps/eV
keV

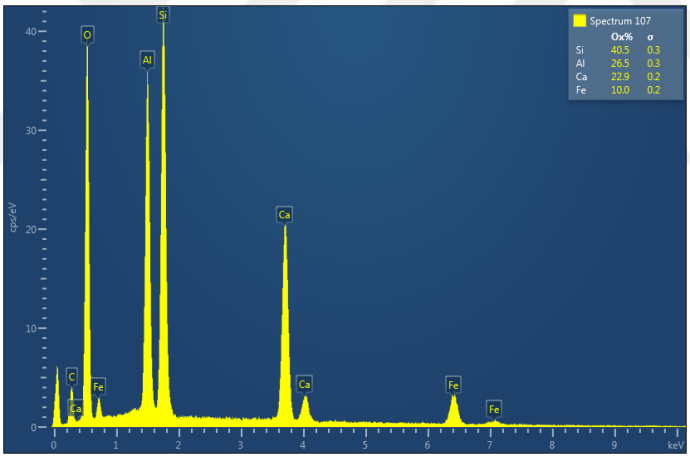

Spectrum 103
Ox% σ
Si 40.9 0.3
Al 26.5 0.2
Ca 22.9 0.2
Fe 9.7 0.2
O
Si
Al
C
Ca
Fe
cps/eV
keV

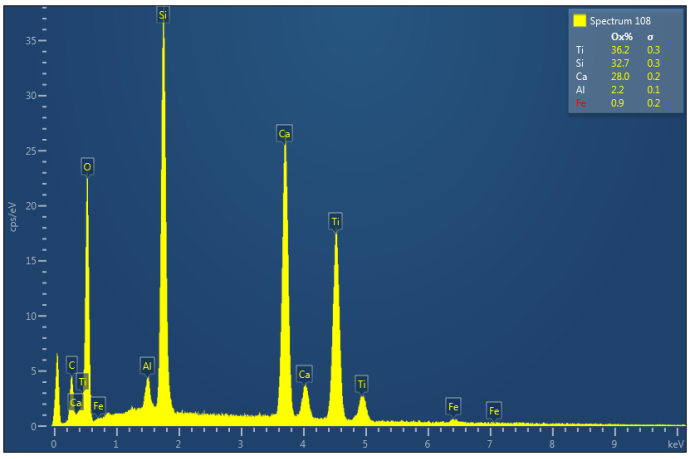

Spectrum 104
Ox% σ
Si 34.9 0.3
Mg 26.4 0.2
Al 22.7 0.2
Fe 15.6 0.2
Ca 0.5 0.1
O
Mg
Si
Al
C
Fe
Ca
cps/eV
keV

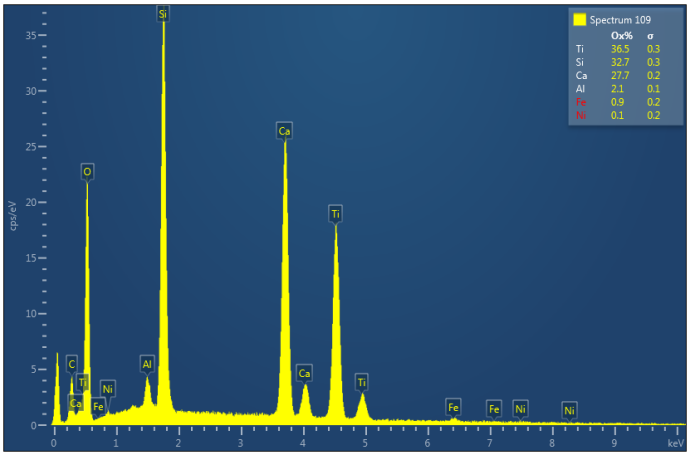

Spectrum 105
Ox% σ
Si 41.2 0.3
Al 25.7 0.2
Ca 22.0 0.2
Fe 11.1 0.2
O
Si
Al
Ca
C
Fe
Ca
Ca
Fe
Fe
cps/eV
keV

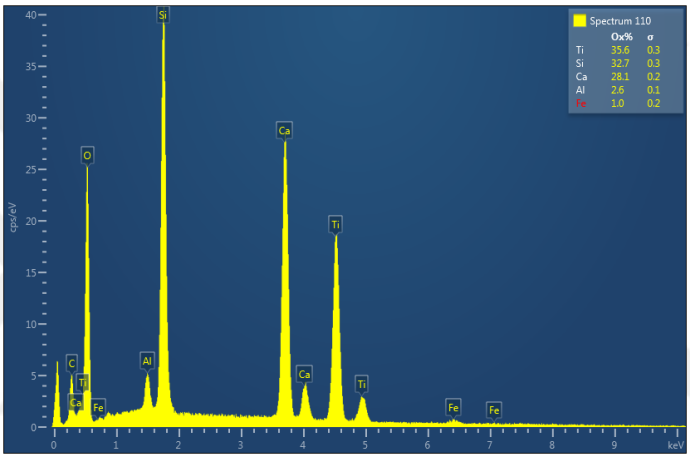

Spectrum 106
Ox% σ
Si 33.7 0.3
Mg 24.7 0.2
Al 23.3 0.3
Fe 17.9 0.3
Ca 0.3 0.1
O
Mg
Si
Al
C
Fe
Ca
Ca
Ca
Fe
Fe
cps/eV
keV

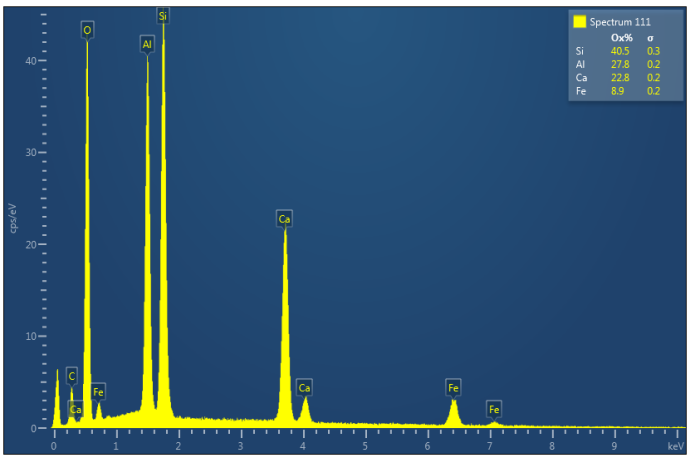

Electron Image 10
Spectrum 107
Spectrum 111
Spectrum 108
Spectrum 109
Spectrum 110
Spectrum 112
Spectrum 115
Spectrum 114
Spectrum 117
Spectrum 118
Spectrum 119
Spectrum 116
Spectrum 126
Spectrum 125
Spectrum 120
Spectrum 121
Spectrum 122
Spectrum 123
Spectrum 124
100µm

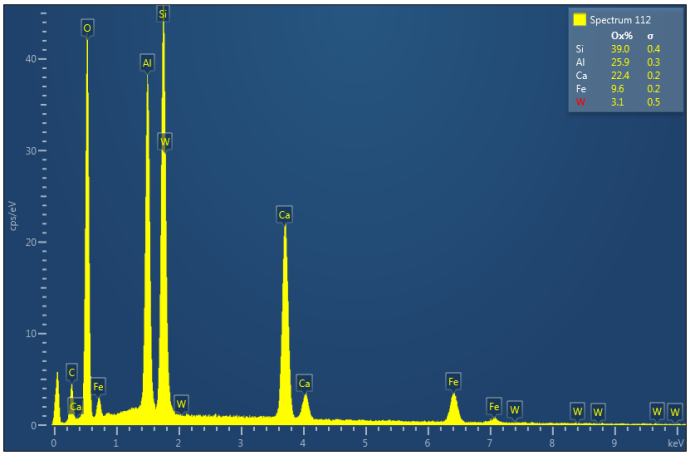

Spectrum 107
Ox% σ
Si 40.5 0.3
Al 26.5 0.3
Ca 22.9 0.2
Fe 10.0 0.2
O
Si
Al
Ca
C
Fe
Ca
Fe
Fe
cps/eV
keV

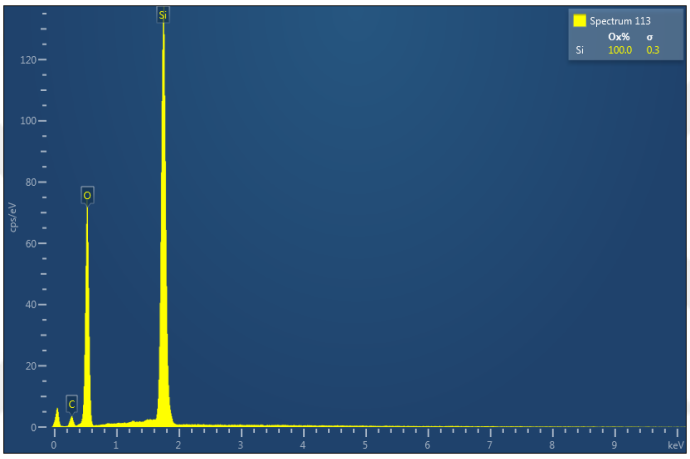

Spectrum 108
Ox% σ
Ti 36.2 0.3
Si 32.7 0.3
Ca 28.0 0.2
Al 2.2 0.1
Fe 0.9 0.2
Si
Ca
O
Ti
C
Al
Ti
Ca
Ti
Fe
Fe
cps/eV
keV

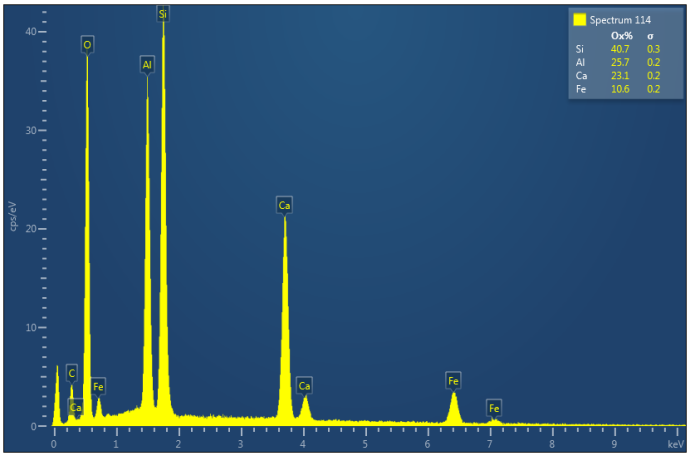

Spectrum 109
Ox% σ
Ti 36.5 0.3
Si 32.7 0.3
Ca 27.7 0.2
Al 2.1 0.1
Fe 0.9 0.2
Ni 0.1 0.2
cps/eV
keV

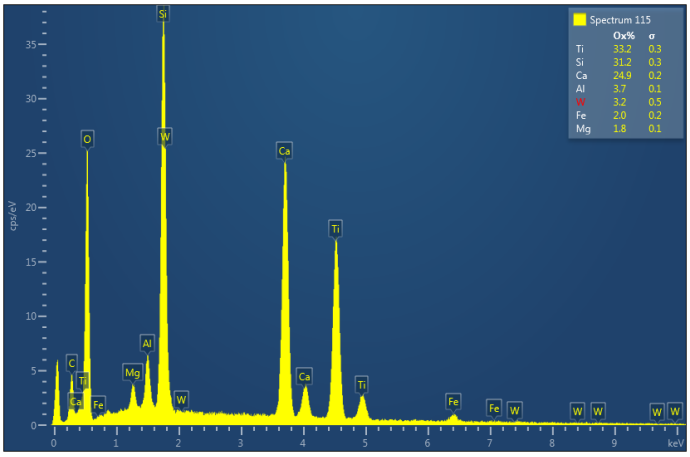

Spectrum 110
Ox% σ
Ti 35.6 0.3
Si 32.7 0.3
Ca 28.1 0.2
Al 2.6 0.1
Fe 1.0 0.2
cps/eV
keV

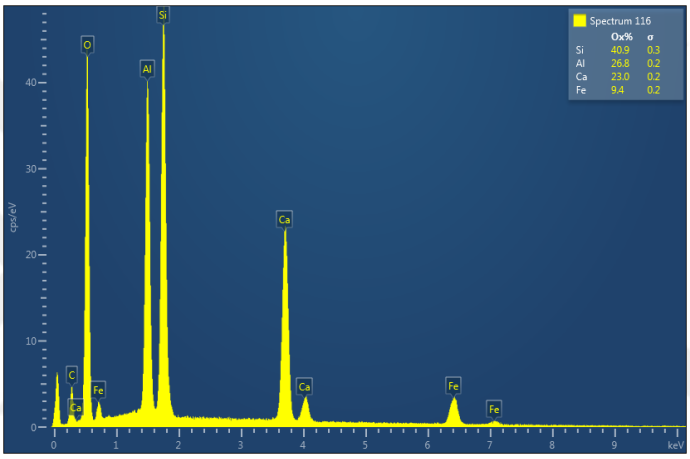

Spectrum 111
Ox% σ
Si 40.5 0.3
Al 27.8 0.2
Ca 22.8 0.2
Fe 8.9 0.2
cps/eV
keV

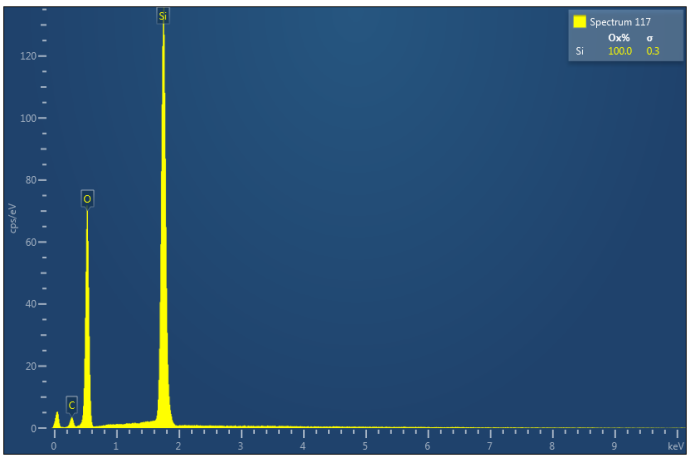

Spectrum 112
Ox%
σ
Si 39.0 0.4
Al 25.9 0.3
Ca 22.4 0.2
Fe 9.6 0.2
W 3.1 0.5
cps/eV
keV

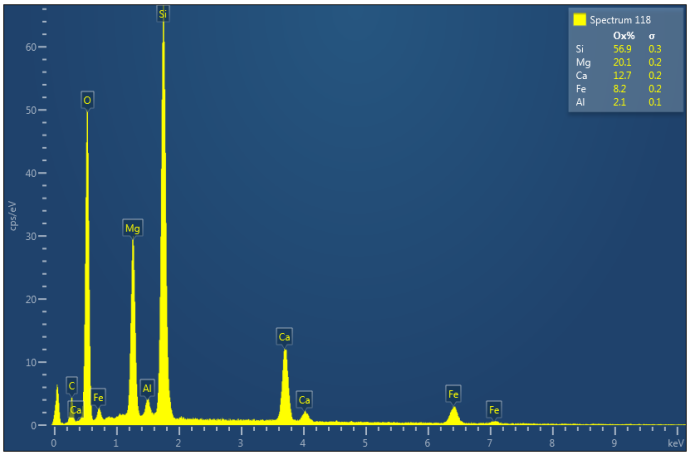

Spectrum 113
Ox%
σ
Si 100.0 0.3
cps/eV
keV

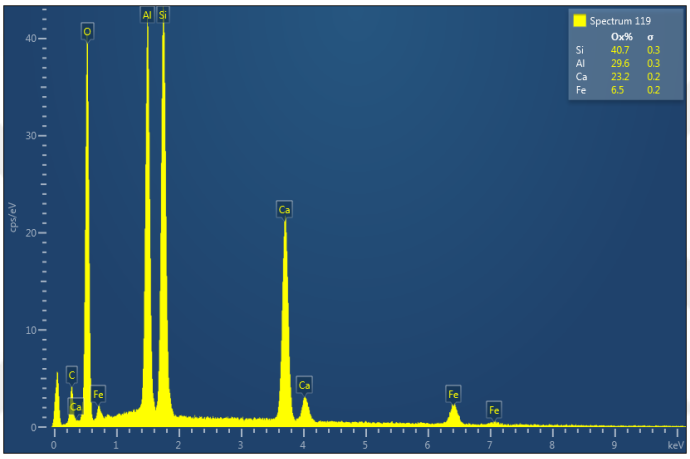

Spectrum 114
Ox%
σ
Si 40.7 0.3
Al 25.7 0.2
Ca 23.1 0.2
Fe 10.6 0.2
cps/eV
keV

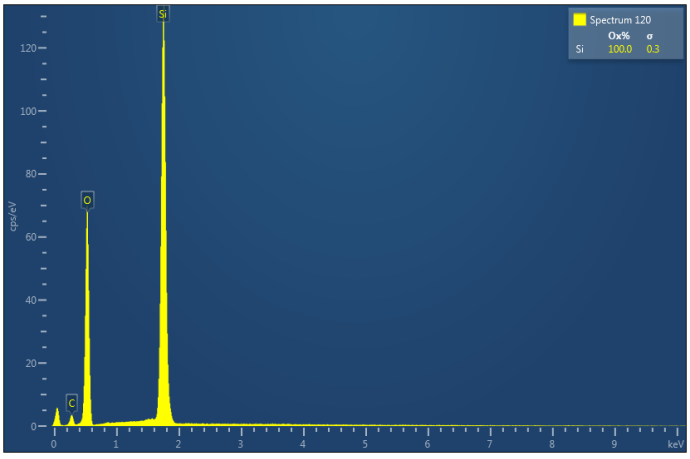

Spectrum 115
Ox% σ
Ti 33.2 0.3
Si 31.2 0.3
Ca 24.9 0.2
Al 3.7 0.1
W 3.2 0.5
Fe 2.0 0.2
Mg 1.8 0.1
cps/eV
keV

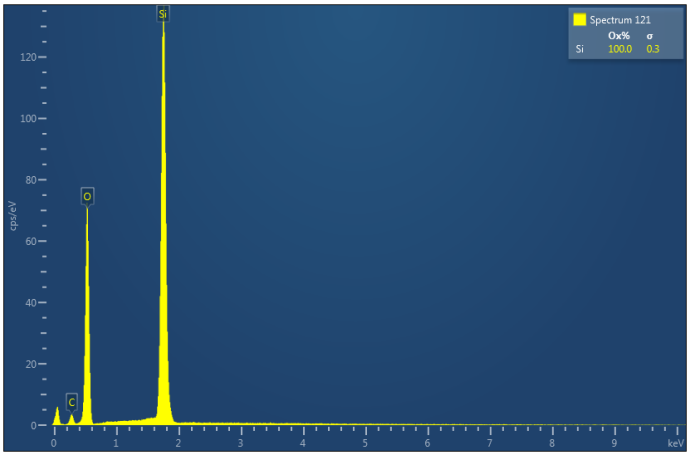

Spectrum 116
Ox% σ
Si 40.9 0.3
Al 26.8 0.2
Ca 23.0 0.2
Fe 9.4 0.2
cps/eV
keV

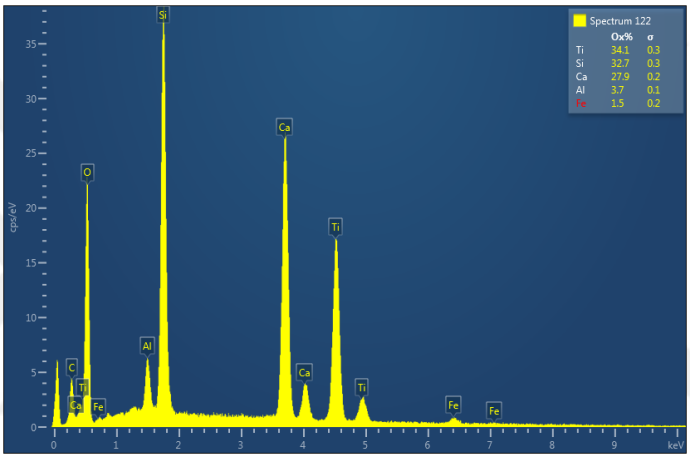

Spectrum 117
Ox% σ
Si 100.0 0.3
cps/eV
keV

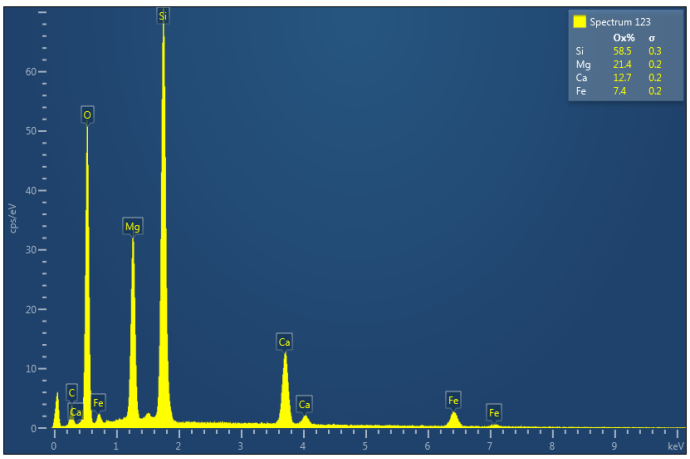

Spectrum 118
Ox%
σ
Si 56.9 0.3
Mg 20.1 0.2
Ca 12.7 0.2
Fe 8.2 0.2
Al 2.1 0.1
cps/eV
keV

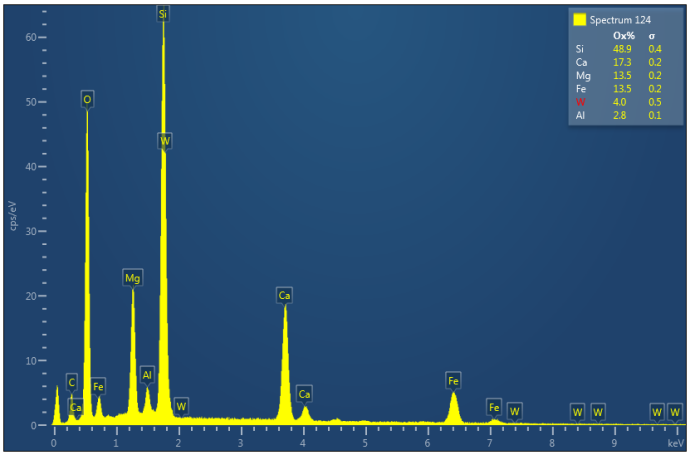

Spectrum 119
Ox%
σ
Si 40.7 0.3
Al 29.6 0.3
Ca 23.2 0.2
Fe 6.5 0.2
cps/eV
keV

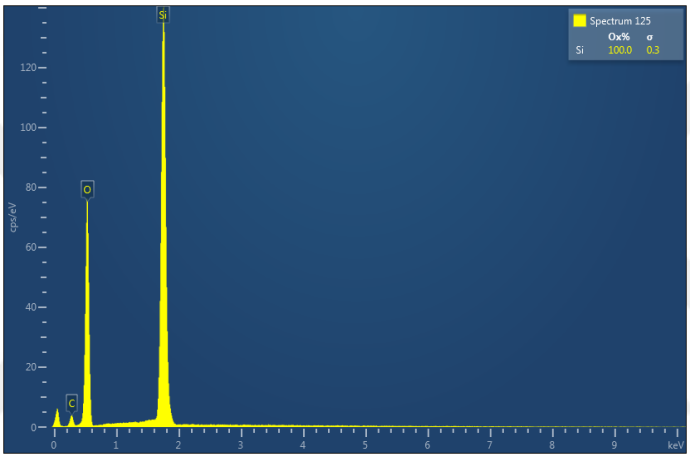

Spectrum 120
Ox%
σ
Si 100.0 0.3
cps/eV
keV

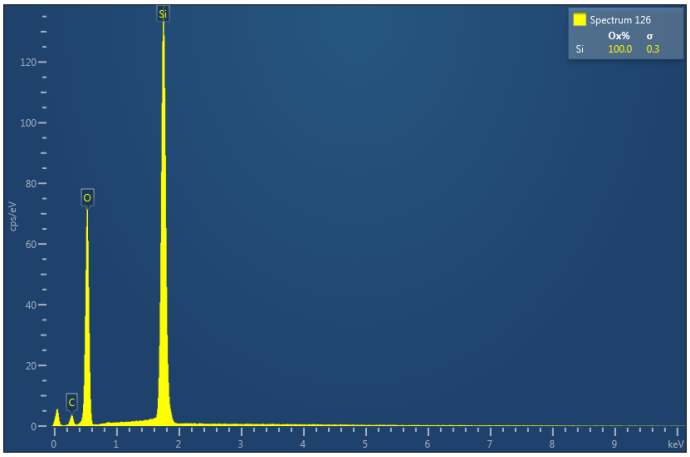

Spectrum 121
Ox%
σ
Si 100.0 0.3
cps/eV
keV
Si
O
C


Spectrum 122
Ox%
σ
Ti 34.1 0.3
Si 32.7 0.3
Ca 27.9 0.2
Al 3.7 0.1
Fe 1.5 0.2
cps/eV
keV
Si
O
Ca
Ti
Al
C
Ti
Ca
Fe
Ca
Ti
Fe
Fe

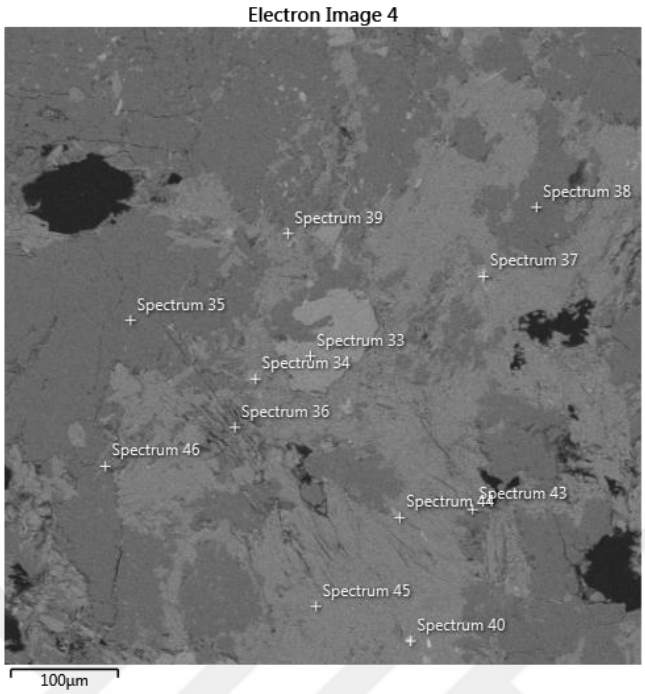

Spectrum 123
Ox%
σ
Si 58.5 0.3
Mg 21.4 0.2
Ca 12.7 0.2
Fe 7.4 0.2
cps/eV
keV
Si
O
Mg
Ca
C
Ca
Fe
Ca
Fe
Fe

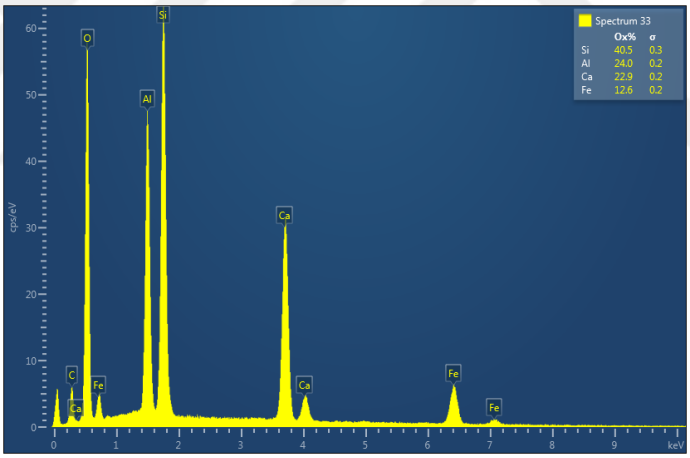


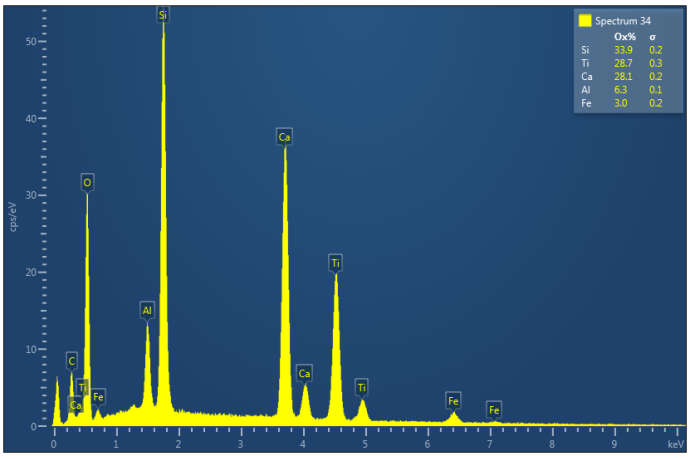


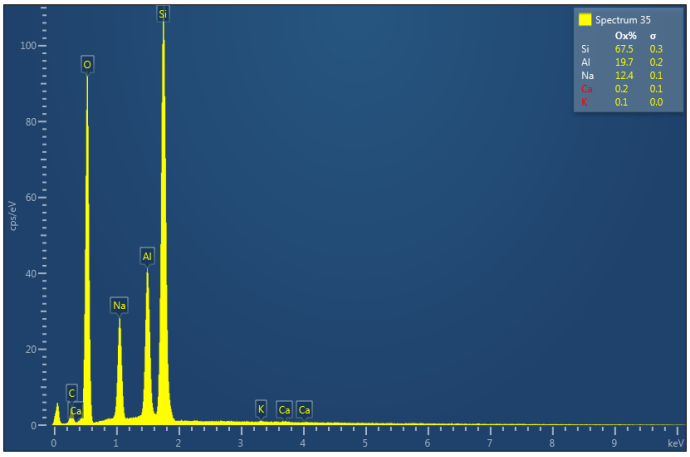


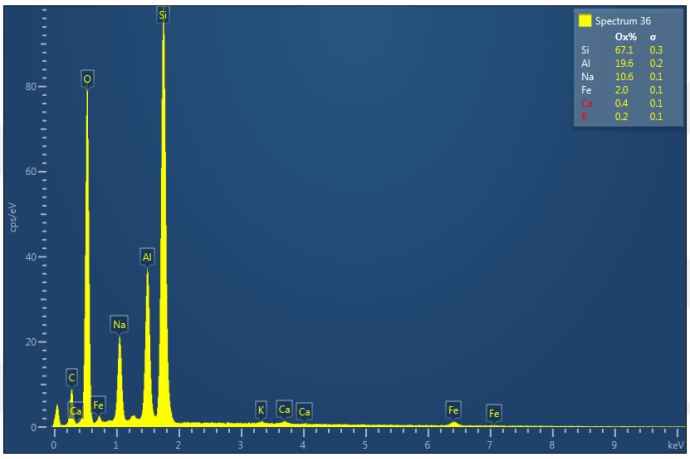
Sample KC-7-17

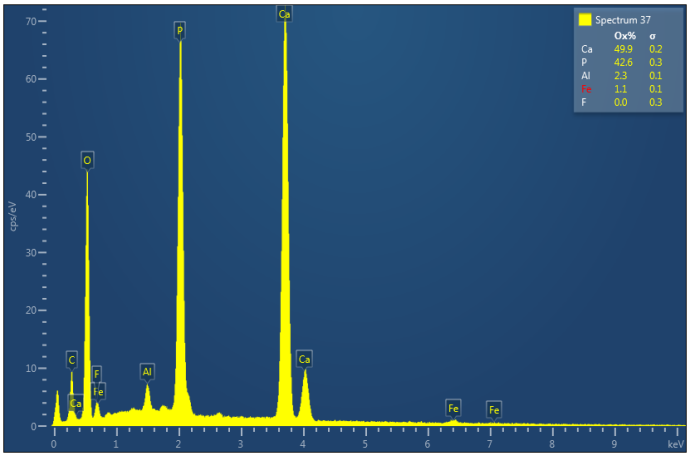

Electron Image 4
Spectrum 38
Spectrum 39
Spectrum 37
Spectrum 35
Spectrum 33
Spectrum 34
Spectrum 36
Spectrum 46
Spectrum 43
Spectrum 44
Spectrum 45
Spectrum 40
100µm

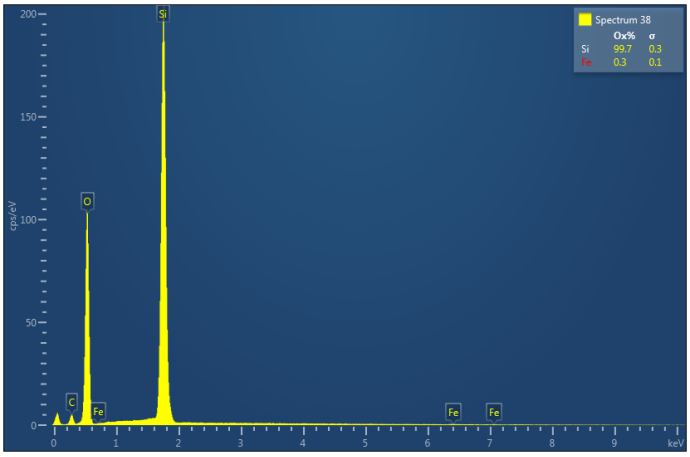

Spectrum 33
Ox%
Si 40.5 0.3
Al 24.0 0.2
Ca 22.9 0.2
Fe 12.6 0.2
O
Si
Al
Ca
Fe
C
cps/eV
keV

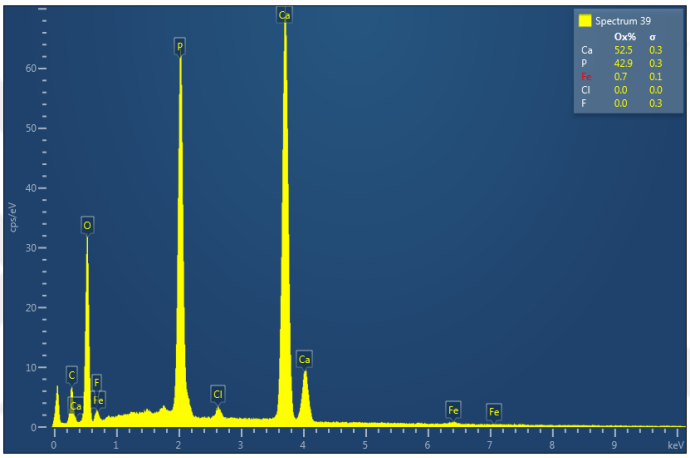

Spectrum 34
Ox%
Si 33.9 0.2
Ti 28.7 0.3
Ca 28.1 0.2
Al 6.3 0.1
Fe 3.0 0.2
O
Si
Ca
Ti
Al
C
Fe
cps/eV
keV

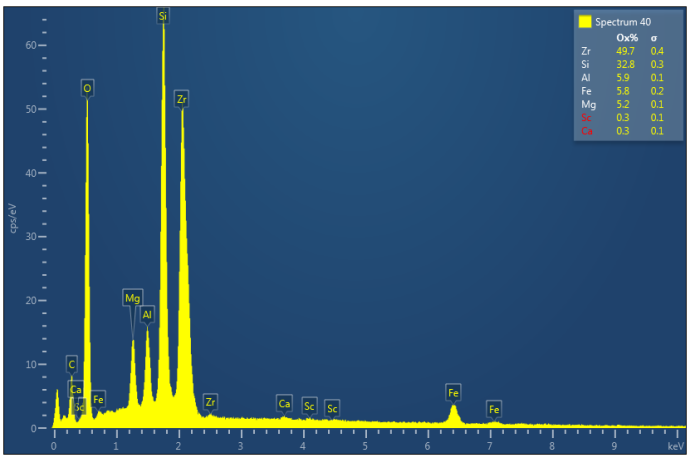

Spectrum 35
Ox% σ
Si 67.5 0.3
Al 19.7 0.2
Na 12.4 0.1
Ca 0.2 0.1
K 0.1 0.0
Si
O
Al
Na
C
Ca
K
Ca
Ca
cps/eV
keV

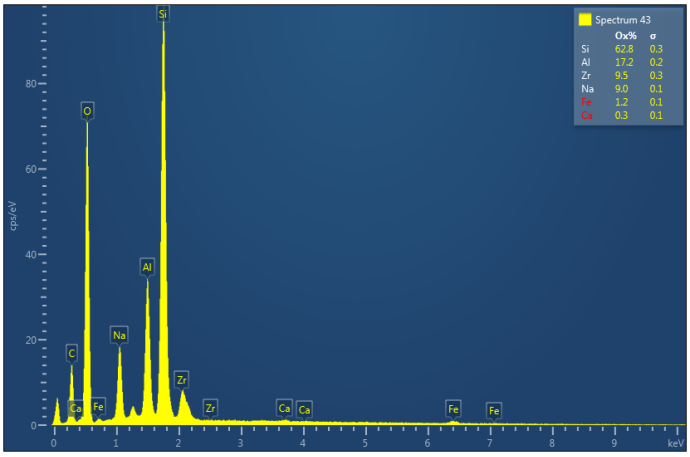

Spectrum 36
Ox% σ
Si 67.1 0.3
Al 19.6 0.2
Na 10.6 0.1
Fe 2.0 0.1
Ca 0.4 0.1
K 0.2 0.1
Si
O
Al
Na
C
Ca
Fe
K
Ca
Ca
Fe
Fe
cps/eV
keV

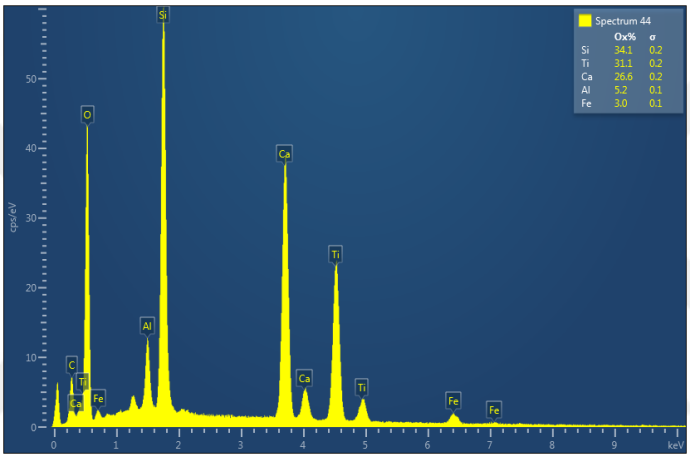

Spectrum 37
Ox% σ
Ca 49.9 0.2
P 42.6 0.3
Al 2.3 0.1
Fe 1.1 0.1
F 0.0 0.3
P
Ca
O
C
Ca
F
Fe
Al
Ca
Fe
Fe
cps/eV
keV

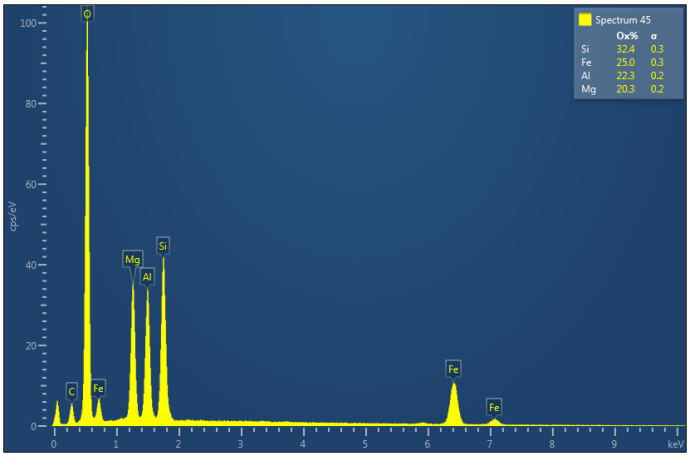

Spectrum 38
Ox%
σ
Si 99.7 0.3
Fe 0.3 0.1
cps/eV
keV
Si
O
C
Fe
Fe
Fe

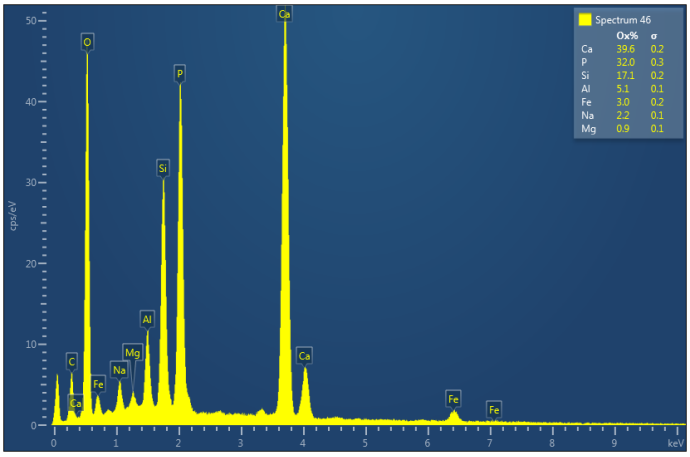

Spectrum 39
Ox%
σ
Ca 52.5 0.3
P 42.9 0.3
Fe 0.7 0.1
Cl 0.0 0.0
F 0.0 0.3
cps/eV
keV
Ca
P
O
C
F
Ca
Fe
Cl
Ca
Fe
Fe


Spectrum 40
Ox%
σ
Zr 49.7 0.4
Si 32.8 0.3
Al 5.9 0.1
Fe 5.8 0.2
Mg 5.2 0.1
Sc 0.3 0.1
Ca 0.3 0.1
cps/eV
keV
Si
O
Zr
Mg
Al
C
Ca
Fe
Zr
Ca
Sc
Sc
Fe
Fe

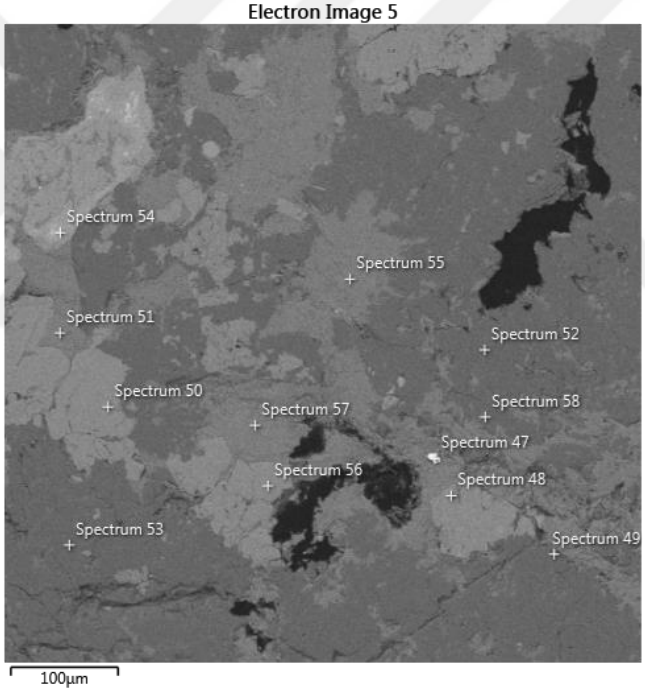

Spectrum 43
Ox% σ
Si 62.8 0.3
Al 17.2 0.2
Zr 9.5 0.3
Na 9.0 0.1
Fe 1.2 0.1
Ca 0.3 0.1
cps/eV
keV

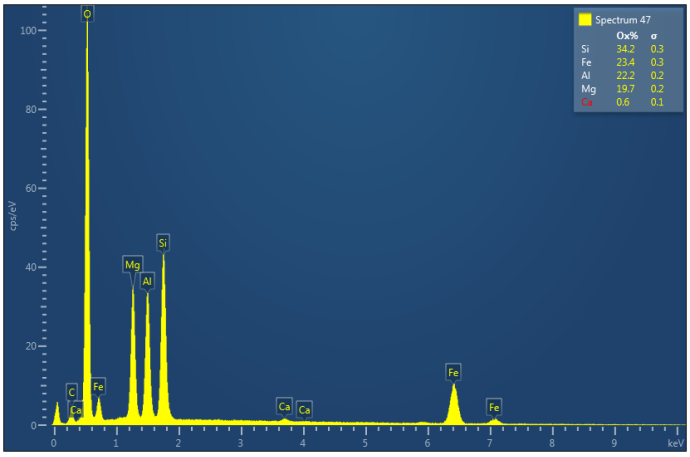

Spectrum 44
Ox% σ
Si 34.1 0.2
Ti 31.1 0.2
Ca 26.6 0.2
Al 5.2 0.1
Fe 3.0 0.1
cps/eV
keV

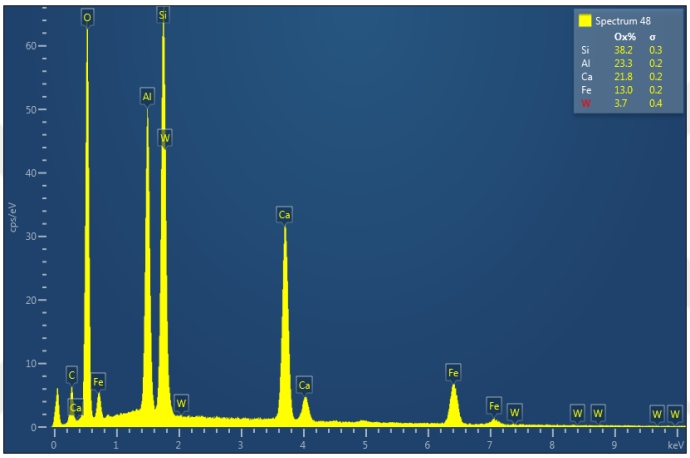

Spectrum 45
Ox% σ
Si 32.4 0.3
Fe 25.0 0.3
Al 22.3 0.2
Mg 20.3 0.2
cps/eV
keV

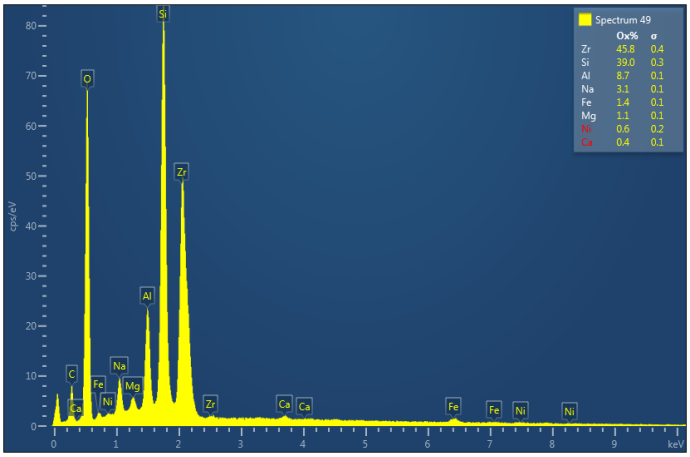


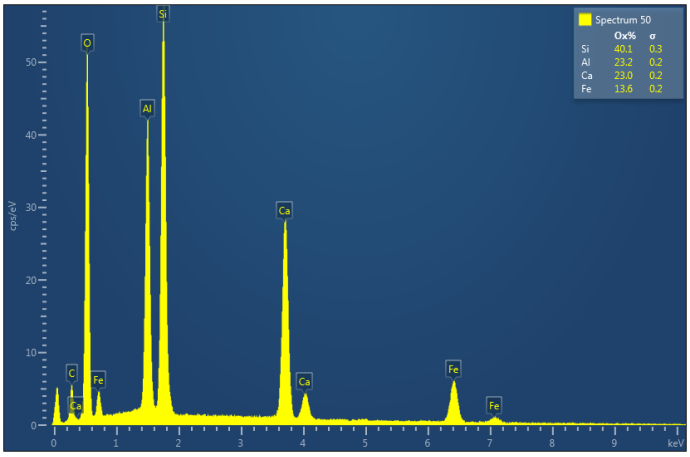
Electron Image 5

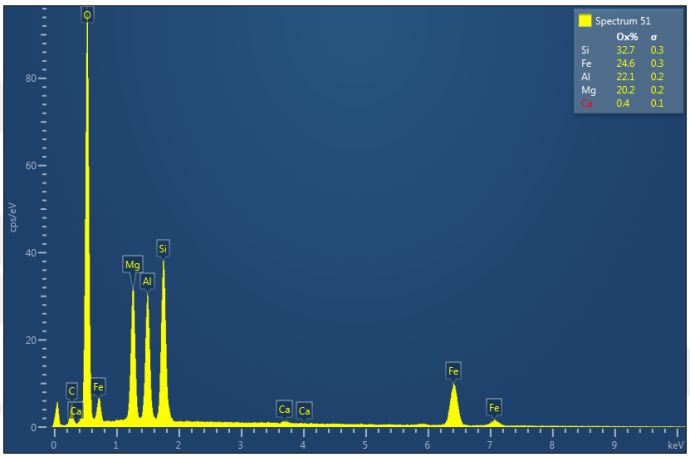


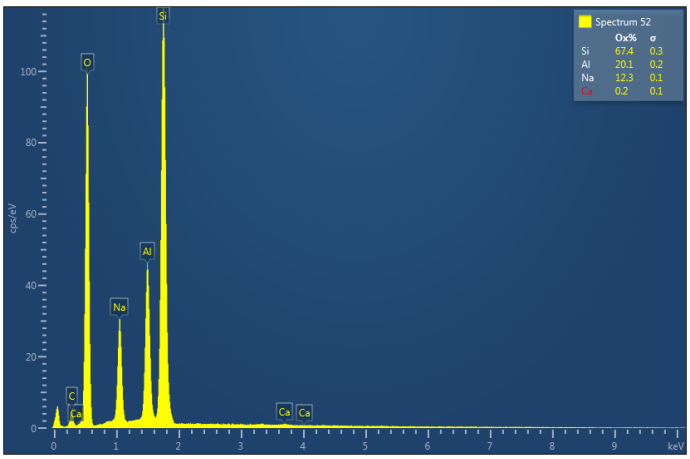

Spectrum 47
Ox% σ
Si 34.2 0.3
Fe 23.4 0.3
Al 22.2 0.2
Mg 19.7 0.2
Ca 0.6 0.1
O
Si
Mg
Al
C
Fe
Ca
Ca
Fe
Fe
cps/eV
keV

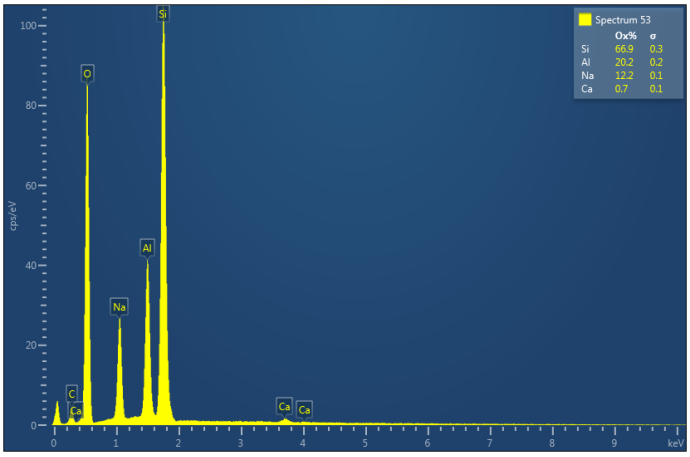

Spectrum 48
Ox% σ
Si 38.2 0.3
Al 23.3 0.2
Ca 21.8 0.2
Fe 13.0 0.2
W 3.7 0.4
O
Si
Al
W
Ca
C
Fe
Ca
W
Fe
Fe
W
W W
W W
cps/eV
keV

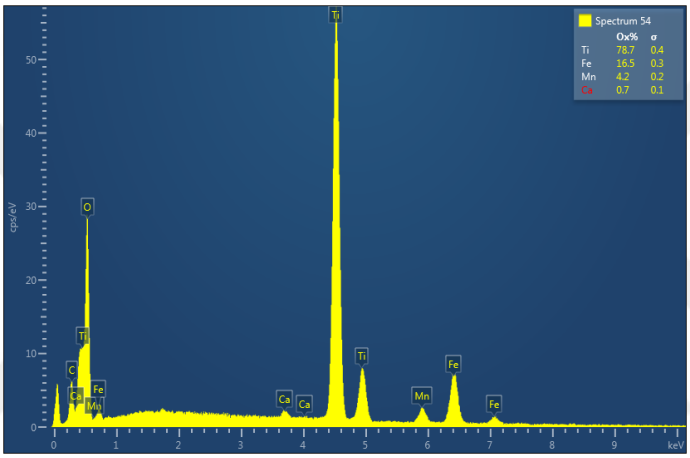

Spectrum 49
Ox% σ
Zr 45.8 0.4
Si 39.0 0.3
Al 8.7 0.1
Na 3.1 0.1
Fe 1.4 0.1
Mg 1.1 0.1
Ni 0.6 0.2
Ca 0.4 0.1
Si
O
Zr
Al
Na
C
Fe
Mg
Ca
Ni
Zr
Ca
Fe
Fe
Ni
Ni
cps/eV
keV

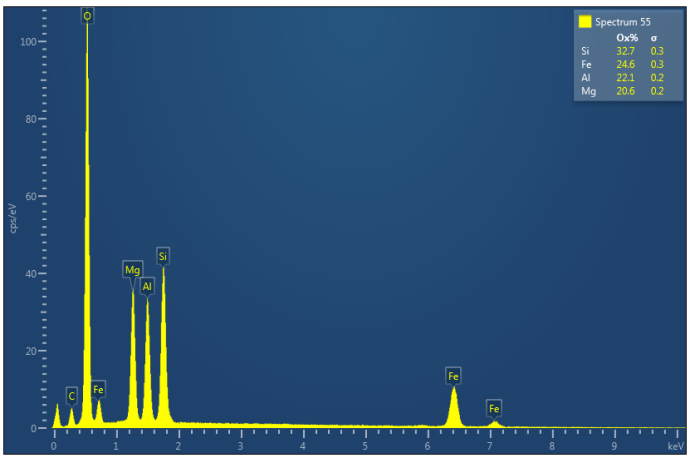

Spectrum 50
Ox%
σ
Si 40.1 0.3
Al 23.2 0.2
Ca 23.0 0.2
Fe 13.6 0.2
cps/eV
keV
O
Si
Al
Ca
C
Fe
Ca
Ca
Fe
Fe

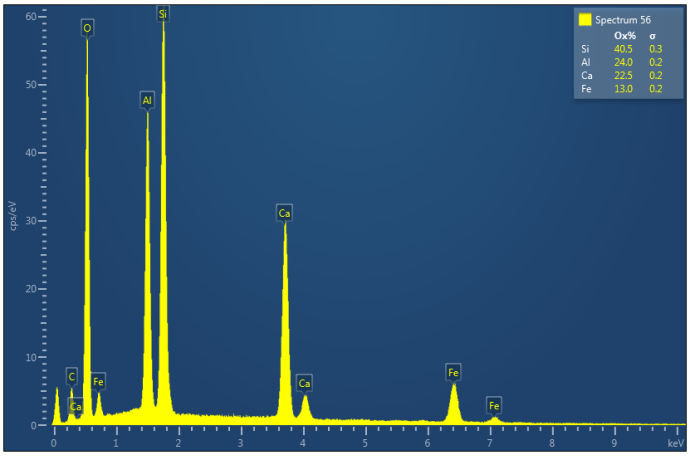

Spectrum 51
Ox%
σ
Si 32.7 0.3
Fe 24.6 0.3
Al 22.1 0.2
Mg 20.2 0.2
Ca 0.4 0.1
cps/eV
keV
O
Mg
Al
Si
C
Ca
Fe
Ca
Ca
Fe

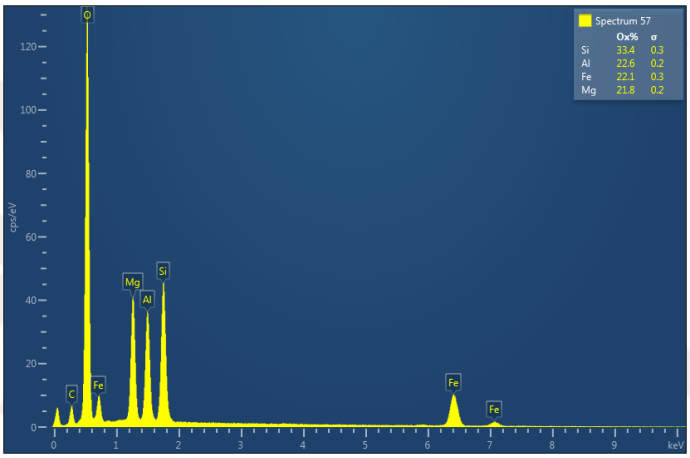

Spectrum 52
Ox%
σ
Si 67.4 0.3
Al 20.1 0.2
Na 12.3 0.1
Ca 0.2 0.1
cps/eV
keV
O
Si
Al
Na
C
Ca
Ca
Ca

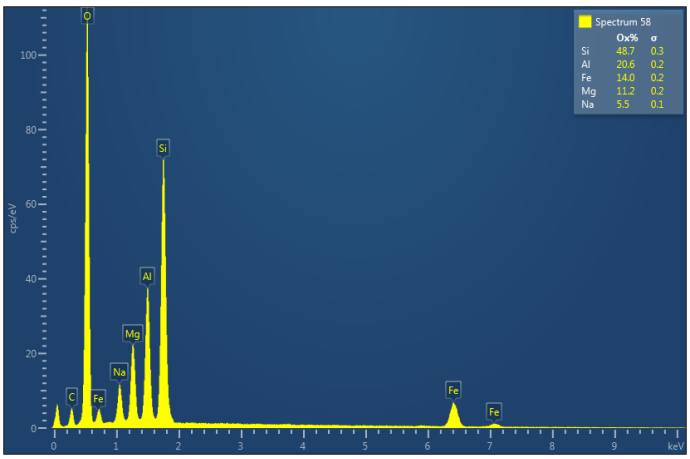

Spectrum 53
Ox% σ
Si 66.9 0.3
Al 20.2 0.2
Na 12.2 0.1
Ca 0.7 0.1
cps/eV
keV
O
Si
Al
Na
C
Ca
Ca
Ca

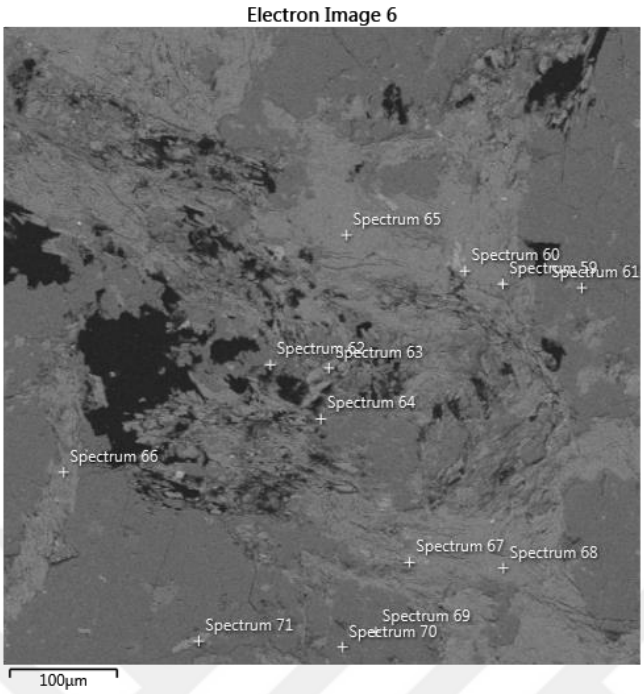

Spectrum 54
Ox% σ
Ti 78.7 0.4
Fe 16.5 0.3
Mn 4.2 0.2
Ca 0.7 0.1
cps/eV
keV
O
Ti
Ti
Ti
C
Ca
Fe
Mn
Ca
Ca
Mn
Fe
Fe

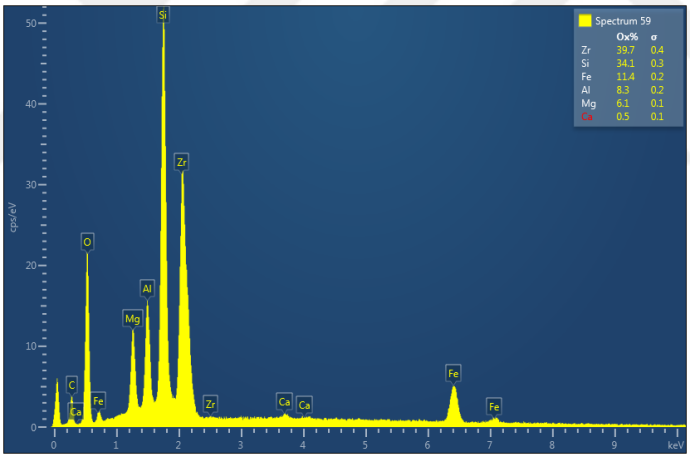

Spectrum 55
Ox% σ
Si 32.7 0.3
Fe 24.6 0.3
Al 22.1 0.2
Mg 20.6 0.2
cps/eV
keV
O
Mg
Si
Al
C
Fe
Fe
Fe

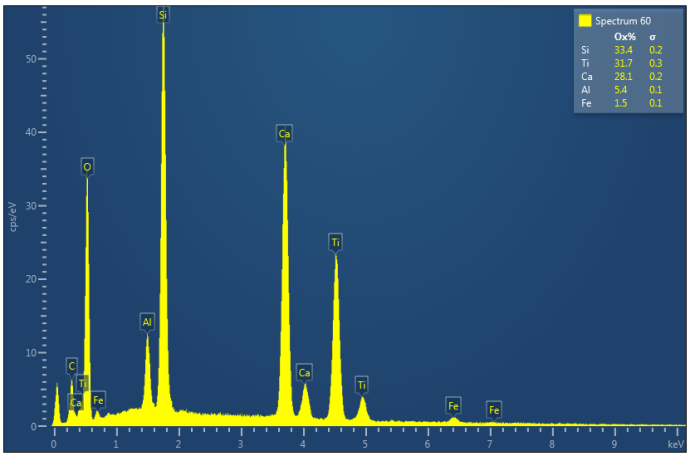

Spectrum 56
Ox% σ
Si 40.5 0.3
Al 24.0 0.2
Ca 22.5 0.2
Fe 13.0 0.2
O
Si
Al
Ca
C
Fe
Ca
Fe
Fe
cps/eV
keV

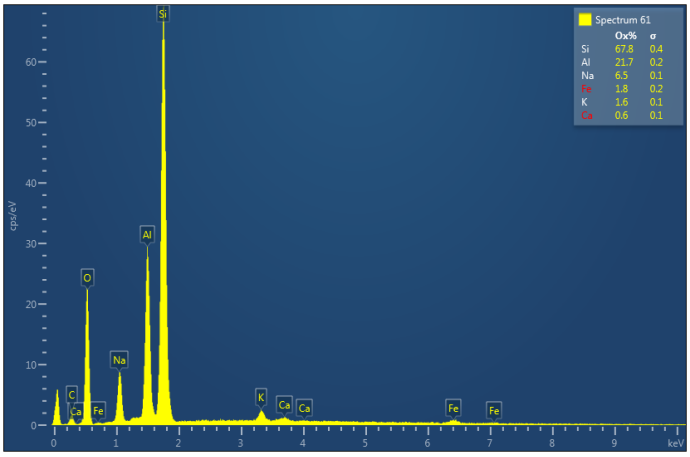

Spectrum 57
Ox% σ
Si 33.4 0.3
Al 22.6 0.2
Fe 22.1 0.3
Mg 21.8 0.2
O
Mg
Si
Al
C
Fe
Fe
Fe
cps/eV
keV

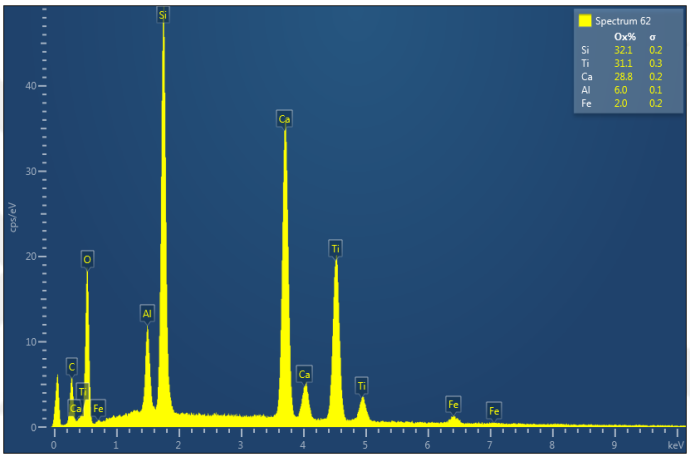

Spectrum 58
Ox% σ
Si 48.7 0.3
Al 20.6 0.2
Fe 14.0 0.2
Mg 11.2 0.2
Na 5.5 0.1
O
Si
Al
Mg
Na
C
Fe
Fe
Fe
cps/eV
keV

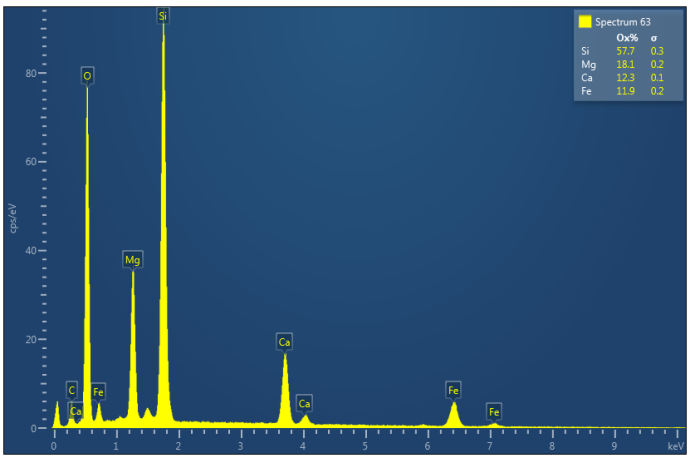

Electron Image 6
Spectrum 65
Spectrum 60
Spectrum 59
Spectrum 61
Spectrum 62
Spectrum 63
Spectrum 64
Spectrum 66
Spectrum 67
Spectrum 68
Spectrum 69
Spectrum 70
Spectrum 71
100µm

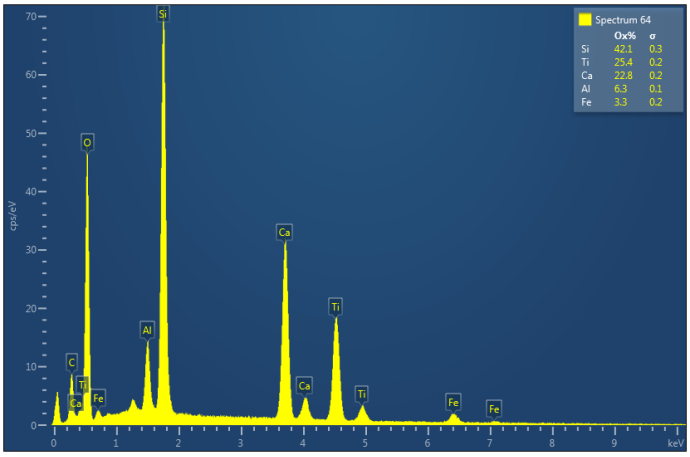

Spectrum 59
Ox% σ
Zr 39.7 0.4
Si 34.1 0.3
Fe 11.4 0.2
Al 8.3 0.2
Mg 6.1 0.1
Ca 0.5 0.1
cps/eV
keV

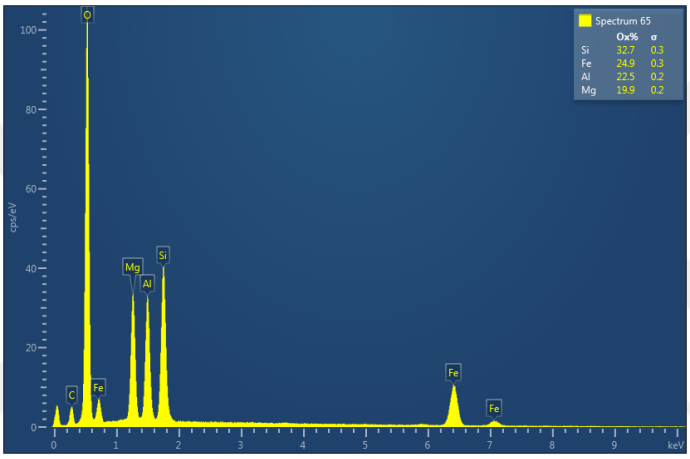

Spectrum 60
Ox% σ
Si 33.4 0.2
Ti 31.7 0.3
Ca 28.1 0.2
Al 5.4 0.1
Fe 1.5 0.1
cps/eV
keV

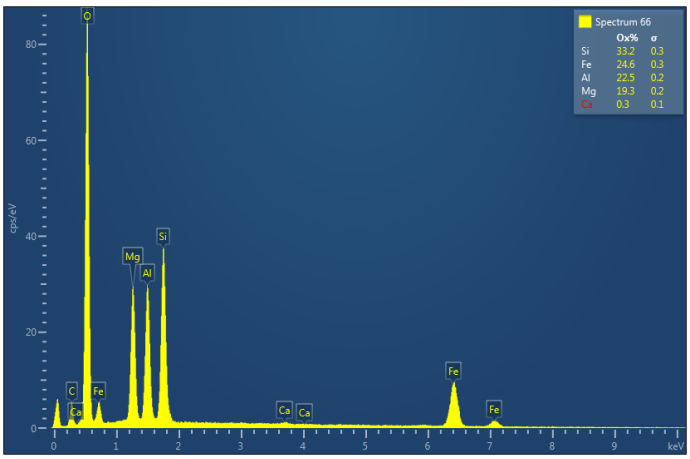

Spectrum 61
Ox%
σ
Si 67.8 0.4
Al 21.7 0.2
Na 6.5 0.1
Fe 1.8 0.2
K 1.6 0.1
Ca 0.6 0.1
cps/eV
keV
Si
O
Al
Na
C
Ca
Fe
K
Ca
Ca
Fe
Fe

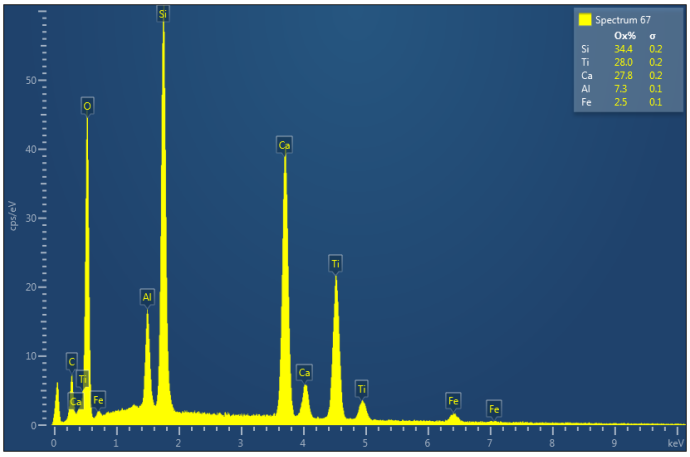

Spectrum 62
Ox%
σ
Si 32.1 0.2
Ti 31.1 0.3
Ca 28.8 0.2
Al 6.0 0.1
Fe 2.0 0.2
cps/eV
keV
Si
Ca
O
Ti
Al
C
Ti
Ca
Fe
Ca
Ti
Fe
Fe

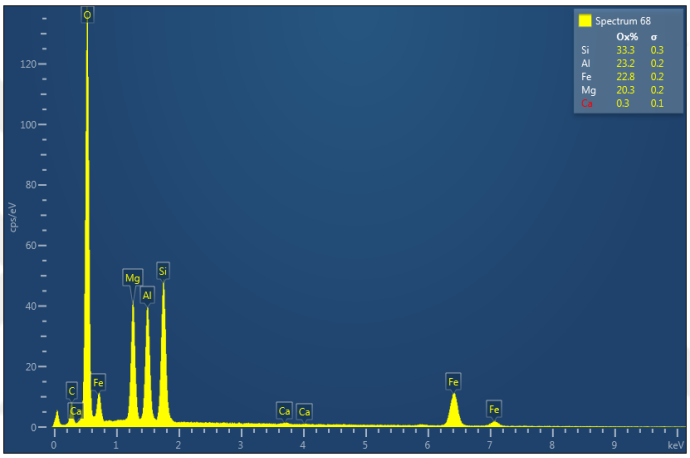

Spectrum 63
Ox%
σ
Si 57.7 0.3
Mg 18.1 0.2
Ca 12.3 0.1
Fe 11.9 0.2
cps/eV
keV
Si
O
Mg
Ca
C
Ca
Fe
Ca
Fe
Fe

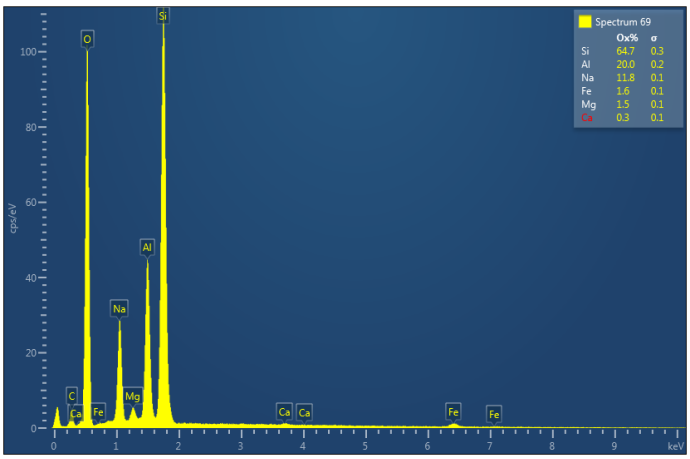

Spectrum 64
Ox% σ
Si 42.1 0.3
Ti 25.4 0.2
Ca 22.8 0.2
Al 6.3 0.1
Fe 3.3 0.2
cps/eV
keV
O
Si
Ca
Ti
Al
C
Ti
Ca
Fe
Ca
Ti
Fe
Fe

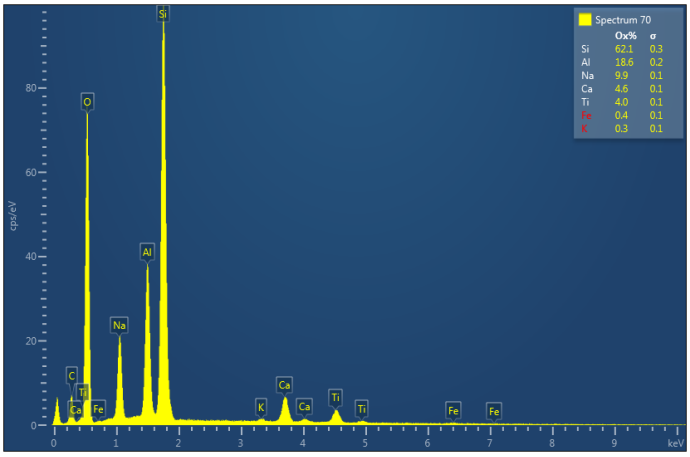

Spectrum 65
Ox% σ
Si 32.7 0.3
Fe 24.9 0.3
Al 22.5 0.2
Mg 19.9 0.2
cps/eV
keV
O
Mg
Al
Si
C
Fe
Fe
Fe

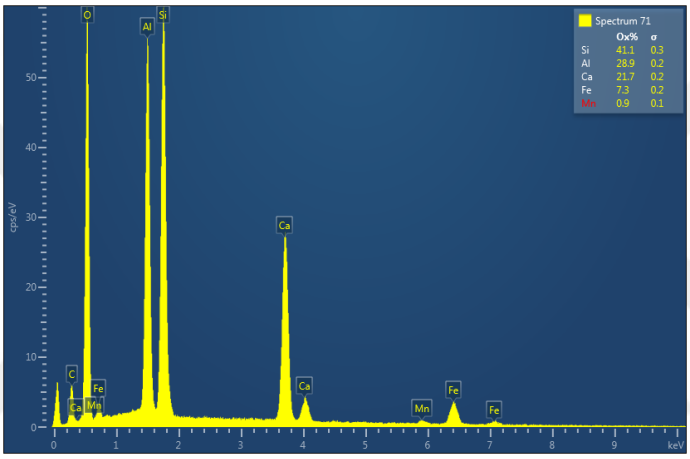

Spectrum 66
Ox% σ
Si 33.2 0.3
Fe 24.6 0.3
Al 22.5 0.2
Mg 19.3 0.2
Ca 0.3 0.1
cps/eV
keV
O
Mg
Al
Si
C
Ca
Fe
Ca
Ca
Fe
Fe


Spectrum 67
Ox%
σ
Si 34.4 0.2
Ti 28.0 0.2
Ca 27.8 0.2
Al 7.3 0.1
Fe 2.5 0.1
cps/eV
keV
O
Si
Ca
Ti
Al
C
Ca
Ti
Fe
Ca
Ti
Fe
Fe

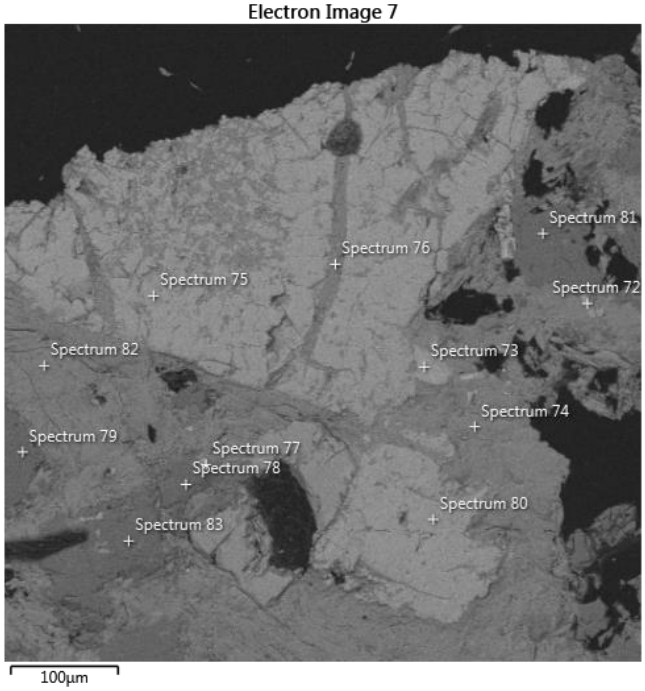

Spectrum 68
Ox%
σ
Si 33.3 0.3
Al 23.2 0.2
Fe 22.8 0.2
Mg 20.3 0.2
Ca 0.3 0.1
cps/eV
keV
O
Mg
Si
Al
C
Fe
Ca
Ca
Ca
Fe
Fe

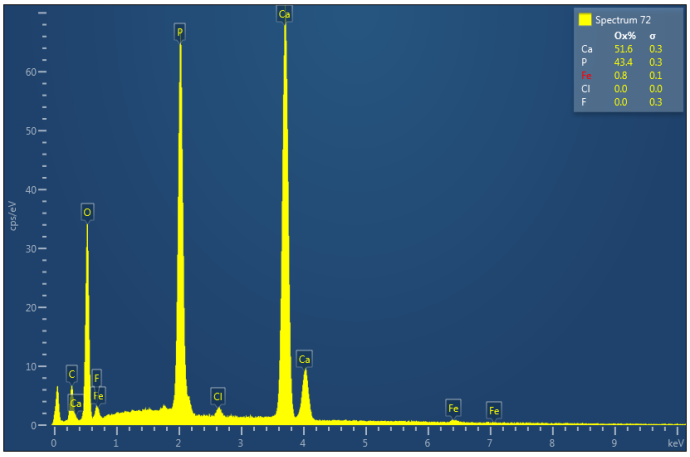

Spectrum 69
Ox%
σ
Si 64.7 0.3
Al 20.0 0.2
Na 11.8 0.1
Fe 1.6 0.1
Mg 1.5 0.1
Ca 0.3 0.1
cps/eV
keV
O
Si
Al
Na
C
Ca
Fe
Mg
Ca
Ca
Fe
Fe

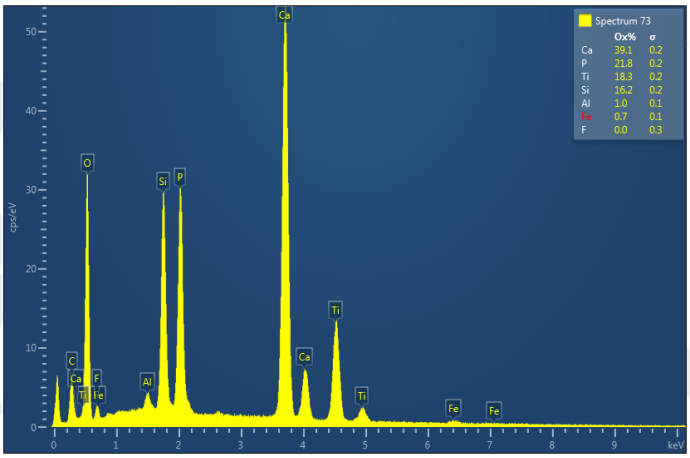


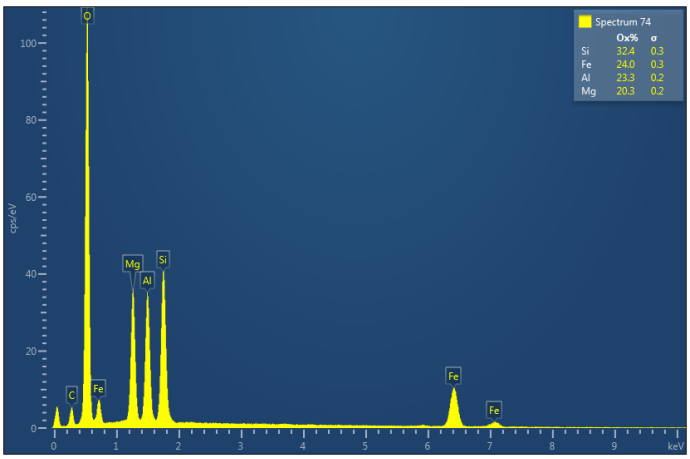


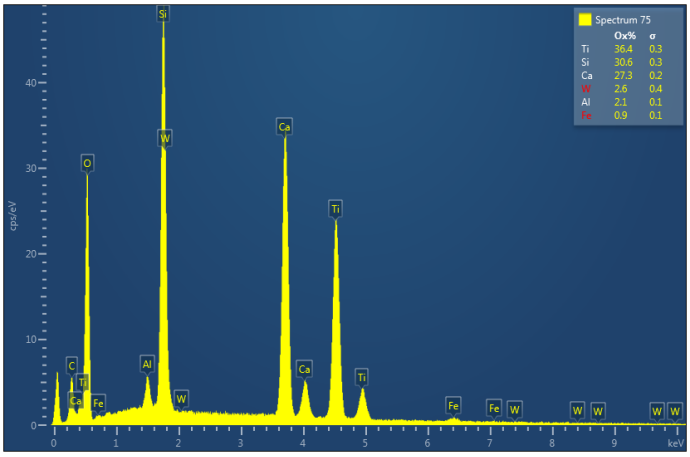
Electron Image 7

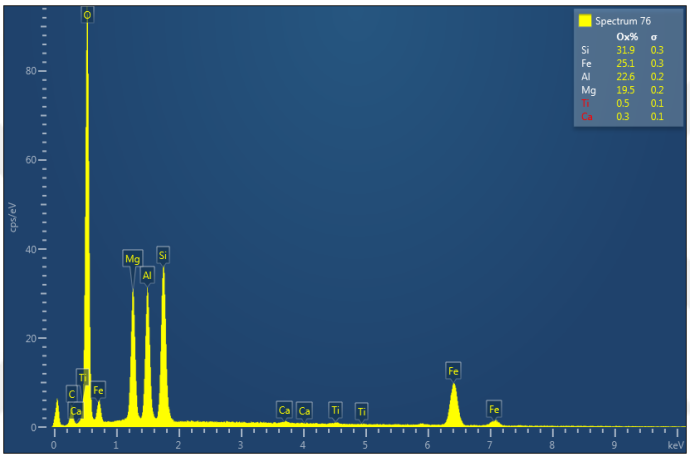


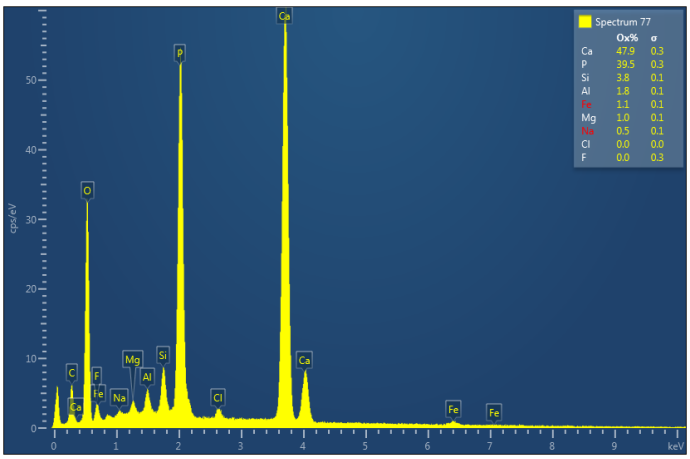

Spectrum 72
Ox% σ
Ca 51.6 0.3
P 43.4 0.3
Fe 0.8 0.1
Cl 0.0 0.0
F 0.0 0.3
cps/eV
keV

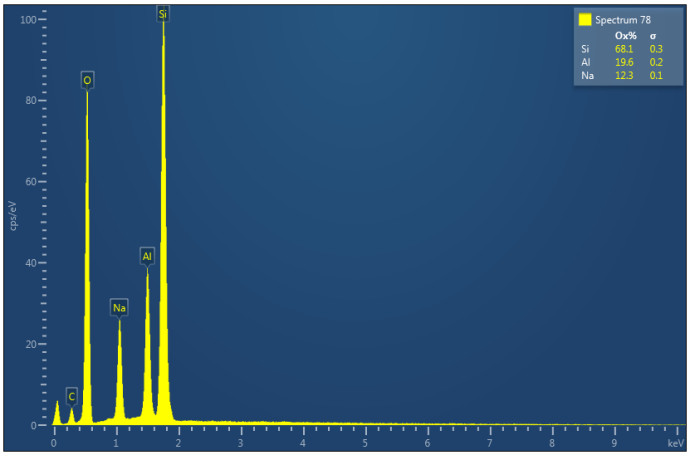

Spectrum 73
Ox% σ
Ca 39.1 0.2
P 21.8 0.2
Ti 18.3 0.2
Si 16.2 0.2
Al 1.0 0.1
Fe 0.7 0.1
F 0.0 0.3
cps/eV
keV

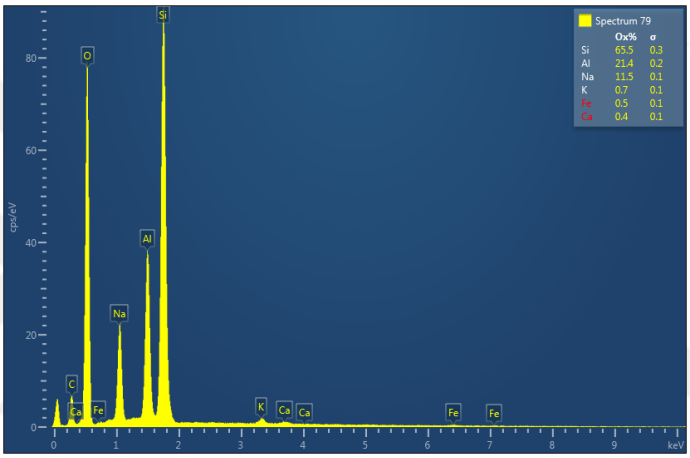

Spectrum 74
Ox% σ
Si 32.4 0.3
Fe 24.0 0.3
Al 23.3 0.2
Mg 20.3 0.2
cps/eV
keV

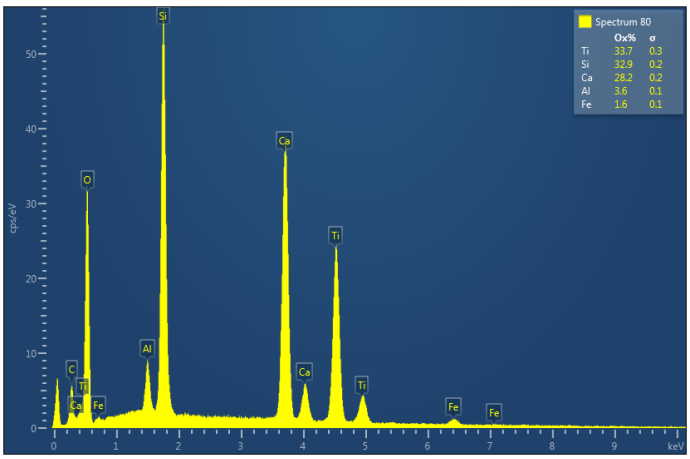

Spectrum 75
Ox%
Ti 36.4
Si 30.6
Ca 27.3
W 2.6
Al 2.1
Fe 0.9
cps/eV
keV

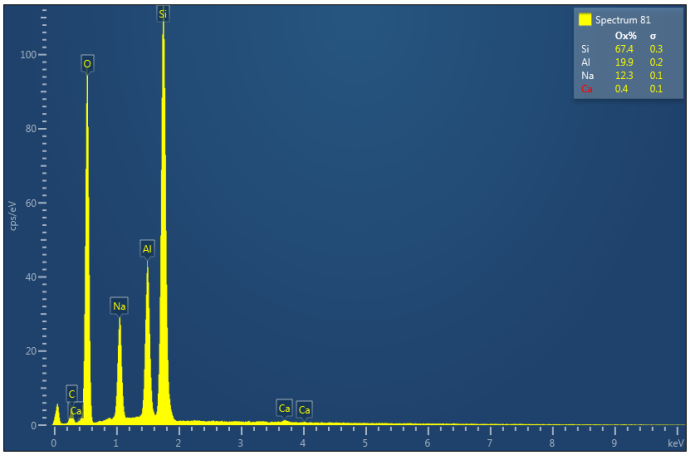

Spectrum 76
Ox%
Si 31.9
Fe 25.1
Al 22.6
Mg 19.5
Ti 0.5
Ca 0.3
cps/eV
keV

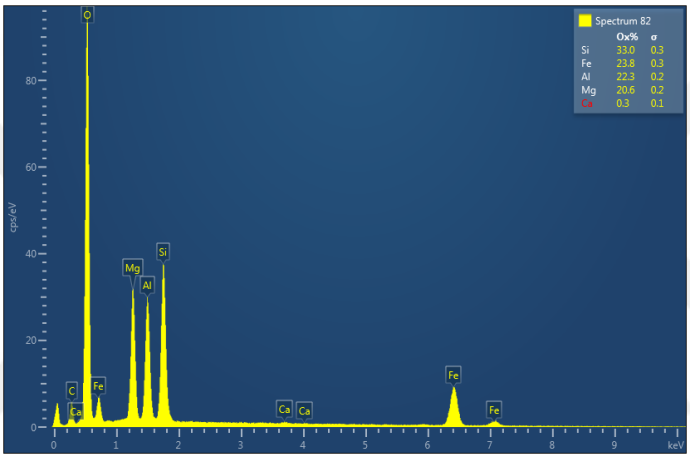

Spectrum 77
Ox%
Ca 47.9
P 39.5
Si 3.8
Al 1.8
Fe 1.1
Mg 1.0
Na 0.5
Cl 0.0
F 0.0
cps/eV
keV

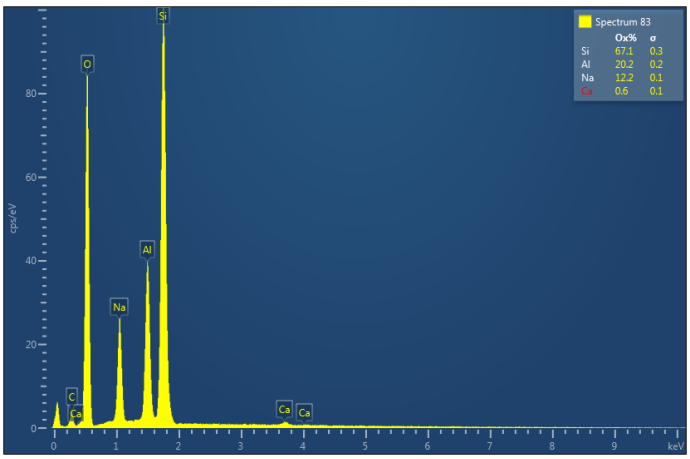

Spectrum 78
Ox%
σ
Si 68.1 0.3
Al 19.6 0.2
Na 12.3 0.1
cps/eV
keV
Si
O
Al
Na
C


Spectrum 79
Ox%
σ
Si 65.5 0.3
Al 21.4 0.2
Na 11.5 0.1
K 0.7 0.1
Fe 0.5 0.1
Ca 0.4 0.1
cps/eV
keV
Si
O
Al
Na
C
Ca
Fe
K
Ca
Ca
Fe
Fe


Spectrum 80
Ox%
σ
Ti 33.7 0.3
Si 32.9 0.2
Ca 28.2 0.2
Al 3.6 0.1
Fe 1.6 0.1
cps/eV
keV
Si
Ca
O
Ti
Al
C
Ti
Ca
Fe
Ca
Ti
Fe
Fe

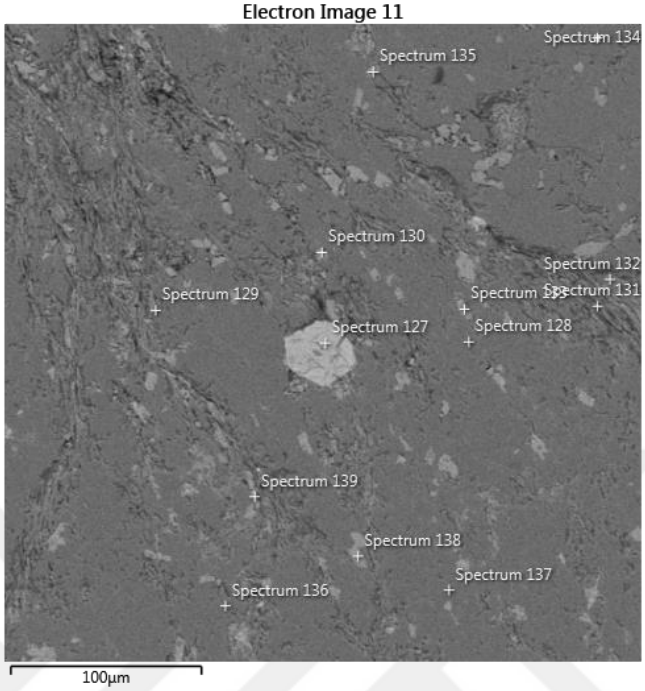

Spectrum 81
Ox% σ
Si 67.4 0.3
Al 19.9 0.2
Na 12.3 0.1
Ca 0.4 0.1
Si
O
Al
Na
C
Ca
Ca
Ca
cps/eV
keV

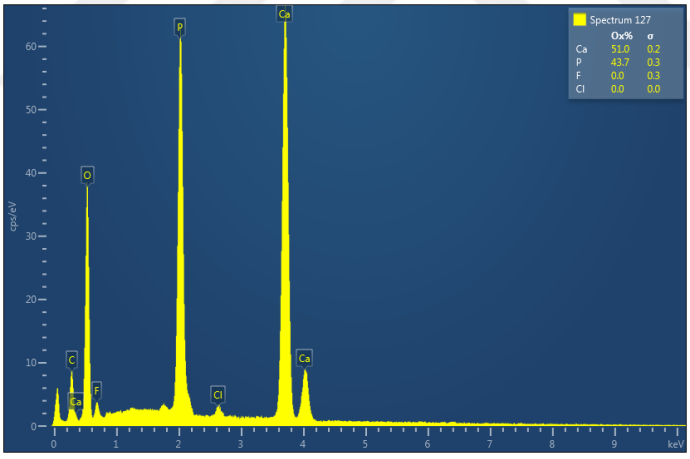

Spectrum 82
Ox% σ
Si 33.0 0.3
Fe 23.8 0.3
Al 22.3 0.2
Mg 20.6 0.2
Ca 0.3 0.1
O
Si
Mg
Al
C
Fe
Ca
Ca
Fe
Fe
cps/eV
keV

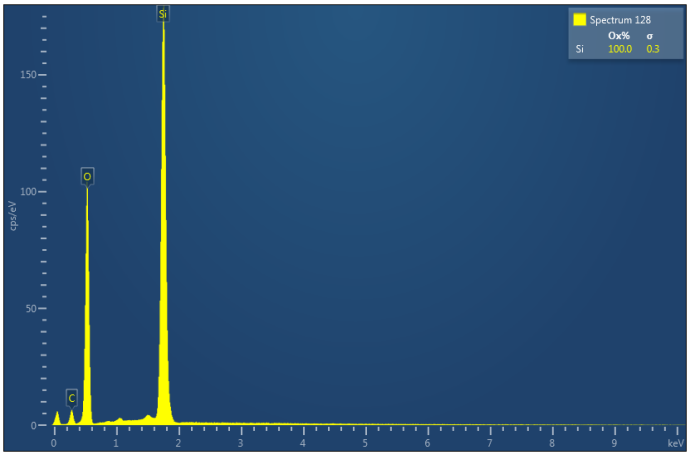

Spectrum 83
Ox% σ
Si 67.1 0.3
Al 20.2 0.2
Na 12.2 0.1
Ca 0.6 0.1
Si
O
Al
Na
C
Ca
Ca
Ca
cps/eV
keV

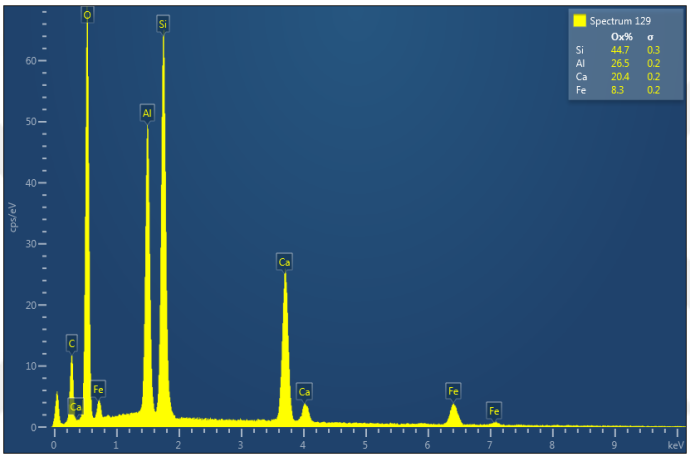
Sample 76

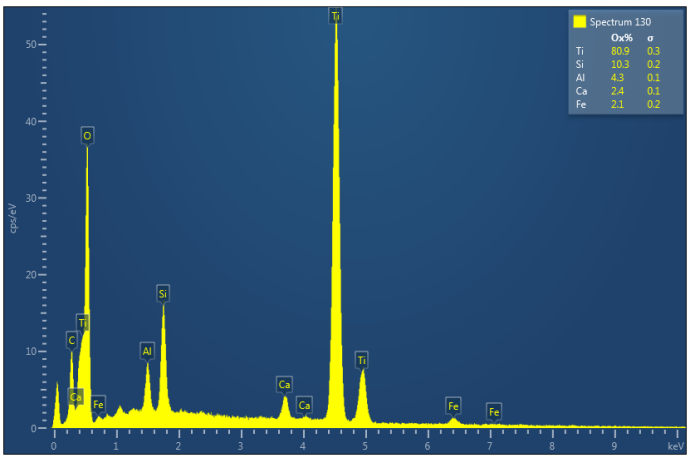
Electron Image 11

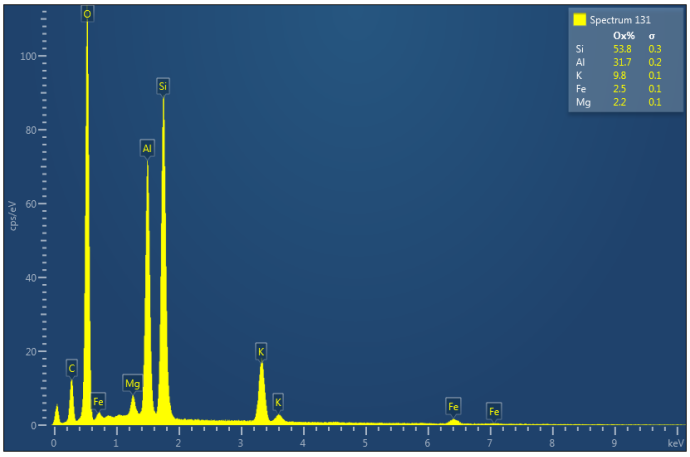


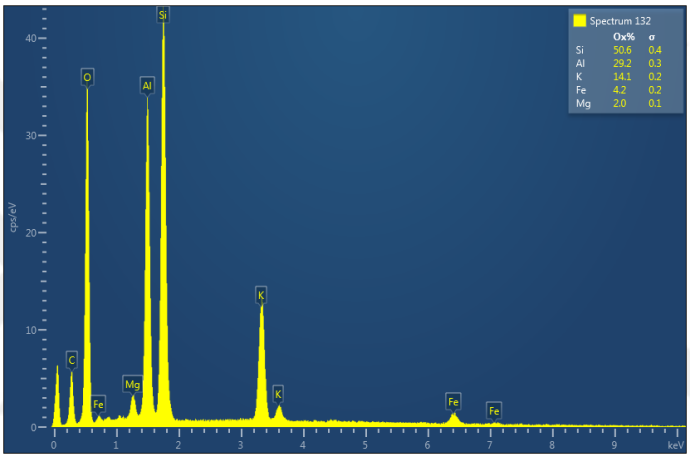


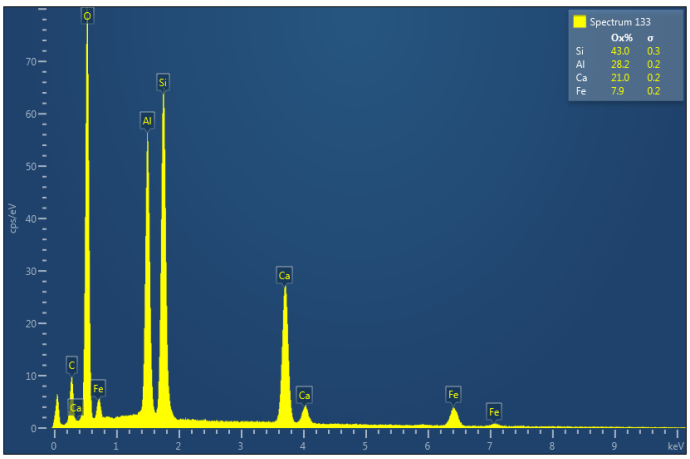

Spectrum 128
Ox%
σ
Si 100.0 0.3
Si
O
C
cps/eV
keV

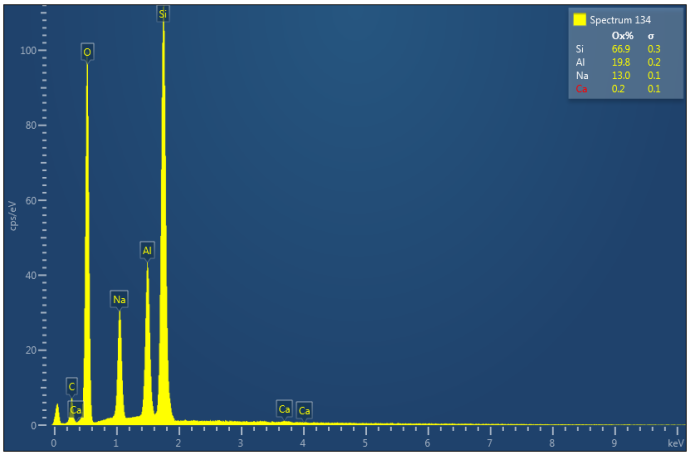

Spectrum 129
Ox%
σ
Si 44.7 0.3
Al 26.5 0.2
Ca 20.4 0.2
Fe 8.3 0.2
O
Si
Al
Ca
C
Fe
cps/eV
keV

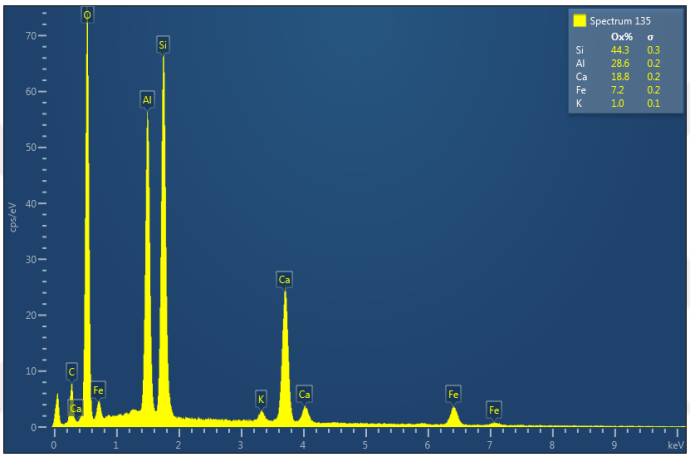

Spectrum 130
Ox%
σ
Ti 80.9 0.3
Si 10.3 0.2
Al 4.3 0.1
Ca 2.4 0.1
Fe 2.1 0.2
Ti
O
Si
C
Al
Ca
Fe
cps/eV
keV

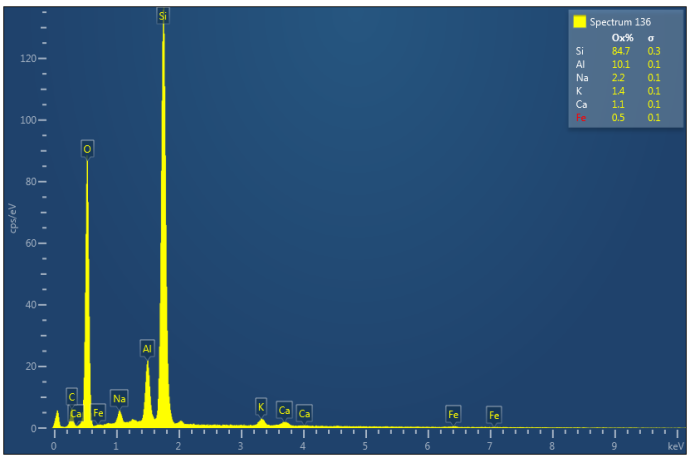

Spectrum 131
Ox%
σ
Si 53.8 0.3
Al 31.7 0.2
K 9.8 0.1
Fe 2.5 0.1
Mg 2.2 0.1
O
Si
Al
C
Fe
Mg
K
K
Fe
Fe
cps/eV
keV

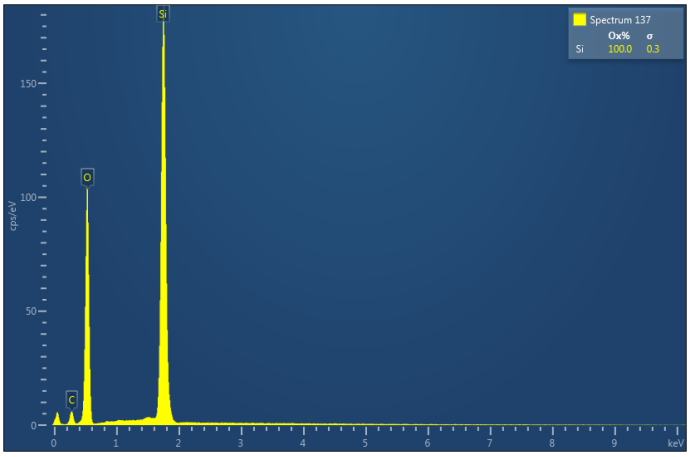

Spectrum 132
Ox%
σ
Si 50.6 0.4
Al 29.2 0.3
K 14.1 0.2
Fe 4.2 0.2
Mg 2.0 0.1
Si
O
Al
K
C
Mg
Fe
K
Fe
Fe
cps/eV
keV

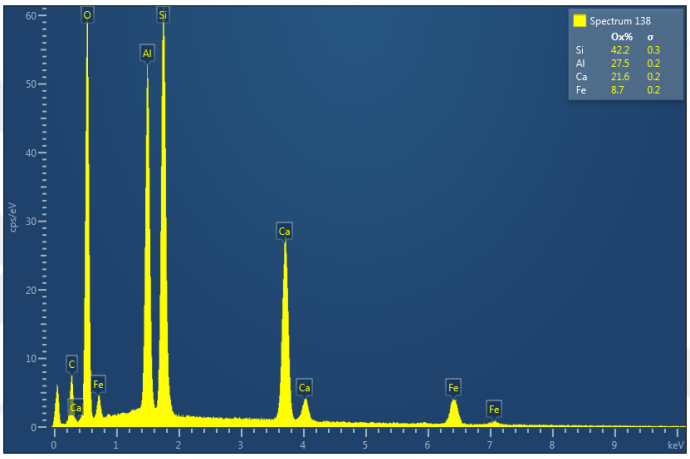

Spectrum 133
Ox%
σ
Si 43.0 0.3
Al 28.2 0.2
Ca 21.0 0.2
Fe 7.9 0.2
O
Si
Al
Ca
C
Fe
Ca
Ca
Fe
Fe
cps/eV
keV

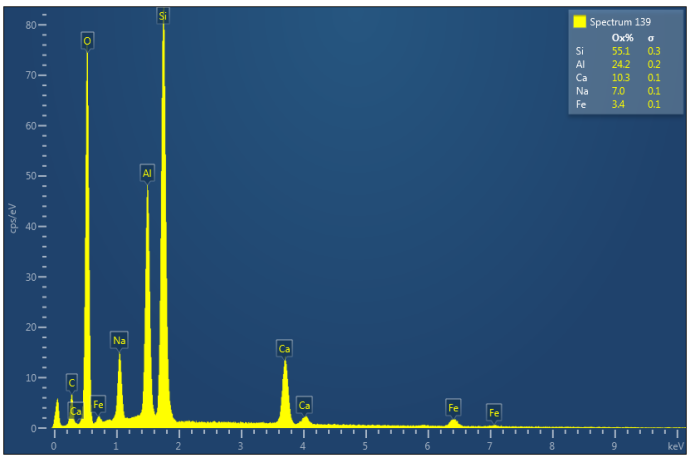

Spectrum 134
Ox%
σ
Si 66.9 0.3
Al 19.8 0.2
Na 13.0 0.1
Ca 0.2 0.1
O
Si
Al
Na
C
Ca
Ca
Ca
cps/eV
keV

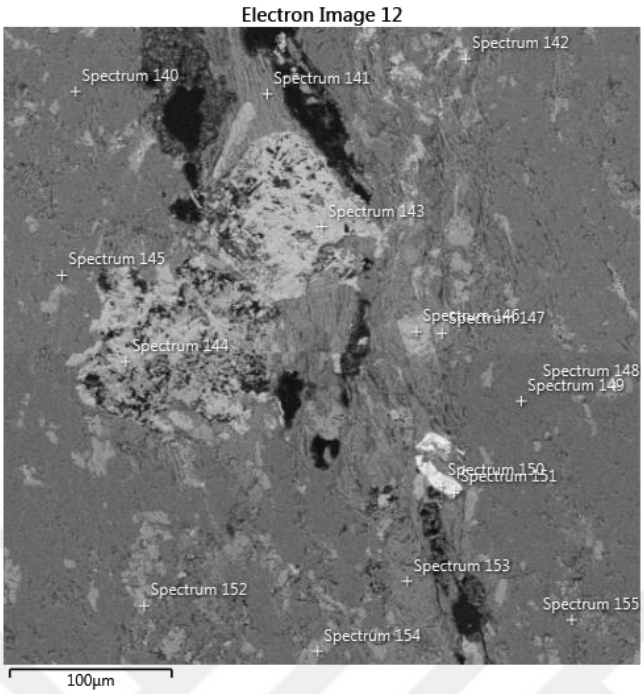

Spectrum 135
Ox%
σ
Si 44.3 0.3
Al 28.6 0.2
Ca 18.8 0.2
Fe 7.2 0.2
K 1.0 0.1
O
Si
Al
Ca
C
Fe
Ca
K
Ca
Fe
Fe
cps/eV
keV

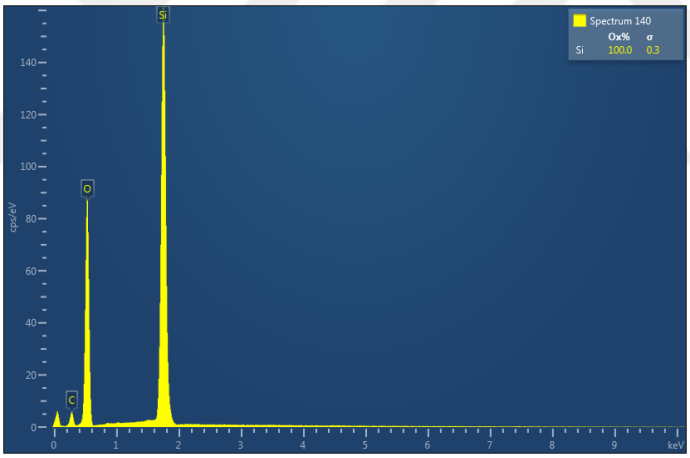

Spectrum 136
Ox%
σ
Si 84.7 0.3
Al 10.1 0.1
Na 2.2 0.1
K 1.4 0.1
Ca 1.1 0.1
Fe 0.5 0.1
Si
O
Al
C
Ca
Fe
Na
K
Ca
Ca
Fe
Fe
cps/eV
keV

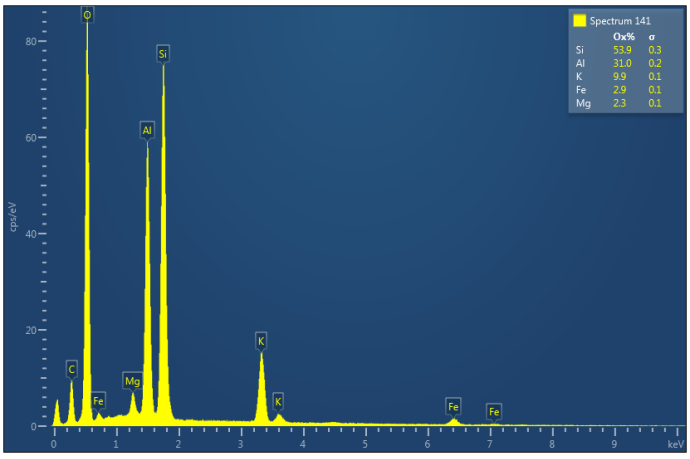

Spectrum 137
Ox% σ
Si 100.0 0.3
Si
O
C
cps/eV
keV

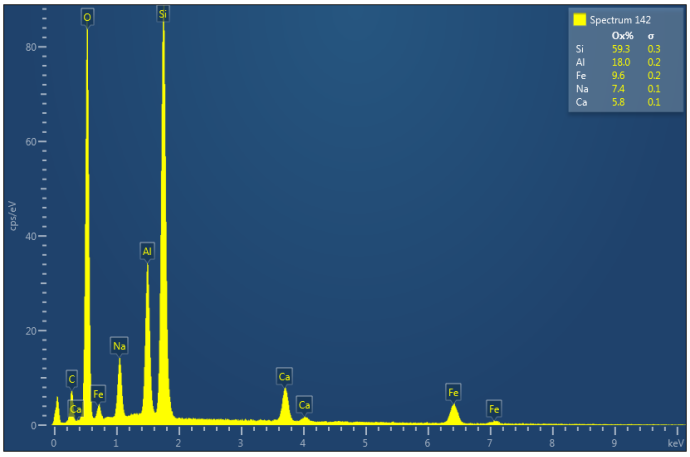

Spectrum 138
Ox% σ
Si 42.2 0.3
Al 27.5 0.2
Ca 21.6 0.2
Fe 8.7 0.2
O
Si
Al
Ca
C
Fe
Ca
Fe
Fe
cps/eV
keV

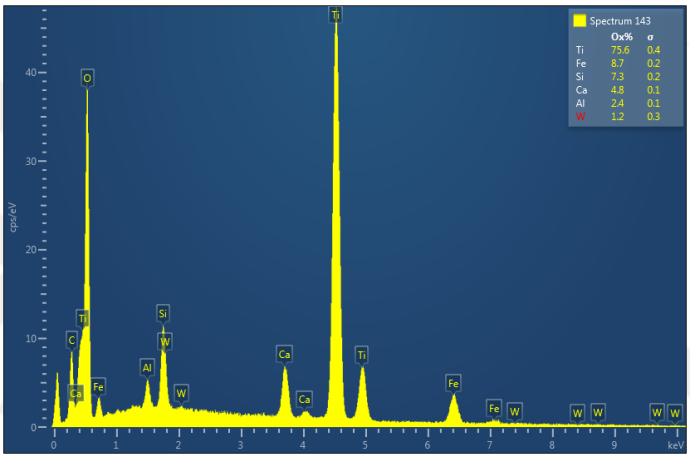

Spectrum 139
Ox% σ
Si 55.1 0.3
Al 24.2 0.2
Ca 10.3 0.1
Na 7.0 0.1
Fe 3.4 0.1
Si
O
Al
Na
Ca
C
Ca
Fe
Ca
Fe
Fe
cps/eV
keV

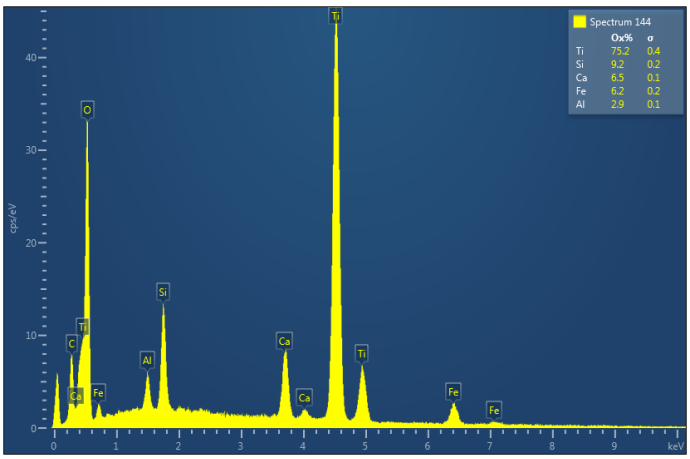

Electron Image 12
Spectrum 140
Spectrum 141
Spectrum 142
Spectrum 143
Spectrum 144
Spectrum 145
Spectrum 146
Spectrum 147
Spectrum 148
Spectrum 149
Spectrum 150
Spectrum 151
Spectrum 152
Spectrum 153
Spectrum 154
Spectrum 155
100µm

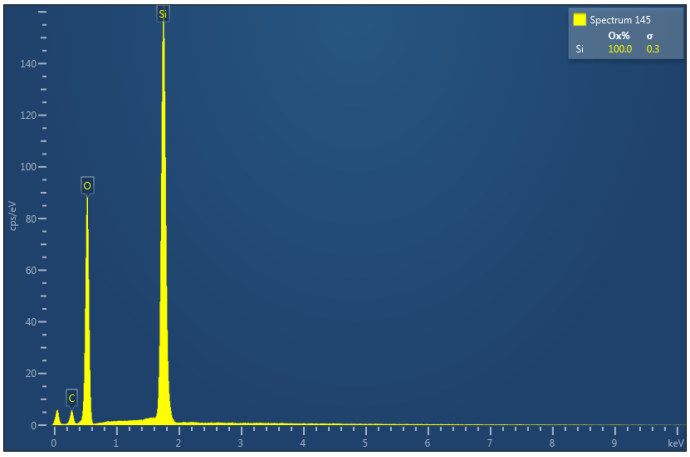

Spectrum 140
Ox%
σ
Si 100.0 0.3
Si
O
C
cps/eV
keV

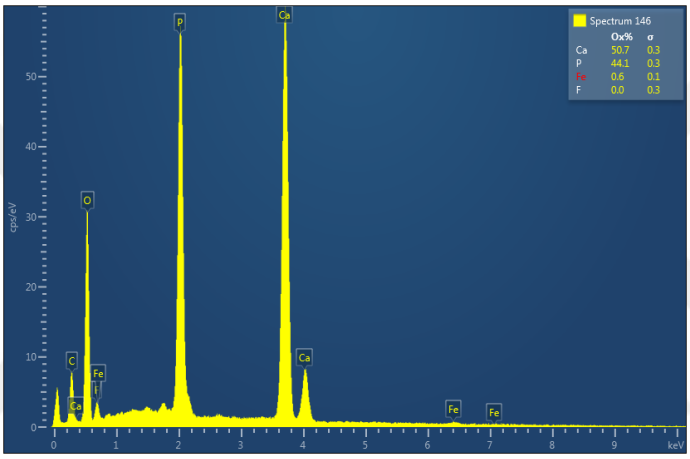

Spectrum 141
Ox%
σ
Si 53.9 0.3
Al 31.0 0.2
K 9.9 0.1
Fe 2.9 0.1
Mg 2.3 0.1
O
Si
Al
K
C
Mg
Fe
cps/eV
keV

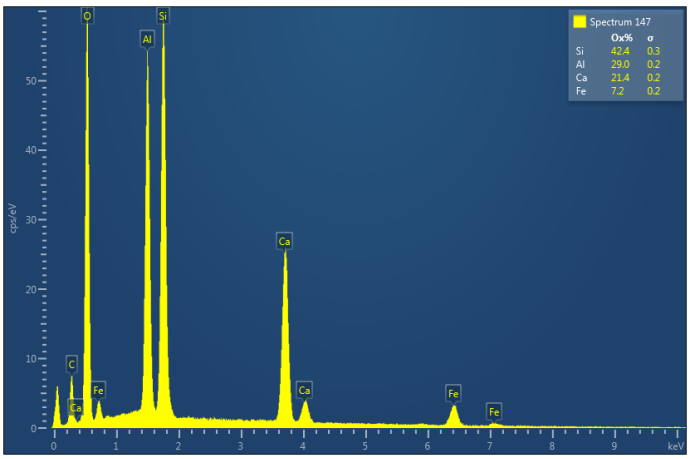

Spectrum 142
Ox% σ
Si 59.3 0.3
Al 18.0 0.2
Fe 9.6 0.2
Na 7.4 0.1
Ca 5.8 0.1
O
Si
Al
Na
C
Fe
Ca
Ca
Fe
Fe
cps/eV
keV

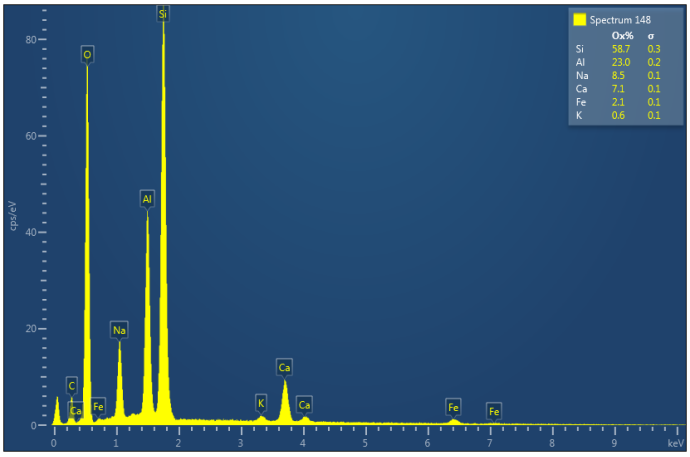

Spectrum 143
Ox% σ
Ti 75.6 0.4
Fe 8.7 0.2
Si 7.3 0.2
Ca 4.8 0.1
Al 2.4 0.1
W 1.2 0.3
Ti
O
Si
C
Ti
W
Al
Ca
Fe
Ca
W
Ca
Ti
Fe
Fe
W
W
W
W
cps/eV
keV

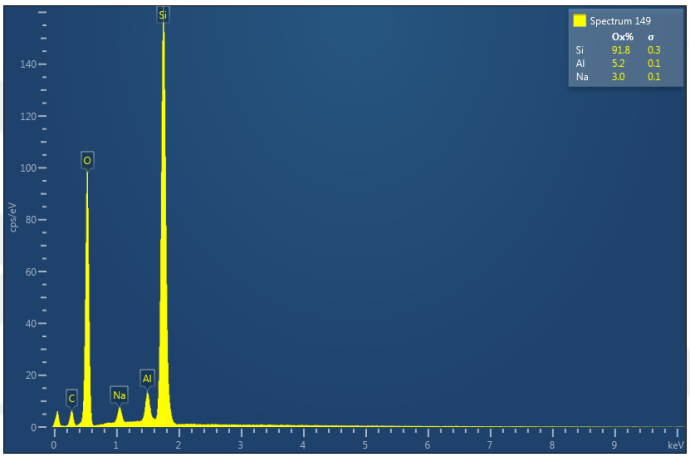

Spectrum 144
Ox% σ
Ti 75.2 0.4
Si 9.2 0.2
Ca 6.5 0.1
Fe 6.2 0.2
Al 2.9 0.1
Ti
O
Si
Ti
C
Al
Ca
Ca
Fe
Ti
Fe
Fe
cps/eV
keV

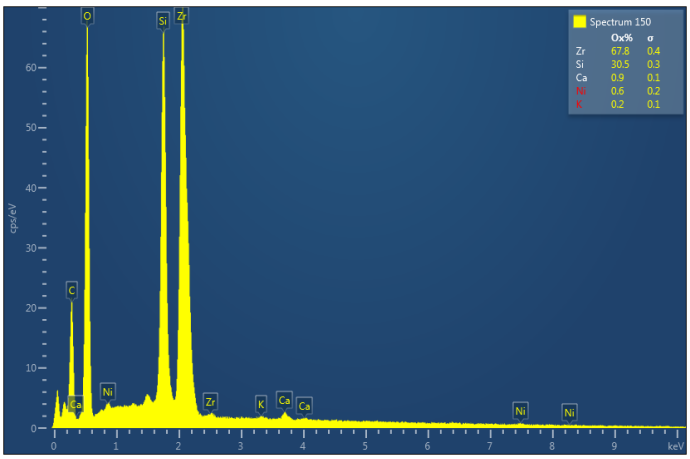

Spectrum 145
Ox%
σ
Si 100.0 0.3
Si
O
C
cps/eV
keV

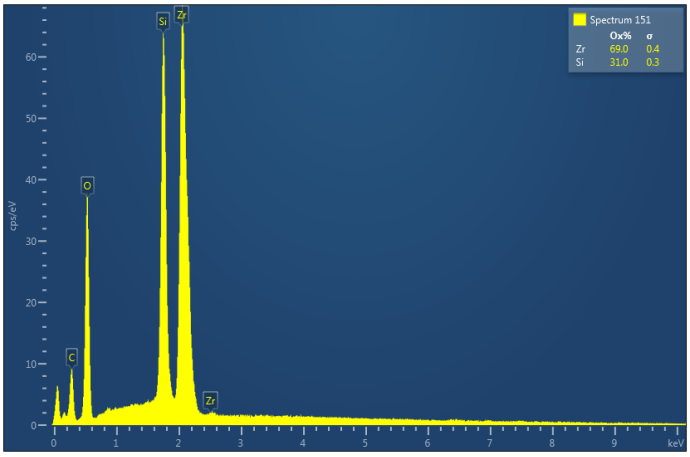

Spectrum 146
Ox%
σ
Ca 50.7 0.3
P 44.1 0.3
Fe 0.6 0.1
F 0.0 0.3
P
Ca
O
C
Fe
Ca
Fe
Fe
cps/eV
keV

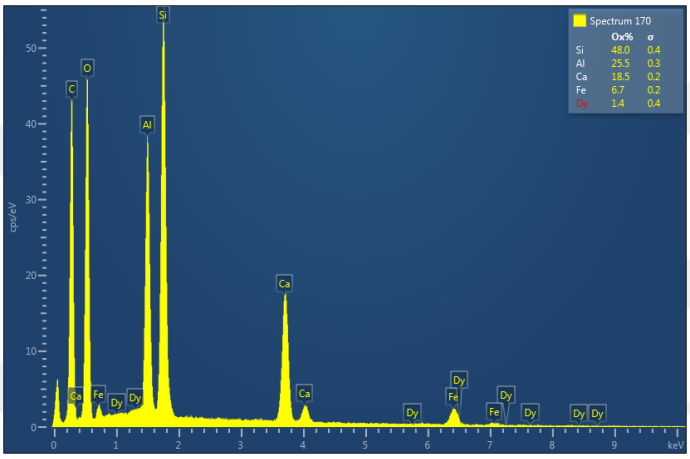

Spectrum 147
Ox%
σ
Si 42.4 0.3
Al 29.0 0.2
Ca 21.4 0.2
Fe 7.2 0.2
O
Si
Al
Ca
C
Fe
Ca
Fe
Fe
cps/eV
keV

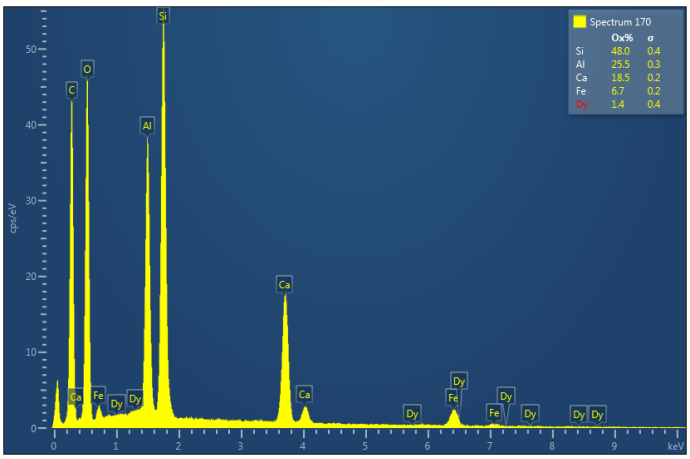

Spectrum 148
Ox% σ
Si 58.7 0.3
Al 23.0 0.2
Na 8.5 0.1
Ca 7.1 0.1
Fe 2.1 0.1
K 0.6 0.1
cps/eV
keV
O
Si
Al
Na
C
Ca
Fe
K
Ca
Fe
Fe

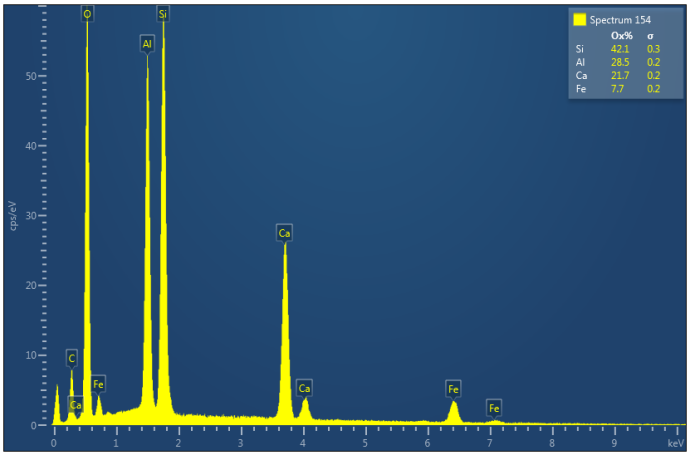

Spectrum 149
Ox% σ
Si 91.8 0.3
Al 5.2 0.1
Na 3.0 0.1
cps/eV
keV
Si
O
C
Na
Al

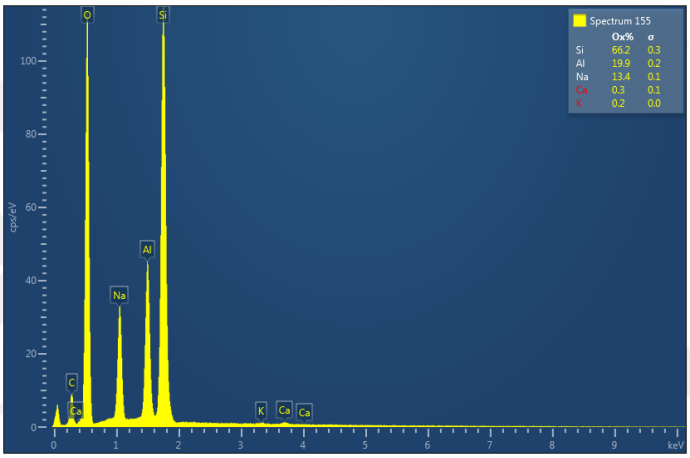

Spectrum 150
Ox% σ
Zr 67.8 0.4
Si 30.5 0.3
Ca 0.9 0.1
Ni 0.6 0.2
K 0.2 0.1
cps/eV
keV
O
Si
Zr
C
Ca
Ni
Zr
K
Ca
Ca
Ni
Ni


Spectrum 151
Ox%
σ
Zr 69.0 0.4
Si 31.0 0.3
Si
Zr
O
C
Zr
cps/eV
keV

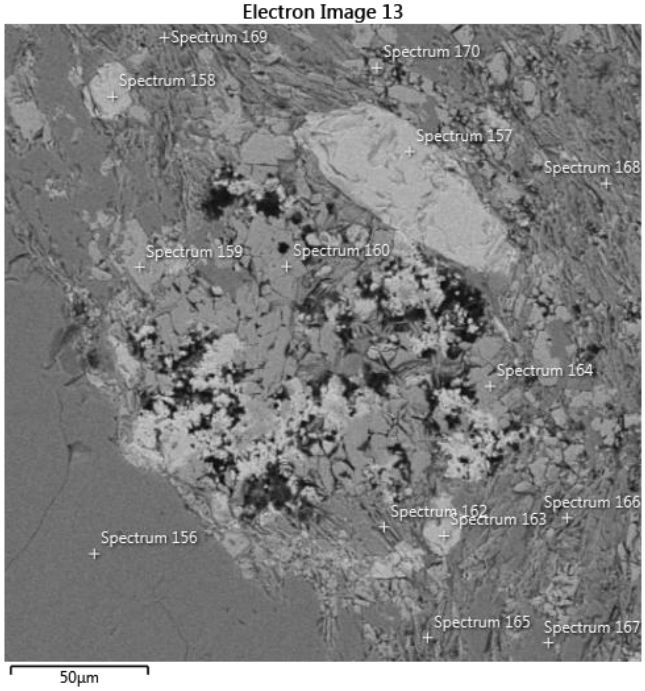

Spectrum 170
Ox%
σ
Si 48.0 0.4
Al 25.5 0.3
Ca 18.5 0.2
Fe 6.7 0.2
Dy 1.4 0.4
Si
C
O
Al
Ca
Ca
Fe
Dy
Dy
Dy
Fe
Fe
Dy
Dy
Dy
cps/eV
keV

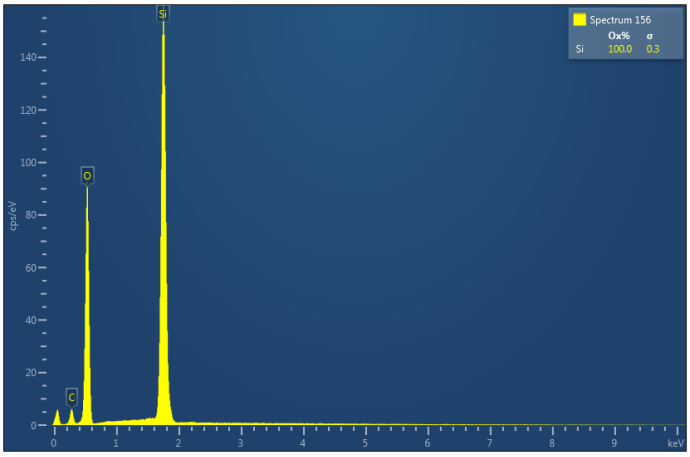

Spectrum 170
Ox%
σ
Si 48.0 0.4
Al 25.5 0.3
Ca 18.5 0.2
Fe 6.7 0.2
Dy 1.4 0.4
Si
C
O
Al
Ca
Ca
Fe
Dy
Dy
Dy
Fe
Fe
Dy
Dy
Dy
cps/eV
keV

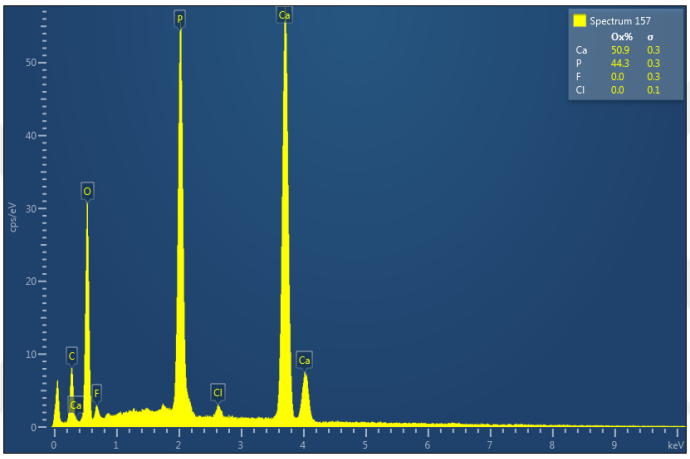


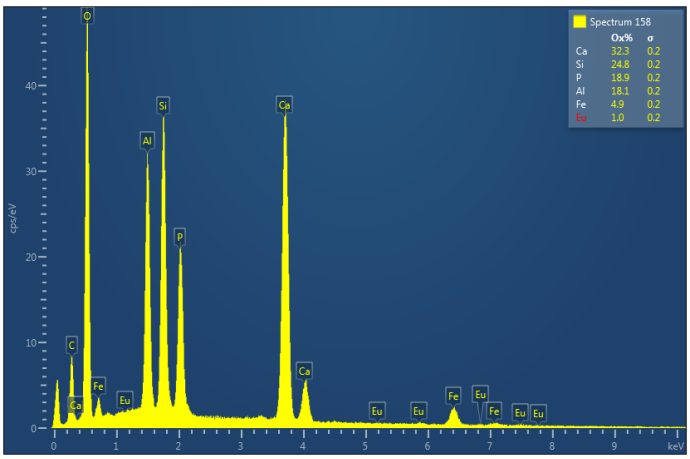


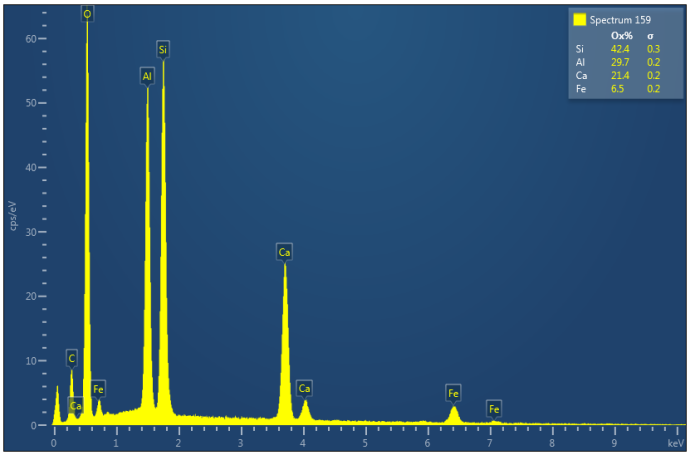
Electron Image 13

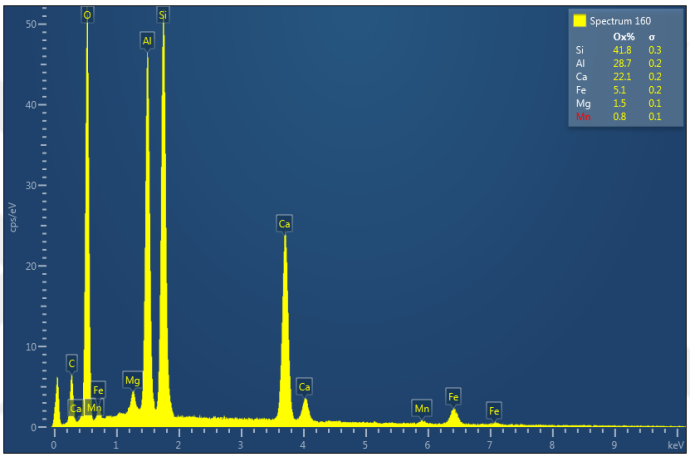


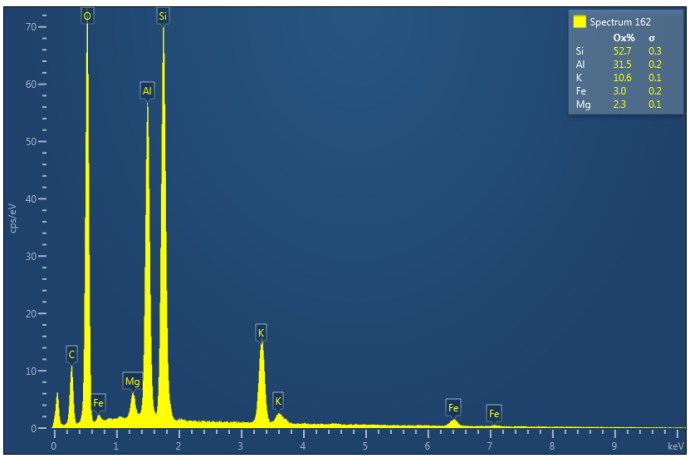

Spectrum 156
Ox%
σ
Si 100.0 0.3
cps/eV
keV
Si
O
C

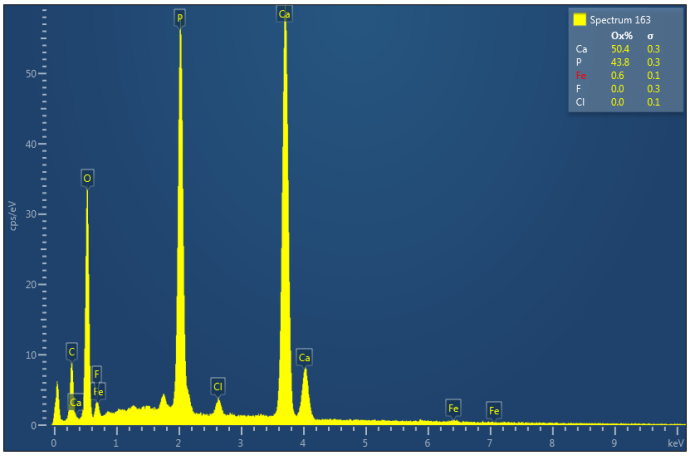

Spectrum 157
Ox%
σ
Ca 50.9 0.3
P 44.3 0.3
F 0.0 0.3
Cl 0.0 0.1
cps/eV
keV
P
Ca
O
C
Ca
F
Cl
Ca

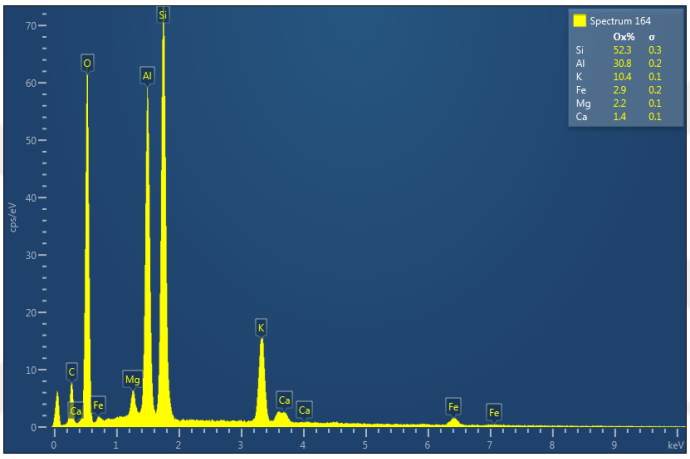

Spectrum 158
Ox%
σ
Ca 32.3 0.2
Si 24.8 0.2
P 18.9 0.2
Al 18.1 0.2
Fe 4.9 0.2
Eu 1.0 0.2
cps/eV
keV
O
Si
Ca
Al
P
C
Fe
Eu
Ca
Eu
Eu
Fe
Eu
Fe
Eu
Eu

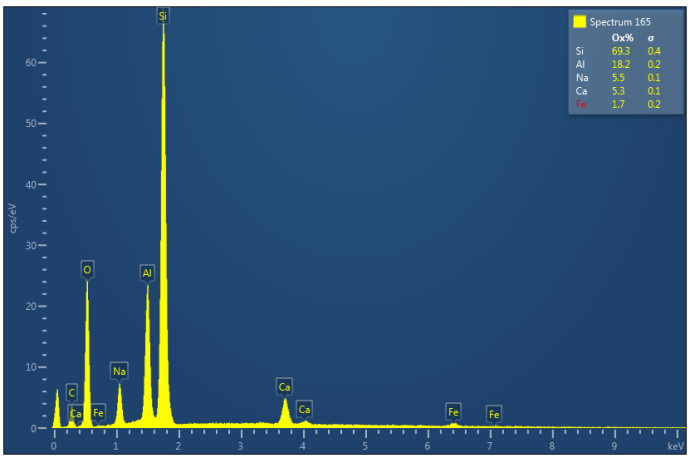

Spectrum 159
Ox% σ
Si 42.4 0.3
Al 29.7 0.2
Ca 21.4 0.2
Fe 6.5 0.2
O
Si
Al
Ca
C
Fe
Ca
Ca
Fe
Fe
cps/eV
keV

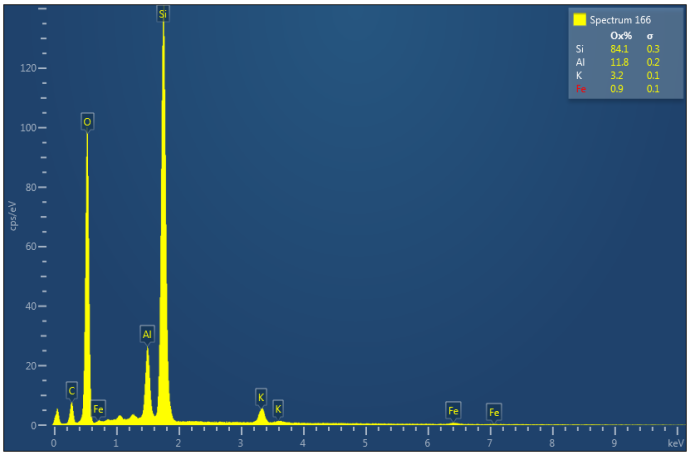

Spectrum 160
Ox% σ
Si 41.8 0.3
Al 28.7 0.2
Ca 22.1 0.2
Fe 5.1 0.2
Mg 1.5 0.1
Mn 0.8 0.1
O
Si
Al
Ca
C
Fe
Mg
Ca
Ca
Mn
Mn
Fe
Fe
cps/eV
keV

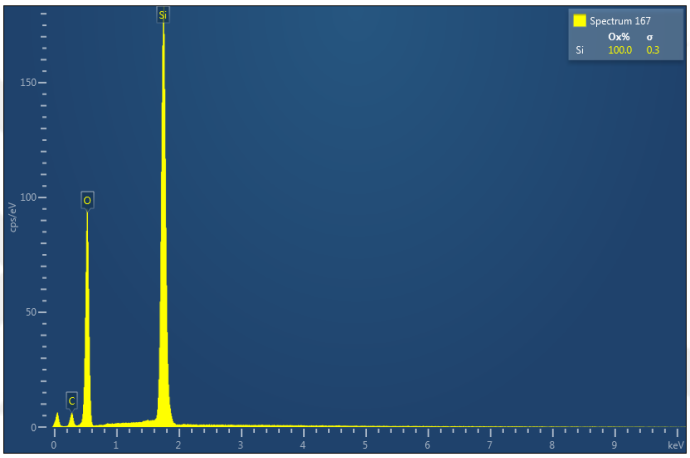

Spectrum 162
Ox% σ
Si 52.7 0.3
Al 31.5 0.2
K 10.6 0.1
Fe 3.0 0.2
Mg 2.3 0.1
O
Si
Al
K
C
Mg
Fe
K
Fe
Fe
cps/eV
keV

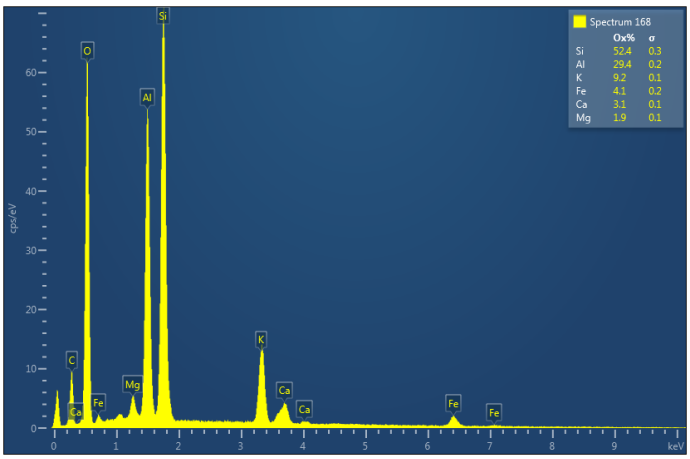

Spectrum 163
Ox% σ
Ca 50.4 0.3
P 43.8 0.3
Fe 0.6 0.1
F 0.0 0.3
Cl 0.0 0.1
P
Ca
O
C
F
Fe
Ca
Cl
Ca
Fe
Fe
cps/eV
keV

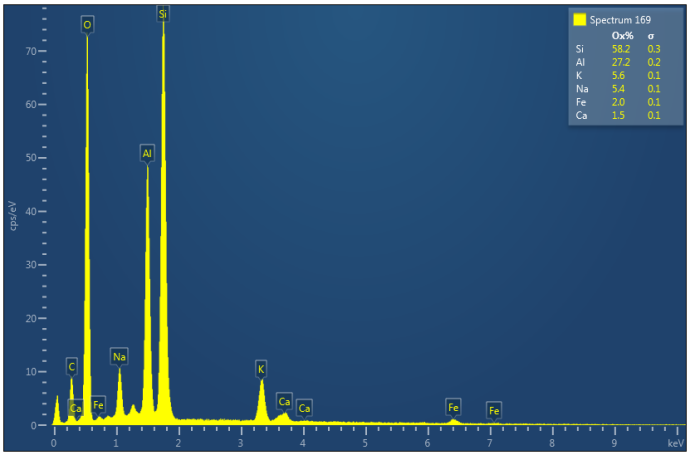

Spectrum 164
Ox% σ
Si 52.3 0.3
Al 30.8 0.2
K 10.4 0.1
Fe 2.9 0.2
Mg 2.2 0.1
Ca 1.4 0.1
Si
O
Al
K
C
Mg
Ca
Fe
Ca
Ca
Fe
Fe
cps/eV
keV

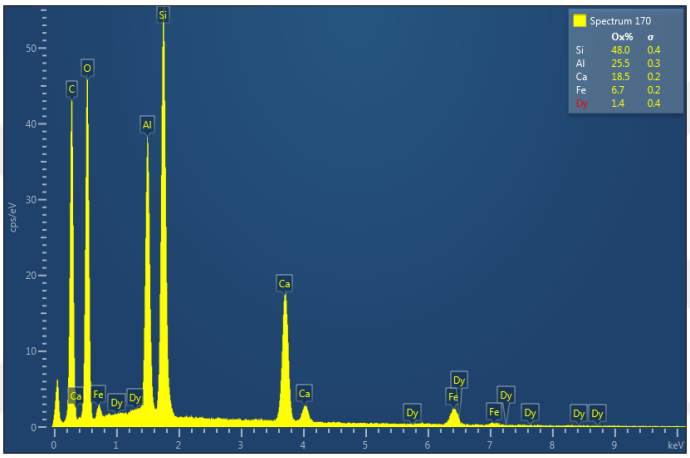

Spectrum 165
Ox% σ
Si 69.3 0.4
Al 18.2 0.2
Na 5.5 0.1
Ca 5.3 0.1
Fe 1.7 0.2
Si
O
Al
Na
C
Ca
Fe
Ca
Ca
Fe
Fe
cps/eV
keV


Spectrum 166
Ox%
σ
Si 84.1 0.3
Al 11.8 0.2
K 3.2 0.1
Fe 0.9 0.1
Si
O
Al
C
Fe
K
K
Fe
Fe
cps/eV
keV


Spectrum 167
Ox%
σ
Si 100.0 0.3
Si
O
C
cps/eV
keV

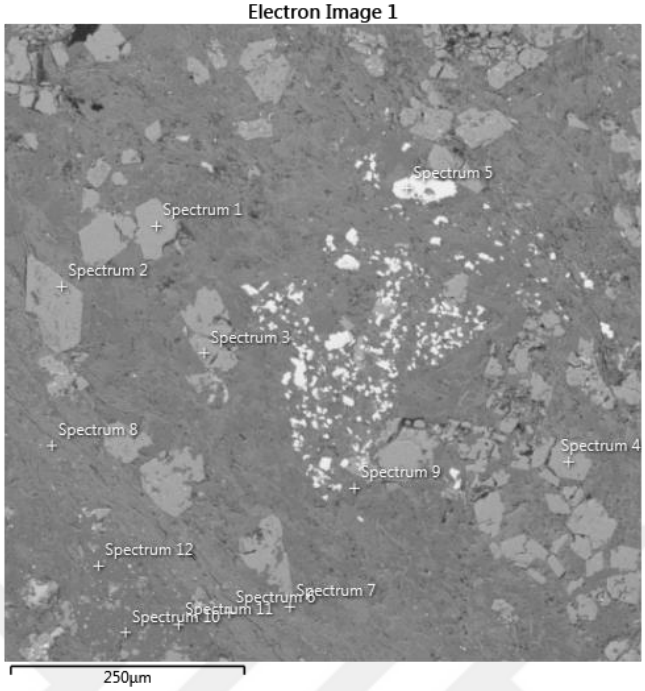

Spectrum 168
Ox%
σ
Si 52.4 0.3
Al 29.4 0.2
K 9.2 0.1
Fe 4.1 0.2
Ca 3.1 0.1
Mg 1.9 0.1
Si
O
Al
K
C
Mg
Ca
Ca
Fe
Fe
Fe
cps/eV
keV

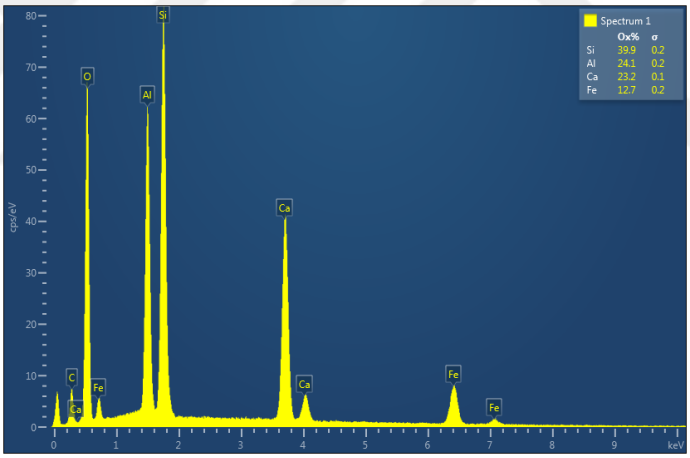


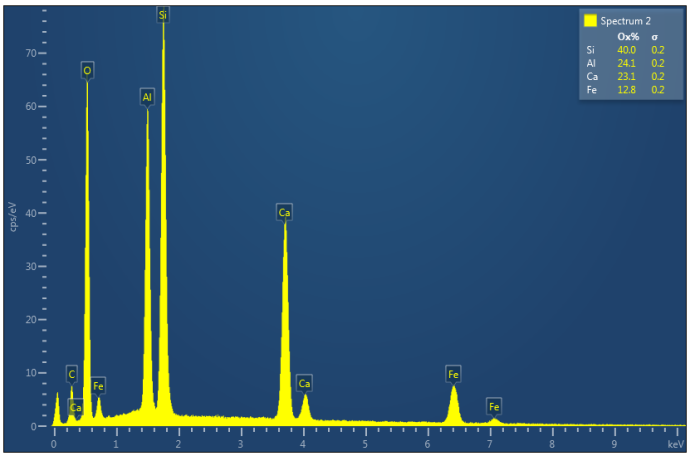


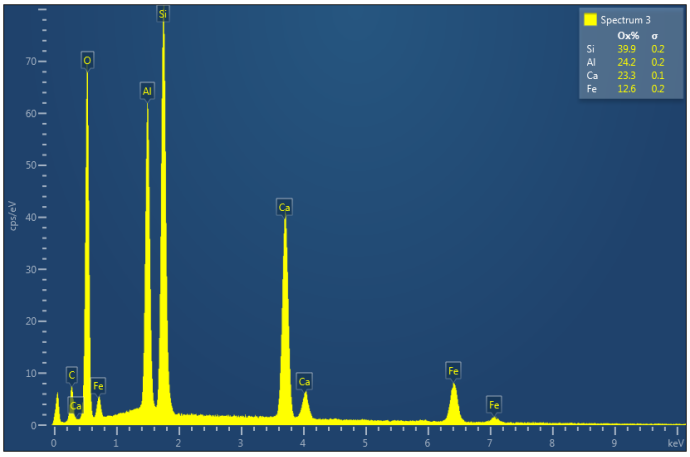
Sample AD-2-18

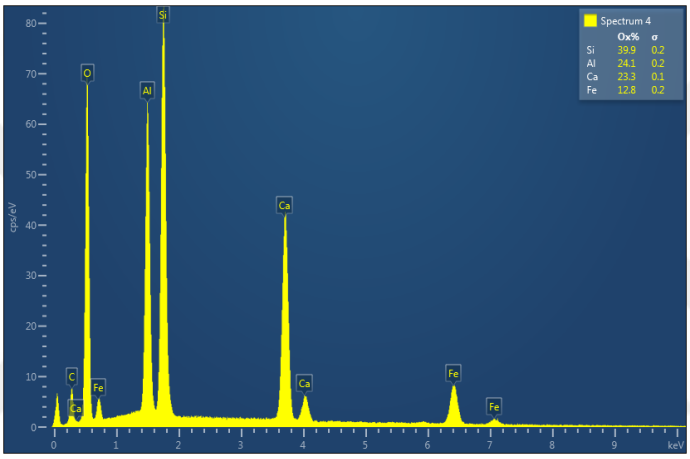
Electron Image 1

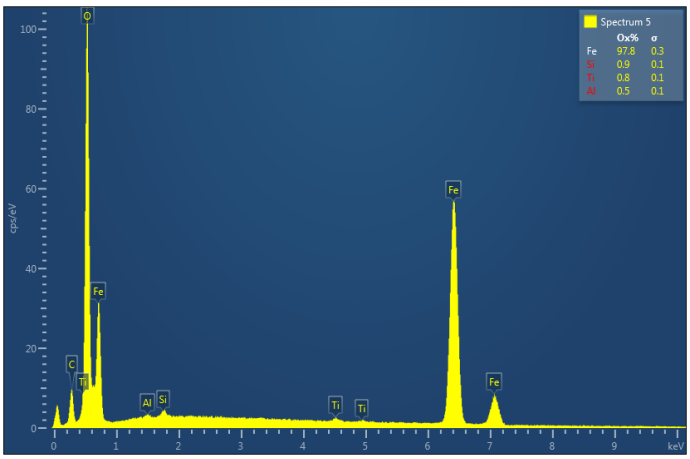


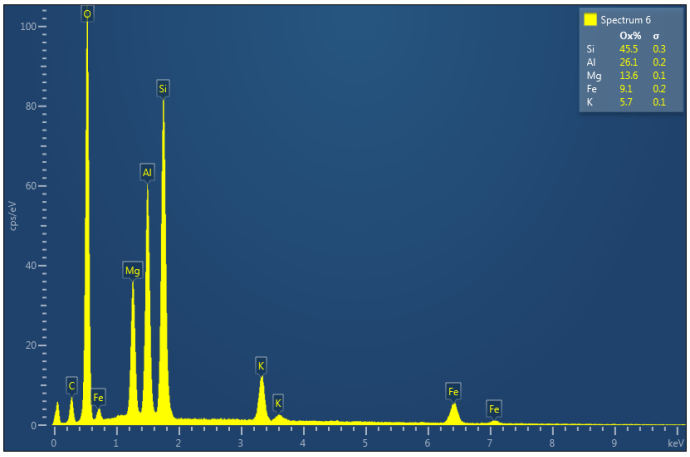


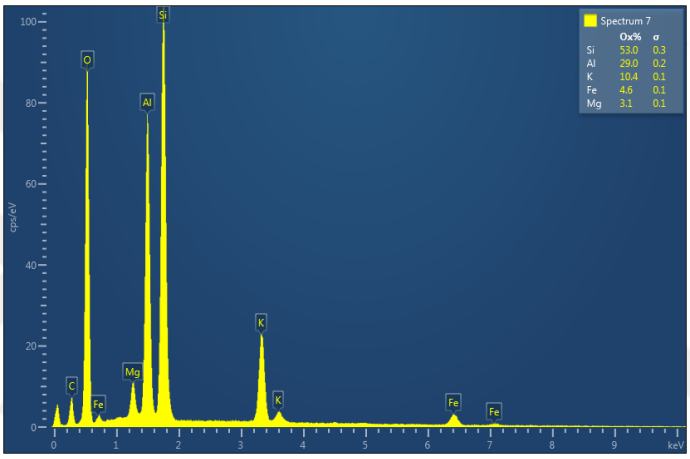


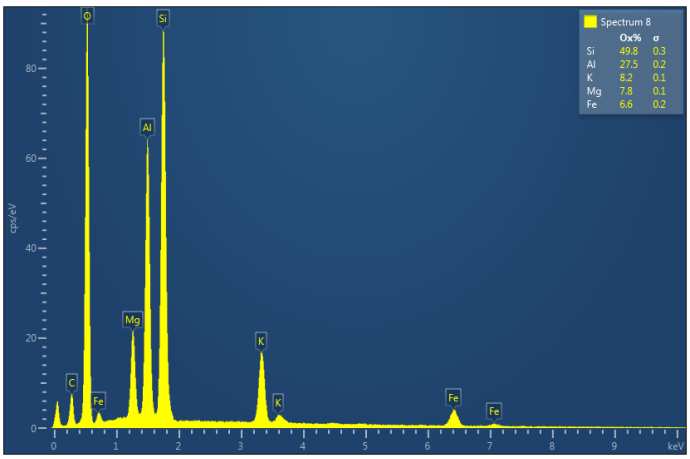

Spectrum 3
Ox% σ
Si 39.9 0.2
Al 24.2 0.2
Ca 23.3 0.1
Fe 12.6 0.2
cps/eV
keV
O
Si
Al
Ca
Fe
C

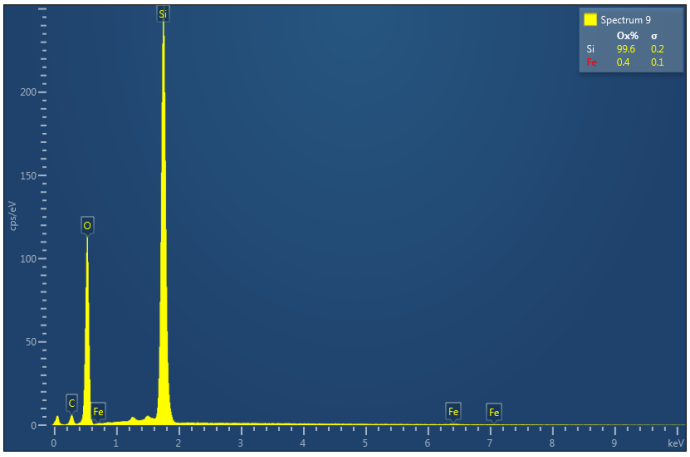

Spectrum 4
Ox% σ
Si 39.9 0.2
Al 24.1 0.2
Ca 23.3 0.1
Fe 12.8 0.2
cps/eV
keV
O
Si
Al
Ca
Fe
C

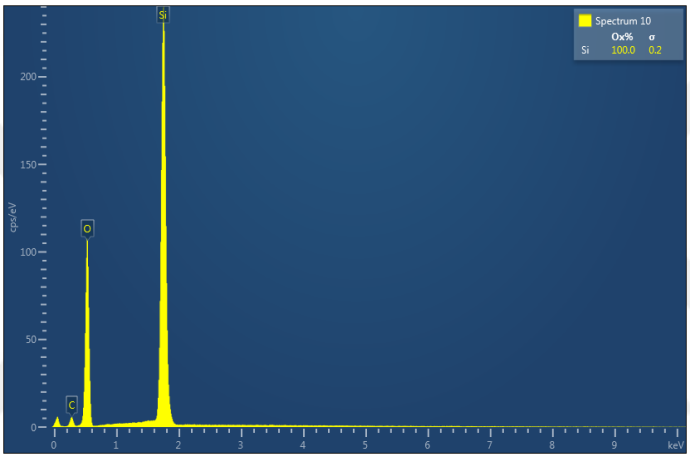

Spectrum 5
Ox% σ
Fe 97.8 0.3
Si 0.9 0.1
Ti 0.8 0.1
Al 0.5 0.1
cps/eV
keV
O
Fe
C
Ti
Al
Si

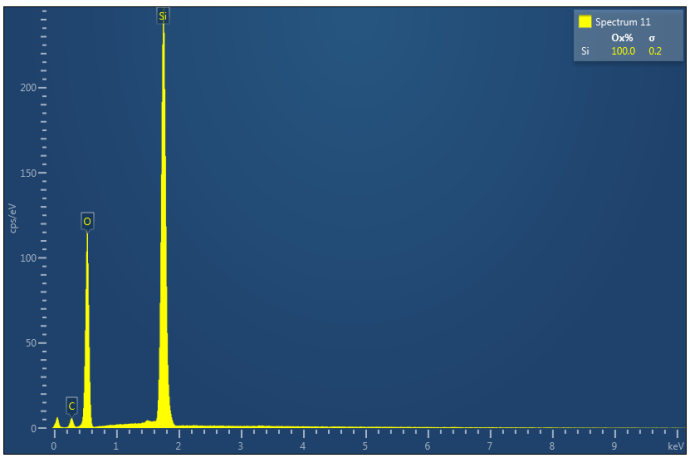

Spectrum 6
Ox% σ
Si 45.5 0.3
Al 26.1 0.2
Mg 13.6 0.1
Fe 9.1 0.2
K 5.7 0.1
O
Si
Al
Mg
C
Fe
K
Fe
Fe
cps/eV
keV

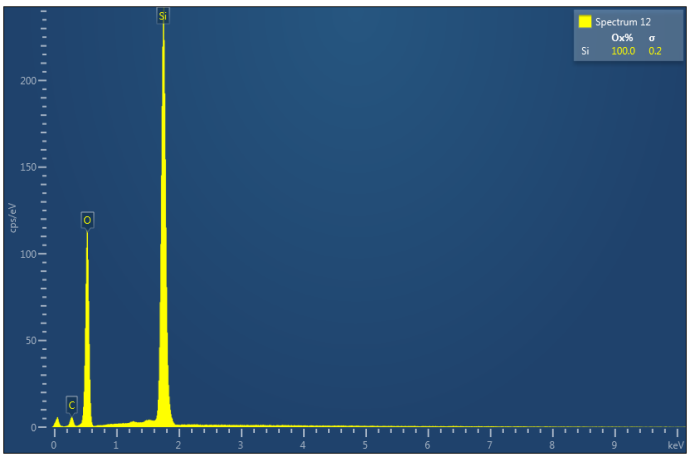

Spectrum 7
Ox% σ
Si 53.0 0.3
Al 29.0 0.2
K 10.4 0.1
Fe 4.6 0.1
Mg 3.1 0.1
O
Si
Al
K
Mg
C
Fe
K
Fe
Fe
cps/eV
keV


Spectrum 8
Ox% σ
Si 49.8 0.3
Al 27.5 0.2
K 8.2 0.1
Mg 7.8 0.1
Fe 6.6 0.2
O
Si
Al
Mg
K
C
Fe
K
Fe
Fe
cps/eV
keV

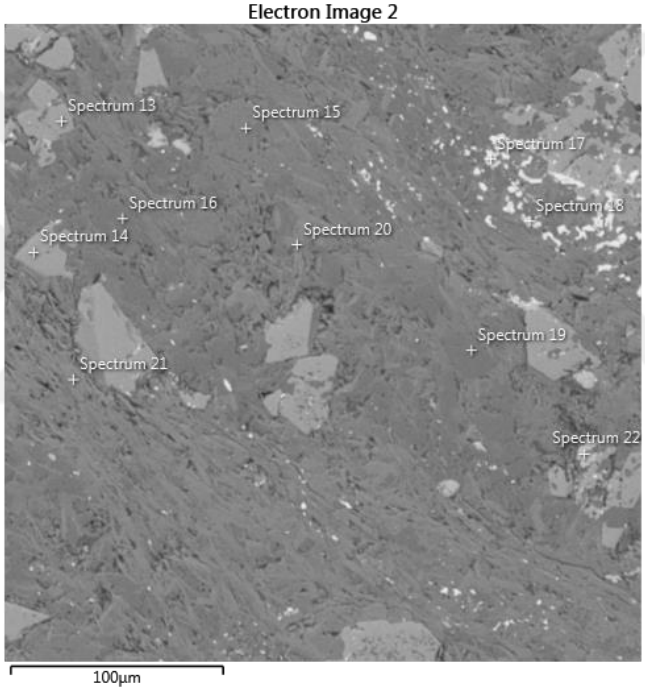

Spectrum 9
Ox%
σ
Si
99.6
0.2
Fe
0.4
0.1
Si
O
C
Fe
Fe
Fe
cps/eV
keV

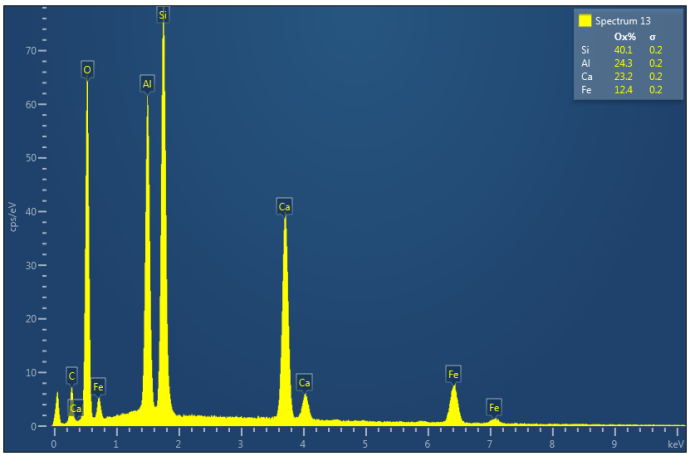

Spectrum 10
Ox%
σ
Si
100.0
0.2
Si
O
C
cps/eV
keV

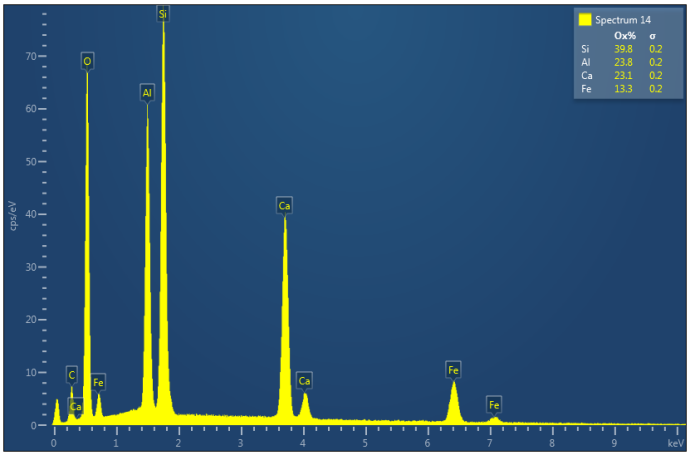

Spectrum 11
Ox%
σ
Si
100.0
0.2
Si
O
C
cps/eV
keV

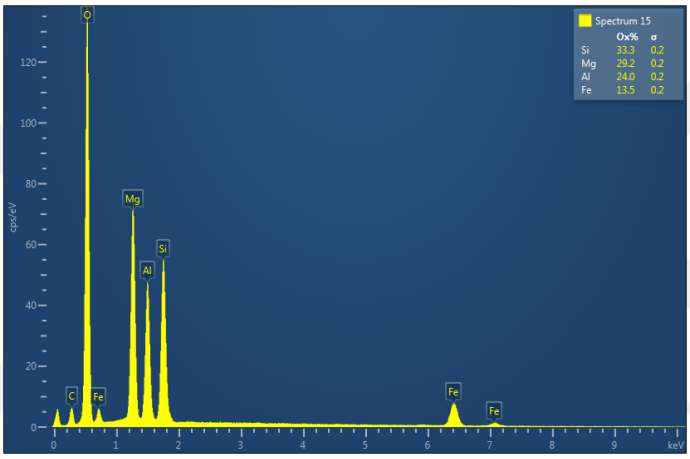


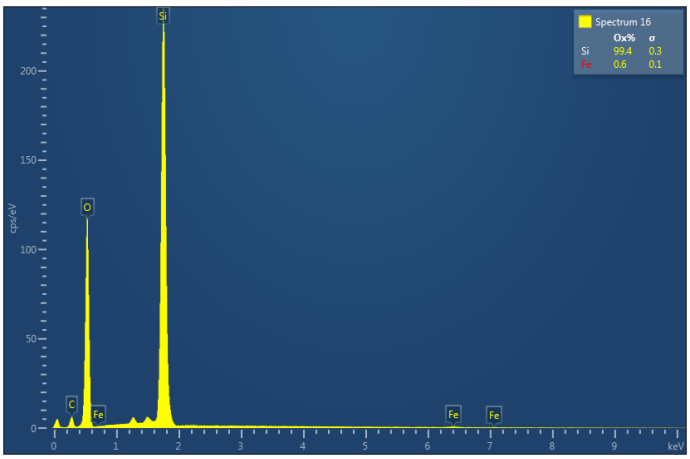
Electron Image 2

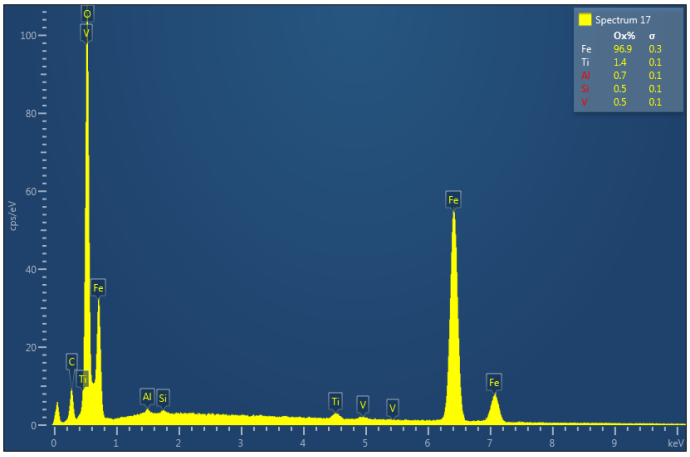


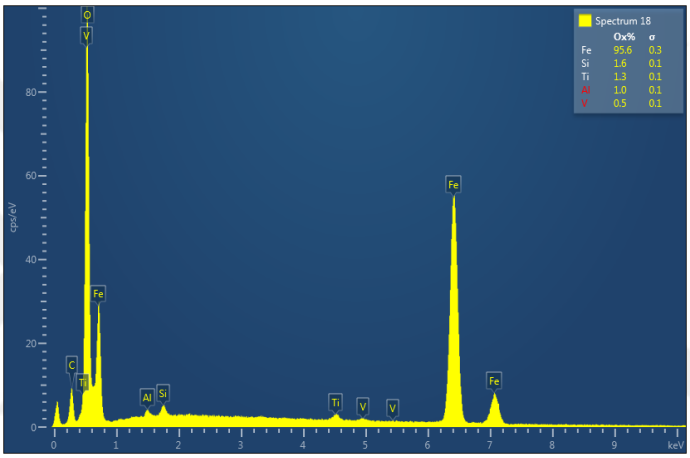


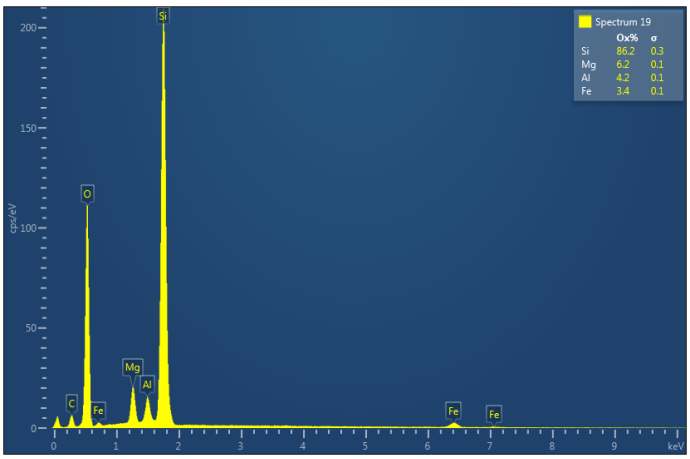

Spectrum 14
Ox%
σ
Si 39.8 0.2
Al 23.8 0.2
Ca 23.1 0.2
Fe 13.3 0.2
cps/eV
keV
O
Si
Al
Ca
C
Fe
Ca
Fe
Ca
Fe
Fe

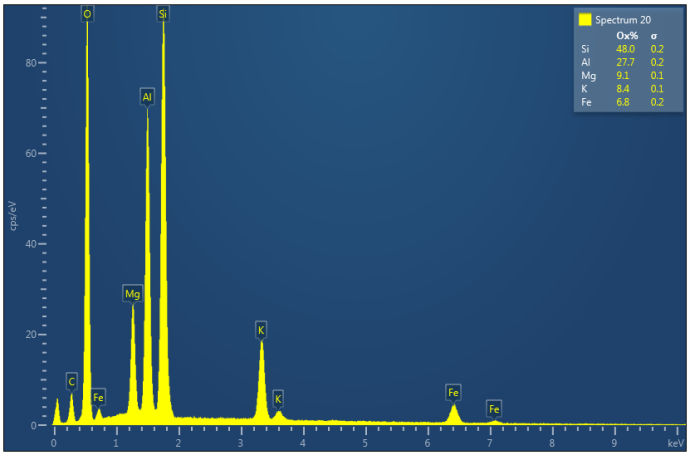

Spectrum 15
Ox%
σ
Si 33.3 0.2
Mg 29.2 0.2
Al 24.0 0.2
Fe 13.5 0.2
cps/eV
keV
O
Mg
Si
Al
C
Fe
Fe
Fe

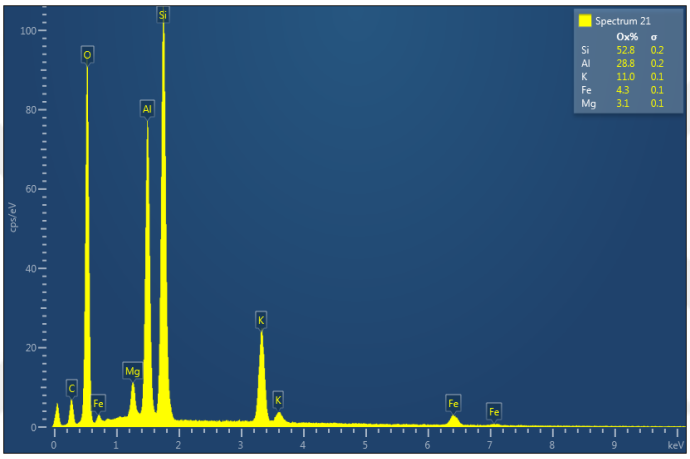

Spectrum 16
Ox%
σ
Si 99.4 0.3
Fe 0.6 0.1
cps/eV
keV
Si
O
C
Fe
Fe
Fe

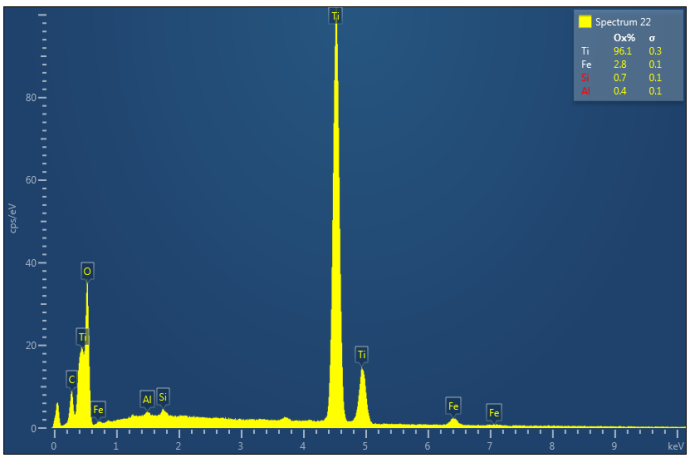

Spectrum 17
Ox%
σ
Fe 96.9 0.3
Ti 1.4 0.1
Al 0.7 0.1
Cr 0.5 0.1
V 0.5 0.1
O
C
Ti
Al
Si
Ti
V
V
Fe
Fe
Fe
cps/eV
keV


Spectrum 18
Ox%
σ
Fe 95.6 0.3
Si 1.6 0.1
Ti 1.3 0.1
Al 1.0 0.1
V 0.5 0.1
O
C
Ti
Al
Si
Ti
V
V
Fe
Fe
Fe
cps/eV
keV

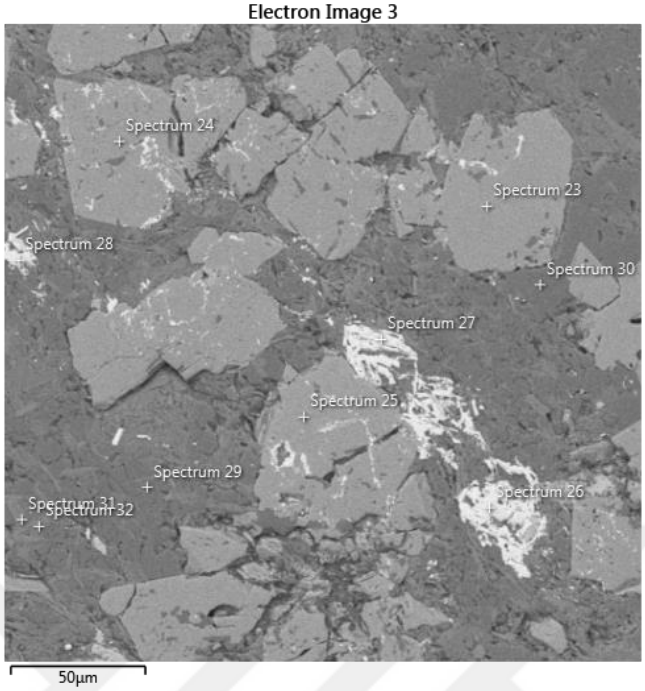

Spectrum 19
Ox%
σ
Si 86.2 0.3
Mg 6.2 0.1
Al 4.2 0.1
Fe 3.4 0.1
Si
O
C
Fe
Mg
Al
Fe
Fe
cps/eV
keV

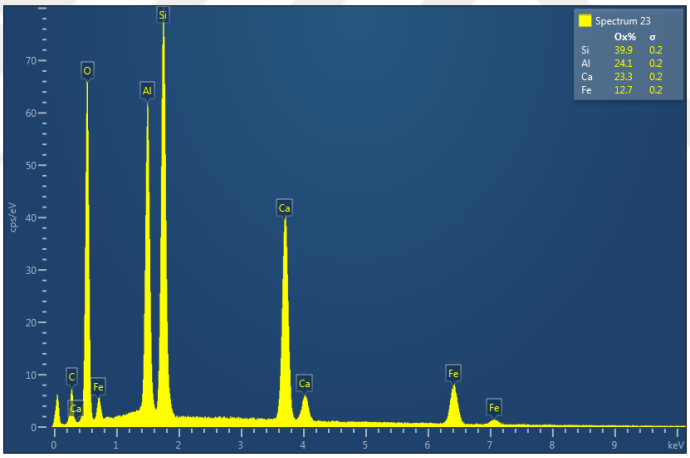

Spectrum 20
Ox%
σ
Si 48.0 0.2
Al 27.7 0.2
Mg 9.1 0.1
K 8.4 0.1
Fe 6.8 0.2
O
Si
Al
Mg
K
C
Fe
cps/eV
keV

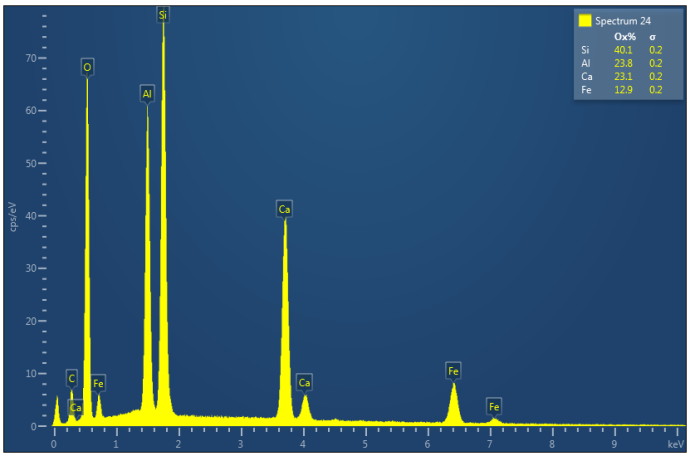

Spectrum 21
Ox%
σ
Si 52.8 0.2
Al 28.8 0.2
K 11.0 0.1
Fe 4.3 0.1
Mg 3.1 0.1
Si
O
Al
K
Mg
C
Fe
cps/eV
keV

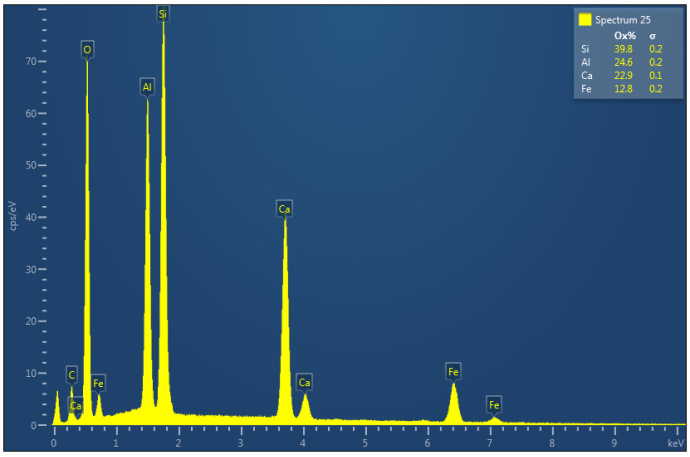

Spectrum 22
Ox%
σ
Ti 96.1 0.3
Fe 2.8 0.1
Si 0.7 0.1
Al 0.4 0.1
Ti
O
C
Fe
Al
Si
cps/eV
keV

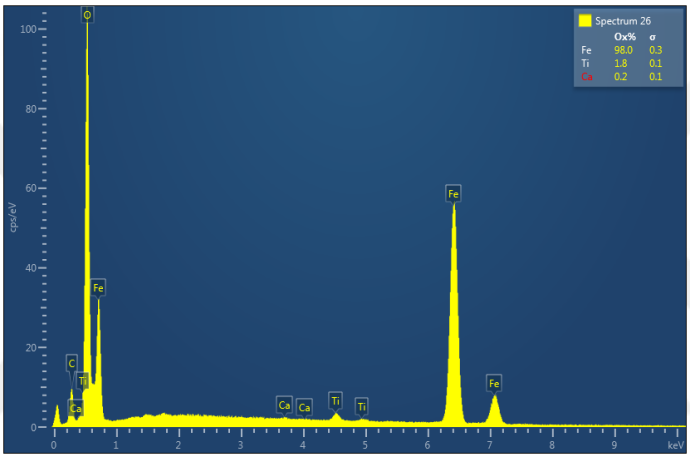
Electron Image 3

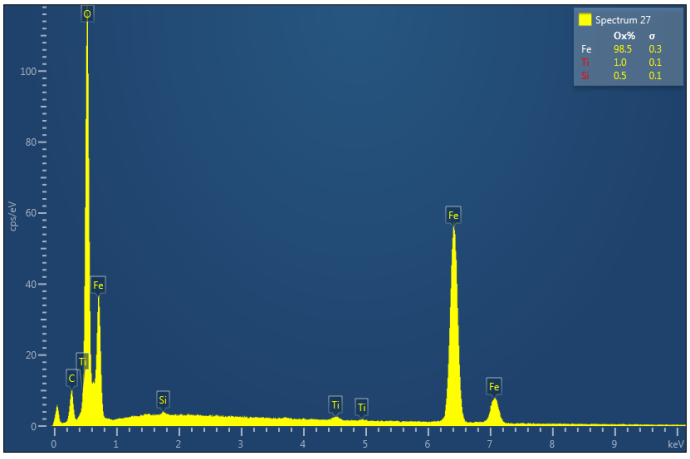


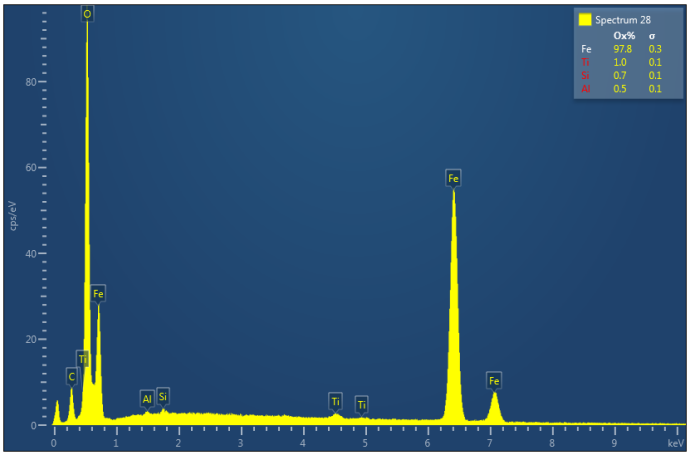


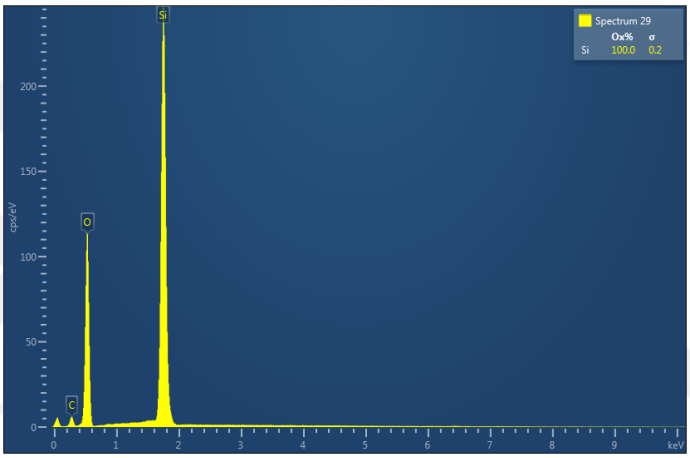


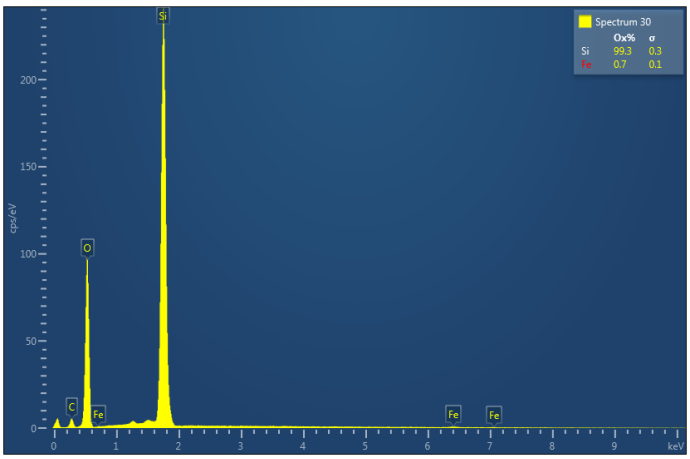

Spectrum 25
Ox%
σ
Si 39.8 0.2
Al 24.6 0.2
Ca 22.9 0.1
Fe 12.8 0.2
O
Si
Al
Ca
C
Fe
Ca
Ca
Fe
Fe
cps/eV
keV

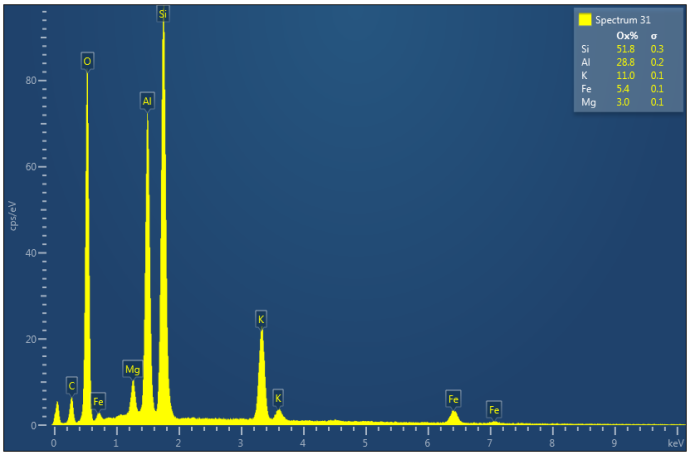

Spectrum 26
Ox%
σ
Fe 98.0 0.3
Ti 1.8 0.1
Ca 0.2 0.1
O
Fe
Fe
C
Ti
Ca
Ca
Ca
Ti
Ti
Fe
Fe
cps/eV
keV

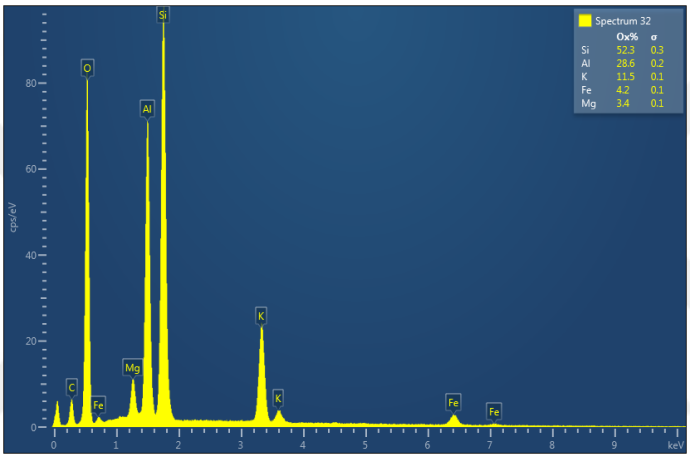

Spectrum 27
Ox%
σ
Fe 98.5 0.3
Ti 1.0 0.1
Si 0.5 0.1
O
Fe
Fe
Ti
C
Si
Ti
Ti
Fe
Fe
cps/eV
keV


Spectrum 28
Ox%
σ
Fe 97.8 0.3
Ti 1.0 0.1
Si 0.7 0.1
Al 0.5 0.1
O
Fe
Ti
C
Al
Si
Ti
Ti
Fe
Fe
cps/eV
keV


Spectrum 29
Ox%
σ
Si 100.0 0.2
Si
O
C
cps/eV
keV


Spectrum 30
Ox%
σ
Si 99.3 0.3
Fe 0.7 0.1
Si
O
C
Fe
Fe
Fe
cps/eV
keV


Spectrum 31
Ox% σ
Si 51.8 0.3
Al 28.8 0.2
K 11.0 0.1
Fe 5.4 0.1
Mg 3.0 0.1
Si
O
Al
K
Mg
C
Fe
K
Fe
Fe
cps/eV
keV


Spectrum 32
Ox% σ
Si 52.3 0.3
Al 28.6 0.2
K 11.5 0.1
Fe 4.2 0.1
Mg 3.4 0.1
Si
O
Al
K
Mg
C
Fe
K
Fe
Fe
cps/eV
keV

B. Detailed age data for the Kösdağ Metavolcanics

Detailed Age Data for the **197**

Grain #	207/235	2σ Prop	206/238	2σ Prop	RHO	207/235 Age Ma	2σ Prop	206/238 Age (Ma)	2σ Prop	207/206 Age (Ma)	2σ Prop	Best age (Ma)	2σ Prop
TM22_10.FIN2	0.095	0.01	0.01495	0.00054	0.091013	90.7	9.4	95.7	3.4	60	200	95.7	3.4
TM22_14.FIN2	0.0931	0.0094	0.0143	0.00061	0.054324	89.5	8.7	91.5	3.9	90	190	91.5	3.9
TM22_15.FIN2	0.11	0.018	0.0151	0.00097	0.22869	105	17	96.6	6.1	210	290	96.6	6.1
TM21_67.FIN2	0.097	0.011	0.0149	0.00048	0.026271	94	10	95.3	3	70	200	95.3	3

Detailed Age Data for the **AB-6-17**

Grain #	207/235	2σ Prop	206/238	2σ Prop	RHO	207/235 Age Ma	2σ Prop	206/238 Age (Ma)	2σ Prop	207/206 Age (Ma)	2σ Prop	Best age (Ma)	2σ Prop
AB-6-17	0.1033	0.0079	0.01497	0.00042	0.11205	99.2	7.2	95.8	2.6	180	140	95.8	2.6
AB-6-17	0.091	0.012	0.0143	0.00063	0.24441	89	12	91.5	4	0	210	91.5	4
AB-6-17	0.105	0.011	0.01505	0.00047	0.09101	100.1	9.6	96.3	3	140	180	96.3	3
AB-6-17	0.114	0.022	0.01525	0.00074	0.18655	108	19	97.6	4.7	240	340	97.6	4.7
AB-6-17	0.104	0.012	0.01505	0.00066	0.018701	100	11	96.3	4.2	220	220	96.3	4.2
AB-6-17	0.1	0.0049	0.01459	0.00033	0.1299	96.6	4.5	93.4	2.1	148	93	93.4	2.1
AB-6-17	0.1009	0.0046	0.01492	0.00027	0.13346	97.4	4.3	95.4	1.7	133	87	95.4	1.7
AB-6-17	0.1069	0.0083	0.01484	0.00049	0.10694	102.6	7.6	95	3.1	250	150	95	3.1
AB-6-17	0.0925	0.0082	0.01469	0.00052	0.17175	90.3	7.9	94	3.3	10	160	94	3.3
AB-6-17	0.0993	0.0098	0.01512	0.00063	0.20745	95.2	9	96.7	4	130	190	96.7	4
AB-6-17	0.098	0.012	0.01523	0.00068	0.2341	94	11	97.4	4.3	20	210	97.4	4.3
AB-6-17	0.1023	0.0038	0.01496	0.00032	0.34399	98.7	3.5	95.7	2	172	70	95.7	2
AB-6-17	0.097	0.011	0.0149	0.00053	0.021343	93	10	95.3	3.4	20	200	95.3	3.4
AB-6-17	0.1138	0.0093	0.01568	0.0005	0.077909	108.7	8.5	100.3	3.2	260	160	100.3	3.2
AB-6-17	0.0985	0.0036	0.01484	0.0003	0.15748	95.3	3.3	94.9	1.9	106	71	94.9	1.9
AB-6-17	0.1023	0.0038	0.01484	0.00028	0.34833	98.7	3.5	94.9	1.8	177	68	94.9	1.8
AB-6-17	0.093	0.01	0.01431	0.00052	0.087499	91	10	91.6	3.3	80	200	91.6	3.3
AB-6-17	0.101	0.011	0.01468	0.00052	0.18077	96.7	9.9	93.9	3.3	130	200	93.9	3.3

Detailed Age Data for the **KR-5-18**

						207/235		206/238		207/206		Best age	
Grain #	207/235	2σ Prop	206/238	2σ Prop	RHO	Age Ma	2σ Prop	Age (Ma)	2σ Prop	Age (Ma)	2σ Prop	(Ma)	2σ Prop
KR-5-18	0.09670	0.00460	0.01458	0.00033	0.01511	93.6	4.3	93.3	2.1	116.0	99.0	93.3	2.1
KR-5-18	0.09840	0.00840	0.01457	0.00051	0.03395	94.6	7.9	93.2	3.2	160.0	170.0	93.2	3.2
KR-5-18	0.10850	0.00410	0.01562	0.00034	0.52796	104.5	3.7	99.9	2.1	214.0	69.0	99.9	2.1
KR-5-18	0.09420	0.00880	0.01500	0.00048	0.07622	90.7	8.1	96.0	3.0	10.0	160.0	96	3
KR-5-18	0.10300	0.01100	0.01610	0.00075	0.16493	99.2	10.0	102.9	4.7	60.0	190.0	102.9	4.7
KR-5-18	0.11400	0.01400	0.01549	0.00056	0.24525	109.0	13.0	99.1	3.6	310.0	210.0	99.1	3.6
KR-5-18	0.10480	0.00820	0.01554	0.00051	0.19191	100.7	7.5	99.4	3.2	170.0	150.0	99.4	3.2
KR-5-18	0.09830	0.00340	0.01471	0.00029	0.21758	95.1	3.1	94.1	1.8	130.0	66.0	94.1	1.8
KR-5-18	0.10010	0.00410	0.01508	0.00032	0.21571	96.7	3.8	96.5	2.0	119.0	78.0	96.5	2
KR-5-18	0.10190	0.00280	0.01526	0.00031	0.23436	98.5	2.6	97.6	2.0	140.0	58.0	97.6	2
KR-5-18	0.10190	0.00610	0.01548	0.00040	0.04030	98.1	5.6	99.0	2.5	100.0	110.0	99	2.5
KR-5-18	0.11400	0.01100	0.01602	0.00068	0.02707	108.9	9.8	102.4	4.3	270.0	190.0	102.4	4.3
KR-5-18	0.10290	0.00290	0.01535	0.00030	0.26064	99.4	2.7	98.2	1.9	139.0	55.0	98.2	1.9
KR-5-18	0.10160	0.00770	0.01512	0.00043	0.14434	97.7	7.1	96.7	2.7	130.0	140.0	967	2.7
KR-5-18	0.10110	0.00440	0.01413	0.00032	0.09653	97.7	4.0	90.4	2.1	275.0	91.0	90.4	2.1
KR-5-18	0.10000	0.00780	0.01468	0.00042	0.05160	96.5	7.1	93.9	2.7	170.0	150.0	93.9	2.7
KR-5-18	0.09970	0.00380	0.01519	0.00028	0.09040	96.3	3.5	97.2	1.8	93.0	72.0	97.2	1.8
KR-5-18	0.10400	0.01400	0.01487	0.00078	0.03423	99.0	12.0	95.1	4.9	150.0	230.0	95.1	4.9
KR-5-18	0.09690	0.00560	0.01429	0.00033	0.13553	94.4	5.4	91.4	2.1	170.0	110.0	91.4	2.1
KR-5-18	0.09980	0.00270	0.01532	0.00027	0.12818	96.9	2.6	98.0	1.7	82.0	55.0	98	1.7
KR-5-18	0.09920	0.00680	0.01592	0.00041	0.04376	95.6	6.3	101.8	2.6	20.0	120.0	101.8	2.6
						207/235		206/238		207/206		Best age	

Detailed Age Data for the **KR-13-17**

Grain #	207/235	2σ Prop	206/238	2σ Prop	RHO	Age Ma	2σ Prop	Age (Ma)	2σ Prop	Age (Ma)	2σ Prop	(Ma)	2σ Prop
KR-13-17	0.101	0.016	0.01513	0.00073	0.05	95	14	96.8	4.7	20	260	96.8	4.7
KR-13-17	0.0965	0.0053	0.01431	0.00037	0.14	93.4	4.9	91.6	2.3	150	120	91.6	2.3
KR-13-17	0.126	0.016	0.01699	0.00083	0.08	120	14	108.6	5.2	270	240	108.6	5.2
KR-13-17	0.0909	0.0048	0.0124	0.00029	0.37	88.3	4.5	79.4	1.8	320	110	79.4	1.8
KR-13-17	0.122	0.031	0.0155	0.0013	0.28	115	28	99.2	8.4	290	450	99.2	8.4
KR-13-17	0.1249	0.0054	0.01512	0.00031	0.14	119.3	4.8	96.7	2	566	92	96.7	2.0

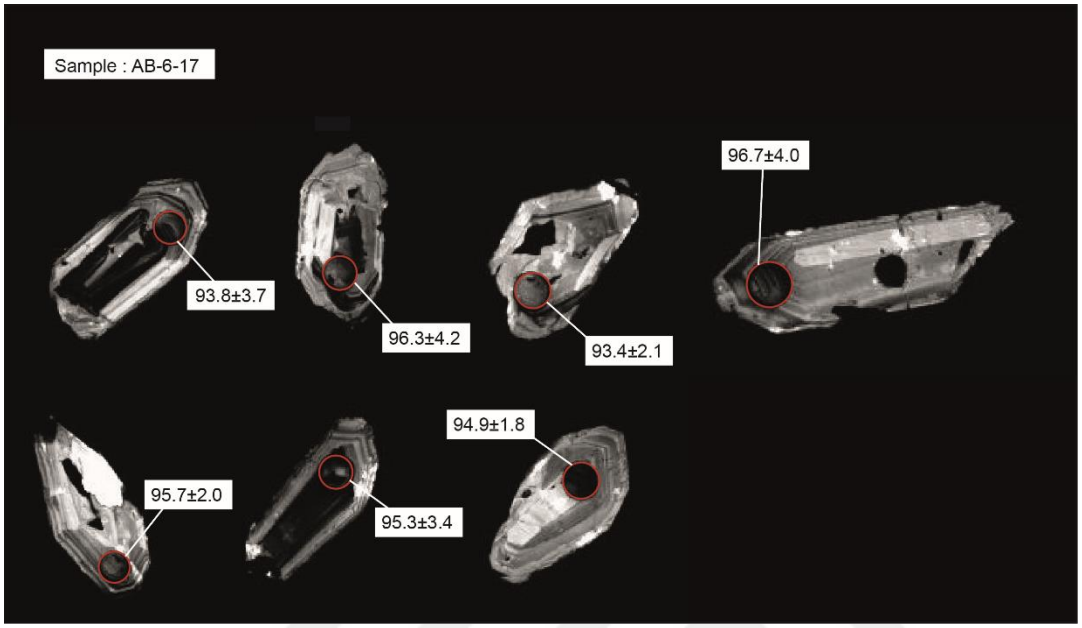
Detailed Age Data for the **YD-1-18**

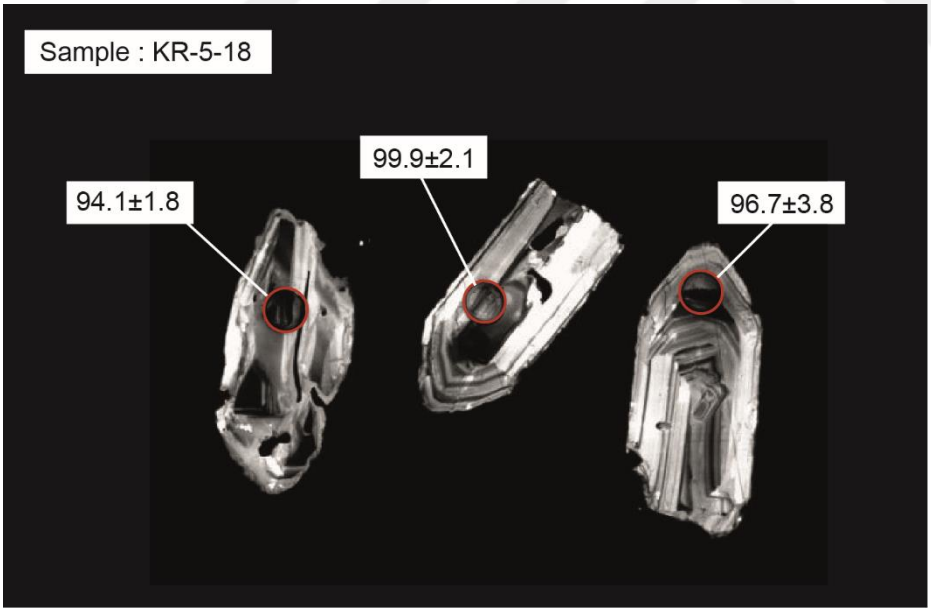
						207/235		206/238		207/206		Best age	
Grain #	207/235	2σ Prop	206/238	2σ Prop	RHO	Age Ma	2σ Prop	Age (Ma)	2σ Prop	Age (Ma)	2σ Prop	(Ma)	2σ Prop
YD-1-18	0.091	0.011	0.01439	0.00059	0.04	87.5	9.8	92.1	3.7	93.1	35	92.1	3.7
YD-1-18	0.0975	0.004	0.01452	0.00031	0.04	94.3	3.7	92.9	2	125	83	92.9	2
YD-1-18	0.095	0.0063	0.0146	0.00046	0.24	91.8	5.8	93.4	2.9	70	120	93.4	2.9
YD-1-18	0.1024	0.0056	0.0149	0.00037	0.25	98.8	5.2	95.4	2.4	180	110	95.4	2.4

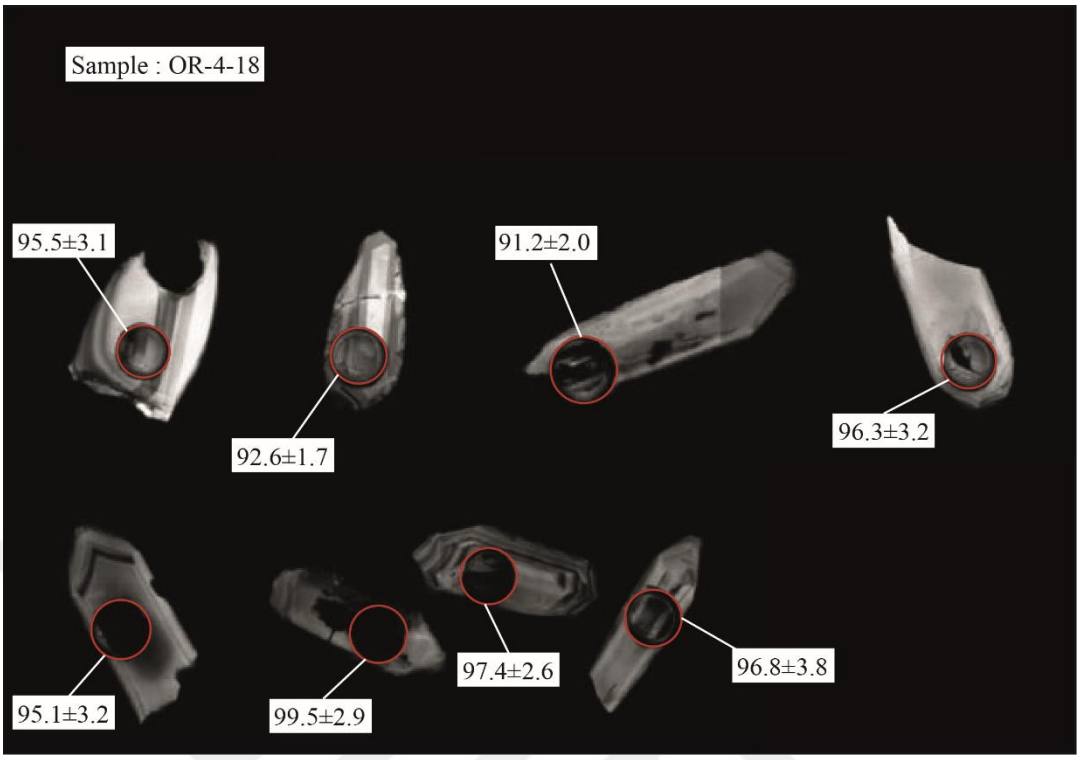
Detailed Age Data for the **OR-4-18**

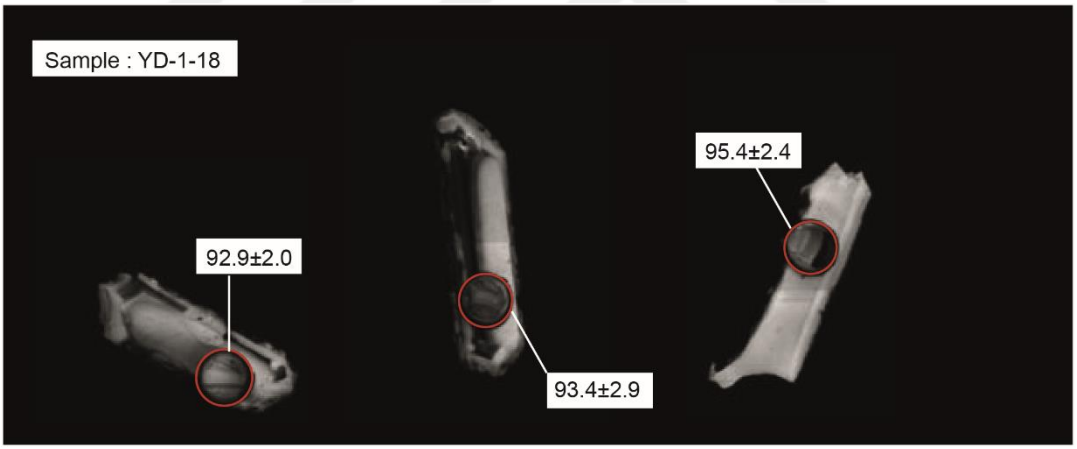
						207/235		206/238		207/206		Best age	
Grain #	207/235	2σ Prop	206/238	2σ Prop	RHO	Age Ma	2σ Prop	Age (Ma)	2σ Prop	Age (Ma)	2σ Prop	(Ma)	2σ Prop
OR-4-18	0.1031	0.0082	0.01492	0.00049	0.05	98.9	7.5	95.5	3.1	190	150	95.5	3.1
OR-4-18	0.097	0.011	0.01505	0.00069	0.30	93.1	9.6	96.3	4.4	80	200	96.3	4.4
OR-4-18	0.0984	0.0097	0.01467	0.00058	0.12	94.3	8.9	93.9	3.7	140	190	93.9	3.7
OR-4-18	0.1032	0.0095	0.01483	0.00052	0.09	98.9	8.7	94.8	3.3	210	170	94.8	3.3
OR-4-18	0.0978	0.0062	0.01469	0.00038	0.16	94.4	5.7	94	2.4	90	120	94.0	2.4
OR-4-18	0.0941	0.0078	0.015	0.00047	0.11	90.7	7.2	96	3	-10	140	96.0	3.0
OR-4-18	0.1	0.011	0.01526	0.00057	0.17	95	10	97.6	3.6	50	180	97.6	3.6
OR-4-18	0.1022	0.0038	0.01446	0.00027	0.18	98.7	3.5	92.6	1.7	248	80	92.6	1.7
OR-4-18	0.103	0.011	0.01496	0.00055	0.02	99	9.7	95.7	3.5	150	190	95.7	3.5
OR-4-18	0.1009	0.0055	0.01491	0.00037	0.00	97.3	5.1	95.4	2.4	130	110	95.4	2.4
OR-4-18	0.1022	0.0069	0.01425	0.00031	0.04	98.5	6.3	91.2	2	240	140	91.2	2.0
OR-4-18	0.0928	0.0094	0.01447	000052	0.03	89.2	8.7	92.6	3.3	40	180	92.6	3.3
OR-4-18	0.105	0.011	0.01513	0.0006	0.13	100	10	96.8	3.8	160	190	96.8	3.8
OR-4-18	0.1032	0.0065	0.01523	0.00042	0.09	99.3	6	97.4	2.6	140	130	97.4	2.6
OR-4-18	0.0957	0.0068	0.01495	0.00042	0.05	92.3	6.3	95.7	2.6	40	130	95.7	2.6
OR-4-18	0.104	0.013	0.01492	0.00059	0.23	99	12	95.5	3.7	160	230	95.5	3.7
OR-4-18	0.111	0.012	0.01507	0.00059	0.18	106	11	96.4	3.8	320	220	96.4	3.8
OR-4-18	0.0908	0.0093	0.01476	0.00061	0.06	88.8	9	94.4	3.9	20	190	94.4	3.9
OR-4-18	0.1045	0.0089	0.01486	0.0005	0.11	100.1	8.1	95.1	3.2	210	160	95.1	3.2
OR-4-18	0.0996	0.0088	0.01505	0.0005	0.04	95.6	8.1	96.3	3.2	100	160	96.3	3.2

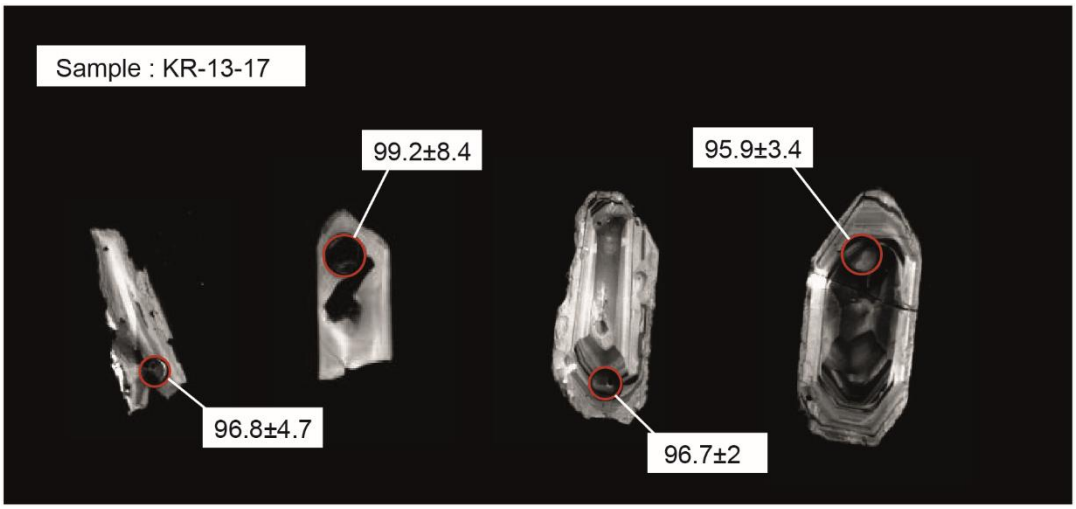
C. CL Images of the zircon grains from the Kösdağ Metavolcanics

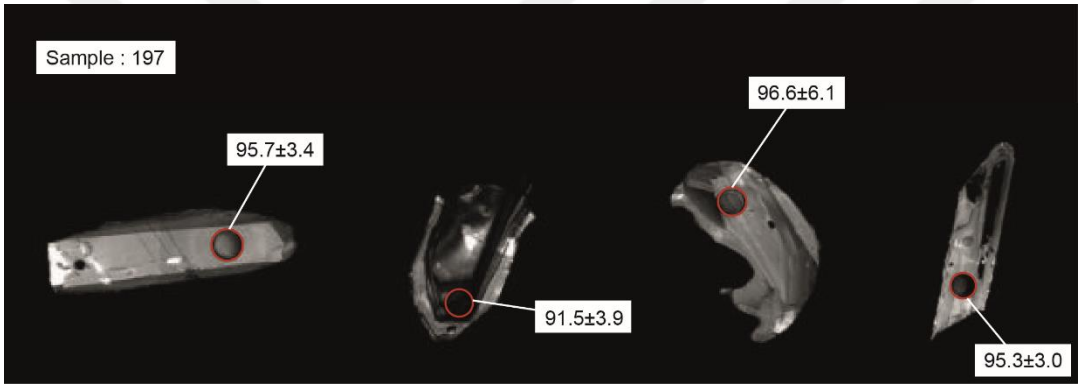





Sample : OR-4-18
95.5±3.1
92.6±1.7
91.2±2.0
96.3±3.2
95.1±3.2
99.5±2.9
97.4±2.6
96.8±3.8


Sample : YD-1-18
92.9±2.0
93.4±2.9
95.4±2.4


Sample : KR-13-17
99.2±8.4
95.9±3.4
96.8±4.7
96.7±2


Sample : 197
96.6±6.1
95.7±3.4
91.5±3.9
95.3±3.0

CURRICULUM VITAE

Surname, Name: Berber, Faruk
Nationality: Turkish (T.C)
Date and Place of Birth: 29 October 1986, Çanakkale

EDUCATION

Degree	Institution	Year of Graduation
MS	METU Geological Engineering	2015
BS	KTU Geological Engineering	2011
High School	Çan High School, Çanakkale	2005

WORK EXPERIENCE

Year	Place	Enrollment
2012-2018	METU Dept. of Geological Eng.	Research Assistant
2018-2021	Atatürk Uni. Dept. of Geological Eng.	Research Assistant

FOREIGN LANGUAGES

English

PUBLICATIONS

1. Berber, F., Sayıt, K., Göncüoğlu, M.C. 2021. Geochemistry and U-Pb ages from the Kösdağ Metavolcanics in the southern Central Pontides (Turkey): Complementary data for early Late Cretaceous island arc development in the Northern Neotethys, Turkish Journal of Earth Sciences, 30(1), 59-80

Poster/Oral Presentation

1. Berber, F., Sayıt, K., Göncüoğlu, M.C., and Crowley, Q. 2016. Geochemistry, Geochronology and Petrology of the Kösedağ Metavolcanic Rocks to the South of Tosya Central Pontides. 69. Geological Congress of Turkey, Ankara.

2. Berber, F., Göncüoğlu, M.C., and Sayıt, K. 2015. Geochemistry and Petrology of the Kösedağ metavolcanic rocks, Sakarya Composite Terrane, Northern Turkey. Goldschmidt Conference, Prag, Czech Republic.

3. Berber, F., Göncüoğlu, M.C., and Sayıt, K. 2015. Geochemistry and Tectonic Significance of the Kösedağ Metavolcanic Rocks from the Sakarya Zone, Northern Turkey. 20th CBGA Congress, Tirana, Albania.

PROJECTS

Petrology and Geology of the Kösdağ Metavolcanics, METU BAP Project BAP-03-09-2015-002 / Researcher – Completed